High Temperature Superconducting Devices

by

Marcos Tavares De Melo

A thesis submitted to the Faculty of Engineering
of The University of Birmingham
for the degree of
DOCTOR OF PHILOSOPHY

School of Electronic and Electrical Engineering
Faculty of Engineering
The University of Birmingham
December 1996

Synopsis

This thesis is split into two main areas. The main objective of the first part is to obtain surface resistance values for superconducting thin films using a wide microstrip resonator. The thin films are deposited on only one side of a magnesium oxide (MgO) substrate. Thick films made by pyrolysis deposited on one side of zirconia (YSZ) substrate are also measured. The microstrip consists of a copper ground plane and a superconducting second conductor with MgO (or YSZ) dielectric spacer. An expression for the unloaded quality factor of the resonator is developed considering the effect of both thickness and penetration depth for superconducting thin film. The penetration depth is the same order as the thickness of the film. This calculation proved to be more accurate in the extraction of surface resistance from unloaded quality factor results. This is in comparison to the classical calculation which considers the penetration depth to be much less than the thickness of the film.

In the second part of this work a superconducting coplanar instantaneous frequency measurement (IFM) subsystem is investigated. In order to design the delay lines of the interferometers without bends, a slow wave structure is optimised to achieve the desired delay times. Keeping all the other parameters fixed and varying the finger length from 0.6 mm to 4.2 mm, coplanar strips interdigital delay lines are simulated, fabricated and measured for a frequency range of 0.5-3 GHz. In order to avoid the use of air bridges a special coplanar strip power splitter is optimised. Based on this power splitter, a coplanar unequal output impedance power splitter is designed to feed the different delays of each interferometer. Simulated and experimental results of characteristic impedances and group delay of the interdigital delays are used together to design the different delay lines required. Coplanar wave guide, coplanar strips, coplanar unequal output impedance power splitter and coplanar interdigital delay line are integrated without bends or air bridges. Two interferometers with delay differences of 0.6ns and 1.6ns are designed, fabricated and measured at the central frequency of 2GHz over a bandwidth of 1GHz. Theoretical and experimental responses are given together and are in good agreement. A prototype of a 2-bit IFM is measured, connecting the two interferometers. A high temperature superconducting coplanar IFM is proposed to overcome the additional loss.

To my father

Milton Tavares De Melo

and to the memory of my mother

Enilza Soares De Melo

Acknowledgements

Firstly I would like to thank my supervisor Dr Mike Lancaster for his patience, attention and many helpful discussions. In the School of Physics and Space Research I would like to thank Prof. Colin Gough for his support and enthusiasm for superconductivity.

In the School of Electronic and Electrical Engineering I would like to thank Dr J. S. Hong, who has always been around for advice. I would also like to thank all fellow members of the Superconducting Group at Birmingham University mainly A. Elston, Dr H. Cheng, D. S. Hung, Dr J. Powell, Dr A Porch, Dr F. Huang, Dr P Woodall, Dr M Esa, Dr. B. Avenhaus, Dr H. Yokota, M. Holroyd, S. Watcham and A. P. Kharel for their encouragement and stimulating discussions.

I also wish to thank my sponsors: The CNPq-Conselho Nacional de Desenvolvimento Científico e Tecnológico (CNPq) of the Ministery for Science and Technology of Brazil and the UFPE (Universidade Federal de Pernambuco-Brasil).

With very special thanks to my wife MARIA and
my sons MARCOS Jr. And DANIEL
for everything.

Contents

Chapter 2 Surface Impedance

Chapter 3 Superconducting Microstrip Line

Chapter 4

Effective Surface Impedance of Superconducting Thin Films

Chapter 5 Superconducting materials

Chapter 6 Microstrip Resonator Experimental Results

Chapter7 Coplanar Structures

Chapter 8 Transmission Line Theory

Chapter 9 Instantaneous Frequency Meter Subsystem

9.3 Simulation Process

    9.3.2 Coplanar Strips Interdigital Delay Lines

9.4 Power Divider

Chapter 10

Experimental Results on Digital Instantaneous Frequency Measurement Subsystems

Chapter 11 Conclusions and Further Work

Appendix III Mathcad Programs

Chapter 1

Introduction

Superconductivity is the name given to a remarkable combination of electric and magnetic properties which appear in certain metals when they are cooled to extremely low temperatures. This was discovered by a Dutch physicist called Heike Karmerlingh Onnes in 1911 [1.1]. The first superconductor he discovered was mercury (Hg). When he cooled down the purified mercury to the liquid helium temperature, 4.2K, the resistance abruptly dropped to zero at a critical temperature, T_c [1.2]. Since then and until 1986, even though many metals, alloys and some composite materials were found to be superconductors, the rise of T_c has been very slow. Since the discovery of the superconductor properties of $YBa_2Cu_3O_{7-\delta}$ at temperatures ranging higher than 77K a great number of investigations has been carried out.

Superconductors can greatly impact selective passive microwave device applications because of two properties that differ from the properties of normal metals at high frequencies. Much lower surface resistance can be obtained with superconductors, corresponding to much higher quality factors in microwave system components. Superconductors have a frequency-independent penetration depth that determines field penetration into the material rather than a frequency-dependent skin depth as for normal conductors. This means that superconductors introduce very little dispersion into a microwave device to frequencies as high as 200 MHz, although dielectric losses may still produce dispersion[1.3].

There are several microwave applications of high temperature superconductors that have been demonstrated. The earliest applications of HTS technology in practical microwave systems will most likely be found in satellites. Partial passive cooling may be feasible, or the weight and volume advantages of the superconducting component make up for the additional cooling equipment and power consumption. With the rapid progress being currently made in the efficiency and size of cryogenic coolers, HTS applications should also become feasible in a variety of airborne and even land-mobile communications systems [1.4].

Substrate material is a critical parameter in the successful development of high Tc films for microwave devices. Acceptable substrate materials must fulfil two major requirements. They must promote crystalline growth of the high Tc films and must have low loss tangents. The most common single crystal substrates currently in use are magnesium oxide (MgO) and lanthanum aluminate ($LaAlO_3$). MgO is hydrophilic and becomes more lossy when exposed to moisture; $LaAlO_3$ exhibits an inhomogeneity in dielectric constant by several percent over 1cm × 1cm substrate.

Several techniques have been used for the fabrication of superconducting films. One of the most successful process of deposition is laser ablation. An important issue in the fabrication of an operational HTS circuit is the post processing of the laser ablated film. Since the majority of circuits are in a microstrip configuration, the application of a ground plane to the substrate and a patterning process is essential. During the laser ablation a thermally conductive and adhesive silver paste is used to hold the substrate to the heater, which is still adhered to the back to the substrate after the process. The complete cleaning process is not an easy task and includes a plasma cleaning followed by a silver etch [1.5]. The difficulty in producing double-side HTS substrate has created interest in structure requiring a single conducting plane.

This work here aims to investigate two specific applications of superconductors. They will be microstrip resonator and coplanar instantaneous frequency measurement subsystem.

Microwave resonators are used in a variety of applications, including filters, oscillators, frequency meters and tuned amplifiers. The potential of HTC superconducting microstrip resonator applications seems to be very large. Some of the obvious advantages of using microstrip resonators are: simple design, discrete components are easily connected into the circuit, no direct electrical contact needs to be made to the material. The resonance curves associated with this structure can be observed with transmission-type measurements, plotting the insertion loss as a function of the frequency. Chapters 2, 3, 4, 5 and appendix 2 will present some physical concepts and the techniques used to take data from the experimental results and transform scattering parameters into numerical values of surface resistance. Surface resistance equations derived from two-fluid model, taking into account the thickness of the films, will be also used to analyse the performance of the superconducting films fabricated by both laser ablation and pyrolysis processes.

Instantaneous frequency measurement (IFM) subsystems are widely used in electronic warfare (EW) and electronic intelligent (ELINT) systems for the determination of the frequency of unknown signals over a broad frequency band [1.6]. They perform this function by the comparison of the phase of the unknown signal with the phase of a time delayed replica of it. Digital instantaneous receivers using delay-line discriminators were developed in the early 1960s specifically as wideband and accurate analysers of pulsed radar signals [1.7]. The frequency resolution of the IFM depends on the length of the delays, which become in practice the principal elements of the subsystem. The delay lines are often designed with high numbers of bends in order to achieve the desired resolution in a small area. However, these bends increase the mutual reflections through the delays. Combining the results of group delay and characteristic impedance for a coplanar strip interdigital delay, it looks possible to integrate these delays with coplanar power splitters and then form uniplanar IFM systems, without bends. Superconducting delay lines offer the highest bandwidth with lowest loss and dispersion compared to currently available technology. The IFM system described in this work is proposed to use high temperature superconductors to overcome the additional loss.

Chapter 2

Surface Impedance

2.1. Introduction

The main objective of this chapter is to review some of the classical procedures used to calculate surface impedance for both normal conducting slabs and superconducting slabs.

At very low frequencies, current distributes itself uniformly throughout the cross section of a normal conductor. As the frequency increases, the current redistributes, crowding towards the surface of the conductor. At microwave frequencies, the current is effectively confined to a thin skin just inside the surface of the conductor [2.1.1]. For a superconductor the rf magnetic field penetrates into the surface to a depth equal to the London penetration depth, which is independent of the frequency. The rf magnetic field induces a time varying electric field. Due to the inertia of the superconducting electrons the induced electric field is not shunted to zero. As long as the superconducting penetration depth is very small compared to the skin depth, it is the factor limiting the penetration of the rf magnetic field into the superconductor and thus dominates the surface impedance.

2.2. Normal Metal

At microwave frequencies, the skin effect governs the penetration of currents and magnetic fields into the surface of a normal metal. The depth of the penetration depends on the frequency and on the properties of the conductive material. The behaviour toward high frequency alternating current becomes a surface phenomenon rather than a volume phenomenon when the depth of the penetration is much smaller than the thickness of the conductor. Thus, this effect is called the skin effect due to the current being concentrated in the outer surface of the conductor.

Figure 2.2.1 shows the geometry to be analysed. It consists of two parallel slab conductors, each assumed to be very thick, with width w. A sinusoidal current density of the form $J_0e^{j\omega t}$ is applied on x-direction, as shown. Here, $\omega = 2\pi f$ and f is the frequency. This structure is a wide microstrip transmission line, the current is going along the top slab in the x-direction and returning through the bottom one. For the sake of symmetry, we shall focus our calculation on the bottom slab only.

J_x is the vector component of the current in the x-direction and H_y is the vector component of the induced magnetic field in the y-direction.

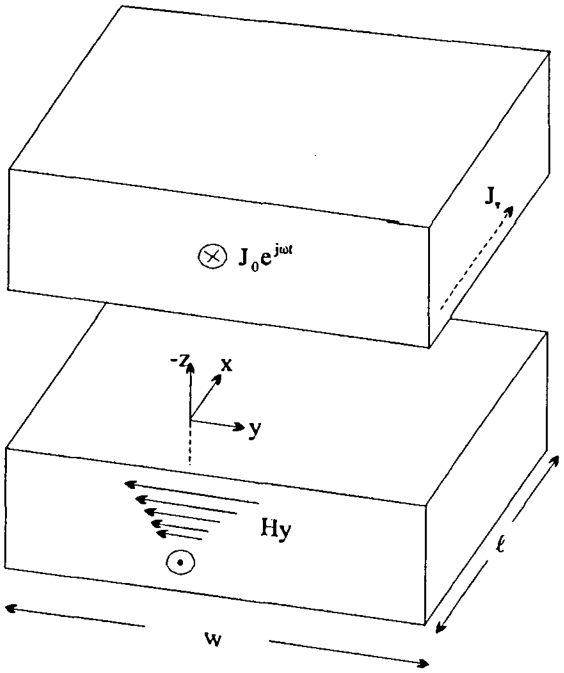

Figure 2.2.1: Two parallel and infinitely thick slabs [2.2.1].

In a linear, isotropic, charge free and homogeneous region, Maxwell's equations inside a good conductor, assuming sinusoidal time variation for the fields are then given by

$$\underline{\nabla} \times \underline{E} = -j\omega\mu\underline{H} \qquad \text{equation 2.2.1}$$

$$\underline{\nabla} \times \underline{H} = \underline{J} \qquad \text{equation 2.2.2}$$

$$\underline{\nabla} . \underline{H} = 0 \qquad \text{equation 2.2.3}$$

$$\underline{\nabla} . \underline{E} = 0 \qquad \text{equation 2.2.4}$$

In equation 2.2.2 we assumed the approximation of zero displacement current as in a good conductor, i.e. $\sigma >> \omega\varepsilon$. μ, σ and ε, are the permeability, conductivity and the permittivity of the slab material, respectively.

Taking the curl of both sides of equation 2.2.2 and using $\underline{\nabla} \times \underline{\nabla} \times \underline{H} = \nabla(\underline{\nabla} . \underline{H}) - \nabla^2 \underline{H}$, $\underline{J} = \sigma\underline{E}$ and equation 2.2.3 we get

$$\nabla^2 \underline{H} = -\sigma(\underline{\nabla} \times \underline{E}) \qquad \text{equation 2.2.5}$$

Substituting equation 2.2.1 into equation 2.2.5 we find

$$\nabla^2 \underline{H} = (j\omega\mu\sigma)\underline{H} \qquad \text{equation 2.2.6}$$

Here $\underline{H} = H_x \underline{a}_x + H_y \underline{a}_y + H_z \underline{a}_z$.

The above equation is the general Helmholtz equation, for $\underline{H}$. A basic plane wave solution to the equation 2.2.6 can be obtained considering a magnetic field with only an $\underline{a}_y$ component, and uniform (no variation) in x and y directions. So one has

$$\frac{\partial^2 H_y}{\partial z^2} = j\omega\mu\sigma H_y \qquad \text{equation 2.2.7}$$

The wave is travelling in the z-direction ($z \geq 0$) in the thick slab. The solution of the equation 2.2.7 is

$$H_y = H_0 e^{-\gamma z} \qquad \text{equation 2.2.8}$$

Where

$$\gamma^2 = (\alpha + j\beta)^2 = j\omega\mu\sigma \qquad \text{equation 2.2.9}$$

Here γ is the complex propagation constant. The real and imaginary parts α and β represent the attenuation and the phase of the travelling wave.

Using $\sqrt{j} = \frac{1+j}{\sqrt{2}}$ into equation 2.2.9, we have

$$\gamma = \alpha + j\beta = (1+j)\sqrt{\frac{\mu\omega\sigma}{2}} \qquad \text{equation 2.2.10}$$

We can now define a characteristic depth δ, well known as skin depth given by

$$\sqrt{\frac{2}{\omega\mu\sigma}} = \frac{1}{\alpha} = \delta \qquad \text{equation 2.2.11}$$

The amplitude of the fields in the slab decay by an amount $1/e$ after travelling a distance of one skin depth. At microwave frequencies, for a good conductor, this distance is very small.

H. A. Wheeler was one of the first who, in 1942 [2.1.1], evaluated the internal impedance of a slab of width w and length ℓ by considering the skin effect. In order to review his calculation, figure 2.2.2 shows a second diagram of the bottom slab from figure 2.2.1.

Using equation 2.2.10 and equation 2.2.11 one can rewrite equation 2.2.8 as

$$H_y = H_0 e^{-(1+j)\frac{z}{\delta}} \qquad \text{equation 2.2.12}$$

The alternating current density $\underline{J}$ in the surface can be found substituting equation 2.2.12 into equation 2.2.2, where $\underline{\nabla} \times \underline{H} = -\frac{\partial H_y}{\partial z}\underline{a}_x = \underline{J}$, and then we find

$$\underline{J} = J_0 e^{-(1+j)\frac{z}{\delta}} \underline{a}_x \qquad \text{equation 2.2.13}$$

Here $J_0 = J_x$ at the surface, where z=0.

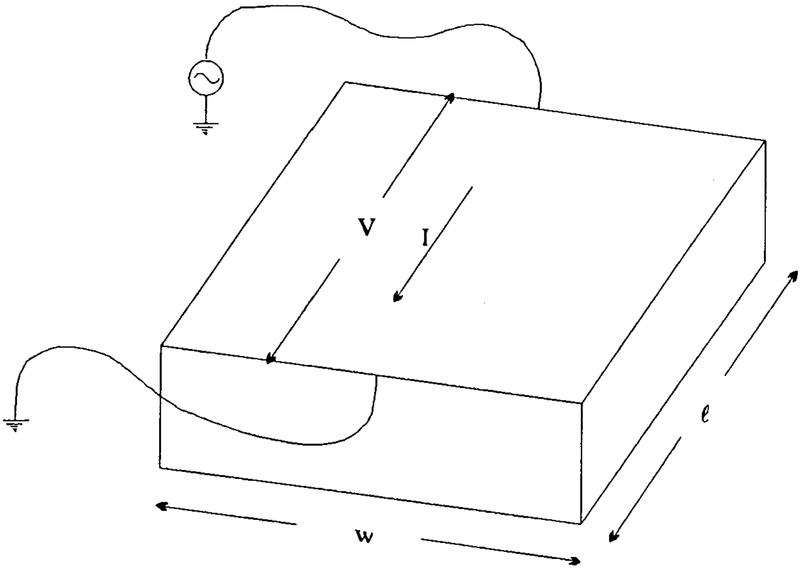

Figure 2.2.2: Section of length ℓ of the bottom strip shown in figure 2.2.1.

This way, the current density is concentrated in the upper surface and decreases with depth z. The total current through across the slab is given by the integral of J_x for infinite depth, over the width w [2.2.2].

$$I = w\int_0^\infty J_0\, e^{-(1+j)\frac{z}{\delta}} dz = \frac{J_0 w\delta}{1+j} \qquad \text{equation 2.2.14}$$

The voltage V across the slab surface, shown in figure 2.2.2, is expressed by

$$V = J_0 \ell \rho \qquad \text{equation 2.2.15}$$

where ρ is the resitivity of the slab material.

The internal impedance of the slab surface is found by

$$Z_a = \frac{V}{I} = (1+j)\frac{\rho\ell}{w\delta} = (1+j)\frac{\ell}{w}\frac{1}{\delta\sigma} \qquad \text{equation 2.2.16}$$

This way, the internal resistance of the slab surface is given by the real part of equation 2.2.16

$$R_a = \frac{\ell}{w}\sqrt{\pi f \mu \rho} = \frac{\ell}{w}\cdot\frac{1}{\delta\sigma} \qquad \text{equation 2.2.17}$$

The internal reactance of the slab surface is the imaginary part

$$X_a = \omega L_i = \frac{\ell}{w}\cdot\frac{1}{\delta\sigma} \qquad \text{equation 2.2.18}$$

where L_i is the internal inductance. When $\ell = w$ (i.e. the slab is a square) we have the surface resistance R_s and the surface reactance X_s given by

$$R_s = \frac{1}{\delta\sigma} \qquad \text{equation 2.2.19}$$

$$X_s = \frac{1}{\delta\sigma} \qquad \text{equation 2.2.20}$$

It should be noted that the above derivation assumes the local electrodynamics where the mean free path ℓ^*, i.e. the intrinsic average distance between scattering events from Drude's theory [2.2.3] is much less than the classical skin depth δ.

Equation 2.2.16 assumes that Ohm's law holds true for the propagation into the metal. In this case the current density $\underline{J}$ and the microwave field $\underline{E}$ are related to a more general equation [2.2.4]. Another point is that the thickness of the slab is supposed to be must greater than δ otherwise that thickness has to be taken into account in the equation 2.2.16 [2.2.5].

2.3 Superconductors

2.3.1 Londons' Phenomenological Equations

Originally, superconductivity was believed to be the limiting case of zero resistance. However, if we take the Faraday's law of induction

$$\underline{\nabla} \times \underline{E} = -\frac{\partial \underline{B}}{\partial t} \qquad \text{equation 2.3.1.1}$$

For $\underline{E} = 0$ we have that $\underline{B}$ is constant. From the Meissner effect we know that inside a superconductor the flux density $\underline{B}$ is not only constant but the value of this constant is always zero.

F. and H. London [2.3.1.1 and 2.3.1.2] started with the idea that one has to modify the usual electrodynamics equation in order to describe the Meissner effect. Assuming that the superconductor is composed of a number of free electrons per unit volume n_s with mass m_s charge e_s, they are accelerated by

$$\underline{a}_s = \frac{d\underline{v}_s}{dt} = \frac{-e_s\underline{E}}{m_s} \qquad \text{equation 2.3.1.2}$$

where $\underline{v}_s$ is the velocity of the superelectrons. The current density can be related to $\underline{v}_s$ by the following equation

$$\underline{J}_s = -e_s n_s \underline{v}_s$$

or

$$\frac{d\underline{J}_s}{dt} = -e_s n_s \frac{d\underline{v}_s}{dt} \qquad \text{equation 2.3.1.3}$$

Substituting equation 2.3.1.2 into equation 2.3.1.3 we find the first London equation

$$\frac{d\underline{J}_s}{dt} = \frac{\underline{E}}{\mu\lambda^2} \qquad \text{equation 2.3.1.4}$$

where

$$\lambda^2 = \frac{m_s}{\mu n_s e_s^{\ 2}} \qquad \text{equation 2.3.1.5}$$

Substituting equation 2.3.1.4 into equation 2.3.1.1 we have [2.3.1.3]

$$\frac{\partial}{\partial t}\left(\underline{\nabla} \times \underline{J} + \frac{\underline{B}}{\mu\lambda_L^{\ 2}}\right) = 0 \qquad \text{equation 2.3.1.6}$$

This relation, together with the Maxwell equation

$$\underline{\nabla} \times \underline{B} = \mu J \qquad \text{equation 2.3.1.7}$$

Determines the magnetic fields and current densities that can exist within a perfect conductor. Note in particular that any static field $\underline{B}$ determines a static current density $\underline{J}$. This is incompatible with the observed behaviour of superconductivity, which permit no fields in their interior. F. London and H. London discovered that this characteristic behaviour of superconductivity could be obtained by restricting the full set of solutions of equation 2.3.1.6 to those that obey

$$\underline{\nabla} \times \underline{J} = -\frac{\underline{B}}{\mu \lambda_L^{2}} \qquad \text{equation 2.3.1.8}$$

Which is the second London equation.

If we consider now a uniform infinite superconductor half-plane ($x > 0$) and apply the magnetic field parallel to the surface, the current density equation inside the superconductor can be found by taking the curl of equation 2.3.1.8 we get

$$\underline{\nabla}^{2} \underline{J} = \frac{1}{\lambda_L^{2}} \underline{\nabla} \times \underline{\underline{H}} \qquad \text{equation 2.3.1.9}$$

Substituting equation 2.3.1.7 into equation 2.3.1.9 we have

$$\underline{\nabla}^{2} \underline{J}_s = \frac{\underline{J}_s}{\lambda_L^{2}} \qquad \text{equation 2.3.1.10}$$

By similarity to the solution of equation 2.2.6 we have

$$\underline{J}_{xs} = J_{os} e^{-z/\lambda_L} \underline{a}_x \qquad \text{equation 2.3.1.11}$$

Here λ_L is defined as the London penetration depth that measures the extension of the penetration of the magnetic field inside the superconductor. J_{so} is the intensity of the current density at the surface $z=0$.

2.3.2 Local Versus Non Local Electrodynamics

At the end of section 2.2 the Local and non Local Electrodynamics issues were slightly introduced for the case of normal metal. Now, in this section, we shall try to focus on it for the case of superconductors. As an aid in understanding this problem we start reviewing, using the concept of coherent length.

The theory of Bardeen, Cooper and Schrieffer (BCS) [2.3.2.1] defines coherence length ξ_0 as the distance between two electrons of cooper pairs within the highly correlated coherent superconducting state. In other words, ξ_0 is an intrinsic parameter derived from the uncertainty principle of quantum mechanics [2.3.2.2], which is given by

$$\xi_0 = \frac{ahv_f}{kT_c} \qquad \text{equation 2.3.2.1}$$

Here h is Planck's constant, v_f is the electron velocity at the Fermi surface, k is the Boltzmann's constant and 'a' is the numerical constant of order unity.

The Local electrodynamics of the Londons' equations can be seen clearly if we rewrite equation 2.3.1.8 as a function of magnetic vector potential $\underline{A}$. Taking the curl of equation 2.3.1.8 and afterwards considering that $\underline{\nabla} \times \underline{A} = \underline{B}$ we get

$$\underline{J}_s(\underline{r}) = -\frac{\underline{A}}{\mu\lambda_L^{2}} \qquad \text{equation 2.3.2.2}$$

The current density $\underline{J}_s(r)$ at a point is directly proportional to the magnetic vector potential $\underline{A}$ at that point. This local electrodynamics is only true when the coherence length ξ_0 is smaller than the penetration depth λ_L. The London theory and resulting equation already presented in this chapter are only true for type-II superconductors where $\lambda_L > \xi_0$.

The equation 2.3.2.2 was well accepted until about 1950. At that time Pippard started measurements of microwave surface impedance of superconductors and reported that for pure superconductors ($\lambda_L \ll \xi_0$), as tin and aluminium (for a=0.15), the Londons' equations should be replaced by a non-local equation. In this new equation, Pippard relates $\underline{J}_s(r)$ to a weighted average of all vector potential in some neighbourhood of each point by the following relation [2.3.2.3]:

$$\underline{J}_s(\underline{r}) = -\frac{3ne^2}{4\pi\xi_0 m_s}\int \frac{\underline{R}[\underline{R}.\underline{A}(\underline{r}')]}{R^4}\exp(-R/\xi_p)\,d^3\underline{r}' \qquad \text{equation 2.3.2.3}$$

Where $\underline{R} = \underline{r} - \underline{r}'$ and $R = |\underline{R}|$. The Pippard coherence length ξ_P is given by

$$\frac{1}{\xi_P} = \frac{1}{\xi_0} + \frac{1}{\ell^*} \qquad \text{equation 2.3.2.3}$$

Here for pure material $\xi_P = \xi_0$ and for impure material $\xi_P = \ell^*$. In other words, the current density at a point is related to the values of the vector potential within a distance ξ_P about the point. However, in most practical superconductors and also in HTSC, $\lambda_L \gg \xi_0$. Thus, we will not consider such a complication further in this thesis.

The Table 2.3.2.1 shows some physical parameters for three superconductors. In accordance with these data, the parameters of YBCO allow the use of the two-fluid model, which will be described in the next section.

Table 2.3.2.1: Important material parameters for microwave application. Δ_0 is the energy gap at T=0K, from BCS theory [2.3.2.4].

Material	T_c [K]	Δ_0/kT_c	ℓ^* [nm]	$\xi_0(0)$ [nm]	$\lambda(0)$ [nm]	$\mu_0 H_c(0)$ [T]
Nb	9.2	1.97	>100	39	40	0.20
Nb_3Sn	18	2.20	>1	5.7	100	0.535
$YBa_2Cu_3O_7$ (preliminary)	93	1.5-4 (anisotr.?)	>1	ab:<2 c:<0.4	I_{ab}:140 I_c:770	1.0-1.4

2.3.3 Complex Conductivity

The two-fluid model [2.3.3.1] separates the charge carriers into the superconducting charge and the normal charge carriers. We shall review this model and find an appropriate expression for Z_s in the superconducting state. We start defining both the normal fluid and the superconducting fluid.

a) Normal fluid: consists of unpaired charge carriers, which are identical with the conduction electrons above T_c. The normal current density is given by

$$\underline{J}_n = \sigma_1 \underline{E} \qquad \text{equation 2.3.3.1}$$

where [2.3.3.1]

$$\sigma_1 = \frac{n_n e^2 \tau}{m\left(1+\omega^2\tau^2\right)} \qquad \text{equation 2.3.3.2}$$

In this expression n_n represents the number of unpaired charge carriers per unit volume, 'e' the electron charge, τ the scattering time from Drude's theory for metal and 'm' the electron mass.

b) Superconducting fluid: consists of paired charge carriers with supercurrent density expressed by

$$\underline{J}_s(t) = -j\sigma_2(t)\underline{E} \qquad \text{equation 2.3.3.3}$$

where [2.3.3.1]

$$\sigma_2 = \frac{n_s e^2}{m\omega} + \frac{n_n e^2 (\omega\tau)^2}{m\omega\left(1+\omega^2\tau^2\right)} \qquad \text{equation 2.3.3.4}$$

Thus, one has two contributions to the total current density, ie. the "two fluid model".

$$\underline{J} = \underline{J}_n + \underline{J}_s = \sigma\underline{E} \qquad \text{equation 2.3.3.5}$$

where

$$\sigma = \sigma_1 - j\sigma_2 \qquad \text{equation 2.3.3.6}$$

As one can see, equation 2.3.3.5 resembles Ohm's Law. Substituting equation 2.3.3.6 into equation 2.2.16 one can rewrite Z_s, as

$$Z_s = \left[j\omega\mu_o / (\sigma_1 - j\sigma_2)\right]^{1/2} = R_s + jX_s \qquad \text{equation 2.3.3.7}$$

Let us show how to find both R_s and X_s: [2.3.3.2]

$$Z_s = \frac{(j\omega\mu)^{1/2}}{(-j\sigma_2)^{1/2}\left(1 + j\frac{\sigma_1}{\sigma_2}\right)^{1/2}} \qquad \text{equation 2.3.3.8}$$

Assuming $\omega^2\tau^2 << 1$, which is typically for $f < 10^{11}$Hz, equation 2.3.3.2 and equation 2.3.3.6 become

$$\sigma_1 \cong \sigma_n\left(\frac{n_n}{n}\right) \qquad \text{equation 2.3.3.9}$$

and

$$\sigma_2 \cong \frac{n_s e^2}{m\omega} = \frac{1}{\mu\omega\lambda_L^{\ 2}} \qquad \text{equation 2.3.3.10}$$

where 'n' represents the total density of charge carriers and σ_n the conductivity in the normal state, which is equal to $\frac{ne^2\tau}{m}$. From the Gorter and Casimir two fluid model [2.3.3.1] one has

$$\frac{n_s}{n} = 1 - \left(\frac{T}{T_C}\right)^4 \qquad \text{equation 2.3.3.11}$$

and

$$\frac{n_n}{n} = \left(\frac{T}{T_C}\right)^4 \qquad \text{equation 2.3.3.12}$$

Substituting equation 2.3.3.11 into equation 2.3.3.10 one obtains

$$\lambda_L(T) = \lambda_L(0)[1-(T/T_c)^4]^{-1/2} \qquad \text{equation 2.3.3.13}$$

where $\lambda_L(0)$ is the penetration depth at T=0K, which is defined by

$$\lambda^2(0) = \frac{m_s}{\mu n e^2} \qquad \text{equation 2.3.3.14}$$

For $T < T_c$ one has $\sigma_1 << \sigma_2$.. The reason for this behaviour can be seen by having a look at equations from 2.3.3.9 to 2.3.3.13. In this range of temperatures a large amount of conducting electrons are condensed into Cooper pairs. As a result, n_n becomes small compared with n_s. Due to the small penetration depth even at Gigahertz frequencies $\sigma_2(\omega,t)$ becomes large compared with σ_1. Thus, for $\sigma_1 << \sigma_2$, one can combine the elements of the equation 2.3.3.8 in order to use the approximation $(1+j\sigma_1/\sigma_2)^{-1/2} \cong 1-j\sigma_1/2\sigma_2$ to give

$$Z_s = j\left(\frac{\omega\mu}{\sigma_2}\right)^{1/2}\left(1+j\frac{\sigma_1}{\sigma_2}\right)^{-1/2} \cong \left(\frac{\omega\mu}{\sigma_2}\right)^{1/2}\left(j+\frac{\sigma_1}{2\sigma_2}\right) \qquad \text{equation 2.3.3.15}$$

or

$$Z_s = \frac{(\omega\mu)^{1/2}}{2\sigma_2^{3/2}}\sigma_1 + j\frac{(\omega\mu)^{1/2}}{\sigma_2^{1/2}} \qquad \text{equation 2.3.3.16}$$

Substituting equation 2.3.3.10 into the last equation we finally have

$$R_s = \frac{\omega^2\mu_o^2\lambda^3\sigma_1}{2} \qquad \text{equation 2.3.3.17}$$

and

$$X_s = \omega\mu_o\lambda = \omega L_s \qquad \text{equation 2.3.3.18}$$

where [2.3.3.3]

$$L_s = L_i + L_k \qquad \text{equation 2.3.3.19}$$

and

$$L_i = \frac{1}{2}\mu\lambda \qquad \text{equation 2.3.3.20}$$

$$L_k = \frac{1}{2}\mu\lambda \qquad \text{equation 2.3.3.21}$$

X_s represents the surface inductive reactance of the superconducting slab and R_s represents the surface resistance of the superconducting slab. L_i is the internal inductance and represents the magnetic energy storage in the superconductors, L_k is the kinetic inductance and represents the kinetic energy storage in the supercurrent due to their inertia and L_s is the total inductance inside the superconductors. For a perfect conductor the rf surface impedance is assumed to be zero. However for a superconductor the substantial inertia of the superelectrons makes a non-vanishing rf electric field appear, which is concentrated within the skin depth at the superconductor surface [2.3.3.4].

2.3.4 Effective Penetration Depth of Granular Superconductor

Superconducting thick film ceramic is an extremely granular 3D-like material. In YBCO the intergrain regions behave like weak links or tunnel junctions limiting severely its bulk critical current density. The aim of this section is to study the influence of weak-links on microwave properties of HTC superconductors. For simplicity, we shall consider a uniform distribution of identical grains, where the distance between two immediate grain centres is defined as ‘a’. Figure 2.3.4.1 shows a highly idealised model for a granular superconductor [2.3.4.1].

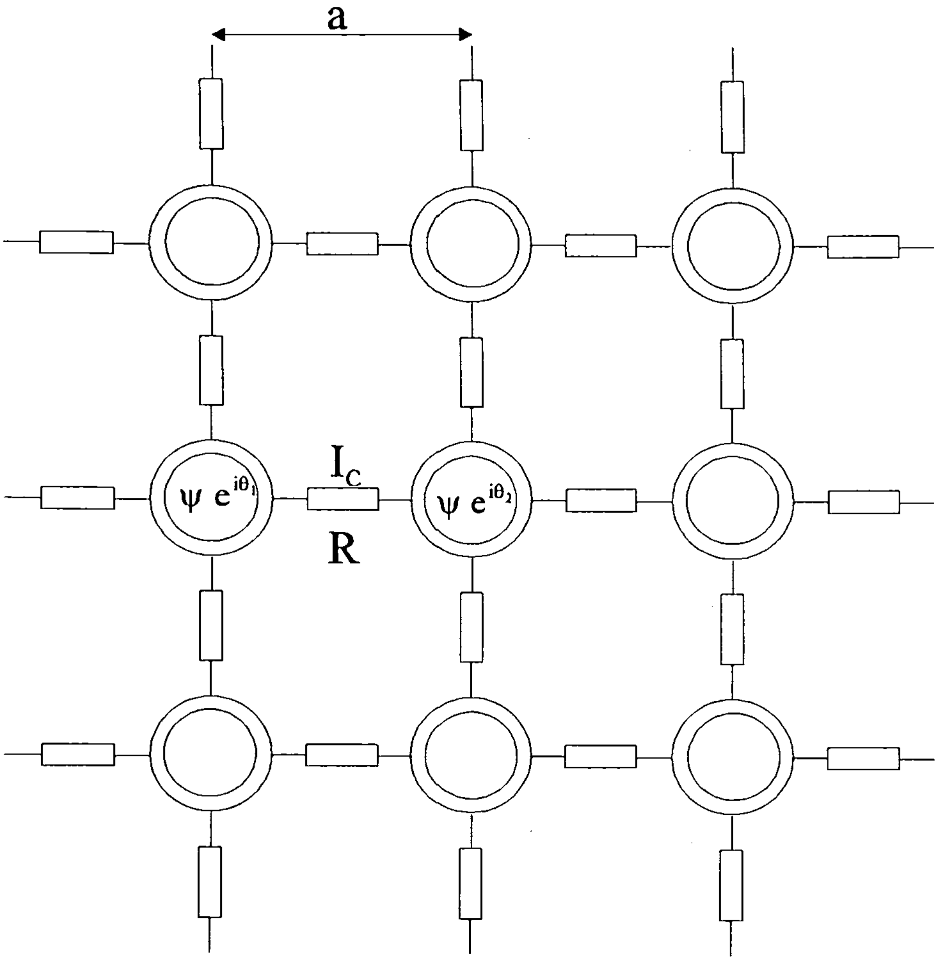

Figure 2.3.4.1: Idealised model for a granular superconductor [2.3.4.1].

I_c is the critical current and R is the parallel resistor of the intergranular material. The smaller circle represents the region from which magnetic flux can not penetrate. θ_1 and θ_1 are the phases of the respective order parameters $|\psi_1|e^{j\theta_1}$ and $|\psi_2|e^{j\theta_2}$. From the DC Josephson Effect we know that the supercurrent which flows between two superconductors separated by a tunnel barrier is given by

$$I = I_0 \sin(\theta_2 - \theta_1) \qquad \text{equation 2.3.4.1}$$

AC Josephson Effect gives for the voltage-phase relation the following equation

$$\Delta\theta(t) = \theta_2(t) - \theta_1(t) = \frac{2\pi}{\phi_0}\int V(t)dt \qquad \text{equation 2.3.4.2}$$

where ϕ_0 is the flux quantum and V(t) is the drop voltage across the junction in the direction of the current flow. Making an analogy with circuit theory, figure 2.3.4.2 presents the equivalent circuit of Josephson junction.

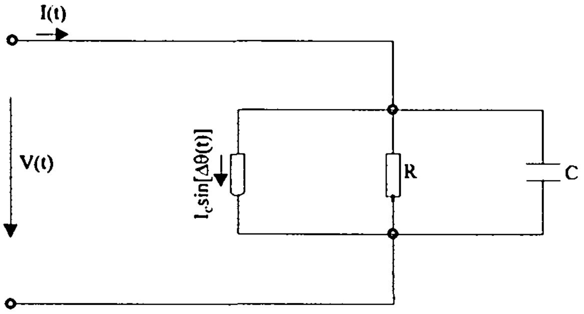

Figure 2.3.4.2 General equivalent circuit of Josephson junction [2.3.4.2].

For the sake of simplicity, the effect of capacitance will not be taken into account in this calculation. Hence, the total current across the junction is apparently given by

$$I(t) = \frac{V(t)}{R} + I_C \sin[\frac{2\pi}{\phi_0}\int V(t)dt] \qquad \text{equation 2.3.4.3}$$

Differentiating equation 2.3.4.3 with respect to time we have

$$\frac{dI(t)}{dt} = \frac{1}{R}\frac{dV(t)}{dt} + \frac{2\pi I_c V(t)}{\phi_0}\cos[\frac{2\pi}{\phi_0}\int V(t)dt] \qquad \text{equation 2.3.4.4}$$

In order to work out further simplifications, we shall carry on three steps from equation 2.3.4.4: divide all by a^2, substitute E=V/a and assume a small microwave current. So, one obtains

$$\frac{dJ}{dt} = \frac{1}{aR}\frac{dE}{dt} + \frac{2\pi I_c E}{\phi_0 a} \qquad \text{equation 2.3.4.5}$$

The above equation may be compared to the equivalent circuit of an inductor $L=\phi_0/2\pi I_c$ in parallel with resistor R, as can be seen in figure 2.3.4.3

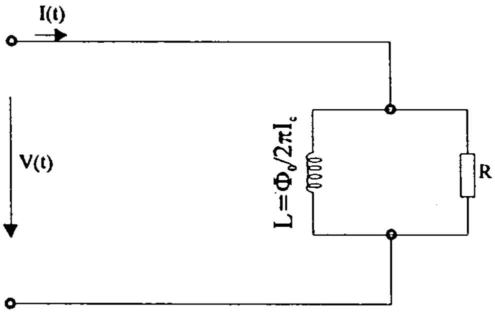

Figure 2.3.4.3 Equivalent circuit based on the equation 2.3.4.5

Using equations 2.3.3.5 and 2.3.3.6 we have $J = \sigma_1 E - j\sigma_2 E$, where σ_1 and σ_2 are given by equations 2.3.3.9 and 2.3.3.10, respectively. So we get $J = \sigma_n \frac{n_n}{n} E - j\frac{1}{\omega\mu\lambda^2} E$. Differentiating this equation with respect to the time one obtains

$$\frac{dJ}{dt} = \sigma_n \frac{n_n}{n}\frac{dE}{dt} - j\frac{1}{\omega\mu\lambda^2}\frac{dE}{dt} \qquad \text{equation 2.3.4.6}$$

Assuming a sinusoidal time variation for the fields equation 2.3.4.6 may be set up the following way

$$\frac{dJ}{dt} = \sigma_n \frac{n_n}{n}\frac{dE}{dt} + \frac{1}{\mu\lambda^2} E \qquad \text{equation 2.3.4.7}$$

Comparing equation 2.3.4.7 with equation 2.3.4.5 the effective penetration depth for the granular superconductor is given by

$$\lambda^2_g = \frac{\phi_0 a}{2\pi\mu I_c} \qquad \text{equation 2.3.4.8}$$

and the granular conductivity

$$\sigma_g = \frac{1}{aR} \qquad \text{equation 2.3.4.9}$$

This way, the granular effective penetration depth value is governed by a kind of competition between the intergranular distance and the critical current density. In addition to this, the granular conductivity depends on both intergranular distance and intergranular resistance. The granular effective penetration depth λ_g in a granular superconductor plays much the same role as the London penetration depth λ_L in a conventional type-II superconductor. Below a lower intergranular critical field H_{c1g} any external field penetrates only to a distance λ_g at the surface. Above this field, flux penetrates as giant flux lines, which will be pinned by sample inhomogeneities, leading to additional microwave loss. This state persists until H_{c2g} corresponding to one flux quantum per grain, when the continuum model clearly breaks down [2.3.4.1].

Chapter 3

Superconducting Microstrip Line

3.1. Introduction

Microstrip transmission lines are very useful for the microwave and millimetre wave hybrid integrated circuit. Because of their planar structure, microstrip lines are commonly required for solid-state and more recently for superconducting microwave devices. In comparison with conventional coaxial and waveguide circuit technology, circuits built with microstrip transmission lines have the great advantage of deposition on a single dielectric substrate at a substantially lower cost and convenience [3.1.1].

Microstrip line consists of a conductor of width 'w' and thickness 't' suspended from a distance 'h' above a conducting ground plane by a uniform dielectric of relative permittivity ε_r, as shown in figure 3.1.1.

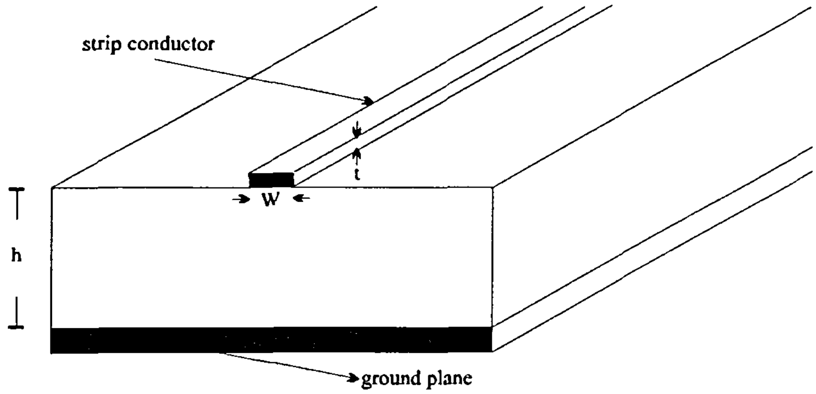

Figure 3.1.1 Microstrip line [3.1.2].

This open side configuration is very suitable to be used in Microwave Integrated Circuits (MICs) as discrete lumped devices can be mounted in the circuit. On the other hand, it implies that the electromagnetic field is not confined to the dielectric but is partly in the air space as shown in figure 3.1.2. This gives rise to more complicated modes of propagation.

As it can be seen in figure 3.1.2, both the electric field and the magnetic field are drawn as traverse (TEM propagation mode) which is valid only at low microwave frequency.

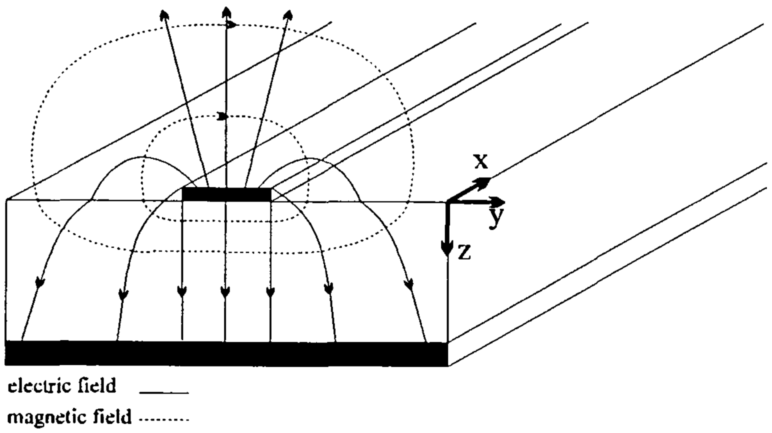

Figure 3.1.2 Pattern of the electromagnetic field of a microstrip line [3.1.3].

For simplicity, section 3.2 will start with the wide microstrip line case where w/h >> 1.

3.2. Wide Microstrip Line

When the width of the strip is much greater than the dielectric thickness h, the calculations are greatly simplified.

It will be assumed that there is no variation of any quantity in the $\underline{a}_x$ direction and that $\underline{E}$ is everywhere normal and $\underline{H}$ is parallel to the conductor surface. Thus, one can apply the Gauss' law and find the electric field between plates as given by

$$E_z = \frac{Q}{\varepsilon w \Delta \ell} \qquad \text{equation 3.2.1}$$

Here Q is the total charge on either plate and ε is the permittivity of the dielectric.

The voltage between the plates is expressed by

$$V_o = E_x h \qquad \text{equation 3.2.2}$$

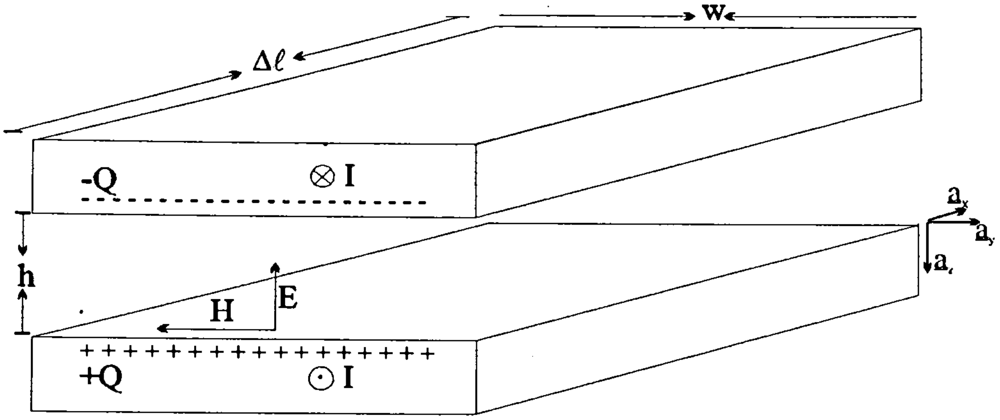

Figure 3.2.1 Approximated sketch of microstrip line for w/h >> 1 [3.2.1].

From equation 3.2.1 and 3.2.2 one find the capacitance per unit length as

$$C = \varepsilon \frac{w}{h} \qquad \text{equation 3.2.3}$$

In order to determine the induced magnetic field $\underline{B}$, the Ampère's circuital law $\oint \underline{H} \cdot d\underline{\ell} = I$ might be used following the path around the bottom plate of figure 3.2.1 suggested below

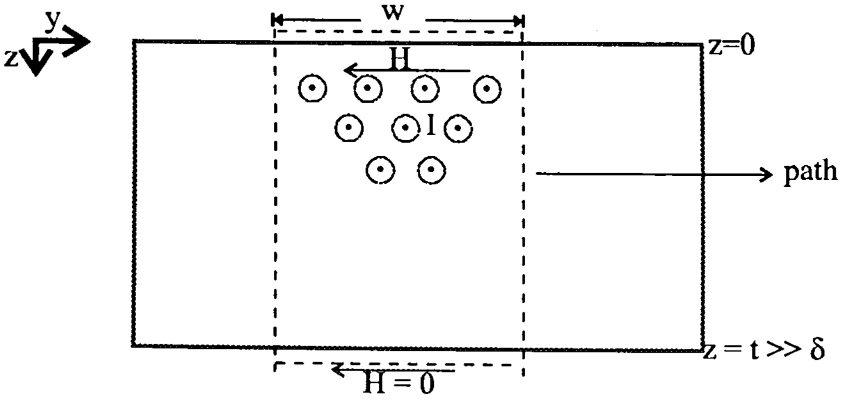

Figure 3.2.2 Path of integration. Assume the thickness must be greater than the skin depth.

So

$$\int_0^w \underline{H}(z=0)\cdot d\underline{\ell} + \int_w^0 \underline{H}(z=t)\cdot d\underline{\ell} = I \qquad \text{equation 3.2.4}$$

Assuming $t >> \delta$ we have $\underline{H}(z=t)=0$. So, one has

$$\int_0^w \frac{\underline{B}.dy}{\mu} = I$$

However, $\underline{B}$ is parallel to y direction and it is only varying in $\underline{a}_z$ direction. Thus, one obtains

$$B_y = \frac{\mu I}{w} \qquad \text{equation 3.2.5}$$

In order to find the inductance it is necessary to know first the total flux between the plates. Thus, we have

$$\phi = \int_0^{\Delta\ell} dx \int_0^h B_y dz = B_y h \Delta\ell \qquad \text{equation 3.2.6}$$

Here $\Delta\ell$ is a length of integration at $\underline{a}_x$ direction.

From equation 3.2.5 and equation 3.2.6 the inductance per unit length is given by

$$L = \mu \frac{h}{w} \qquad \text{equation 3.2.7}$$

From transmission line theory and equations 3.2.3 and 3.2.7 the characteristic impedance for a lossless transmission is given by

$$Z = \sqrt{\frac{L}{C}} = \left(\frac{\mu_0 \mu_r}{\varepsilon_0 \varepsilon_r} \right)^{1/2} \frac{h}{w} \qquad \text{equation 3.2.8}$$

where μ_o and ε_o are the permeability and the permittivity of free space, respectively. μ_r and ε_r are the relative permeability and the relative permittivity of the dielectric spacer given by $\mu_r = \mu/\mu_0$ and $\varepsilon_r = \varepsilon/\varepsilon_0$, respectively. For an air-spaced wide microstrip, where $\mu_r=1$ and $\varepsilon_r=1$, if we substitute the relation $(\mu_0/\varepsilon_0)^{1/2} \cong 120\pi\,\Omega$ into the equation 3.2.8 we obtain

$$Z = 120\pi \left(\frac{h}{w} \right) \qquad \text{equation 3.2.9}$$

3.3. Wide Microstrip Resonator

A transmission line acts as a resonator at those frequencies for which it is an integer number (n) of half wavelengths long. The unloaded quality factor Q_o of a TEM resonator is given by [3.3.1]

$$Q_o = \frac{\omega_n L}{R} = \frac{2\pi f_n L}{R} \qquad \text{equation 3.3.1}$$

where f_n represents the resonant frequencies of the resonator. 'R' is the series resistance of the transmission line, which is calculated by [3.3.2]

$$R = \frac{R_s}{I^2} \int_{c_1+c_2} \underline{H} \cdot \underline{H}^* dy \qquad \text{equation 3.3.2}$$

Here c_1 and c_2 are the paths of integration over the top plate and the bottom plate, respectively.

Defining R_{s1} as the surface resistance of the strip and R_{s2} as the surface resistance of the ground plane and substituting equation 3.2.5 into equation 3.3.2, the integration can be carried out as follows

$$R = \frac{R_{s1}}{I^2}\int_0^w \frac{I^2}{w^2}dy + \frac{R_{s2}}{I^2}\int_0^w \frac{I^2}{w^2}dy \qquad \text{equation 3.3.3}$$

Assume I is constant. So eq. 3.3.3 becomes

$$R = \frac{R_{s1} + R_{s2}}{w} \ \frac{\text{Ohms}}{\text{meter}} \qquad \text{equation 3.3.4}$$

Substituting equation 3.3.4 and equation 3.2.7 into equation 3.3.1, one gets

$$Q = \frac{2\pi f \mu h}{R_{s1} + R_{s2}} \qquad \text{equation 3.3.5}$$

It is important to recall that the previous equation came from a very particular case where $w >> h$ and $\delta << t$.

3.4. Microstrip

For the more general microstrip, i.e. for $w \geq h$, equation 3.3.3 may be conveniently expressed as a function of current density $\underline{J}$ as follow [3.4.1]:

$$R = R_{s1}\int_c \frac{J_1{}^2 dy}{I^2} + R_{s2}\int_{-\infty}^{+\infty}\frac{J_2{}^2 dy}{I^2} \qquad \text{equation 3.4.1}$$

where

J_1 → Surface current density in the strip

J_2 → Surface current density in the ground plane and

I → Magnitude of the total current per conductor

The integral $\int_c$ implies integration of the surface current density around all surfaces of the strip conductor.

Figure 3.4.1 shows the sketch of the current distribution for a strip of nonzero thickness. J(x) is not uniform in both conductors because of the finite strip width. The big problem is in fact to find the correct expression for the current density. For simplicity, some authors assume that 'J' is uniform in both conductors. However, this assumption can only be used for $w/h >> 1$.

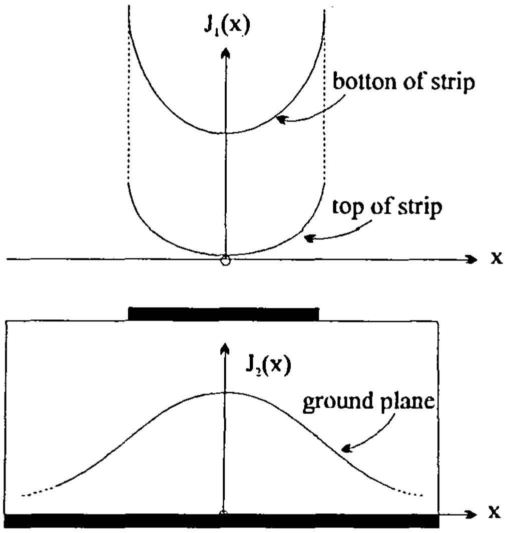

Figure 3.4.1 Sketch of the current distribution on microstrip conductors [3.4.1].

The calculation is not done here, however the closed form expression for the characteristic impedance obtained by series expansion approximations [3.4.2] is given by

$$Z = \frac{Z_0}{\sqrt{\varepsilon_{eff}}} \qquad \text{equation 3.4.2}$$

where $$Z_o = \frac{120\pi}{\frac{w}{h} + 2.42 - 0.44\frac{h}{w} + \left(1 - \frac{h}{w}\right)^6} \qquad \frac{w}{h} \geq 1 \qquad \text{equation 3.4.3}$$

$$Z_0 = 60\ln\left(\frac{8h}{w} + \frac{w}{4h}\right) \qquad \frac{w}{h} \leq 1 \qquad \text{equation 3.4.4}$$

Here Z_0 is the characteristic impedance of the microstrip line with the dielectric spacer replaced by air. The effective dielectric constant is [3.4.3] given by

$$\varepsilon_{\text{eff}} = \frac{\varepsilon_r + 1}{2} + \frac{\varepsilon_r - 1}{2}\left(1 + \frac{10h}{w}\right)^{-1/2} \qquad \text{equation 3.4.5}$$

Note that, for very wide strips, where w>>h, the equation 3.4.3 reduces to the equation 3.2.9, where the effect of fringing of the field at the edges is negligible.

3.5 Application of the Wheeler Incremental Inductance Rule to Microstrip Line

This method gives the resistance caused by the skin effect in the surface of the conductors. It is based entirely on the inductance computation. According to Wheeler Rule [3.5.1] the change of inductance is the same as caused by the surface receding to the depth $(\delta/2)$, where δ is the classical skin depth.

From section 2.2, the series surface impedance Z is given by

$$Z = R + jX \qquad \text{equation 3.5.1}$$

where

$$R = X = \omega L_i \qquad \text{equation 3.5.2}$$

In accordance with this incremental inductance rule, for each surface (j) the incremental inductance is given by [3.5.1, 3.5.2]

$$L_j = \frac{\mu_j}{\mu_o} . \frac{\delta_j}{2} . \frac{\partial L}{\partial n_j} \qquad \text{equation 3.5.3}$$

where L is the external inductance, $\partial L / \partial n_j$ denotes the derivative of 'L' with respect to the incremental recession of wall 'j' and n_j the distance normal to this wall.

Thus, to take all the metallic surfaces (j) into account in the calculation, one uses

$$L_i = \sum_j \frac{\mu_j}{\mu_o} . \frac{\partial L}{\partial n_j} . \frac{\delta_j}{2} \qquad \text{equation 3.5.4}$$

So one gets

$$R = \omega L_i = \sum_j \frac{1}{\mu_o} . \frac{\partial L}{\partial n_j} . R_{sj} \qquad \text{equation 3.5.5}$$

where R_{sj} is the surface resistance of wall 'j' given by

$$R_{sj} = \frac{\omega \delta_j \mu_j}{2} \qquad \text{equation 3.5.6}$$

Here $\delta_j = \sqrt{1/\pi f \mu_j \sigma_j}$, f is the operating frequency and σ_j is the conductivity of the metallic surface j. Now, equation 3.5.5 will be applied to the microstrip line shown in figure 3.5.1.

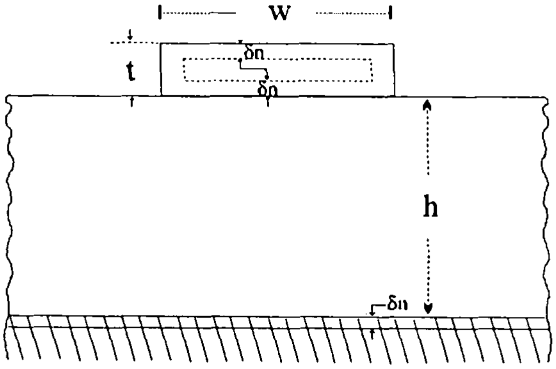

Figure 3.5.1 Sketch of the surfaces recessions.

The inductance for a microstrip which supports a transverse electromagnetic mode (TEM) is given by: $L = \sqrt{\varepsilon_0\mu_0}\left(Z\sqrt{\varepsilon_{eff}}\right)$. Using now equation 3.4.2 we have [3.5.3]

$$L = \left(\varepsilon_o\mu_o\right)^{1/2} Z_o \qquad \text{equation 3.5.7}$$

Substituting equation 3.5.7 into equation 3.5.5, we find

$$R = \left(\frac{\varepsilon_o}{\mu_o}\right)^{1/2} \sum_j \frac{\partial Z_0}{\partial n_j} \cdot R_{sj} \qquad \text{equation 3.5.8}$$

Initially it will be assumed that the surface resistance of the ground plane (R_{s1}) is different from the surface resistance of the strip (R_{s2}). Before calculating 'R' it is necessary to return to figure 3.5.1 and assume that

$R_1 \rightarrow$ Resistance owing to the ground plane

$R_2 \rightarrow$ Resistance owing to the strip

And
$$\delta n_j = \begin{cases} \delta h \ (\text{recession of ground plane}) \\ \delta h \ (\text{recession of bottom of strip conductor}) \\ -\delta w (\text{recession of either edge of strip conductor}) \\ -\delta t \ (\text{recession of top and of bottom of strip conductor}) \end{cases}$$

This way, applying equation 3.5.8 to find R_1 and R_2, one has

$$R_1 = \left(\frac{\varepsilon_o}{\mu_o}\right)^{1/2} R_{s1} \cdot \frac{\partial Z_0}{\partial h} \qquad \text{equation 3.5.9}$$

$$R_2 = \left(\frac{\varepsilon_o}{\mu_o}\right)^{1/2} R_{s2} \left[\frac{\partial Z_o}{\partial h} - 2\frac{\partial Z_o}{\partial w} - 2\frac{\partial Z_0}{\partial t}\right] \qquad \text{equation 3.5.10}$$

Where the total resistance is given by

$$R_T = R_1 + R_2 \qquad \text{equation 3.5.11}$$

For an all-copper microstrip line we have $R_{s1} = R_{s2} = R_{sc}$. As a result, one finds

$$R_T = 2\left(\frac{\varepsilon_o}{\mu_o}\right)^{1/2} R_S \left[\frac{\partial Z_o}{\partial h} - \frac{\partial Z_o}{\partial w} - \frac{\partial Z_o}{\partial t}\right] \qquad \text{equation 3.5.12}$$

Assuming that $Z_0 = Z_0\,(w/h)$ and $w = w(t)$, where t represents the thickness of the strip , we might use partial derivative for each term and find

$$\frac{\partial Z_o}{\partial w} = \frac{1}{h}\frac{\partial Z_o}{\partial\left(\frac{w}{h}\right)} \qquad \text{equation 3.5.13a}$$

$$\frac{\partial Z_o}{\partial h} = -\frac{w}{h^2}\frac{\partial Z_o}{\partial\left(\frac{w}{h}\right)} \qquad \text{equation 3.5.13b}$$

$$\frac{\partial Z_o}{\partial t} = \frac{1}{h}\frac{\partial Z_o}{\partial\left(\frac{w}{h}\right)}\frac{\partial w}{\partial t} \qquad \text{equation 3.5.13c}$$

Substituting equations 3.5.13a, 3.5.13b and 3.5.13c into equation 3.5.12, one obtains

$$R_T = -2\left(\frac{\varepsilon_o}{\mu_o}\right)^{1/2} R_s \frac{\partial Z_o}{\partial\left(\frac{w}{h}\right)}\left[\frac{1+\frac{w}{h}+\frac{\partial w}{\partial t}}{h}\right] \qquad \text{equation 3.5.14}$$

From Wheeler [3.5.4] and Schneider [3.5.5] one has the partial derivative $\frac{\partial w}{\partial t}$ given by

$$\frac{\partial w}{\partial t} = \frac{1}{\pi}\ln\frac{2h}{t} \quad \text{for} \quad \frac{w}{h} \geq \frac{1}{2\pi} \qquad \text{equation 3.5.15}$$

On the other hand, $\partial Z_o / \partial\left(\frac{w}{h}\right)$ may be obtained from the equation 3.4.3. Thus, one finds

$$\frac{\partial Z_o}{\partial\left(\frac{w}{h}\right)} = -\frac{(Z_o)^2}{120\pi}\left[1+0.44\frac{h^2}{w^2}+\frac{6h^2}{w^2}\left(1-\frac{h}{w}\right)^5\right] \qquad \text{equation 3.5.16}$$

Substituting equation 3.5.16 into equation 3.5.14, one gets

$$R_T = R_s\left(\frac{\varepsilon_0}{\mu_0}\right)^{1/2}\left(\frac{Z_0{}^2 AB}{60\pi h}\right) \qquad \text{equation 3.5.17}$$

Here A and B are expressed by

$$A = 1+\frac{0.44h^2}{w^2}+\frac{6h^2}{w^2}\left(1-\frac{h}{w}\right)^5 \qquad \text{equation 3.5.18a}$$

and

$$B = 1 + \frac{w}{h} + \frac{1}{\pi}\ln\frac{2h}{t} \qquad \text{equation 3.5.18b}$$

Substituting equations 3.5.17, 3.5.7 and 3.4.3 into equation 3.3.1, the unloaded quality factor for a resonator made of a $\lambda/2$ length of microstrip is given by

$$Q = \frac{\Gamma}{R_s} = \frac{\pi f \mu h\left(\frac{E}{AB}\right)}{R_s} \qquad \text{equation 3.5.19}$$

where

$$E = \frac{w}{h} + 2.42 - 0.44\frac{h}{w} + \left(1 - \frac{h}{w}\right)^6 \qquad \text{equation 3.5.20}$$

In equation 3.5.19, Γ is the geometry factor. Comparing the equation 3.5.19 with the equation 3.3.5 for $R_{s1} = R_{s2}$, we notice that Γ changed by a factor of E/AB.

In order to compare numerically equation 3.5.19 with equation 3.3.5, we will assume, as an example, the following geometric data: $h = 5\cdot 10^{-4}\text{m}$, $w = 2.4\cdot 10^{-3}\,\text{m}$ and $t = 3\cdot 10^{-4}\,\text{m}$. Substituting these values into equation 3.5.19, one obtains for the microstrip

$$\Gamma \cong \pi f \mu h(1.084) \qquad \text{equation 3.5.21}$$

From equation 3.3.5 the wide microstrip value of Γ, for $R_{s1} = R_{s2}$, is

$$\Gamma \cong \pi f \mu h \qquad \text{equation 3.5.22}$$

Apparently, the equation 3.3.5 $(\text{where } w >> h)$ may be used in the copper microstrip resonator calculations with good accuracy.

Chapter 4

Effective Surface Impedance of Superconducting Thin Films

4.1 Introduction

The surface resistance and surface reactance of very thick superconducting films have been already determined by equations 2.3.3.17 and 2.3.3.18. However most high-T_c superconducting thin films have a penetration depth of the order of the film thickness. In this case, correction of the intrinsic surface impedance is required for values of Rs and Xs to be extracted from measurements. In some structures, as the penetration depth is comparable or smaller than the thickness of the film, there are large differences between the effective surface impedance (Z_{eff}) and the intrinsic surface impedance (Z_s) [4.1.1, 4.1.2, 4.1.3, 4.1.4]. Taking these differences into account, section 4.2 will present some calculations based on the two-fluid model and on the standard transmission line theory. In section 4.3, this calculation and the wide microstrip line approximations will be applied together to try to find the intrinsic surface resistance of some laser ablated thin films used in hybrid copper/superconducting resonators.

4.2 Effective Surface Impedance of Superconducting films of any Thickness

Before applying any technique this section starts by producing the sketch of the wide microstrip already discussed in section 3.2. The sketch in figure 4.2.1 emphasises the interface between the thin film and the free space. For simplicity, consider free space between plates.

Klein N. et. al [4.2.1] described how to establish the difference between the effective surface impedance and the intrinsic surface impedance. We shall now review that calculation step by step.

The film can be treated as a short length of transmission line with propagation in the z-direction. Standard transmission line theory can be applied considering wave propagating between plates and normal to the surface. The load impedance Z_{load} is transformed to a new impedance Z_{input} by [4.2.2]

$$Z_{input} = Z_C \frac{Z_{load} + Z_C \tanh \gamma d}{Z_C + Z_{load} \tanh \gamma d} \qquad \text{equation 4.2.1}$$

Here Z_C is the characteristic impedance of the transmission line, Z_{load} the load impedance, d the length of the transmission line and γ the complex propagation constant. Specifically, as seen in figure 4.2.1, Z_{input} is the characteristic impedance of the top plate of thickness d looking toward the $z = 0$ from $z = -d$.

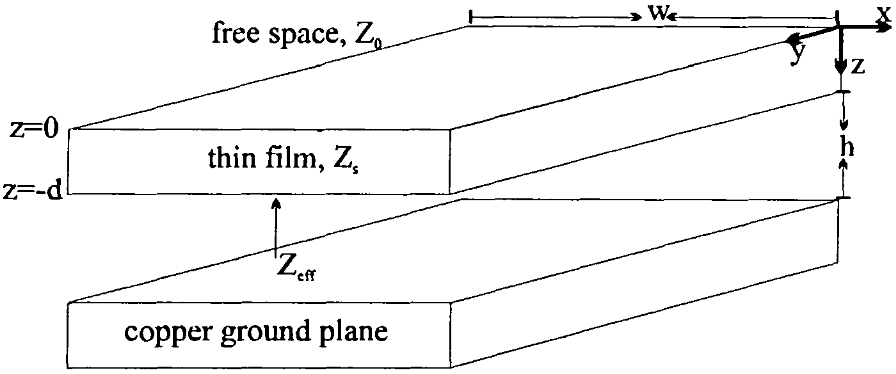

Figure 4.2.1 Sketch of wide microstrip (w>>h) emphasises the interface between the thin film and the free space.

From figure 4.2.1 one can assume the following equivalencies:

$Z_{input} \rightarrow Z_{eff}$ (effective impedance of the thin film taking into account the thickness)

$Z_c \rightarrow Z_s$ (intrinsic impedance of the thin film)

$d \rightarrow t_i$ (thickness of the film)

$Z_{load} \rightarrow Z_o$ (impedance of the free space)

In this way, one can rewrite equation 4.2.1 as follows

$$Z_{eff} = Z_s \frac{Z_o + Z_s \tanh(\gamma\, t_i)}{Z_s + Z_o \tanh(\gamma\, t_i)} \qquad \text{equation 4.2.2}$$

Where

$$Z_o = \sqrt{\frac{\mu_o}{\varepsilon_o}} \qquad \text{equation 4.2.3}$$

and

$$Z_s = \sqrt{\frac{j\omega\mu_o}{\sigma}} = R_s + jX_s \qquad \text{equation 4.2.4}$$

and from chapter 2

$$\gamma = \sqrt{j\omega\mu_o\sigma} \qquad \text{equation 4.2.5}$$

So, making the above substitutions we find

$$Z_{eff} = \frac{Z_s\left\{1 + \left(\frac{\varepsilon_o j\omega}{\sigma}\right)^{1/2} \tanh\left[\left(j\omega\mu_o\sigma\right)^{1/2} t_i\right]\right\}}{\left(\frac{j\omega\varepsilon_o}{\sigma}\right) + \tanh\left[\left(j\omega\mu_o\sigma\right)^{1/2} t_i\right]} \qquad \text{equation 4.2.6}$$

At microwave frequencies $\sigma \gg \omega\varepsilon_0$. So one gets

$$Z_{eff} = Z_s \coth\left[(j\omega\mu_o\sigma)^{1/2} t_i\right] \qquad \text{equation 4.2.7}$$

However, for a superconductor σ is the complex conductivity from the two-fluid discussed in chapter 2. So one has

$$(j\omega\mu_o\sigma)^{1/2} = \left[j\omega\mu_o(\sigma_1 - j\sigma_2)\right]^{1/2}$$

and

$$\left[j\omega\mu_o(\sigma_1 - j\sigma_2)\right]^{1/2} = (j\omega\mu_o)^{1/2}(-j\sigma_2)^{1/2}\left(1 + j\frac{\sigma_1}{\sigma_2}\right)^{1/2}$$

So, we have

$$(j\omega\mu_o\sigma)^{1/2} = (\omega\mu_o\sigma_2)^{1/2}\left(1 + j\frac{\sigma_1}{\sigma_2}\right)^{1/2}$$

From chapter 2, $\sigma_2 \gg \sigma_1$. This way, the previous expression becomes

$$(j\omega\mu_o\sigma)^{1/2} \cong (\omega\mu_o\sigma_2)^{1/2}\left(1 + \frac{1}{2}j\frac{\sigma_1}{\sigma_2}\right) \qquad \text{equation 4.2.8}$$

Substituting equation 4.2.8 and afterwards equation 2.3.3.11 into equation 4.2.7 one finds

$$Z_{eff} = Z_s \coth\left[t_i / \lambda\left(1 + j\frac{\sigma_1\omega\mu_o\lambda^2}{2}\right)\right] \qquad \text{equation 4.2.9}$$

This can be split into its real and imaginary parts using equations Ap. I.13 and Ap. I.15 from appendix I. So, one has

$$Z_{eff} = R_{eff} + jX_{eff} \qquad \text{equation 4.2.10}$$

where

$$R_{eff} = R_s \frac{\sinh\left(\frac{t_i}{\lambda}\right)\cosh\left(\frac{t_i}{\lambda}\right)}{\sinh^2\left(\frac{t_i}{\lambda}\right) + \sinh^2\left(\frac{\sigma_1\omega\mu_0\lambda^2}{2\lambda / t_i}\right)} + X_s \frac{\sin\left(\frac{\sigma_1\omega\mu_0\lambda^2}{2\lambda / t_i}\right)\cos\left(\frac{\sigma_1\omega\mu_0\lambda^2}{2\lambda / t_i}\right)}{\sinh^2\left(\frac{t_i}{\lambda}\right) + \sinh^2\left(\frac{\sigma_1\omega\mu_0\lambda^2}{2\lambda / t_i}\right)} \qquad \text{equation 4.2.11}$$

and

$$X_{eff} = X_s \frac{\sinh\left(\frac{t_i}{\lambda}\right)\cosh\left(\frac{t_i}{h}\right)}{\sinh^2\left(\frac{t_i}{\lambda}\right) + \sinh^2\left(\frac{\sigma_1\omega\mu_0\lambda^2}{2\lambda / t_i}\right)} - R_s \frac{\sin\left(\frac{\sigma_1\omega\mu_0\lambda^2}{2\lambda / t_i}\right)\cos\left(\frac{\sigma_1\omega\mu_0\lambda^2}{2\lambda / t_i}\right)}{\sinh^2\left(\frac{t_i}{\lambda}\right) + \sinh^2\left(\frac{\sigma_1\omega\mu_0\lambda^2}{2\lambda / t_i}\right)} \qquad \text{equation 4.2.12}$$

Assuming $\sigma_1 \cong \sigma_n$ and $\delta_n^{\ 2} >> \lambda$ close to T_c and carrying on some manipulations, equation 4.2.10 becomes [4.2.3]

$$Z_{eff} = R_s\left[\coth(t_i / \lambda) + \frac{t_i / \lambda}{\sinh^2(t_i / \lambda)}\right] + jX_s \coth\left(\frac{t_i}{\lambda}\right) \qquad \text{equation 4.2.13}$$

Thus, for a wide strip of width w one obtains from equation 4.2.13, $Z_w = R_w + jX_w$

where

$$R_w = \frac{R_s}{w}\left[\coth(t_i / \lambda) + \frac{t_i / \lambda}{\sinh^2(t_i / \lambda)}\right] \ (\Omega / m) \qquad \text{equation 4.2.14}$$

and

$$X_w = \frac{X_s}{w}\left[\coth(t_i / \lambda)\right] = \omega \frac{L_{keff}}{w} \ (\Omega / m) \qquad \text{equation 4.2.15}$$

Here

$$X_s = \mu_o \omega \lambda \quad \text{and} \quad R_s = \omega\mu \frac{\lambda^3}{\delta_n^{\ 2}}$$

Here $\delta_n = \delta$, the skin depth for normal conductors already discussed in section 2.2 of chapter 2. From both equations 4.2.14 and 4.2.15 one can graphically notice that the real and imaginary parts of Z_s were enhanced to some extent. This depends on the ratio of t_i to λ. Figure 4.2.2 plots the intrinsic resistance R_s as a function of the effective resistance for four different values of the film thickness, assuming a typical value of λ_0=200nm [4.2.4]. Thus, depending on the thickness of the film, one can see a considerable difference between R_s and R_{eff}. From the figure 4.2.2 one can see that for a thickness of 100nm R_{eff} becomes 5.8 times bigger than R_s. For t_i = 100µm as $t_i >> \lambda$ we have $R_s = R_{eff}$.

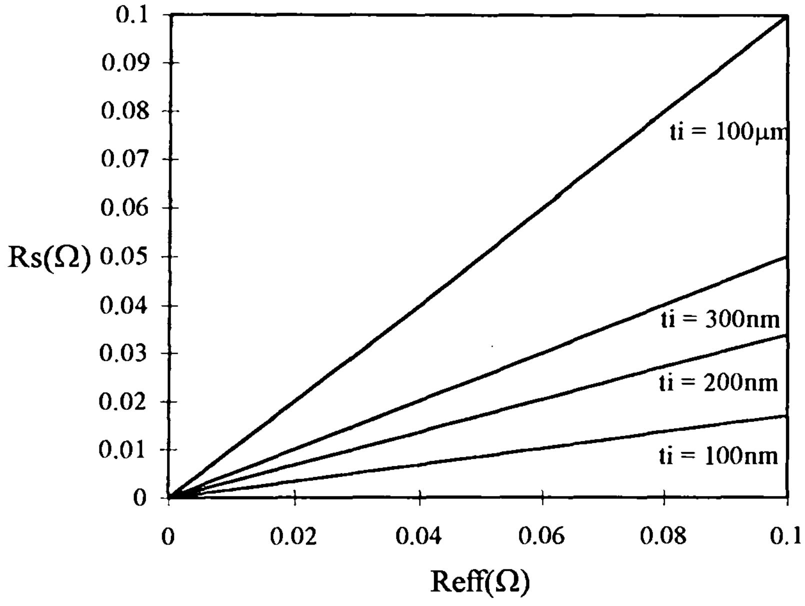

Figure 4.2.2 Intrinsic surface resistance as a function of effective surface resistance for three different film thicknesses: 100nm, 200nm, 300nm and 100µm.

4.3 The Hybrid Copper/Superconducting Resonator

In this section we will apply both the wide microstrip expressions (from section 3.2) and the concepts presented in the previous section to find the quality factor for the hybrid copper superconducting resonator, sketched in figure 4.3.1.

The total inductance per unit of length is given by $L_T = \frac{\phi}{I}$, where I is the current flowing along the line and ϕ is the sum of the flux between the stripline and the ground plane and the flux through the conductor.

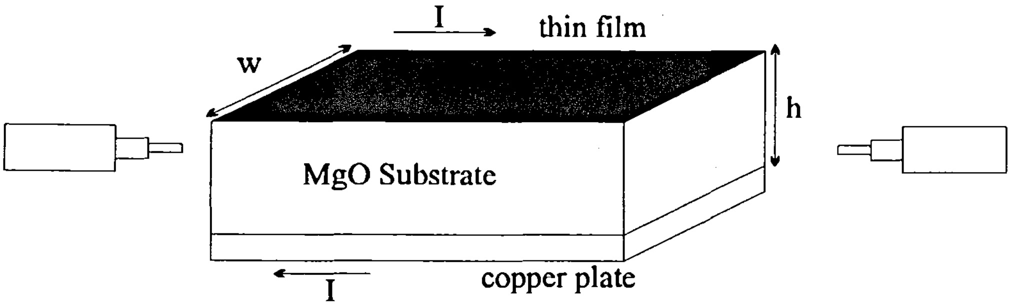

Figure 4.3.1 Sketch of a hybrid copper/superconducting resonator.

The effect of the kinetic inductance of the superconducting carriers on the total inductance enables us to write the total inductance of the wide microstrip L_T as follows [4.3.1].

$$L_T = L + L_{kef} \qquad \text{equation 4.3.1}$$

For simplicity, it will be assumed here that L is basically the magnetic inductance between stripline. By comparison with equation 2.3.3.19 we define L_{kef} as the effective superconducting inductance.

From equation 4.2.15 we have the following expression for a wide strip (per unit length)

$$L_w = \frac{L_{kef}}{w} = \frac{\mu_o \lambda}{w} \coth(t_i / \lambda) \qquad \text{equation 4.3.2}$$

Where L_w is the effective superconducting inductance of the wide superconducting strip. Taking L from equation 3.2.7 one finds

$$L_T = \frac{\mu_o h}{w} + \frac{\mu_o \lambda}{w} \coth(t_i / \lambda) \qquad \text{equation 4.3.3}$$

Using equation 3.3.1 the Q is

$$Q_o = \frac{2\pi f_n L_T}{R_T} \qquad \text{equation 4.3.4}$$

where R_T is the total (series) resistance of the wide microstrip line.

From equation 2.2.17 and equation 4.2.14 one has

$$R_T = \frac{R_{ss}}{w}\left[\coth(t_i / \lambda) + \frac{t_i / \lambda}{\sinh^2(t_i / \lambda)}\right] + \frac{R_{sc}}{w} \qquad \text{equation 4.3.5}$$

Here R_{ss} and R_{sc} represent the surface resistance (intrinsic) of the superconducting film and the surface resistance (intrinsic) of the ohmic copper ground plane per unit length, respectively. Thus, substituting equation 4.3.5 and equation 4.3.3 into equation 4.3.4 and simplifying, one finds

$$Q_o = \frac{2\pi f_n \mu E}{A + R_{sc}} \qquad \text{equation 4.3.6}$$

where

$$A = wR_w \text{ and } E = \frac{wL_T}{\mu_o}$$

Note from equation 4.3.3 that for h >> t_i the total inductance is basically concentrated only between plates, which is given by $\frac{\mu h}{w}$. As the thickness t_i becomes very large compared with λ, the coth term approaches unity and the sinh term becomes very large. Thus, equation 4.3.6 becomes

$$Q_0 = \frac{2\pi f_n \mu_o h}{R_{ss} + R_{sc}} \qquad \text{equation 4.3.7}$$

This is the expression for a simple wide microstrip resonator.

Figure 4.3.2 presents a theoretical curve of Q_o as a function of R_{ss} by using equation 4.3.6, assuming $R_{sc} = 13\mathrm{m}\Omega$ and typical values of $\lambda_0 = 200\mathrm{nm}$ and $t_i = 250\mathrm{nm}$. The value of Q_o for a perfect superconductor, i.e. $Q_o (R_{ss} = 0) \cong 2219$, can be seen clearly in figure 4.3.2.

Even though the use of copper ground plane makes the device economically viable for manufacture, its high value of surface resistance limits the value of Q_o. Appendix-II presents some theoretical results for a 'all superconducting resonator'.

For comparison, figure 4.3.3 plots both the equation 4.3.7 (Q1) and the equation 4.3.6 (Q2) as a function of R_{ss}. For a fixed value of quality factor, equation 4.3.6 gives a smaller value of R_{ss}. In addition, for very low values of R_{ss}, Q1 $\cong$ Q2. Chapter 6 will make use of both expressions to find R_{ss} values from the experimental results.

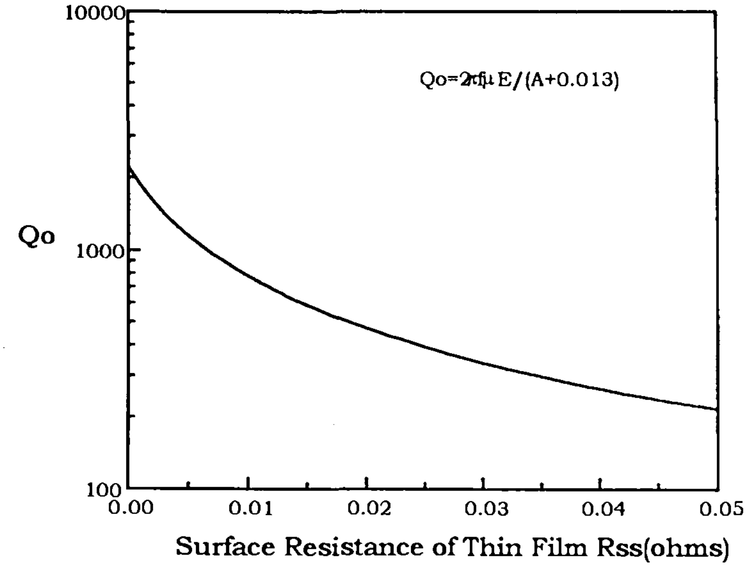

Figure 4.3.2 Unloaded quality factor Q_o as a function of superconducting surface resistance (R_{ss}) from 0 to 50mΩ. R_{sc} = 13mΩ

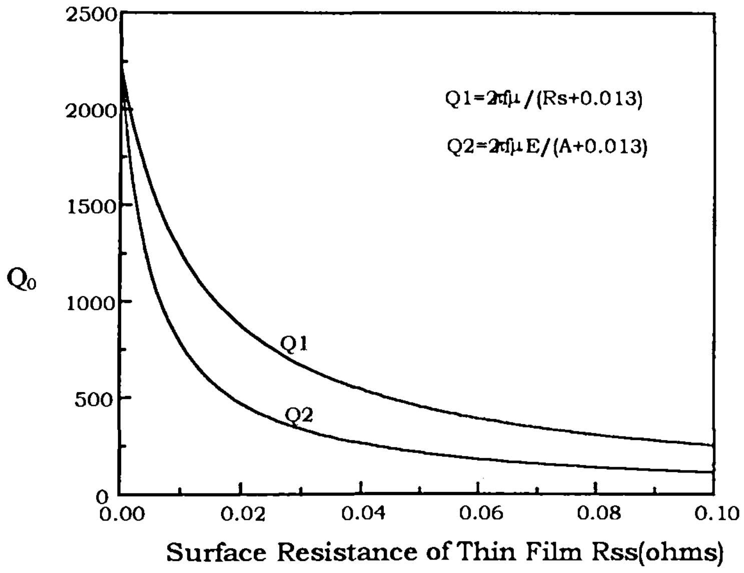

Figure 4.3.3 Unloaded quality factor Q_o as a function of superconducting surface resistance (R_{ss}) from 0 to 50mΩ for the two considered models. R_{sc} = 0.013Ω.

Chapter 5

Superconducting Materials

5.1 Introduction

Copper and gold films for passive microwave applications can be prepared at low temperature by a variety of techniques on almost any material. There is a considerable research effort in superconductivity going on around the world. Improved materials, technologies and applications are publicised every month. Many techniques, including laser ablation have been successfully used to generate thin films of the high temperature superconductors

Laser ablation is a relatively recently developed technique that is proving to be very useful in the deposition of HTSC films. This is one of the most flexible of the commonly used deposition techniques because one laser can be used to ablate from several different targets with minimal changeover problems, or to grow films in several different chambers in one working day [5.1.1]. The major problems are substrate temperature, oxygen pressure, establishing the laser power needed to achieve the stoichiometric transfer and scaling the process up to larger areas.

Dipping pyrolysis process is a promising technique for YBCO film preparation since it does not require vacuum. This technique is capable of forming economically large areas of high quality superconducting films on polycrystalline or metallic substrates for a variety of industrial application. However the films are not epitaxial like those obtained from laser ablation.

$YBa_2Cu_3O_{7-\delta}$ (YBCO) thick films have potential use in microwave devices and magnetic screening application. A major factor in the design of microwave devices is the requirement of using low-loss dielectric substrates such as alumina. Many of these materials are extremely reactive with superconducting films, resulting in poisoning and degradation or loss of superconducting properties. Less reactive substrates materials such yttria stabilised zirconia (YSZ) have higher dielectric loss and therefore have limited application in this field. In recent years, the use of barrier layers to reduce the reaction between the substrate and superconducting film has been extensively researched [5.1.2, 5.1.3]. The technique of producing YSZ barrier layer by Atmospheric/Air Plasma Spraying (APS) onto alumina substrate will also be described here which will be indicated as a technique to be used to fabricate coplanar instantaneous frequency measurement systems in a future work.

5.2 HTSC Substrate

Samples of thin film are needed for a number of applications and a good deal of effort has been expended on discovering reliable techniques for the deposition of HTSC films. The essential problem is the complexity of HTSC superconducting phases containing many elements, needing very precise control over the chemistry of the deposition process. It is well recognised that the epitaxial (i.e. crystalline registration between the film and the underlying substrate) growth of HTSC films for microwave applications requires single-crystalline substrate with a suitable permittivity, low dielectric losses and a small mismatch in lattice parameters and thermal expansion. The real part of the complex dielectric constant determines the achievable degree of miniaturisation and the propagation velocity of the guided wave. The substrate should also be very smooth and chemically inert with respect to the preparation condition relevant for HTSC. The most successfully adopted substrates for $YBa_2Cu_3O_{7-\delta}$ films are magnesium oxide (MgO, despite the lattice mismatch), lanthanum aluminate ($LaAlO_3$, despite its twinning), neodymium gallate ($NdGaO_3$) and yttria-stabilised zirconia (YSZ, despite their high loss tangent) [5.2.1, 5.2.2]. It is clear that in the long run it will be necessary to use cheaper substrate like sapphire or silicon on sapphire (SOS) covered with suitable thin buffer layers like YSZ [5.2.3].

Various microwave components and subsystems have been fabricated on $LaAlO_3$ and MgO, which are close to being commercialised . However, exploiting the full potential of HTSC microwave devices requires the development of novel substrate materials.

5.3 Thin Film Laser Ablation

The laser induced extraction of material from a polycrystalline target is a promising process of HTSC thin film fabrication. Using the figure 5.3.1 we shall describe briefly this process [5.3.1, 5.3.2, 5.3.3].

It offers some advantages when compared with other thin film deposition techniques, such as simplicity of deposition, broad process parameter control for optimisation of film properties and high rates of film formation.

A pulsed laser with a pulse length of a few tens of nanoseconds and energy of about 700mJ is focused so that the beam hits a pellet of bulk polycrystalline YBCO in oxygen at low pressure. A thin surface (~30nm) of the material is then evaporated and emitted from the target in a plasma-plume, where it is condensed on a single-crystal heated substrate of MgO placed near the end of the plume. This process is so quick and highly energetic that the composition of the evaporated material condensed on MgO keeps the stoichiometry of bulk polycrystalline YBCO.

In order to achieve a good deposition with high level of homogeneity the target is rotated in such a way that with every pulse a new area of the target is exposed to the laser. The quality of the deposited thin film depends on some parameters such as laser power, oxygen pressure and substrate temperature. The main difficulty involved in this process still seems to be the compositional uniformity of the thin film if we want to scale the process up to larger areas*.

---

*All films made by laser ablation used in this work were prepared by the Superconductivity Research Group of the School of Electronic and Electrical Engineering of Birmingham University.

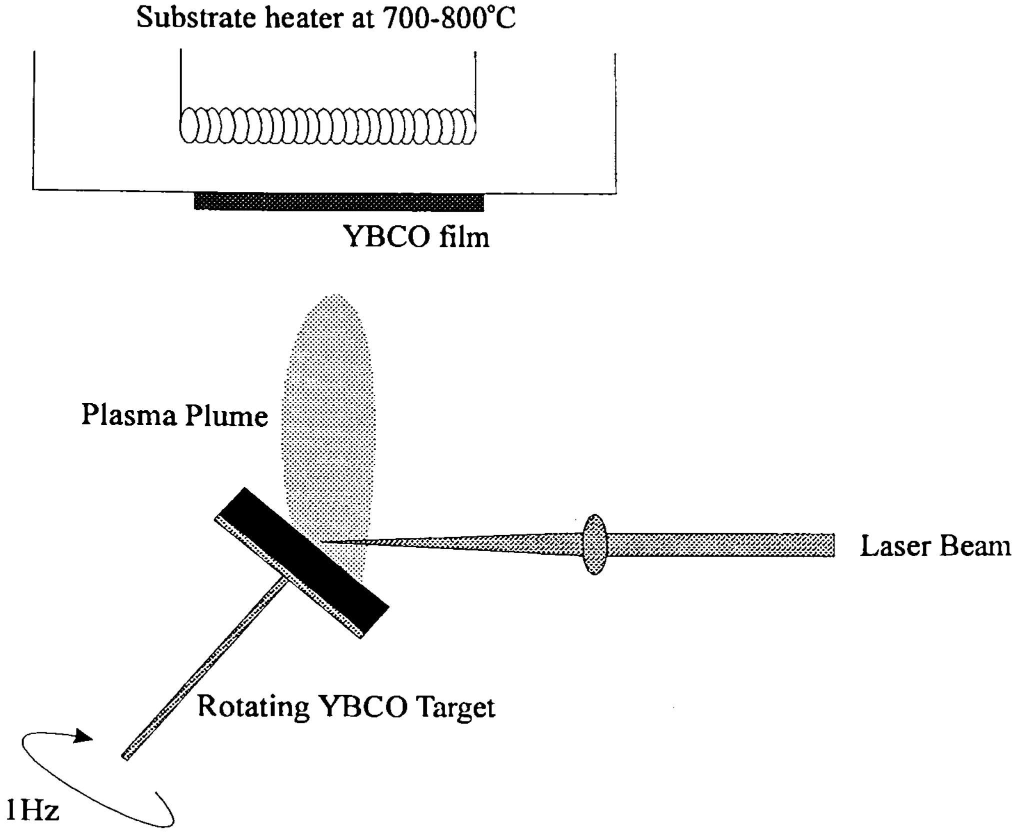

Figure 5.3.1 Laser ablation system [5.3.2].

5.4 Dipping Pyrolysis Process

The dipping pyrolysis process (DP process) [5.4.1, 5.4.2, 5.4.3] looks like an excellent process of superconducting film preparation as far as industrial applications are concerned.

It is known that highly grain-oriented oxide superconductors exhibit low barriers to electrical conductivity in the grain boundaries, thus enabling a high current density (J_c). Using laser ablation process and other processes such as sputtering and evaporation it is possible to fabricate films with J_c of at least 10^6 A/cm^2. However, they are fabricated only for use in small electronic components because single crystal substrate such as MgO, $SrTiO_3$ and $LaAlO_3$ are expensive and films can not be formed over very large areas.

The dipping pyrolysis process requires a combination of a diffusion reaction and thermal decomposition of a coating using metal-organic compounds where a uniform YBCO film of highly oriented grains and high J_c is formed. Besides, neither a single crystal substrate nor a vacuum chamber in the thermal decomposition is necessary use. That can also be easily applicable to substrates of different size and shape. The process is described below.

Homogeneous Y-Ba-Cu and Ba-Cu-Ag solutions with the molar ratio of Y:Ba:Cu=2:1:1 and Ba:Cu:Ag=3:5:X (X=0-1.5)(350) are prepared by mixing the Y-octylate and Ba, Cu and Ag-naphthenates in toluene, see figure 5.4.1. Firstly, the 211 solution is coated on yttria-stabilized-zirconia (YSZ) and heated in air to ~500°C. This is repeated several times to build up a suitable film thickness. The films are then calcined at 900°C for 30-60 minutes to yield a 211 green film. A controlled thickness of 350 (Ag) film is then formed on the surface of the 211 film. The two film sandwich is then heated (~700°C) for at least 6 hours under reduced pressure ($\sim 5 \times 10^{-5}$ atm) to form a silver loaded textured 123-YBCO film of ~ 1μm thickness by solid state reaction on the surface of the YSZ substrate. The films are then annealed under pure oxygen at ~ 450°C.

This process produces a film of a dense (211) phase without any reaction between the substrate and the (211) phase. Adding silver to the (350) phase accelerates diffusion and sintering, this way improving bonding between grains.

The resultant YBCO film has tetragonal and poor superconducting properties due to oxygen insufficiency. Then, the film is subjected to annealing in an oxygen atmosphere at 450°C to improve its properties.

XRD pattern of the a typical YBCO film made by pyrolysis is shown in figure 5.4.2. The sharp peaks means that the grains are highly oriented toward the c-axis normal to the plane of the film, indicating a dominant phase of orthorhombic YBCO. The peaks of the substrate YSZ can also be seen*.

*All films made by dipping pyrolysis used in this work were prepared by the Superconductivity Research Group of the School of Metallurgy and Materials of

Birmingham University.

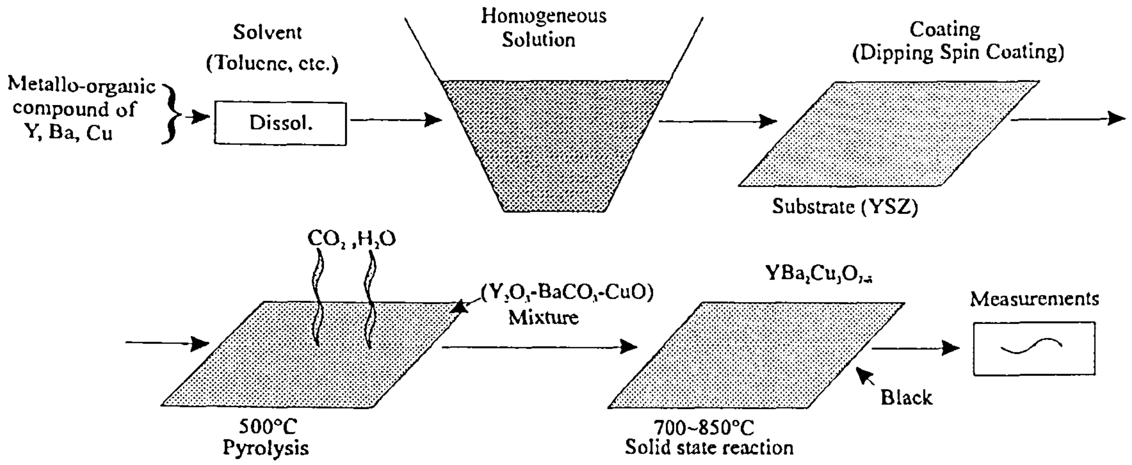

Figure 5.4.1 Sketch of dipping pyrolysis process [5.4.1].

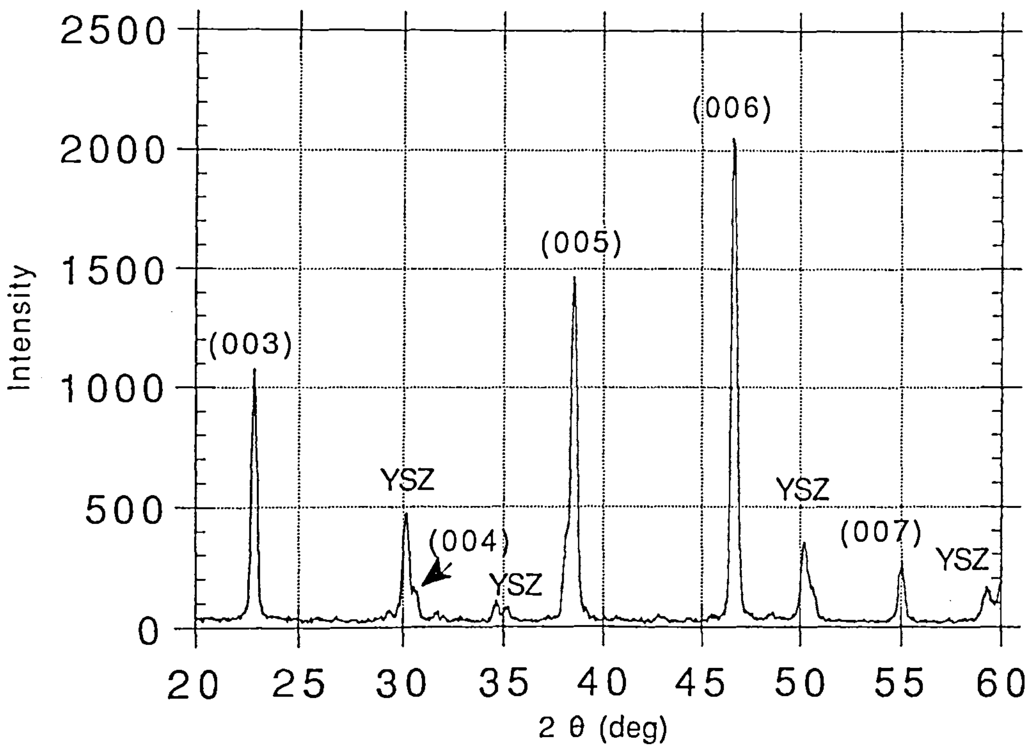

Figure 5.4.2. XRD pattern of a typical YBCO film made by dipping pyrolysis. Result supplied by the Superconductivity Research Group of The School of Metallurgy and Materials of the Birmingham University.

5. 5 Yttria Stabilised Zirconia Barrier Layer

The objective of this section is to describe the production of barrier layer by Atmospheric/Air Plasma Spraying (APS) onto alumina substrates. Results of x-ray diffraction, SEM and surface resistance supplied by Watcham et. al [5.5.1] will be shown and discussed.

Aluminium oxide (alumina, Al_2O_3) substrates seem promising for microwave application because the low value of tanδ. Its well known that $YBa_2Cu_3O_7$ has an orthorhombic structure (axis $a \neq b \neq c$), see figure 5.5.1. This structure has two Cu-O sheets in the ab plane and Cu-O chains along the b-axis.

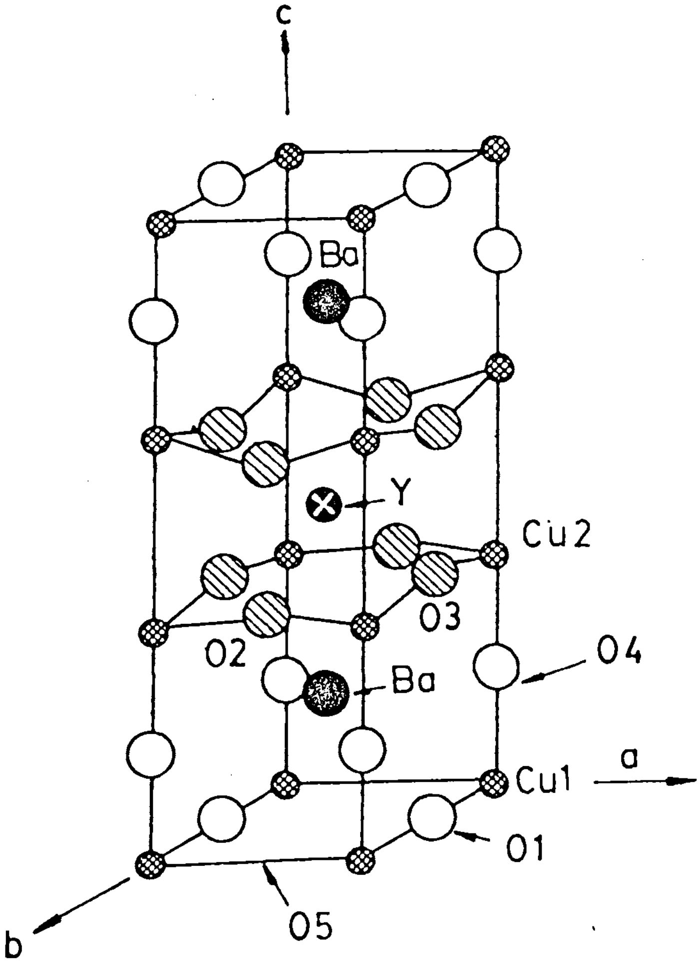

Figure 5.5.1 Structure of $YBa_2Cu_3O_7$. Taken from [5.5.2].

However extensive interactions with $YBa_2Cu_3O_{7-\delta}$ result in substitution of aluminium on the Cu1 sites, see figure 5.5.1, leading to a degradation or loss of superconducting properties. YSZ has a high tanδ, thus, has a limited application in microwave field. However its low reaction with $YBa_2Cu_3O_{7-\delta}$ makes it attractive to barrier layer use, as it can reduce the interaction of $YBa_2Cu_3O_{7-\delta}$ with alumina substrate.

Watcham et al. [5.5.1] used a Plasma Technik F4 system combined with a 4-axis robotic handling system and turntable to deposit the YSZ onto grit blasted 50×50mm 96% alumina substrate. Plasma spraying was carried out using argon as the primary gas, hydrogen as the second gas and a power of 36kW as a stand-off distance of 120mm. The as-sprayed films were then fired for 1 hour at 1450^0C to increase both the adhesion to the substrate and the barrier layer density. A commercially available high purity YBCO powder was passed through a 38 μm thick sieve and then mixed with Blythe 63/2 organic binder in a solid-to-binder ration of 80%. This was printed through a 30μm thick. The YBCO films were then melt textured at 1035 ^{0}C for 6 minutes in flowing oxygen.

Using SEM measurements, figure 5.5.2a and 5.5.2b show the microstructure of the YSZ barrier before and after sintering at 1450 ^{0}C for 1 hour. Using only as-sprayed figure 5.5.2a presents significant amount of microcracking caused by the rapid quench on the substrate. After sintering, the barrier is well adhered to the substrate and a reduction in porosity can be seen in figure 5.5.2b.

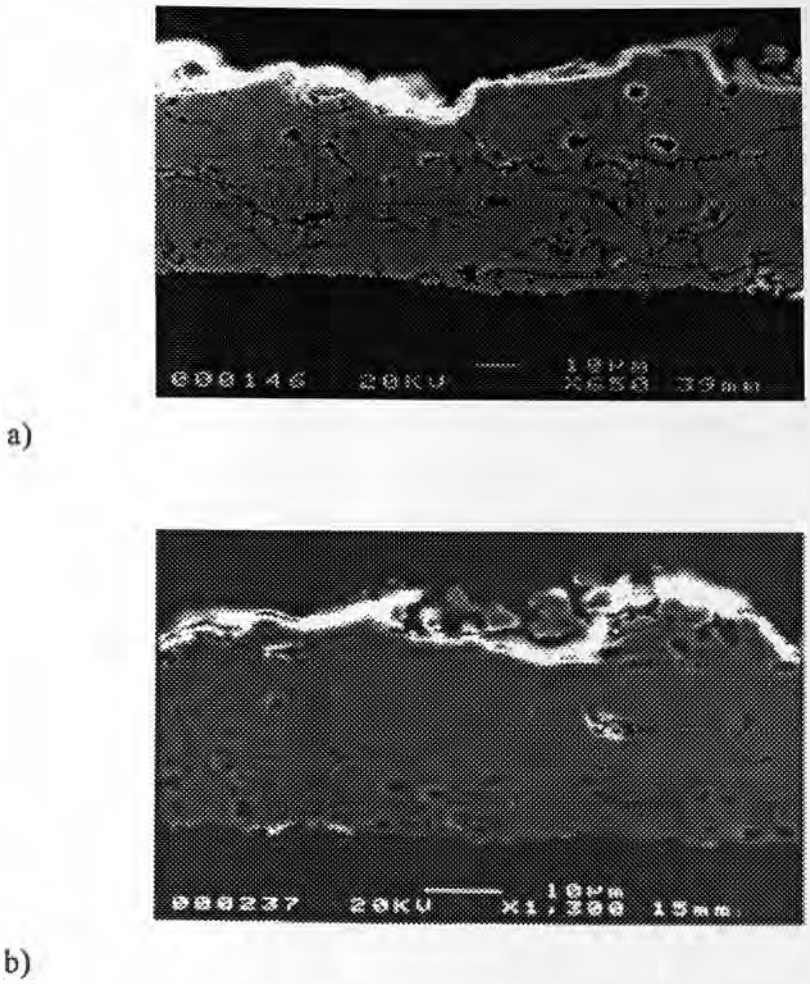

Figure 5.5.2 Scanning electron micrographs of YSZ on 96% Al_2O_3 a) as-sprayed and b) after sintering at 1450 ^{0}C after 1 hour. Supplied by Watcham et. al [5.5.1].

Figure 5.5.3a shows the X-ray diffraction (XRD) pattern for an as-sprayed barrier layer. The interplanar spacing d is identified as belonging mainly to the cubic form of zirconia. We also see a small amount of tetragonal forms. A small amount of understabilised material is present, which on cooling, transform themselves onto the monoclinic phase. Figure 5.5.3b shows the pattern after sintering at 1450 ^{0}C. The increased amount of the monoclinic phase next to the interface indicates that destabilisation of the YSZ has taken place leading to a larger amount of the monoclinic phase being produced on cooling.

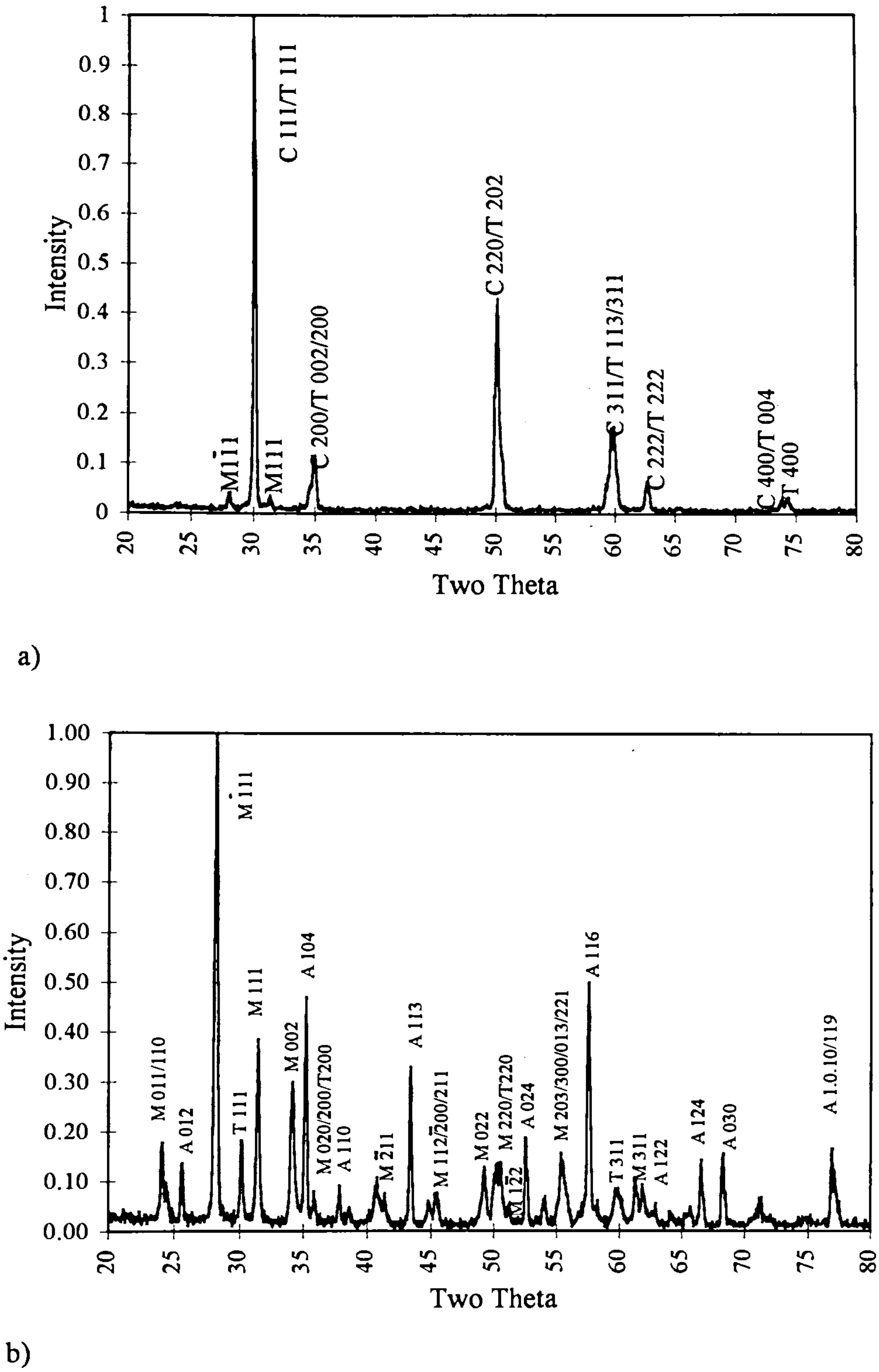

Figure 5.5.3 XRD patterns of plasma sprayed YSZ on 96% Al_2O_3. a) before sintering, b) after sintering. Supplied by Watcham et. al [5.5.1]. Here M, C, T and A stand for Monolithic, Cubic, Tetragonal and Alumina structures, respectively.

Figure 5.5.4 shows a cross-section through a typical alumina/YSZ/YBCO structure. At some points YBCO has penetrated into the barrier layer reacting with the YSZ/Al_2O_3 interface and then forming a parallel reaction layer of (Ba, Cu)ZrO_3. The melt textured YBCO layer is very similar to that observed on YSZ substrate; however it was not observed the same degree of densification of the films during the melting process. The Y_2BaCuO_5 (211) phase is found throughout the film; however these precipitates are relatively large and not evenly distributed throughout the films.

Watcham et. al [5.5.1] presented XRD patterns from an YBCO film melt textured at 1050^{0}C on a YSZ barrier layer 35μm (not shown here). Those results show an enhancement of the 00*l* peaks indicating the presence of preferential orientation (c-axis) within the film.

Figure 5.5.4 Polarised light micrograph of the YBCO/YSZ/Al_2O_3 structure. The major phases existent are shown. Supplied by Watcham et al. [5.5.1].

The results showing the differences in surface resistance (Rs) for films grown on YSZ and YSZ-buffered alumina substrates for low microwave input power at 15GHz are shown in figure 5.5.5. The thick films 1, 2 and 3 were processed at 1035^{0}C, 1040^{0}C and 1045^{0}C, respectively. It is clear that as the processing temperature increases the grain connectivity increases which leads to a decrease in the surface impedance. The film grown on YSZ was processed at 1050 and presents the lowest surface resistance in the plot. However YSZ substrates have high insertion loss and then less application in microwave devices. The process used to fabricate the thick film 3 looks promising for microwave application. Alumina substrate of size 5cm × 5cm and thicknesses 1mm and 0.5mm is already commercially available. In principle the process used here may be used to produce relatively large devices since the sintering stage can be carried out maintaining the same temperature all over the substrate.

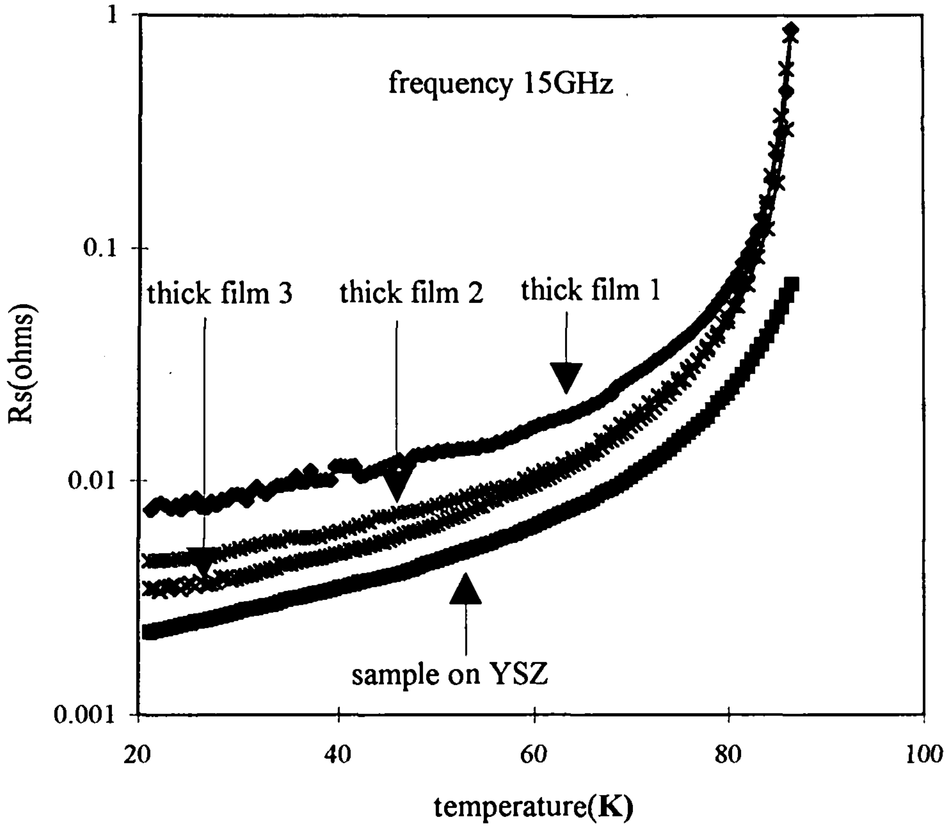

Figure 5.5.5 Surface resistance Rs as a function of temperature for different processing temperature. Supplied by Watcham et al. [5.5.1].

Chapter 6

Microstrip Resonator Experimental Results

6.1 Copper Resonator

Looking back at section 3.3 of chapter 3 the unloaded quality factor of a TEM mode microstrip resonator is given by $Q_0 = 2\pi f_n L/(R_{s1}+R_{s2})$. In the Hybrid Copper/YBCO microstrip resonator, which will be described in section 6.2, R_{s1} and R_{s2} are the surface resistances of the copper and the YBCO materials, respectively. Thus, in order to find the surface resistance of the films we needed at first to find the surface resistance of the copper ground plane. A microstrip resonator with the top strip made of the same material of the ground plane was set up with a copper strip (2.4mm wide, 0.3mm thick and 9.4mm long) and a ground plane separated by a MgO substrate. The substrate dimensions were the same as the strip 2.4mm x 9.4mm x 0.5mm. The strip (film/substrate) was held on the ground plane by using an optical glue. The device was mounted in a brass housing which was built and sealed by soldering the two halves together in order to make it impervious to liquid nitrogen. The microwave power was capacitively coupled into the ends of the resonators using k-connector pins. The coupling gap was kept at about 0.3 mm. The electrical contact between the copper ground plane and the box was aided by a thin layer of indium as well as by a BeCu spring. Figure 6.1.1 presents a cross-section of the resonator in the brass housing.

The resonator response was measured in transmission mode using a HP8720A network analyser. The frequency response around the fundamental resonant mode $f \cong 7.5$ GHz is shown in figure 6.1.2. Now we will consider the equation for the unloaded quality factor of the wide microstrip resonator (equation 3.3.5).

Assuming that the top strip and the ground plane have the same surface resistance ($R_{s1} = R_{s2} = R_{sc}$), we will be able to find the surface resistance of the copper R_{sc} at the central frequency of the response in figure 6.1.2.

The quality factor of the loaded resonator, with the input and output connections present, is given by

$$Q_L^{-1} = Q_0^{-1} + Q_{ext}^{-1} \qquad \text{equation 6.1.1}$$

Where Q_{ext} is the external-circuit-limited quality factor associated with the capacitive coupling to the input source and the output load impedance. Assuming the mode number n = 1 (number of half-wavelengths), Q_{ext} is given by [6.1.1]

$$Q_{ext} = \frac{\pi}{4\omega^2 C^2 Z_0 Z_s} \qquad \text{equation 6.1.2}$$

Here Z_s is the source impedance, Z_0 is the characteristic impedance of the transmission line and C is the capacitance by which the active plate is coupled to 50-ohm source and load impedances.

The loaded quality factor Q_L of the transmission resonator is measured from the measured resonant curve dividing the 3dB width Δf of the resonant curve by the resonant frequency, f_r. The effect of external circuit loading can be corrected for by [6.1.1, 6.1.2]

$$Q_o = \frac{Q_L}{1 - 10^{\frac{I_L}{20}}} \qquad \text{equation 6.1.3}$$

Where I_L is the insertion loss, which is the transmission coefficient between two points in the circuit expressed in dB. Considering $|S_{21}|$, the magnitude of the transmission coefficient from port 1 to port 2, I_L is given by

$$I_L = 20\log|S_{21}| \qquad \text{equation 6.1.4}$$

Taking the values of the insertion loss $I_L \cong -27.5$ dB and $Q_L \cong 1114$ from figure 6.1.2 and assuming a symmetrical coupling as in the derivation of equation 6.1.3 one obtains $Q_o \cong 1163$ at 77K. From the device one has $h = 5.10^{-4}$m. Substituting this data into the equation for the unloaded quality factor of the wide microstrip resonator (equation 3.3.5) for $R_{s1} = R_{s2} = R_{sc}$ one obtains the copper surface impedance as $R_{sc} \cong 13\ m\Omega$ at 77K, which is in good agreement with the result found in the reference [6.1.3].

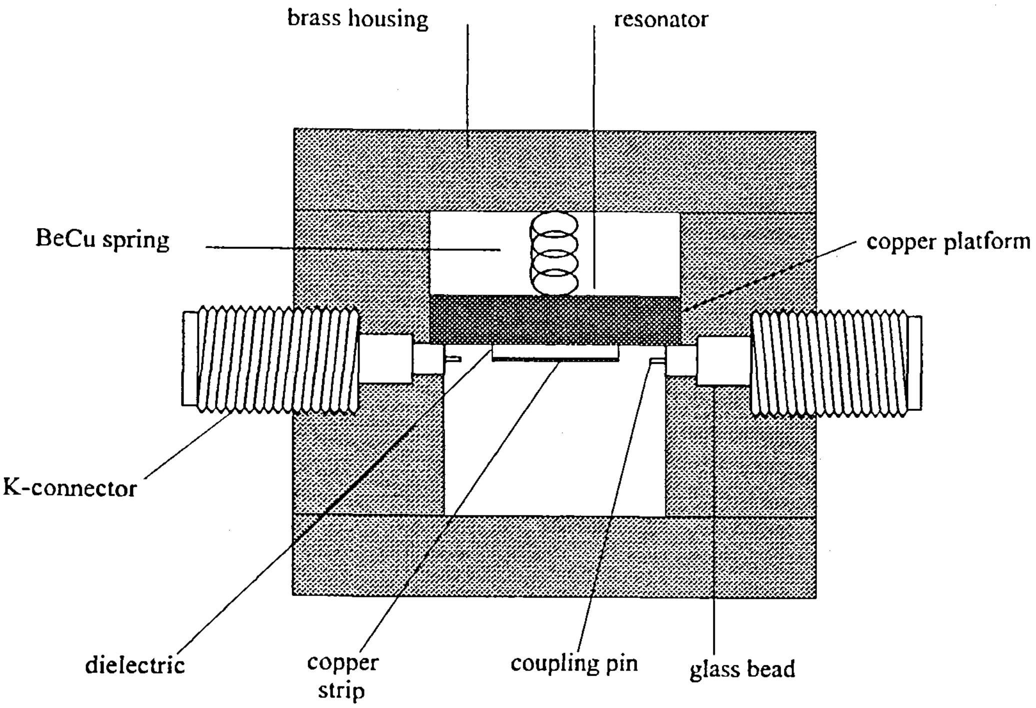

Figure 6.1.1 Cross-section of the all copper microstrip resonator in its housing.

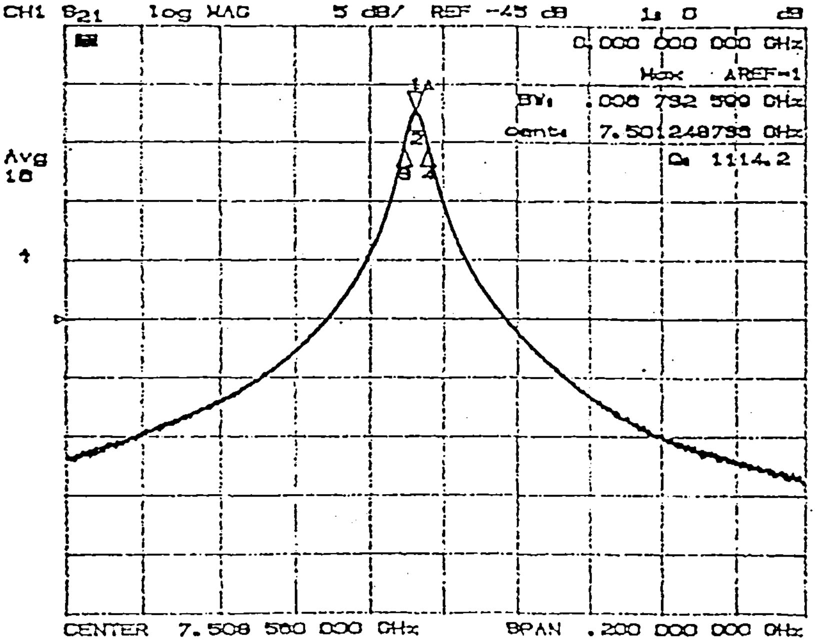

Figure 6.1.2 Frequency response around the first resonant mode of all copper microstrip resonator, at $T \cong 77K$.

6.2 Superconducting Resonator

The superconducting microstrip device has the same appearance as the one presented in figure 6.1.1. The only difference is that there is now HTSC thin film on the top of the substrate instead of copper strip. The devices were fabricated by both laser ablation of $YBa_2Cu_3O_7$ thin film on MgO substrate and dipping pyrolysis of $YBa_2Cu_3O_{7-\delta}$ on yttria-stabilized-zirconia (YSZ) processes (see chapter 5).

The surface resistance of the measured $YBa_2Cu_3O_{7-\delta}$ thin film will now be discussed. At first, we shall consider the laser ablated device.

6.3 Laser Ablation Device Measurement

All laser-ablated films used herein were fabricated by using the process described in chapter 5. Figure 6.3.1 shows, in three dimensions, the hybrid copper/YBCO film made by laser ablation.

The loaded quality factor was found using the same procedure and the same conditions of temperature and frequency as discussed before in section 6.1.

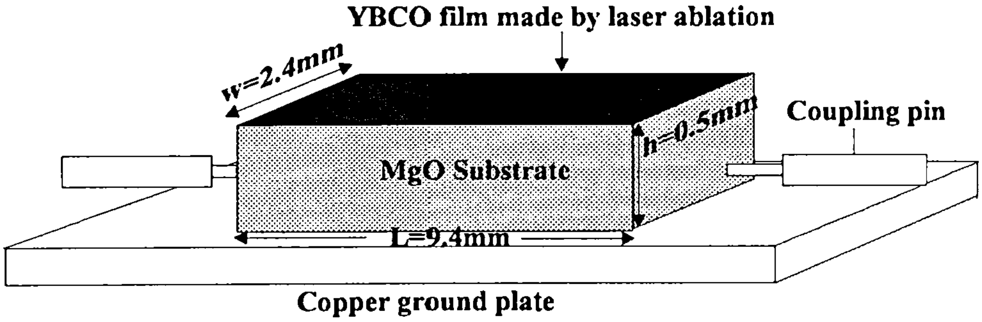

Figure 6.3.1 Hybrid copper/YBCO film made by laser ablation.

In order to find the surface resistance of $YBa_2Cu_3O_{7-\delta}$ thin film made by laser ablation, using the frequency response of the experimental results, we will proceed in two different ways. For comparison, we will firstly take the thickness of the film into account by using equation 4.3.6 and secondly neglect the thickness of the film by using equation 4.3.7. Four laser ablated films were measured.

Figure 6.3.2a presents the frequency response from 0.225 GHz to 20 GHz of the best one. As one can see, there are two peaks in this figure, the fundamental resonant peak at frequency 7.25GHz and also a small unwanted peak. This unwanted resonator seems to be originated from the contact between the housing box and the ground plane. Figure 6.3.2b presents the frequency response around the fundamental resonant peak on a bigger scale.

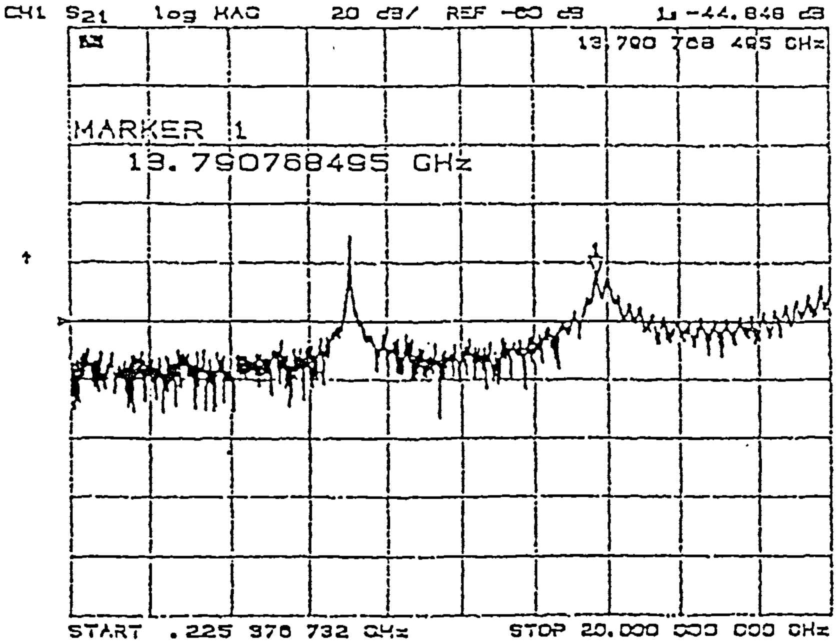

Figure 6.3.2a Frequency response from 0.225 GHz to 20 GHz.

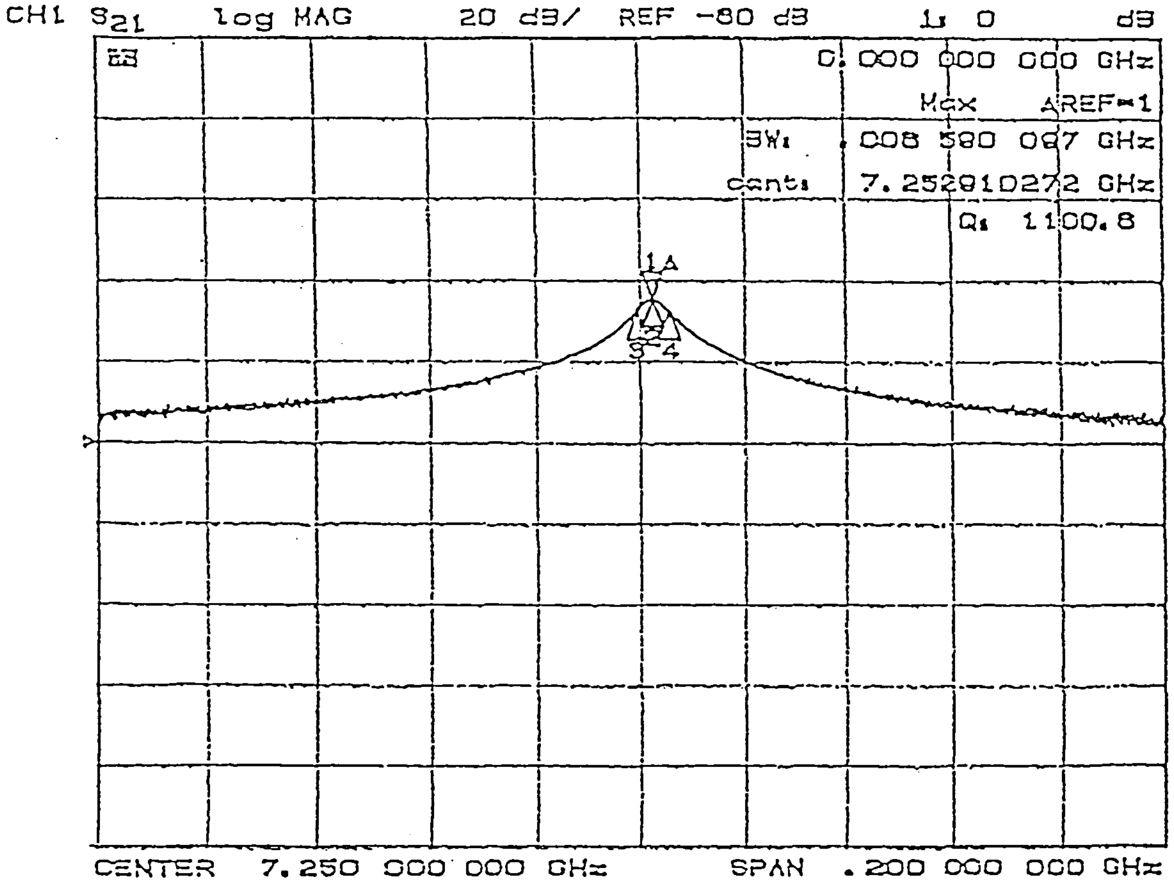

Figure 6.3.2b Frequency response around the fundamental resonant peak.

6.4 Surface Resistance Of the laser-Ablated Thin Films

From figure 6.3.2b we have insertion loss $I_L \cong -26$ dB and $Q_L \cong 1100$. Once again, we can use equation 6.1.3 to convert the loaded quality factor into the unloaded quality factor, which gives $Q_o \cong 1158$. Assuming $T_c \cong 90K$, $\lambda(0) \cong 200nm$, $h = 0.5$ mm, $R_{sc} = 13\ m\Omega$, $w = 2.4$ mm and $t_i = 250nm$ [6.4.1] one can find the surface resistance of this film. Taking into account its thickness by using equation 4.3.6 we obtain $R_{ss}(t_i) \cong 5\ m\Omega$. Applying this data into the simplified expression without taking the thickness into account (equation 4.3.7) one finds $R_{ss} = 12 m\Omega$. The same calculation was assumed for all other laser-ablated films, summarised in table 6.4.1.

Table 6.4.1 presents the unloaded quality factor and the surface resistance of one copper strip and four laser ablated thin films. In this table we listed the findings of the surface resistance of the films by considering the effect of their thicknesses $R_{ss}(t_i)$ and the findings of the surface resistance of the films without considering the effect of their thicknesses R_{ss}.

Table 6.4.1 Unloaded quality factor and surface resistance of the laser ablated films.

SURFACE RESISTANCE RESULTS FOR SEVERAL LASER-ABLATED YBCO THIN FILMS $f_o \cong (7.3 \pm 0.4) \times 10^9$HZ AND T=77.3K (LIQUID NITROGEN) input power = -10dBm			
1	2	3	4
REFERENCE	Q_o	R_{ss}(mΩ) eq. 4.3.7	$R_{ss}(t_i)$ (mΩ) $(\lambda_o = 200 \cdot 10^{-9}\,m)$ $(ti = 250 \cdot 10^{-9}\,m)$ eq. 4.3.6
COPPER ONLY	1163.0	13	-
060193/12	1158.0	12	5
100393/35	662.5	31	13
230793/113	500.3	45	19
260793/114	307.7	81	34

6.5 Dipping Pyrolysis Device Measurement

All YBCO films made by dipping pyrolysis used herein were fabricated using the process described in chapter 5. Once again the films were formed on only one side of the substrate which was yttria stabilised zirconia (YSZ).

The copper/superconducting microstrip resonator was formed by lying a sliced section of the thin film coated YSZ substrate on top of a copper ground plane as shown in figure 6.5.1. The substrate size was ~ 2.4mm x 1.1mm x 9.4mm. The measurement in transmission mode was carried out by following the same procedure as described in section 6.1 using a HP8720A network analyser with a computer interface.

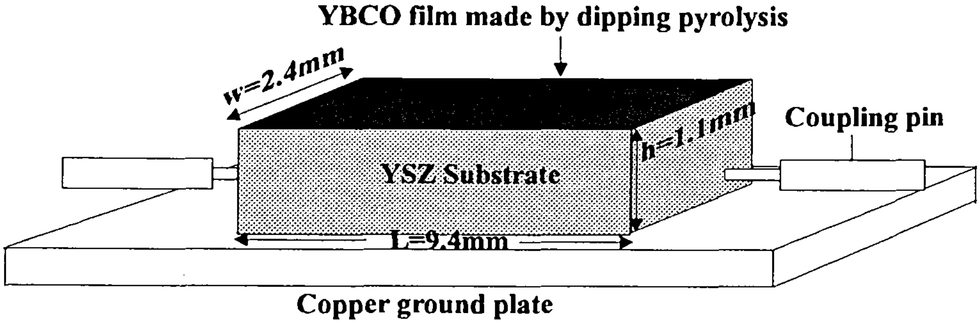

Figure 6.5.1 Hybrid copper/YBCO film made by pyrolysis resonator device.

In order to calculate the surface resistance of the films a hybrid copper ground plane / YSZ substrate / copper strip device was made and measured. Using equation 6.1.3 and equation 3.3.5 it was found $R_{sc} \cong 17m\Omega$ at 77K and ~ 5 GHz. The copper used in figure 6.5.1 and that one used in figure 6.3.1 were from different manufacturers, having different degree of purity. That difference was not important since we used $R_{sc} \cong 17m\Omega$ to calculate the surface resistance of the films made by pyrolysis. The dielectric loss of the YSZ was assumed to be negligible.

In order to organise our discussion about the experimental results the films will be called pyrolysis-film-a, pyrolysis-film-b and pyrolysis-film-c. Frequency response of the pyrolysis-film-a from 0.13GHz to 20GHz is shown in the figure 6.5.2. The substrate size was ~ 2.4mm x 9.4mm x 1.1mm. Four sharp resonant peaks are shown.

The lower frequency resonant peaks are well defined and show no distortion over an extended dynamic range, as seen in figure 6.5.3.

Using a substrate of the same size as that one used in figure 6.5.1 we measured the frequency response of the pyrolysis-film-b from 0.13GHz to 20GHz, as shown in figure 6.5.4. Four resonant peaks are shown. Later on in this section we will compare pyrolysis-film-b with the pyrolysis-film-a, focusing our analysis on distortion and frequency shift of some resonant peaks.

The pyrolysis-film-c of size ~ 2.4mm x 9.4mm x 0.5mm, was measured. Figure 6.5.6 shows the frequency response from 0.13GHz to 20GHz. Figure 6.5.7 shows the frequency response around the fundamental resonant peak of frequency $f_o \cong 6.3348$ GHz.

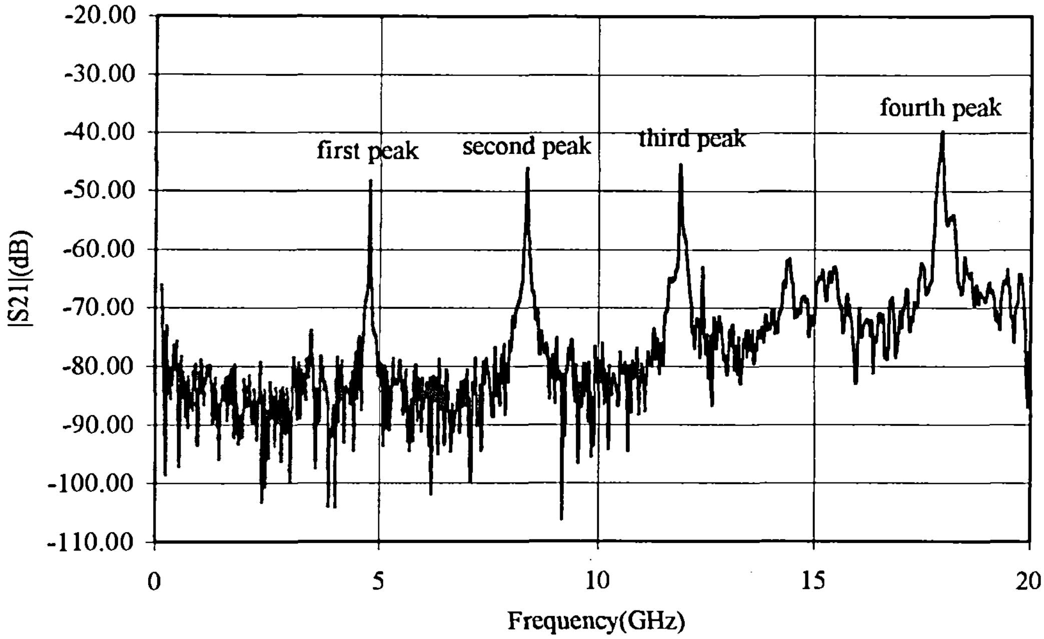

Figure 6.5.2 Pyrolysis-film-a. Frequency response from 0.13GHz to 20GHz. Substrate size ~ 2.4mm x 9.4mm x 1.1mm.

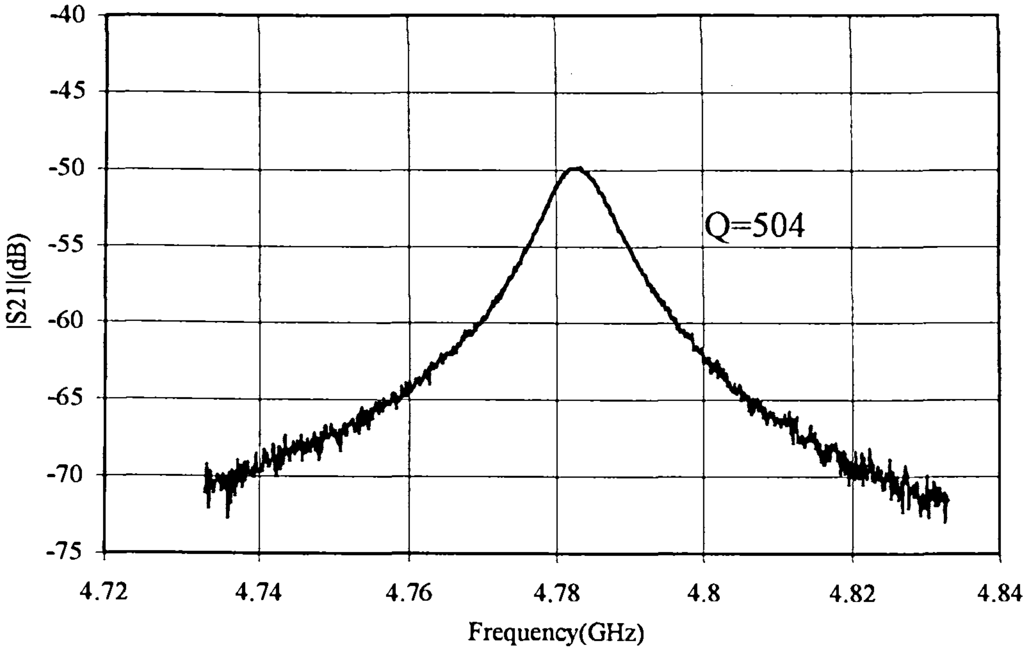

Figure 6.5.3 Pyrolysis-film-a. Frequency response around the fundamental resonant peak of frequency $f_o \cong 4.784$GHz. Loaded Quality factor ≅ 504. Span 0.10 GHz. Substrate size ~ 2.4mm x 9.4mm x 1.1mm.

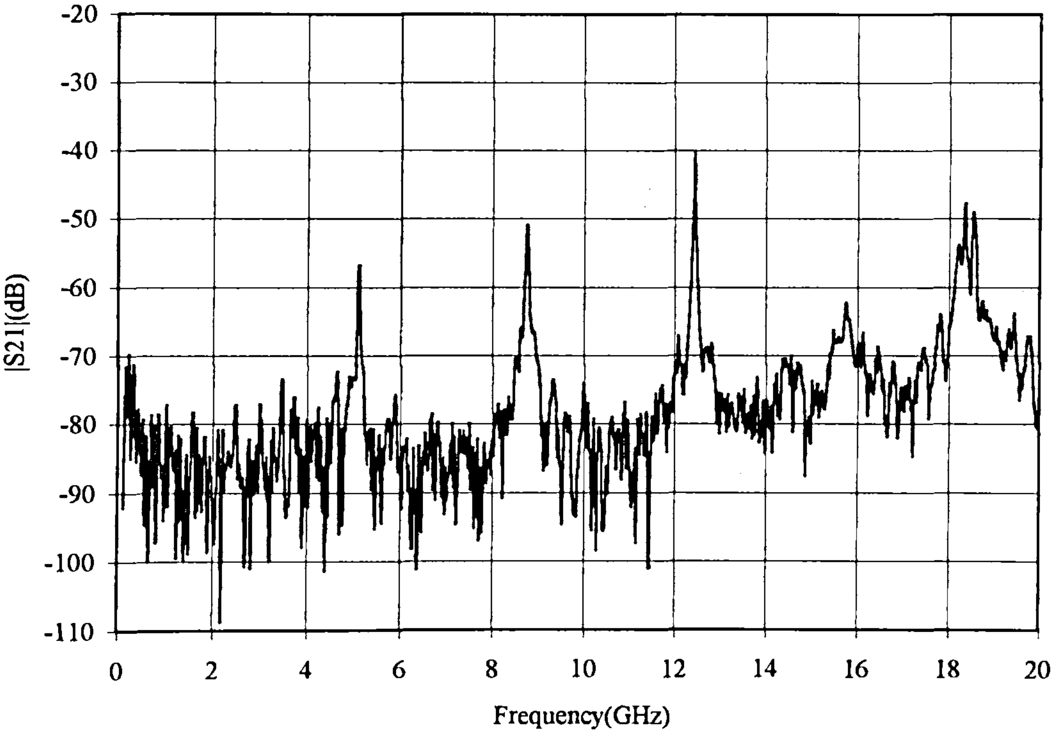

Figure 6.5.4 Pyrolysis-film-b. Frequency response from 0.13GHz to 20GHz. Substrate size ~ 2.4mm x 9.4mm x 1.1mm.

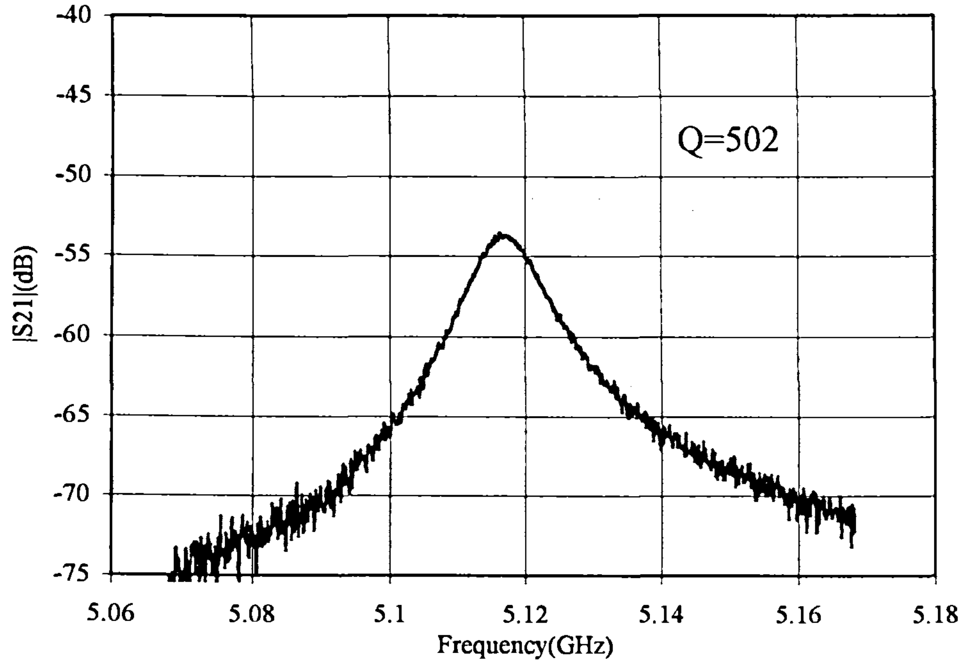

Figure 6.5.5 Pyrolysis-film-b. Frequency response around the fundamental resonant peak of frequency $f_o \cong 5.1169$GHz. Loaded Quality factor ≅ 502. Span 0.10GHz. Substrate size ~ 2.4mm x 9.4mm x 1.1mm.

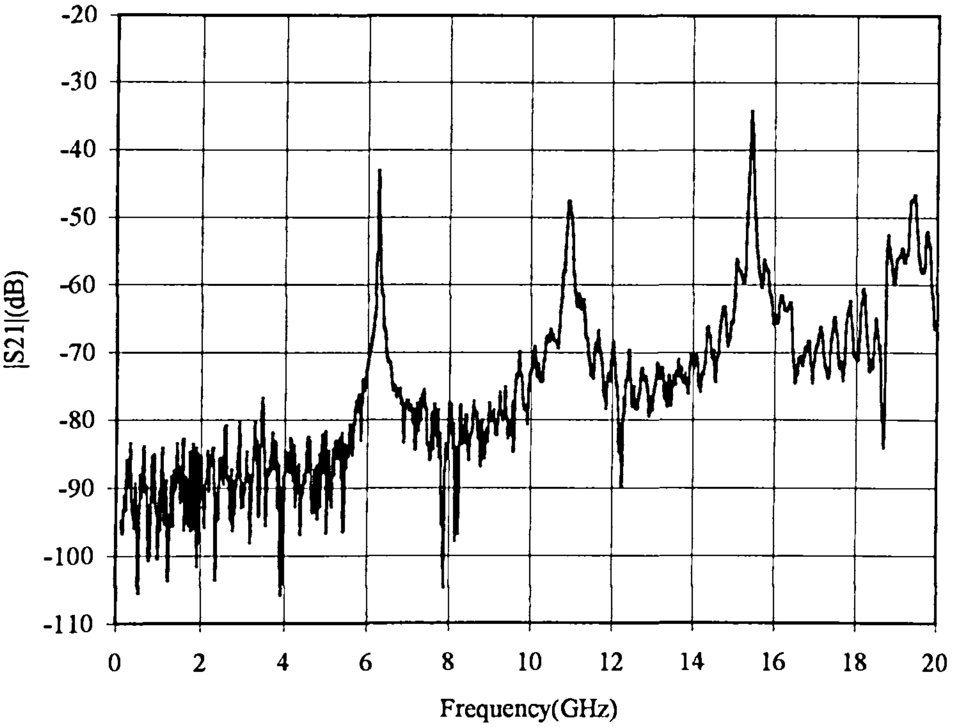

Figure 6.5.6 Pyrolysis-film-c. Frequency response from 0.13GHz to 20GHz. Substrate size ~ 2.4mm x 9.4mm x 0.5mm.

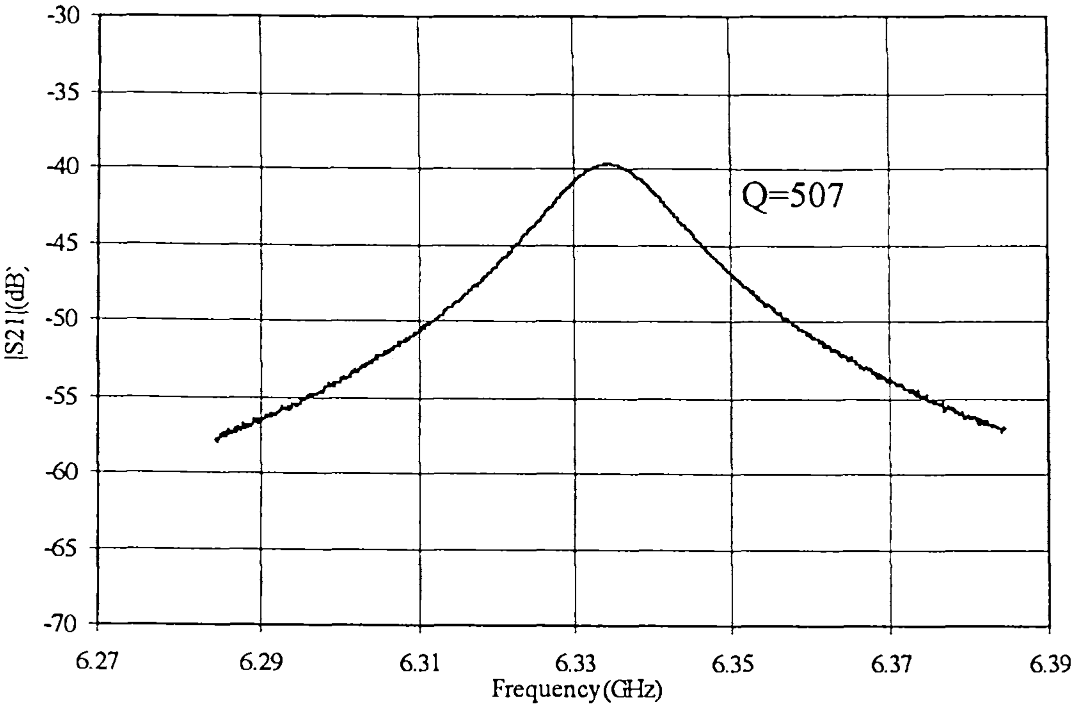

Figure 6.5.7 Pyrolysis-film-c. Frequency response around the fundamental resonant peak of frequency $f_o \cong 6.3348$ GHz. Loaded Quality factor ≅ 507. Span 0.10GHz. Substrate size ~ 2.4mm x 9.4mm x 0.5mm.

6.6 Surface Resistance Of Films made by Pyrolysis

For the resonator in figure 6.5.1, the surface resistance of the pyrolysis-film-a taking into account its thickness ($R_{ss}(t_i)$) can be extracted from the measured frequency response, shown in figure 6.5.3. Using the same procedure as that one used in section 6.4 one can find the unloaded quality factor Q_0.

The films were ~ 1μm thick with a textured granular structure with grain size also ~ 1μm as determined from SEM surface measurements. Assuming the granular model described in section 2.3.4 and substituting $I_c = J_c a^2$ into equation of the effective penetration depth for granular conductors (λ_g), we obtain [6.6.1]

$$\lambda_g = \left(\frac{\phi_o}{2\pi\mu a J_c}\right)^{1/2} \qquad \text{equation 6.6.1}$$

Where J_c is the critical current density. λ_g was estimated from the critical current measured at 77K (2×10^3A/cm^2) to be 3.6μm (i.e. larger than the film thickness). Substituting the values of Q_0 and λ_g into equation 4.3.6 which takes the thickness of the film into account we then derived a value for the surface resistance of ~13mΩ.

Equations 4.3.6 and 4.3.7 assume the loss contribution from the dielectric as negligible. This may work well for the case of MgO substrate at 7GHz ($\tan\delta \approx 10^{-5}$), used in the previous section. YSZ has $\tan\delta \approx 5\times10^{-4}$ at 5GHz and has to be taken into account. Thus, equations 4.3.6 and 4.3.7 become

$$Q_c = \frac{2\pi f_n \mu E}{A + R_{sc}} \qquad \text{equation 6.6.2}$$

$$Q_c = \frac{2\pi f_n \mu_o h}{R_{ss} + R_{sc}} \qquad \text{equation 6.6.3}$$

where [6.6.2]

$$\frac{1}{Q_c} = \frac{1}{Q_0} - \tan\delta \qquad \text{equation 6.6.4}$$

Here A and E were already described in section 4.3 of chapter 4. $1/Q_c$ is the conductor loss contribution and $\tan\delta=1/Q_d$ is the dielectric loss contribution. Carrying on the same calculation described above but now using equation 6.6.2 instead of equation 4.3.6 we find a more accurate value of surface resistance of 9mΩ.

This method of calculation was also assumed for the other films fabricated by dipping pyrolysis, summarised in table 6.6.1. We also have in table 6.6.1 the surface resistance of the films without take into account the thickness, given by equation 6.6.3.

Table 6.6.1 Unloaded Q_o and surface resistance of three films made by dipping pyrolysis. The fourth column represents the values of surface resistance using equation 6.6.2.

SURFACE RESISTANCE RESULTS FOR THREE YBCO THIN FILMS MADE BY DIPPING PYROLYSIS AT T=77.3K (LIQUID NITROGEN)				
REFERENCE	Q_o	freq(GHz)	R_{ss} (mΩ) eq. 6.6.3	$R_{ss}(ti)$(mΩ) $(\lambda_o = 3.6 \cdot 10^{-6}\,\mathrm{m})$ $(ti = 1.4 \cdot 10^{-9}\,\mathrm{m})$ eq. 6.6.2
Film(a) h=1.1mm	504	4.8	45	9
Film(b) h=1.1mm	502	5.1	49	10
Film(c) h=0.5mm	507	6.3	64	20

6.7 General Discussion

In this section we aim to discuss the frequency response of the best measured laser ablated thin film and of the measured pyrolysis-films already presented in this chapter. On the basis of the experimental procedure and using some concepts already presented herein, we will try to explain the behaviour of some peaks and compare them.

Let us start with the frequency response of the best laser ablated film seen in figure 6.3.2a. The unwanted peak, labelled as mark-1 was found to be very sensitive to the amount of indium located at both ends of the ground plane which was used to improve the electrical contact between the ground plane and the box. Thus, this resonate mode seems to be related by the poor contact between the ground plane and the box. Although no definitive explanation can be given.

Comparing the best laser ablated film response seen in figure 6.3.2b with the pyrolysis-film-c response seen in figure 6.5.7, we see two different values of the frequency for the fundamental resonant peak. For the laser ablated thin device we have $f_0 \cong 7.2$GHz and for the pyrolysis-film-c we have $f_0 \cong 6.33$GHz. This behaviour can be attributed to the different values of dielectric constant, $\varepsilon_r \cong 9.6$ for the MgO substrate used to make the laser ablated films and $\varepsilon_r \cong 29$ for the YSZ substrate to make the pyrolysis-films. For a line of length ℓ the fundamental resonant frequency is given by [6.7.1]

$$f_0 = c_0 / 2\ell\sqrt{\varepsilon_r} \qquad \text{equation 6.7.1}$$

The larger the dielectric constant ε_r the lower the fundamental resonant frequency f_0.

Comparing the pyrolysis-film-a response in figure 6.5.3 with the pyrolysis-film-b response in figure 6.5.5 we see a frequency shift in the fundamental resonant peak. Since both devices have the same physical dimension and the same dielectric material, this frequency shift can be explained if we analyse the change in the penetration depth.

Keeping all the other parameters unaltered, the penetration depth changes when the granularity properties of the superconducting film changes. The frequency shift is due to the change in the penetration depth given by [6.7.2]

$$-2\Delta\omega_0 = \Gamma\omega\mu_0\Delta\lambda \qquad \text{equation 6.7.2}$$

Here Γ is the geometry factor already seen in chapter 3. Typically, one attributes the change in the penetration depth to the change in the temperature. In our experiment we measured three pyrolysis-films, always at 77K (liquid nitrogen). For a granular superconductor the penetration depth depends on the intergranular distance a and the critical current density J_c given by the equation $\lambda_g = (\phi_o/2\pi\mu a J_c)^{½}$, as described in section 2.3.4 of chapter 2. From the chapter 5 we see that the bonding between grains is improved adding silver to the (350) phase. This way, at microwave frequency two pyrolysis-films with slight different values of grain size and critical current may have slight different values of penetration depth, which is about 3.6μm for the pyrolysis-films. This may give different values of surface resistance.

The increase in the bandwidth with the frequency as seen in both figures 6.5.2 and 6.5.4 may be explained by [6.7.2]

$$f_B = f_0 R_s/\Gamma \qquad \text{equation 6.7.3}$$

Here f_B is the resonance bandwidth. The superconducting surface resistance derived from two fluids model is given by $R_s = (2\pi f\mu_0)^2 \lambda^3\sigma_1/2$, as it was seen in section 2.3.3 of chapter 2. Assuming all the other parameters fixed, an increase in the frequency makes R_s increase which will make f_B increase, as a result.

From table 6.4.1 we see that the surface resistance of the copper material is smaller than the surface resistance of some laser-ablated films. From chapter 5 we know that the quality of the films depends on parameters such as laser power, oxygen pressure and substrate temperature. These parameters are carefully adjusted to achieve the best quality of the films [6.7.3]. Coming back to table 6.4.1 we see that the best measured thin film has $R_{ss} \cong 5m\Omega$ and $Q_o \cong 1158$. The results in the fourth column of table 6.4.1 take the thickness of the films into account, whereas the ones in the third column do not take it into account. Besides, we can notice that the average value of the third column is about 2.4 times bigger than the average value of the fourth column.

In summary, under the above conditions the calculations of surface resistance using equation 4.3.7 without taking the thickness of the film into account overestimate the intrinsic surface resistance. This is about 2.4 bigger than the calculations taking the thickness of the film into account.

The results shown in table 6.4.1 were taken at early stages of the laser ablation facility. Thus, optimised films will give better results, typically 690$\mu\Omega$ at 16GHz and 77K [6.7.4].

Chapter 7

Coplanar Structures

7.1 Introduction

Microwave Integrated Circuits (MIC's) have been successfully used to develop a large number of microwave components. Microstrip has been widely used as the main transmission line in these circuits. The use of coplanar waveguides (CPW) and coplanar strips (CPS) has increased recently. The term "coplanar lines" is used for the transmission lines which do not use a ground plane on the back side of the substrate. All conductors are in the same plane. These types of structure offer several advantages over conventional microwave line, such as no through holes are needed to connect active and passive devices with the ground conductors. The circuit fabrication process of coplanar MICs is simpler than that of double-sided MICs. In addition, coplanar structures generally have lower radiation losses. The problem of using coplanar lines is their relatively high current concentration at the edges.

The use of superconducting films in transmission lines has many advantages for signal-processing applications, such as low dispersion, low loss and wide bandwidth. The difficulty in producing double-sided HTS films has created interest in structures requiring a single conducting plane. Another advantage is that slow wave structures can be made with much lower velocities than microstrip. This is described later.

Calculations of the wave characteristic impedance and effective dielectric constant of coplanar lines by conformal mapping techniques were first presented by Wen (1969) [7.1.1]. Davis et. Al. (1973) [7.1.2] extended Wen's analysis to the ease of finite substrate thickness. Several trials were made to calculate line parameters taking into account the effect of finite substrate thickness and finite line dimensions using numerical methods. Among these methods we may mention the relaxation method proposed by Hatsuda (1975) [7.1.3] and that one involving Green's functions as presented by Houdart (1976).

Coplanar waveguides (figure 7.2.1), coplanar strips (figure 7.3.1), and coplanar wave guide with finite-extent ground planes (figure 7.4.1) will be used as part of the integrated microwave circuits which are to be presented in this thesis later on. This chapter aims to describe the design techniques.

7.2 Coplanar Waveguide

Coplanar waveguide consists of a center strip conductor with semi-infinite ground planes on either side (i.e., all located on the same surface of the substrate). Figure 7.2.1 presents the sketch of a coplanar waveguide (CPW) of line width w and line spacing s. For simplicity, we will assume both the center strip and the ground plane are of negligible thicknesses. Before starting any analytical formulation, we shall present some practical advantages and disadvantages of using such a transmission line.

Some advantages are: (i) single-side processing, i.e., the circuit only needs HTS films on one side of the substrate, this way the devices become less expensive; (ii) crosstalk reduction, i.e., the ground planes between the lines provide a shielding effect and offer the flexibility of choosing both the line width w and the line spacing s. (iii) Slow wave structures can be made with much lower velocity than microstrip.

Some disadvantages are: (i) an insertion loss which is generally higher than microstrip, because of current concentration at the edges of the strips; (ii) unwanted modes which can be excited by curvature or any asymmetry with respect to the centreline; this may be solved by adding air bridges to link the two grounds.

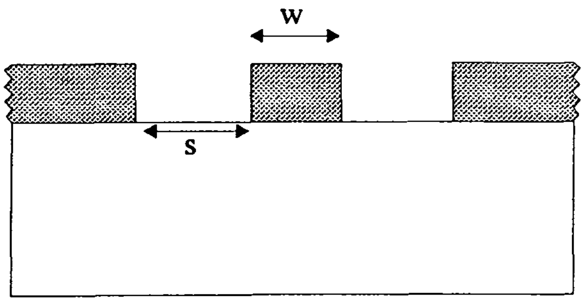

Figure 7.2.1 Coplanar wave guide cross section.

Figure 7.2.2 shows the electric and magnetic field configuration for quasi-static conditions. At high frequencies, a longitudinal component of the magnetic field exists and the mode of propagation becomes non-TEM.

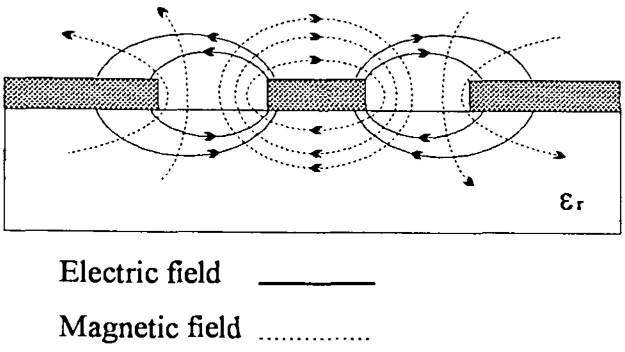

Figure 7.2.2 Electric and magnetic field distribution in CPW [7.2.1].

Calculations and experimental confirmation of wave characteristic impedance and effective dielectric constant by conformal mapping techniques were first presented by Wen [7.2.2]. Assuming that the dielectric substrate is thick enough to be considered infinite and the conductor thickness is negligible, we shall review his calculations.

Let us consider the familiar Schwarz-Christoffel [7.2.3] transformation which maps the dielectric half plane z_1 of CPW (figure 7.2.3.a) into an interior of a rectangle in the z-plane (figure 7.2.3.b), where the dotted lines on the sides of the rectangle represent the air-dielectric interfaces. The transformation equation is given by [7.2.3]

$$\frac{dz}{dz_1} = \frac{A}{\left(z_1^2 - a_1^2\right)^{1/2}\left(z_1^2 - b_1^2\right)^{1/2}} \qquad \text{equation 7.2.1}$$

where A is a constant. Multiplying both sides of the above equation by dz_1 we may carry out the integration and find

$$a + jb = \int_0^{b_1} \frac{A\,dz_1}{\left(z_1^2 - a_1^2\right)^{1/2}\left(z_1^2 - b_1^2\right)^{1/2}} \qquad \text{equation 7.2.2}$$

As a result

$$\frac{a}{b}=\frac{K(k)}{K'(k)} \qquad \text{equation 7.2.3}$$

Here K(k) is the complete elliptical integral of first kind and

$$k=\frac{a_1}{b_1}=\frac{w}{w+2s} \qquad \text{equation 7.2.4}$$

$$K'(k)=K(k') \qquad \text{equation 7.2.5}$$

where k and k' have a mutual dependence given by

$$(k)^2+(k')^2=1 \qquad \text{equation 7.2.6}$$

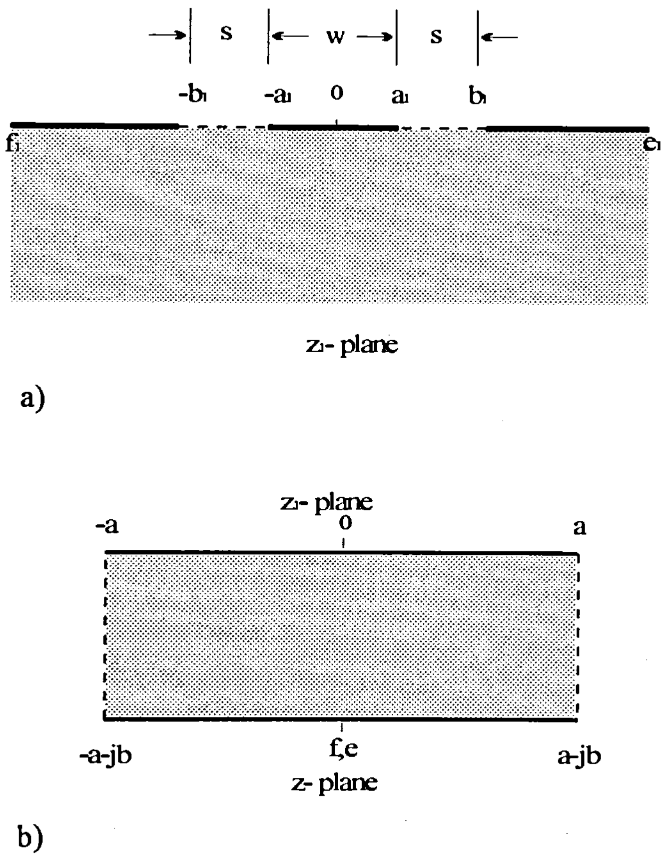

Figure 7.2.3 Conformal transformation planes.

If the dielectric constant of the material inside the rectangle in the z-plane of figure 7.2.3 is ε_r, a uniform electric field $\underline{E}$ is set up in the capacitor with the top and bottom plates charged up to opposite polarities. The capacitance per unit length of the line, including the empty space half-plane is

$$C = 1(\varepsilon_0)\frac{2a}{b} + \varepsilon_r\varepsilon_0\frac{2a}{b} = \varepsilon_0(1+\varepsilon_r)\frac{2a}{b} \qquad \text{equation 7.2.7}$$

The effective dielectric constant may be found by

$$\varepsilon_{re} = \frac{C}{C^a} \qquad \text{equation 7.2.8}$$

Here C^a is the capacitance per unit length of the line when replacing the dielectric by air. So, we have

$$\varepsilon_{re} = \frac{\varepsilon_0(1+\varepsilon_r)\frac{2a}{b}}{\varepsilon_0(1+1)\frac{2a}{b}} = \frac{1+\varepsilon_r}{2} \qquad \text{equation 7.2.9}$$

The approximation simply treats the CPW as a transmission line totally immersed in a dielectric with effective dielectric constant $(\varepsilon_r+1)/2$. Thus, the phase velocity becomes

$$v = \frac{c_0}{(\varepsilon_{eff})^{1/2}} = \left(\frac{2}{\varepsilon_r+1}\right)^{1/2} c_0 \qquad \text{equation 7.2.10}$$

The characteristic impedance may be obtained by

$$Z = \frac{1}{C\,v} \qquad \text{equation 7.2.11}$$

Substituting equation 7.2.7 and equation 7.2.10 into equation 7.2.11 and afterwards equation 7.2.3 we may use the relations

$$\left(\frac{\mu_0}{\varepsilon_0}\right)^{1/2} \cong 120\pi \quad \text{and} \quad c_0 = \frac{1}{\sqrt{\mu_0 \varepsilon_0}}$$

and finally obtain

$$Z = \frac{30\pi}{\sqrt{\frac{\varepsilon_r + 1}{2}}} \frac{K'(k)}{K(k)} \qquad \text{equation 7.2.12}$$

The ratio K'(k)/K(k) has been approximated by Hilberg [7.2.4] to a very good accuracy. It is given by

$$\frac{K(k)}{K'(k)} = \frac{1}{\pi} \ln\left(2 \frac{1+\sqrt{k}}{1-\sqrt{k}}\right) \qquad \text{for } 0.707 \leq k < 1 \qquad \text{equation 7.2.13}$$

$$\frac{K(k)}{K'(k)} = \frac{\pi}{\ln\left(2 \frac{1+\sqrt{k'}}{1-\sqrt{k'}}\right)} \qquad \text{for } 0 \leq k < 0.707 \qquad \text{equation 7.2.14}$$

Using typical data, the Mathcad program in section Ap.III.1 of appendix III provides the data to plot Z as a function of k for different dielectric constants, as shown in figure 7.2.4. Keeping the line width fixed (1.4mm) and the line spacing varying in the range 0.3×10^{-3} mm $\leq$ s $\geq 10\times10^{-3}$ mm, the characteristic impedance decreases as k goes from 0.06 to 0.7. In addition to this, keeping both w and s fixed, the larger the dielectric constant the higher the characteristic impedance. According to Wen's findings, the characteristic impedance increases by less than 10 percent when the thickness of the substrate is reduced from infinity to w. Besides, the thickness of the substrate (h) becomes less critical with higher relative dielectric constant. In Section 7.5 we will present the design equations for coplanar waveguide with finite-extent ground planes, taking the dielectric thickness into account.

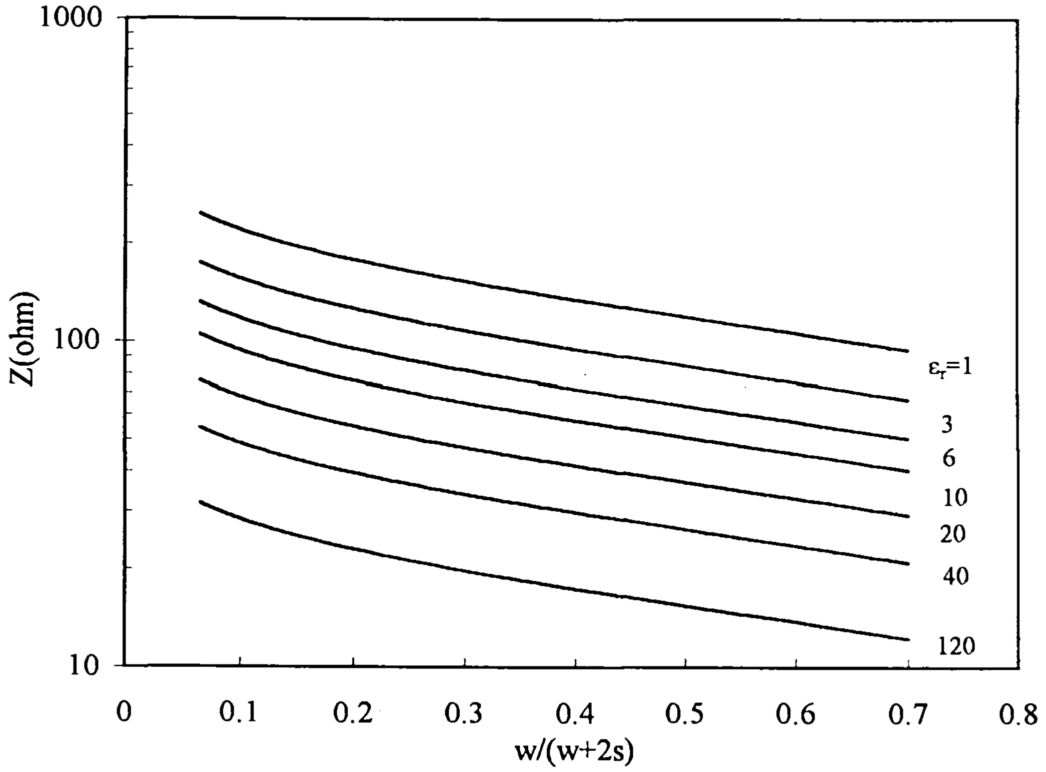

Figure 7.2.4. Characteristic Impedance of coplanar waveguide for different dielectric constants.

7.3 Coplanar Strip Lines

In a curved coplanar waveguide (CPW), poor return loss and large insertion loss are due to the phase distortion of the wavefront as it passes through the bend. The phase distortion is caused by the large difference in the path length between the inner slot and outer slot which guide the CPW mode. Coplanar stripline (CPS) has the potential to overcome these problems [7.3.1]. CPS consists of a pair of strip conductors of width w and separated by a slot width s (i.e., all located on the same surface of the substrate). Figure 7.3.1 presents the cross section of the CPS. The use of comb transmission lines made by coplanar strip fingers as delay lines looks a promising idea. In chapter 9, we will explore this idea in order to design our coplanar instantaneous frequency measurement system.

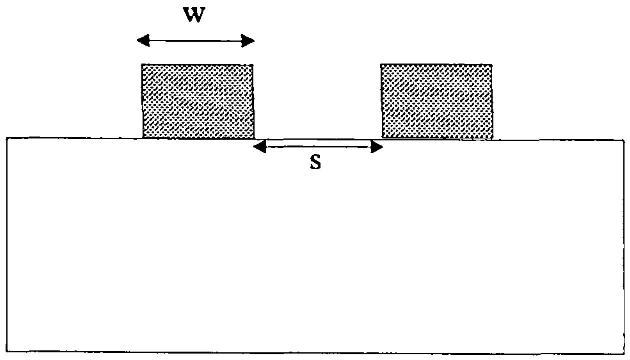

Figure 7.3.1 Coplanar strip cross section.

Figure 7.3.2 shows the electric and magnetic field configuration for quasi-static conditions.

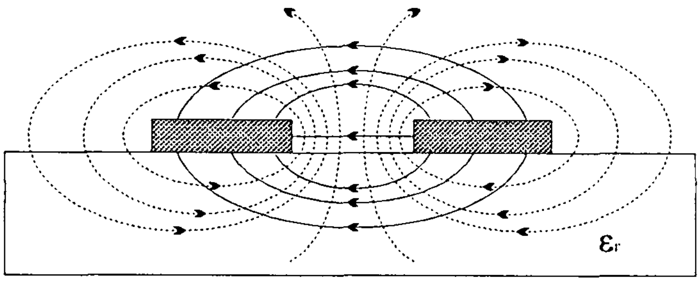

Electric field ______

Magnetic field ....

Figure 7.3.2 Electric and magnetic field distribution in CPS [7.3.2].

Since coplanar strips and coplanar waveguides configurations are complementary to each other, conducting and air-dielectric walls in figure 7.2.3 are interchanged for the analysis of CPS. Thus, keeping the line width as w, figure 7.3.3 shows the CPS conformal transformation planes.

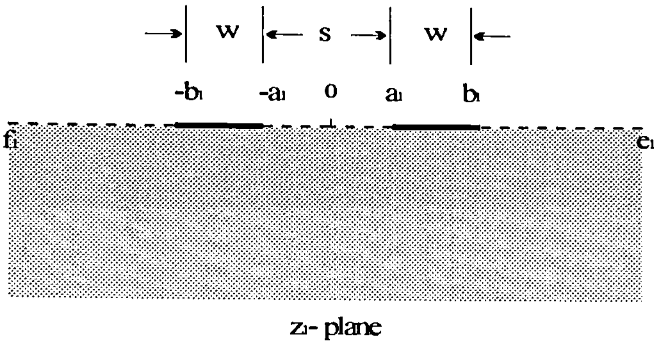

a)

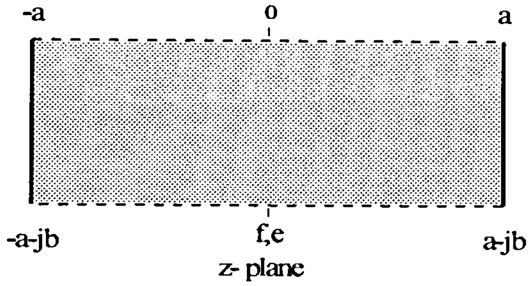

b)

Figure 7.3.3 Conformal transformation planes. Here we kept the line width as w.

The capacitance per unit length of the line, including the empty space half-plane is given by

$$C = (\varepsilon_r + 1)\varepsilon_0 \frac{b}{2a} \qquad \text{equation 7.3.1}$$

Substituting equations 7.3.1 and 7.2.10 into equation 7.2.11, we find after some manipulation

$$Z = \frac{120\pi}{\sqrt{\frac{\varepsilon_r + 1}{2}}} \frac{K(k)}{K(k')} \qquad \text{equation 7.3.2}$$

Using typical data, the Mathcad program in section Ap.III.2 of appendix III provides the data to plot Z as a function of k for different dielectric constants, as shown in figure 7.3.4. Keeping the line width fixed and the line spacing varying in the range 0.01×10^{-3} mm ≤ s ≥6.5×10^{-3} mm, the characteristic impedance increases as k goes from 0.09 to 0.7. As one can see, in figure 7.3.4 Z has the opposite behaviour to that presented in figure 7.2.4, just because CPS and CPW are complementary to each other. Different geometry factors, 2a/b for CPW and 2b/a for CPS, produce different values of capacitance. It should be noted that for reasonable values of ε_r it is difficult to get a 50Ω line without using low ratios of s/s+2w.

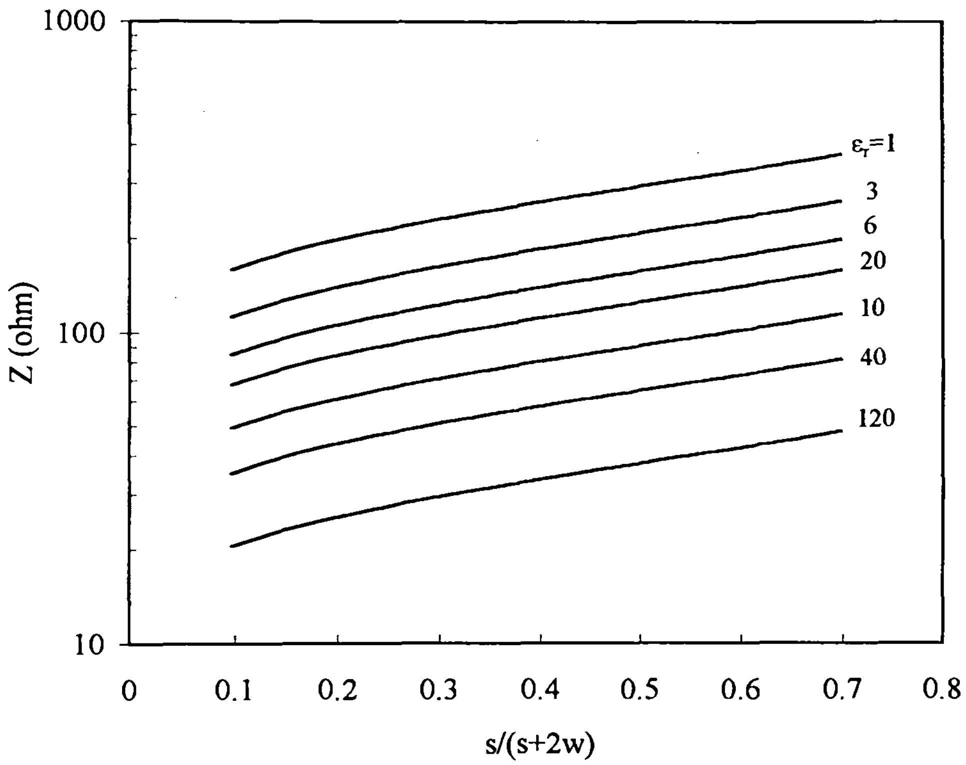

Figure 7.3.4. Characteristic impedance of Coplanar Strips for different dielectric constants.

7.4 Coplanar Waveguide with Finite Dimensions

Coplanar waveguide with finite dimensions consists of a center strip conductor with finite ground planes on either side (i.e., all located on the same surface of the substrate), as shown in figure 7.4.1. Veyres C, et. Al [7.4.1] presented the closed form expressions for CPW with finite line dimensions and substrate thickness using conformal mapping techniques. Let us start calculating the line capacitance.

The line capacity between the central strip and the two ground strips is equal to the sum of the line capacitance C_1 in the absence of the dielectric and the line capacity C_2 when assuming that all electric field is concentrated in the dielectric which relative permittivity is (ε_r-1).

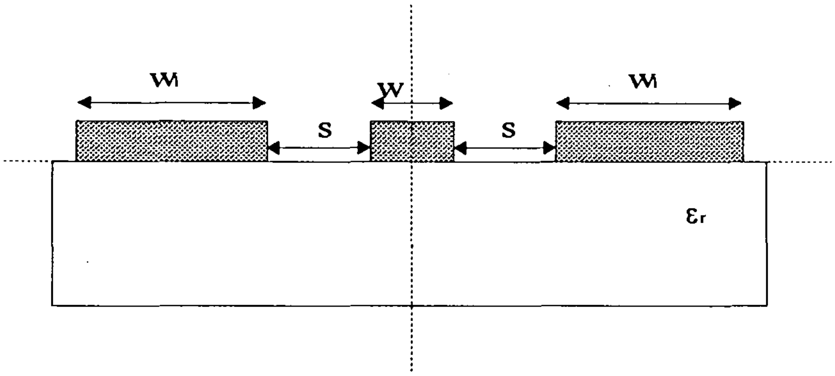

Figure 7.4.1 Coplanar wave guide with finite dimensions. It is divided into 4 quadrants, so that the conformal map techniques can be applied.

The technique for evaluating C_1 involves two conformal mappings which translate the finite-CPW into a parallel-plate capacitor. Let us follow the conformal mappings used by Veyres, et. Al [7.4.1].

In this formulation, we will consider only the lower right hand side quadrant of figure 7.4.1 and multiply the final capacitance by four to obtain C_1. The first mapping is from the z-plane to the t-plane, as shown in from figure 7.4.2. In other words, a point p(z) in the lower right hand side quadrant of the plane-z is mapped into a point p(t) in the upper right hand side quadrant of the plane-t by using

$$t = r + js = \frac{z}{x_3}\sqrt{\frac{x_3^2 - x_1^2}{z^2 - x_1^2}} \qquad \text{equation 7.4.1}$$

Here

$$x_1 = \frac{w}{2} \text{ and } x_3 = \frac{w}{2} + s + w_1$$

To map from the plane-t to the plane-w we use the elliptic function [7.4.2]

$$w = u + jv = \int_0^t \frac{dt}{\sqrt{(t_3^2 - t^2)(t_2^2 - t^2)}} \qquad \text{equation 7.4.2}$$

The mapping gives the separation between the parallel plates as $K(k_1)$, where

$$k_1 = \frac{t_3}{t_2} = \frac{x_3}{x_2}\sqrt{\frac{x_2^2 - x_1^2}{x_3^2 - x_1}} \qquad \text{equation 7.4.3}$$

Here

$$x_2 = \frac{w}{2} + s$$

The width of the plate is $K(k_1')$, where $k_1' = \sqrt{1 - k_1^2}$. Here $K(f)$ is the elliptical integral of the first kind with modulus f. Thus, C_1 is given by [7.4.3, 7.4.4]

$$C_1 = 4\varepsilon_0 \frac{K(k_1')}{K(k_1)} \qquad \text{equation 7.4.4}$$

In order to calculate C_2 we will consider again only the lower right hand side quadrant of figure 7.4.1. It is important to notice that the capacitance for this quadrant will be multiplied by 2 (instead of 4 for C_1). This is because C_2 accounts for the capacitance of the dielectric slab, which is only located in the two lower quadrants. The mapping transformation that maps the z-plane into the q-plane, shown in figure 7.4.3 is given by

$$q = o + jp = \sinh\frac{\pi z}{2h} \qquad \text{equation 7.4.5}$$

As one can be seen, figure 7.4.3b has the same shape of figure 7.4.2a. Thus, we can proceed as before, mapping from the plane-q into the plane-t using equation 7.4.1 and then to the the plane-w using equation 7.4.2. This way, we find

$$C_2 = 2\varepsilon_0(\varepsilon_r - 1)\frac{K(k_2')}{K(k_2)} \qquad \text{equation 7.4.6}$$

where

$$k_2 = \frac{o_3}{o_2}\sqrt{\frac{o_2^{\,2} - o_1^{\,2}}{o_3^{\,2} - o_1^{\,2}}}$$

which gives

$$k_2 = \frac{\sinh\left(\frac{\pi x_3}{2h}\right)}{\sinh\left(\frac{\pi x_2}{2h}\right)}\sqrt{\frac{\sinh^2\left(\frac{\pi x_2}{2h}\right) - \sinh^2\left(\frac{\pi x_1}{2h}\right)}{\sinh^2\left(\frac{\pi x_3}{2h}\right) - \sinh^2\left(\frac{\pi x_1}{2h}\right)}} \qquad \text{equation 7.4.7}$$

and

$$k_2' = \sqrt{1 - k_2^{\,2}}$$

The effective dielectric constant can be found using equation 7.2.8. i.e,

$$\varepsilon_{eff} = \frac{C_1 + C_2}{C_1} = 1 + \frac{C_2}{C_1} \qquad \text{equation 7.4.8}$$

Substituting equation 7.4.4 and equation 7.4.6 into equation 7.4.8 we obtain

$$\varepsilon_{eff} = 1 + \frac{(\varepsilon_r - 1)}{2} \frac{K'(k_2)}{K(k_2)} \frac{K(k1)}{K'(k_1)}$$ equation 7.4.9

In order to find the characteristic impedance of this structure we substitute equation 7.4.9 in equation 7.2.10 and the result into equation 7.2.11. After simple manipulation we find

$$Z = \frac{1}{\sqrt{\varepsilon_{eff}}} \frac{1}{\varepsilon_0 C_0 4} \frac{K(k_1)}{K'(k_1)}$$ equation 7.4.10

Proceeding as in section 7.2 we can now substitute $\left(\frac{\mu_0}{\varepsilon_0}\right)^{1/2} \cong 120\pi$ and $c_0 = \frac{1}{\sqrt{\mu_0 \varepsilon_0}}$ and finally get

$$Z = \frac{30\pi}{\sqrt{\varepsilon_{eff}}} \frac{K(k_1)}{K'(k_1)}$$ equation 7.4.11

Equations 7.4.11, 7.3.2 and 7.2.12 and related expressions were successfully used to design our planar Digital Instantaneous Frequency Measurement System. The experimental results will be presented in chapter 10.

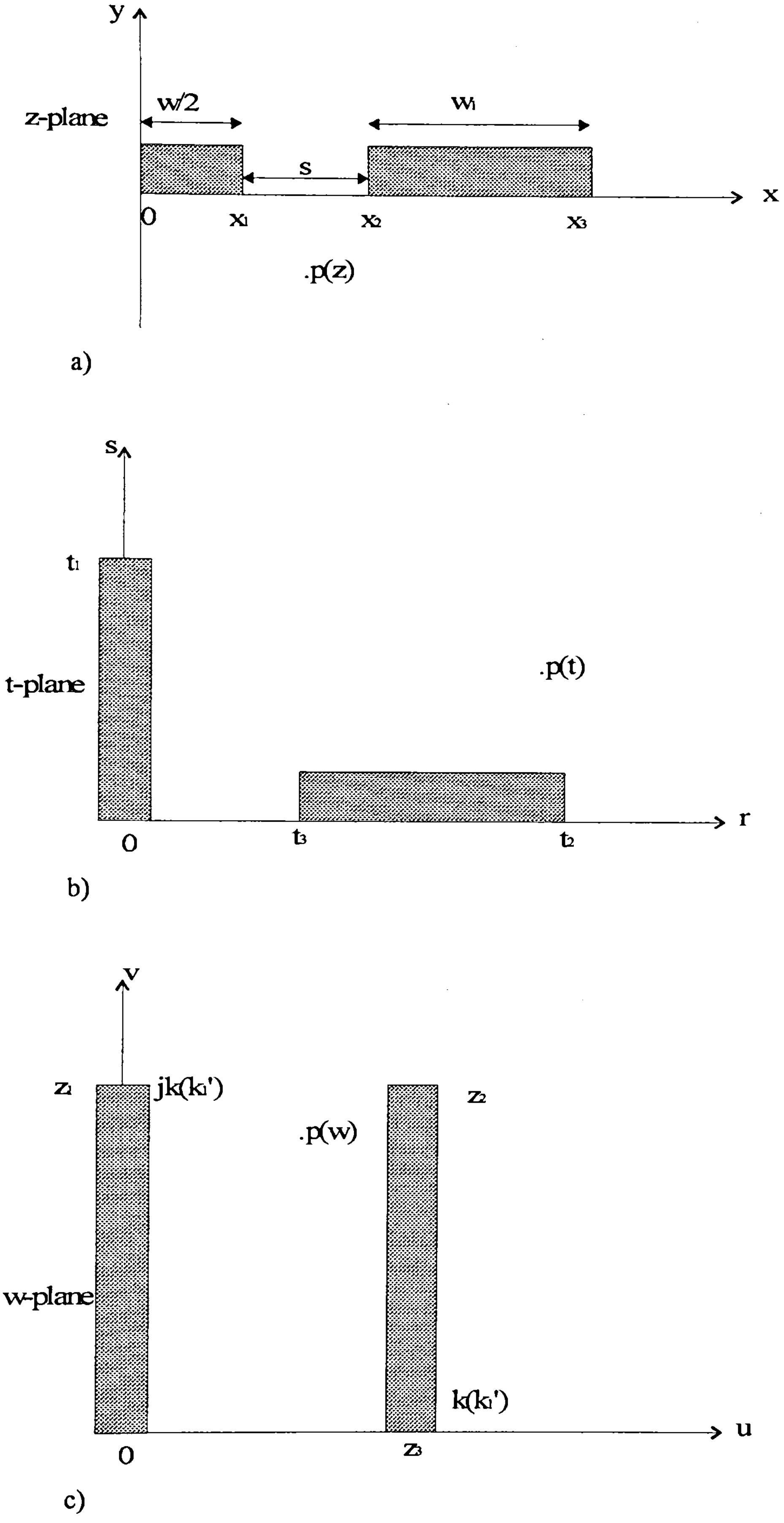

Figure 7.4.2 The conformal mapping transformation used to calculate the line capacitance C_1, where the dielectric has been replaced by air [7.4.4].

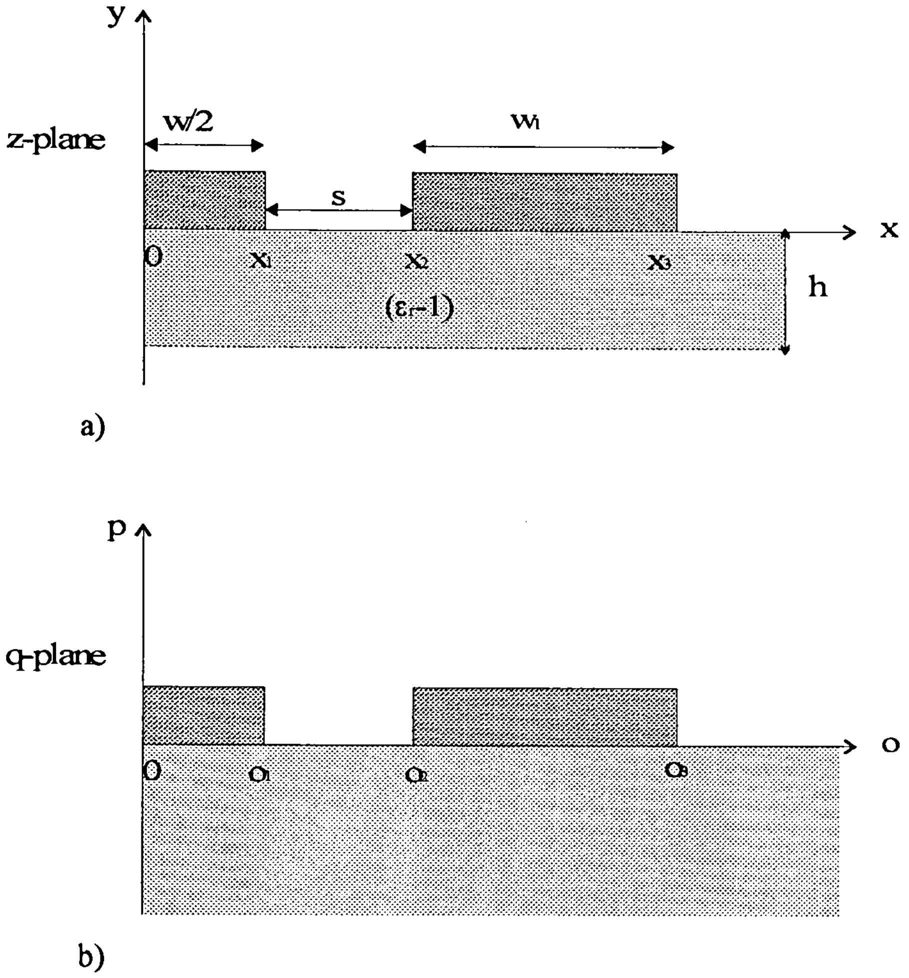

Figure 7.4.3. The conformal mapping transformation for the calculation of the capacitance C_2. a) Finite-thickness dielectric slab. b) Dielectric of infinite thickness [7.4.3].

Chapter 8

Transmission Line Theory

8.1 Introduction

At low frequency, multiport networks may be characterised in terms of voltages and currents at various ports. At microwave frequencies a practical problem exists when trying to measure voltages and currents directly. Measurements usually involve the magnitude (inferred from power) and phase of a wave travelling in a given direction, or of a standing wave. Thus, voltages and currents become somewhat of an abstraction when dealing with high-frequency networks [8.1.1]. At high frequencies, multiport networks are best characterised in terms of scattering parameters, which are defined in terms of travelling wave parameters [8.1.2].

A large variety of microwave components have only a single input port and a single output port. Many microwave circuits are able to be expressed as a cascaded combination of such two-port components. The analysis of these circuits becomes very convenient if the individual two-ports are characterised in terms of ABCD parameters. In this chapter we will briefly review the concepts of S-parameters and ABCD matrix for two-port networks. In addition to this, we will describe how to obtain characteristic impedance, group delay and group velocity using S-parameters.

In chapter 9 we will use time domain responses as an experimental procedure to check the results of characteristic impedance calculation using a simulation. Actually, there are several applications in which a time domain analysis of microwave circuits becomes necessary. These include the design of fast switching digital integrated circuits, broadband radar, communication system and the study of electromagnetic pulses [8.1.3]. Time domain approaches are a good way to check discontinuities and find the characteristic impedance of a transmission line experimentally. Thus, in section 8.6 we will briefly describe step response and impulse response characteristics.

8.2 Scattering Parameters

Figure 8.2.1 shows the voltage of both incident and reflected waves at the input and the output of a two-port microwave device. The index notations for the voltages are [7.2.1]

V_{i1} → Voltage of incident wave on port 1

V_{r1} → Voltage of reflected wave from port 1

V_{i2} → Voltage of incident wave on port 2

V_{r2} → Voltage of reflected wave from port 2

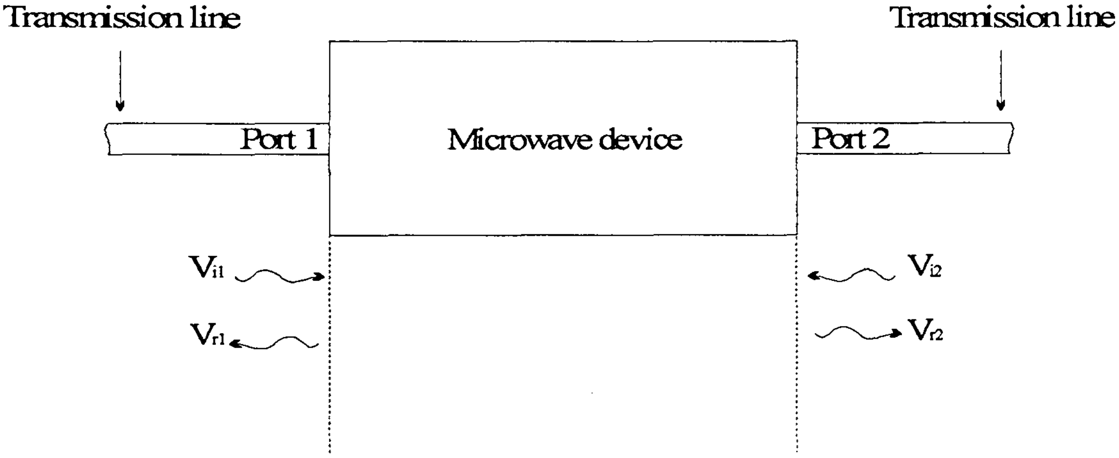

Figure 8.2.1 Incident and reflected waves at the input and the output of a two-port microwave device.

The voltage of transmitted wave away from port 1 is given by

$$V_{b1} = \Gamma_1 V_{i1} + T_{21} V_{i2} \qquad \text{equation 8.2.1}$$

Here Γ_1 is the input reflection coefficient with the output matched, given by

$$\Gamma_1 = \left.\frac{V_{r1}}{V_{i1}}\right|_{V_{i2}=0} \qquad \text{equation 8.2.2}$$

and T_{21} is the forward transmission coefficient with the output matched, given by

$$T_{21} = \left.\frac{V_{r2}}{V_{i1}}\right|_{V_{i2}=0} \qquad \text{equation 8.2.3}$$

The voltage of the transmitted wave away from port 2 is given by

$$V_{b2} = T_{12} V_{i1} + \Gamma_2 V_{i2} \qquad \text{equation 8.2.4}$$

Here Γ_2 is the output reflection coefficient with the input matched, given by

$$\Gamma_2 = \left.\frac{V_{r2}}{V_{i2}}\right|_{V_{i1}=0} \qquad \text{equation 8.2.5}$$

and T_{12} is the reverse transmission coefficient with the input matched, given by

$$T_{12} = \left.\frac{V_{r1}}{V_{i2}}\right|_{V_{i1}=0} \qquad \text{equation 8.2.6}$$

In matrix form we have

$$\begin{bmatrix} V_{b1} \\ V_{b2} \end{bmatrix} = \begin{bmatrix} \Gamma_1 & T_{21} \\ T_{12} & \Gamma_2 \end{bmatrix} \begin{bmatrix} V_{i1} \\ V_{i2} \end{bmatrix} \qquad \text{equation 8.2.7}$$

In S-parameters notation the above equation is usually written as

$$\begin{bmatrix} V_{b1} \\ V_{b2} \end{bmatrix} = \begin{bmatrix} S_{11} & S_{21} \\ S_{12} & S_{22} \end{bmatrix} \begin{bmatrix} V_{i1} \\ V_{i2} \end{bmatrix}$$ equation 8.2.8

Even though the discussion has been in terms of a two-port device, scattering parameters can readily be defined for devices with more than two ports. For an n-port network, we have

$$[V_b] = [S][V_i]$$ equation 8.2.9

where [S] is an n x n matrix. The matrix is known as the scattering matrix of the network [7.2.2].

8.3 ABCD Matrix

Figure 8.3.1 illustrates a two-port device with input total voltage and current V_1, I_1 and output quantities V_2, I_2.

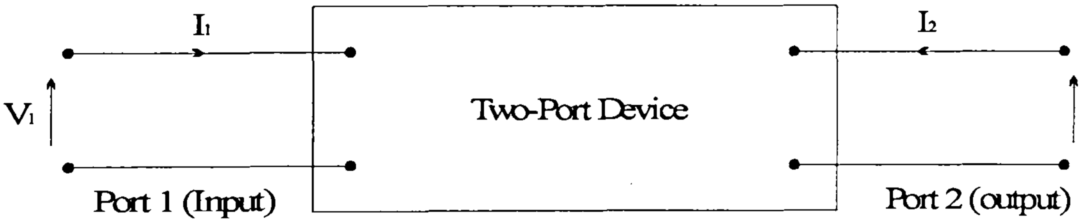

Figure 8.3.1 The voltage and current for a two-port device [8.3.1].

In this linear junction, the dependent variable V_1, I_1 may be related to V_2, I_2 by

$$V_1 = AV_2 - BI_2$$ equation 8.3.1

$$I_1 = CV_2 - DI_2 \qquad \text{equation 8.3.2}$$

In matrix form this becomes

$$\begin{bmatrix} V_1 \\ I_1 \end{bmatrix} = \begin{bmatrix} A & B \\ C & D \end{bmatrix} \begin{bmatrix} V_2 \\ -I_2 \end{bmatrix} \qquad \text{equation 8.3.3}$$

Hence given V_1 and I_1, V_2 and I_2 can be found if the ABCD matrix is known. To determine individual A, B, C, D parameters we have

$$A = \left.\frac{V_1}{V_2}\right|_{I_2=0} \qquad \text{for port 2 open circuit} \qquad \text{equation 8.3.4}$$

$$B = \left.\frac{V_1}{-I_2}\right|_{V_2=0} \qquad \text{for port 2 short circuit} \qquad \text{equation 8.3.5}$$

$$C = \left.\frac{I_1}{V_2}\right|_{I_2=0} \qquad \text{for port 2 open circuit} \qquad \text{equation 8.3.6}$$

$$D = \left.\frac{I_1}{-I_2}\right|_{V_2=0} \qquad \text{for port 2 short circuit} \qquad \text{equation 8.3.7}$$

Let us now derive the ABCD-parameters of a transmission line of length ℓ, shown in figure 8.3.2.

The general solutions for voltage and current on a transmission line can be written as

$$V(z) = V_f e^{-\gamma z} + V_r e^{\gamma z} \qquad \text{equation 8.3.8}$$

$$I(z) = \frac{1}{Z_0}(V_f e^{-\gamma z} - V_r e^{\gamma z}) \qquad \text{equation 8.3.9}$$

where

$$Z_0 = \frac{V_f}{I_f} = \frac{V_r}{I_r} \qquad \text{equation 8.3.10}$$

Here the indexes f and r mean forward and reverse propagation voltage amplitudes.

At the input $z = -\ell$ we have

$$V_1 = V(-\ell) = V_f e^{\gamma\ell} + V_r e^{-\gamma\ell} \qquad \text{equation 8.3.11}$$

$$I_1 = I(-\ell) = \frac{1}{Z_0}(V_f e^{\gamma\ell} - V_r e^{-\gamma\ell}) \qquad \text{equation 8.3.12}$$

At the input $z = 0$ we have

$$V_2 = V(0) = V_f + V_r \qquad \text{equation 8.3.13}$$

$$I_2 = I(0) = \frac{1}{Z_0}(V_f - V_r) \qquad \text{equation 8.3.14}$$

Figure 8.3.2 shows the resultant voltage and current for $z = -\ell$ and $z = 0$. Now let us evaluate the A, B, C and D parameters.

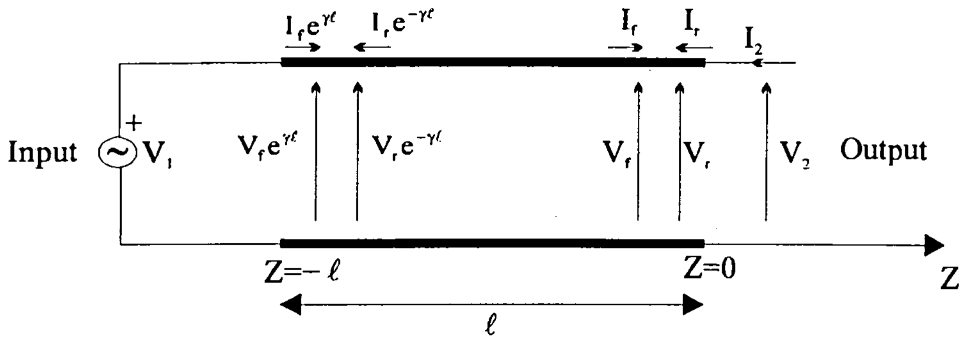

Figure 8.3.2 The forward and reverse voltages and currents at the two ends of a transmission line length ℓ [8.3.1].

Value of A

$$A = \left.\frac{V_1}{V_2}\right|_{I_2=0}$$ i.e. for port 2 open circuit

For $I_2 = 0$ equation 8.3.14 gives $V_f = V_r = V_0$. Thus, we have

$$A = \frac{V_0(e^{\gamma\ell} + e^{-\gamma\ell})}{2V_0} \qquad \text{equation 8.3.15}$$

Hence using

$$\cosh(x) = \frac{e^{x} + e^{-x}}{2} \qquad \text{equation 8.3.16}$$

we find

$$A = \cosh(\gamma\ell) \qquad \text{equation 8.3.17}$$

Value of B

Now $B = \left.\frac{V_1}{-I_2}\right|_{V_2=0}$ for port 2 short circuit

For $V_2 = 0$ equation 8.3.13 gives $-V_f = V_r = V_0$. Thus, we have

$$B = \frac{Z_0 V_0(e^{\gamma\ell} - e^{-\gamma\ell})}{2V_0} \qquad \text{equation 8.3.18}$$

Now using

$$\sinh(x) = \frac{e^{x} - e^{-x}}{2} \qquad \text{equation 8.3.19}$$

we have

$$B = Z_0 \sinh(\gamma\ell) \qquad \text{equation 8.3.20}$$

C and D may be determined in a similar way, but we can simplify the steps if we notice that for a reciprocal and symmetrical two-port network we can consider that A = D and AD - BC = 1 [8.3.2]. So we can easily find $C = Z_0^{-1}\sinh(\gamma\ell)$, where $\gamma = \alpha + j\beta$. Thus, ABCD of a transmission line of length ℓ is given by

$$\begin{bmatrix} A & B \\ C & D \end{bmatrix} = \begin{bmatrix} \cosh(\gamma\ell) & Z_0 \sinh(\gamma\ell) \\ \frac{1}{Z_0}\sinh(\gamma\ell) & \cosh(\gamma\ell) \end{bmatrix} \qquad \text{equation 8.3.21}$$

Since $\cosh(j\beta\ell) = \cos(\beta\ell)$ and $\sinh(j\beta\ell) = j\sin(\beta\ell)$, for a lossless transmission line $(\alpha = 0)$ we have

$$\begin{bmatrix} A & B \\ C & D \end{bmatrix} = \begin{bmatrix} \cos(\beta\ell) & jZ_0 \sin(\beta\ell) \\ \frac{j}{Z_0}\sin(\beta\ell) & \cosh(\beta\ell) \end{bmatrix} \qquad \text{equation 8.3.22}$$

8.4 Characteristic Impedance of a Lossless Transmission Line In Terms of S-parameters

ABCD parameters are related to S-parameters by [8.4.1]

$$\begin{bmatrix} A & B \\ C & D \end{bmatrix} = \begin{bmatrix} \frac{(1+S_{11})(1-S_{22})+S_{12}S_{21}}{2S_{21}} & Z\frac{(1+S_{11})(1+S_{22})-S_{12}S_{21}}{2S_{21}} \\ \frac{1}{Z}\frac{(1-S_{11})(1-S_{22})-S_{12}S_{21}}{2S_{21}} & \frac{(1-S_{11})(1+S_{22})+S_{12}S_{21}}{2S_{21}} \end{bmatrix} \qquad \text{equation 8.4.1}$$

Here Z represents the source and load reference impedances. From equation 8.3.22 we have

$$\frac{B}{C} = \frac{jZ_0 \sin\beta\ell}{\frac{j}{Z_0}\sin\beta\ell} = Z_0^{\,2} \qquad \text{equation 8.4.2}$$

Thus, we can find the characteristic impedance of a lossless transmission line in terms of S-parameters [8.4.2]

$$Z_0 = \sqrt{\frac{B}{C}} = \left[Z^2 \frac{(1+S_{11})(1+S_{22}) - S_{12}S_{21}}{(1-S_{11})(1-S_{22}) - S_{12}S_{21}} \right]^{1/2} \qquad \text{equation 8.4.3}$$

Here we might stress that S-Parameters are complex variables and have magnitudes and phases. In Chapter 9 we will describe the software package used for the simulating results. We will see that the data file provided by Sonnet software package for a two-port device contains magnitude and phase of S_{11}, S_{12}, S_{21} and S_{22}. Since these variables may also be measured using a network analyser, equation 8.4.3 seems to be a convenient expression to calculate the impedance of a transmission line and to optimise different transmission lines.

8.5 Group Delay

If a signal is suddenly applied to a system, the effect is usually not immediately detectable at the output but occurs at a later time. The usual functions for describing this delay are the group delay and phase delay. Group delay is defined as the negative derivative of the phase characteristic with respect to frequency, as follows [8.5.1]

$$D(\omega) = -\frac{d\theta(\omega)}{d\omega} \qquad \text{equation 8.5.1}$$

and phase delay is given by

$$\tau(\omega) = -\frac{\theta(\omega)}{\omega} \qquad \text{equation 8.5.2}$$

These two delays have the same value if the phase function is linear with the frequency.

Network analysers compute group delay from the phase slope, assuming a linear phase change $\phi_{21}(2)-\phi_{21}(1)$ over specified frequency aperture f(2) - f(1), as shown in figure 8.5.1.

So, the group delay is given by [8.5.2]

$$\tau = -\frac{1}{2\pi}\left(\frac{\phi_{21}(2)-\phi_{21}(1)}{f(2)-f(1)}\right) \qquad \text{equation 8.5.3}$$

Here ϕ_{21} is the phase of S_{21}. ϕ_{21} is in degree and f in Hz. It is important to stress that the phase change needs to be ≤ 180°, otherwise there will be errors in the group delay data.

Equation 8.5.3 will be very important in both chapters 9 and 10 for the optimisation of our interdigital delay lines, as we will carry out both simulation and measurement of the group delay.

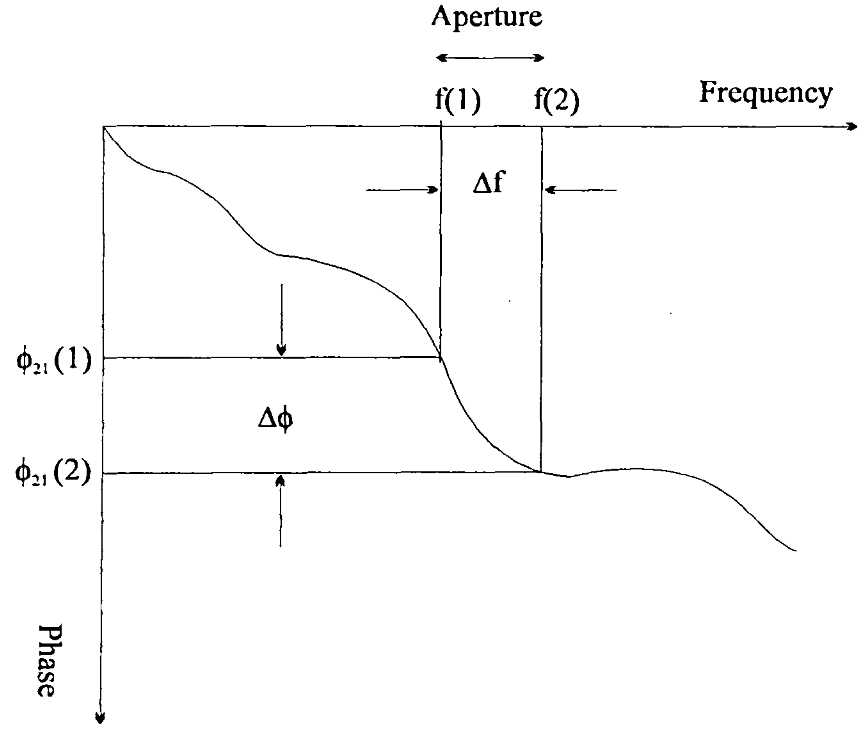

Figure 8.5.1 Phase change in a frequency aperture for the calculation of group delay.

8.6 Time Domain Response

The Fourier transform of an arbitrary time function f(t), indicated by $\Im[f(t)]$ is [8.6.1]

$$\Im[f(t)] = F(\omega) = \int_{-\infty}^{\infty} f(t)e^{-j\omega t}dt \qquad \text{equation 8.6.1}$$

The above equation is the frequency-domain representation of f(t). Here $\omega = 2\pi f$ and f the frequency in Hz.

The time function f(t) can be found by the inversion formula

$$f(t) = \frac{1}{2\pi}\int_{-\infty}^{\infty} F(\omega)e^{j\omega t}d\omega \qquad \text{equation 8.6.2}$$

The above equation is the time-domain representation of $F(\omega)$.

Using equation 8.6.2 we are able to carry out measurements in time domain response with a network analyser. Let us now qualitatively describe impulse response and step response measurements.

Network analysers measure the impulse response by h(t) applying the Fourier inversion integral (equation 8.6.2) over the reflection coefficient response in the frequency domain, computing both magnitude and phase. Displaying reflection coefficient against time is important because we can convert time to distance in TEM propagation systems. Thus, carrying out the correct calibration and adjusting the relative velocity factor it is possible to associate discontinuities along the transmission line with distance.

The step response is the integral of the impulse response which is given by [8.6.2]

$$g(t) = \int_{0}^{t} h(x)dx \qquad \text{equation 8.6.3}$$

In practice, looking at a new section of a transmission line, the difference between the step response and impulse response is that the second tells us whether there is a change in the impedance and the first says what the impedance of the new section is.

Now we will apply the above concepts in a practical example. On top of figure 8.7.1 we have a transmission line with the characteristic impedance changing along its length. Using the diagrams on the bottom of figure 8.7.1 it is possible to understand how both step and impulse responses may be used together to analyse the existent discontinuities in this type of transmission line.

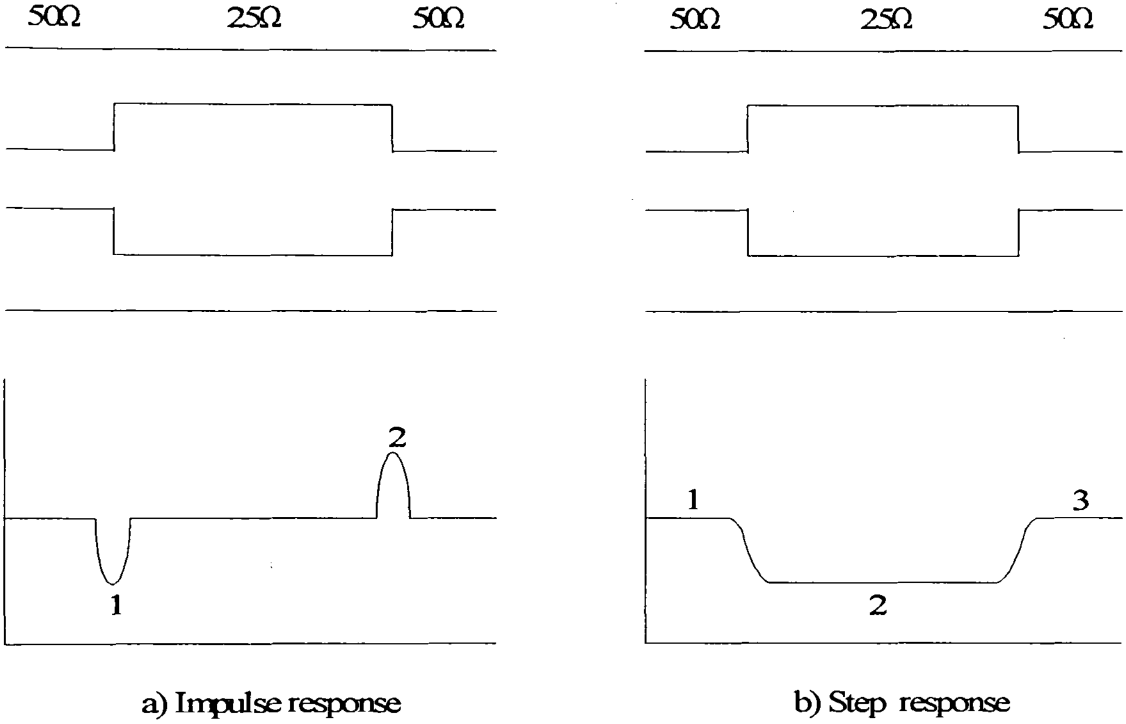

a) Impulse response

b) Step response

Figure 8.6.1 Approximated sketch of the discontinuities based on the expected step and impulse responses using the real format.

Looking at the figure 8.6.1a we see two impulses. The first impulse tell us that the reflection coefficient is negative since we are moving into a lower impedance (from 50Ω to 25Ω). The second impulse tells the opposite as we are moving into a higher impedance (from 25Ω to 50Ω) and the reflection coefficient has to be positive. Between the impulses there is no change in the reflection coefficient because the impedance is constant.

Moving from level 1 into level 2, in figure 8.6.1b, the reflection coefficient drops down and keeps its value for all the length of 25Ω until it jumps up into level 3. The reflection coefficient is related to the characteristic impedance. Thus, it is possible to extract the value of characteristic impedance of an uniform section of a transmission line by using the step response. We will use this idea in chapter 10 to find the characteristic impedances of the delay lines.

Chapter 9

Instantaneous Frequency Meter Subsystem

9.1 Introduction

The principle of measuring frequency in terms of the phase delay of a signal propagated down a known length of transmission line is as old as electromagnetic science [9.1.1]. However, the technique of applying this principle to broad-band receivers without the use of tuned filters or other circuits adjustments is comparatively recent. The first practical delay-line frequency-discriminator circuit for wideband measurement of pulsed microwave signal was demonstrated by Robinson at Mullard Research Laboratories in 1957 [9.1.1]. The digital instantaneous frequency measurement receiver was developed in the early 1960s specifically as a wideband and accurate analyser of pulsed radar signals. Instantaneous frequency measurement (IFM) subsystems are widely used in electronic warfare and electronic intelligence systems for the determination of unknown signals over a broad frequency band with high probability of interception and large dynamic range [9.1.2, 9.1.3, 9.1.4]. Figure 9.1.1 shows an recent IFM.

Each discriminator divides the RF input into two paths. Delaying one path with respect to the other and then by adding the delayed signal to the undelayed signal it can measure the instantaneous frequency. The frequency resolution of the IFM depends on the length of the delays, which become in practice the principal elements of the subsystem.

Conventional IFM systems use delay lines made by coiling coaxial cables or by patterning meander lines of normal metal microstrip. However the loss and the large size of these approaches limit the amount of delays available. Superconductive delay lines offer the highest bandwidth with lowest loss and dispersion compared to the current technology available. It is the ability of superconductors to produce a number of long delays in a suitable small volume that makes this superconducting device interesting. Liang et al., in 1993 [9.1.5] implemented a 5 bit instantaneous frequency measurement subsystem for a bandwidth of 500 MHz and a center frequency of 4MHz with $YBa_2Cu_3O_{7-\delta}$. Delay lines up to 16ns were fabricated using striplines in dual-spiral form on $LaAlO_3$ substrate. The discriminators and a 5-ways microstrip power spliter were fabricated separately in 6 massive aluminium sub-packages. This complex architecture yielded a heavy subsystem with a large number of microwave connections between different types of transmission lines (see figure 9.1.2).

Biehl et al., in 1994 [9.1.6] integrated a 4 bit IFM for the frequency range 9.5 to 10.5 GHz with coplanar $YBa_2Cu_3O_{7-\delta}$ delay lines on a single wafer using coplanar waveguide (CPW). In a curved coplanar waveguide (CPW) poor return loss and large insertion loss are due to the phase distortion of the wavefront as it passes through the bend. The phase distortion is caused by the large difference in path length between the inner slot and the outer slot which guide the CPW mode. This problem increases as a higher frequency resolution is required. The higher the resolution the longer the delay and the larger the numbers of bends. In order to keep the structure balanced after the bends Biehl et. al used air bridges of aluminium ultrasonically bonded at regular intervals. However, implementing these air bridges in the microwave circuit is a time-consuming process. Any residual deposit might increase the parasitic capacitance to the strip that runs underneath [9.1.7].

Coplanar stripline (CPS), as shown in figure 7.3.1 of chapter 7, has the potential to overcome these problems. However, accounting for etching tolerances, a simple coplanar stripline of 50Ω is difficult to attain in practice on medium or low permittivity substrates. For a relative permittivity ε_r = 10.8, the line width w needs to be approximately 20 times bigger than the spacing s to attain a characteristic impedance of 50Ω. One way to overcome this problem is to use a slow wave line. This has the advantage of not only allowing 50Ω line but also increasing the delay. Slow-wave transmission lines are extensively used to reduce the size of monolithic microwave integrated circuits (MMICs).

This work aims to optimise a comb transmission line, shown in figure 9.3.2.1.1 with coplanar strip interdigital fingers to be used as a delay line using a design approach based on the characteristic impedance and group delay. Increasing the finger length, keeping all the other parameters fixed, one can readily achieve a impedance with acceptable 50Ω etching tolerances. This seems to be a flexible way to build uniplanar discriminators in instantaneous frequency measurement systems. A full-wave electromagnetic simulation software produced by Sonnet Software has been employed in this study and will be briefly described in section 9.3.1. Thus, in this chapter we will present the tools necessary to design uniplanar instantaneous frequency measurement systems. Coplanar strips interdigital delay lines, coplanar wave guides and coplanar strips power splitters will be integrated without any air bridges. Such a microwave coplanar integrated circuit seems very promising for superconducting IFM application since it only uses one side of the substrate.

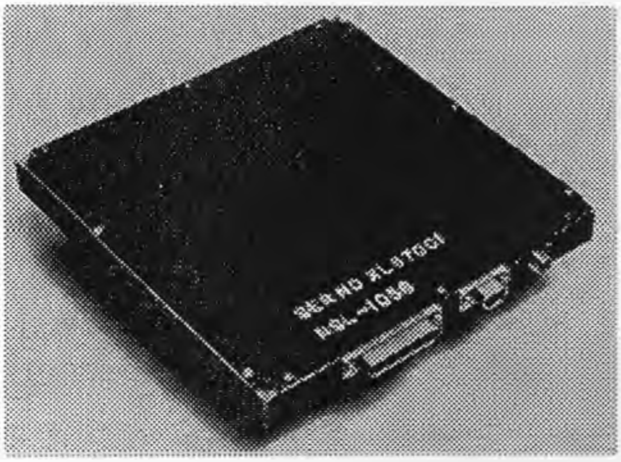

Figure 9.1.1 Wideband instantaneous frequency measurement IFM receiver, 2 to 10GHz, 12 bit, temperature compensated frequency measurement device that includes a seven correlator array and a limiting RF amplifier in a 5" × 5" × 0.5" package dissipating a total power of 15W. Taken from [9.1.3].

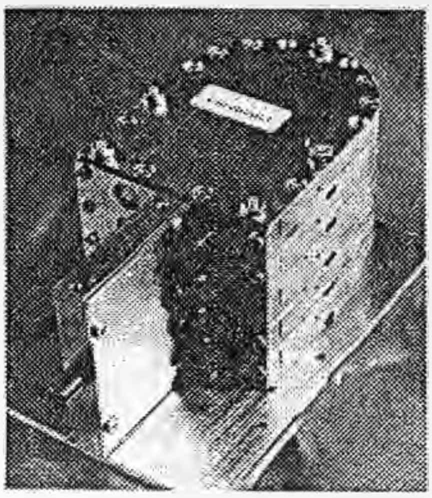

Figure 9.1.2 Cryogenic section of DIFM system. The vertical section (bottom left) is the 5-way power divider. The five discriminator modules (top right) are stacked. Taken from [9.1.5].

9.2 Architecture of a Generalised Instantaneous Frequency Meter

A generalised instantaneous frequency measurement is shown in figure 9.2.1. It consists of power dividers, delay lines, detectors, amplifiers and 1bit A/D converters. The input signal is divided by a power divider to feed the phase discrimination channels, each of which provides one bit of the frequency word. In each channel, the signal is further split into two paths, one of which is applied directly to one input of the combiner while the other is routed through a delay line, before being applied to the other input of the combiner. This configuration produces a grey code, which is then converted to natural binary code after the A/D converters [9.2.1].

The delay lines are essential components of an IFM. The different time delay intervals are used to measure the instantaneous frequency. It is the interference signal from this differential delay that forms the digital signal after detection. The digital code which uniquely identifies the input signal tone over the bandwidth of the device is formed by choosing the delays on each of the channels correctly. Because the device is parallel in nature, any signal at the input is detected even if it is rapidly changing in frequency;

Hence, the probability of interception is 100%. This parallelism, however comes at the price of size and weight.

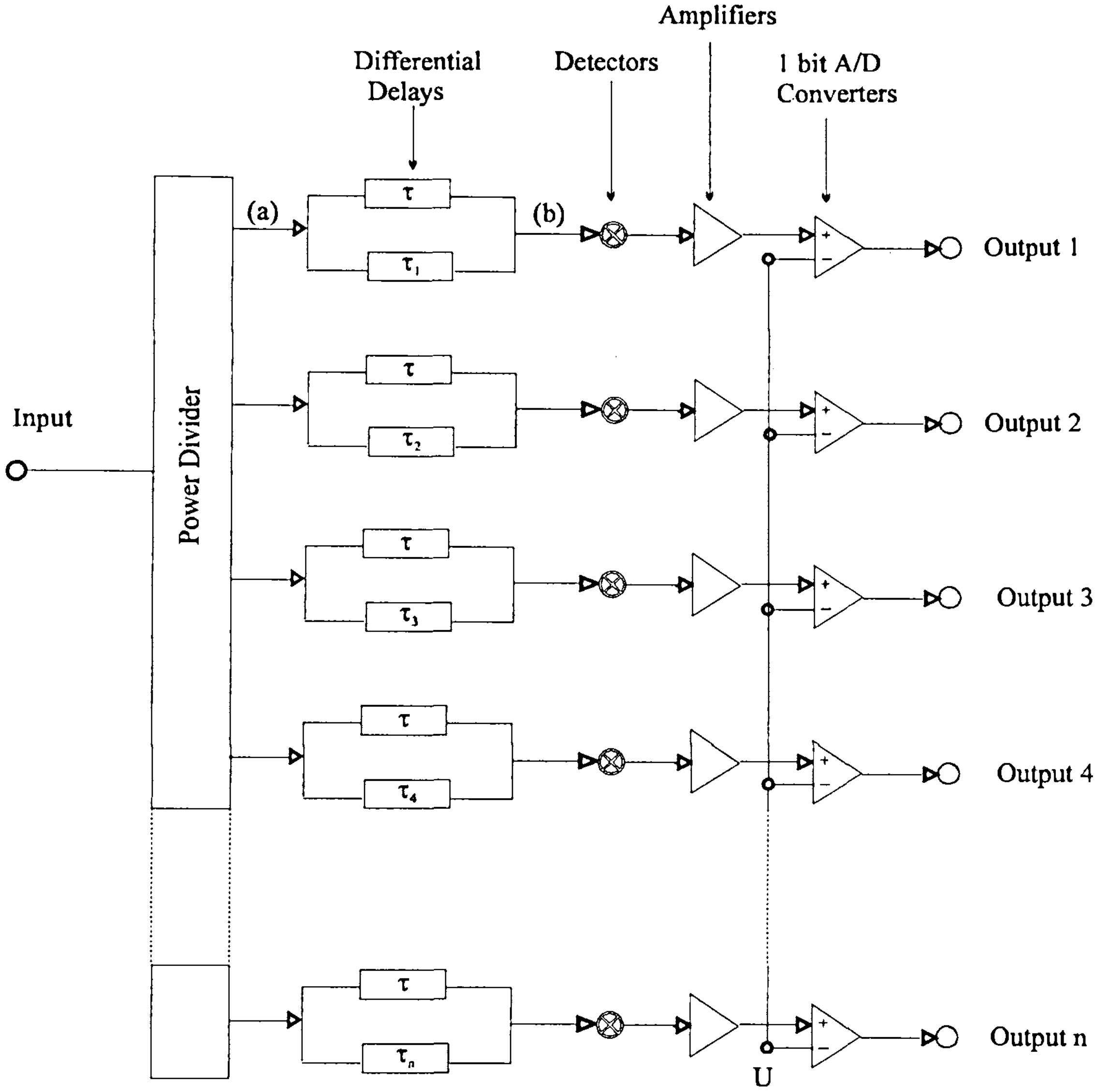

Figure 9.2.1 Schematic diagram of the instantaneous frequency meter system. Taken from [9.2.3]

The minimum length pulses which can be processed is of the order of the time delay of the least significant bit (LSB) discriminator. The longest delay (τ_{max}) is determined by the desired frequency resolution (f_r) by the equation [9.2.2]

$$f_r = \pm\left(2^{n+1}\tau_{max}\right)^{-1}$$ equation 9.2.1

Here n is the order of binary quantization, which is 1 for 1bit A/D converter. Thus, the longer τ_{max} the better the resolution. The resolution may also be enhanced by performing multibit ($n > 1$) phase measurements on the output of the branch with the longest delay (τ_{max}).

If the input signal at point (a) is $\sin(\omega t)$, after the delay and recombination at point (b) the output is given by the equation [9.2.3]

$$s(t) = \frac{1}{2}\sin(\omega t + \omega\tau) + \frac{1}{2}\sin(\omega t + \omega\tau_1 + \phi) = \sin\left[\frac{2\omega t + \omega(\tau + \tau_1)}{2}\right]\cos\left[\frac{\omega(\tau - \tau_1)}{2} - \frac{\phi}{2}\right]$$

equation 9.2.2

Here we have used the equation

$$\frac{1}{2}\sin(A) + \frac{1}{2}\sin(B) = \sin\left(\frac{A+B}{2}\right)\cos\left(\frac{A-B}{2}\right)$$

In equation 9.2.2, ϕ is a frequency independent phase shift. τ and τ_1 are the delays, illustrated in figure 9.2.1. The elements of the above equation are better described in figure 9.2.2.

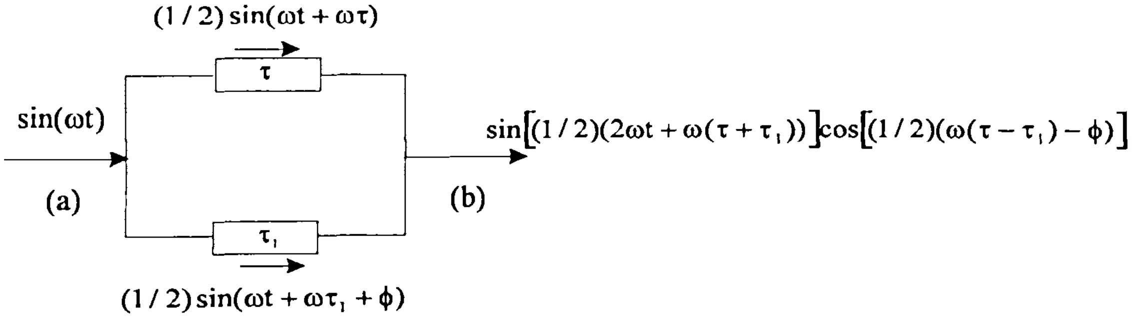

Figure 9.2.2 Single stage of the IFM in figure 9.2.1, from point a) to point b).

Setting ϕ to zero for simplicity, we shall find in which conditions there are peaks and nulls in this output waveform.

The nulls occur when

$$\omega\left(\frac{\tau-\tau_1}{2}\right)=n\pi-\frac{\pi}{2} \qquad \text{equation 9.2.3}$$

Here n is an integer. Substituting $\omega = 2\pi f$ we find

$$f=\frac{n-1/2}{\tau-\tau_1} \qquad \text{equation 9.2.4}$$

The peaks occur when

$$\omega\left(\frac{\tau-\tau_1}{2}\right)=n\pi \qquad \text{equation 9.2.5}$$

Similarly we have

$$f=\frac{n}{\tau-\tau_1} \qquad \text{equation 9.2.6}$$

The frequency difference between both the adjacent peaks and nulls is thus given by

$$f_{n+1}-f_n=\Delta f=\frac{1}{\tau-\tau_1} \qquad \text{equation 9.2.7}$$

The difference in time delay $(\tau-\tau_1)$ can be calculated for a peak or null at any frequency using equations 9.2.4, 9.2.6 and 9.2.7. The shortest delay is determined by the bandwidth to be measured using equation 9.2.7. The difference in frequency to the next peak or null can also be calculated since we know the time delay. Because n is an integer the choice of the design is limited. However, further tuning of the position of the peaks or nulls can be accomplished by inserting a phase difference ϕ in one of the delay lines. In principle any position can be designed in this manner. In practice, phase differences other than ±90° or ±180° are difficult to obtain over the wide bandwidth required.

In order to design the discriminators of an IFM, avoiding further complications, we need to know the following requirements: a) the total bandwidth, b) the central frequency, c) the frequency resolution and d) the digital code. Since we know these values we may calculate the: a) longest delay, b) shortest delay and c) delay differences for each channel.

Now let us investigate a simple example in figure 9.2.3. The responses shown represent the outputs of different stages of a 2 bit IFM. For simplicity, we set $\phi = 0$. The shorter delay deference is 1ns and the longer is 2ns. This gives a system with central frequency 9GHz and bandwidth 1GHz. In practice, the responses in part-a of figure 9.2.3 are the interferometer outputs before the detection. Part-b and part-c of the same figure are the interferometer outputs after the 1 bit A/D converter of each channel. Finally part-d is the resultant digital word.

Actually in a real DIFM there is a large number of additional components. For superconductor applications the cryogenic section of the DIFM system may include not only the delay lines and power dividers, but also conventional GaAs amplifiers can be cooled and may be integrated as a limiting amplifier to reduce the sensitivity to variations in input signal level. A superconducting bandpass filter may be added to the IFM system to remove the effect of the out of band signal. However, the objective of this chapter is only to focus on the integration of the power dividers with the delay lines to form an uniplanar structure.

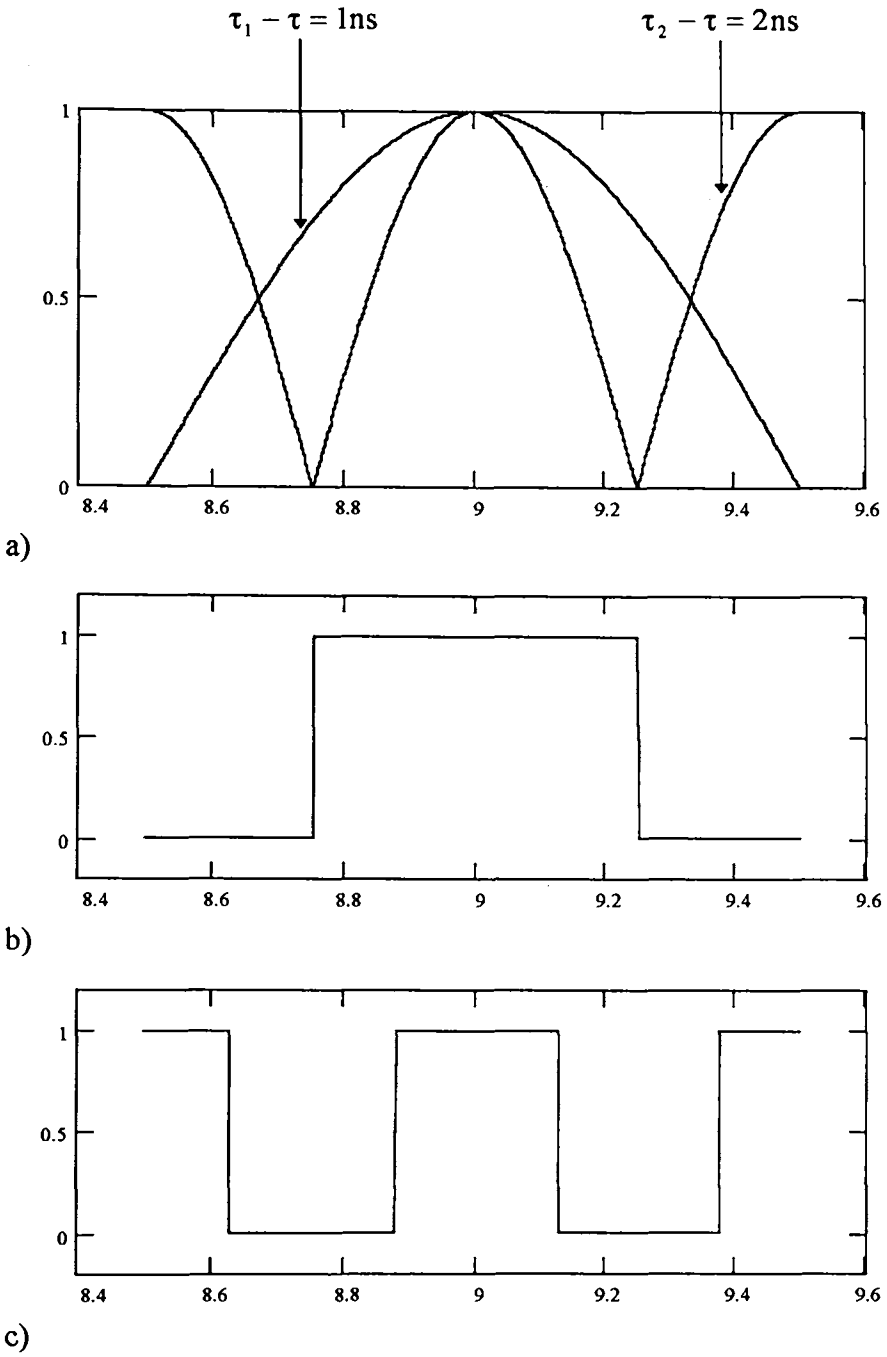

1ns	0	0	1	1	1	1	0	0
2ns	1	0	0	1	1	0	0	1

d)

Figure 9.2.3 2 bit instantaneous frequency meter: a) frequency response before detection of each of the channels, b) digitised version of the trace correspondent to the shortest delay deference channel (1ns), c) digitised version of the trace correspondent to the longest delay deference channel (2ns) and d) table of the binary code.

9.3 Simulation Process

9.3.1 Sonnet Software

Sonnet (Release 2.4) is a full-wave electromagnetic software produced by Sonnet Software, Inc. It offers five programs: ***xgeom***, ***em***, ***patgen*** and ***patvu***. Figure 9.3.1.1 shows the block-diagram indicating the relationship of them [9.3.1.1].

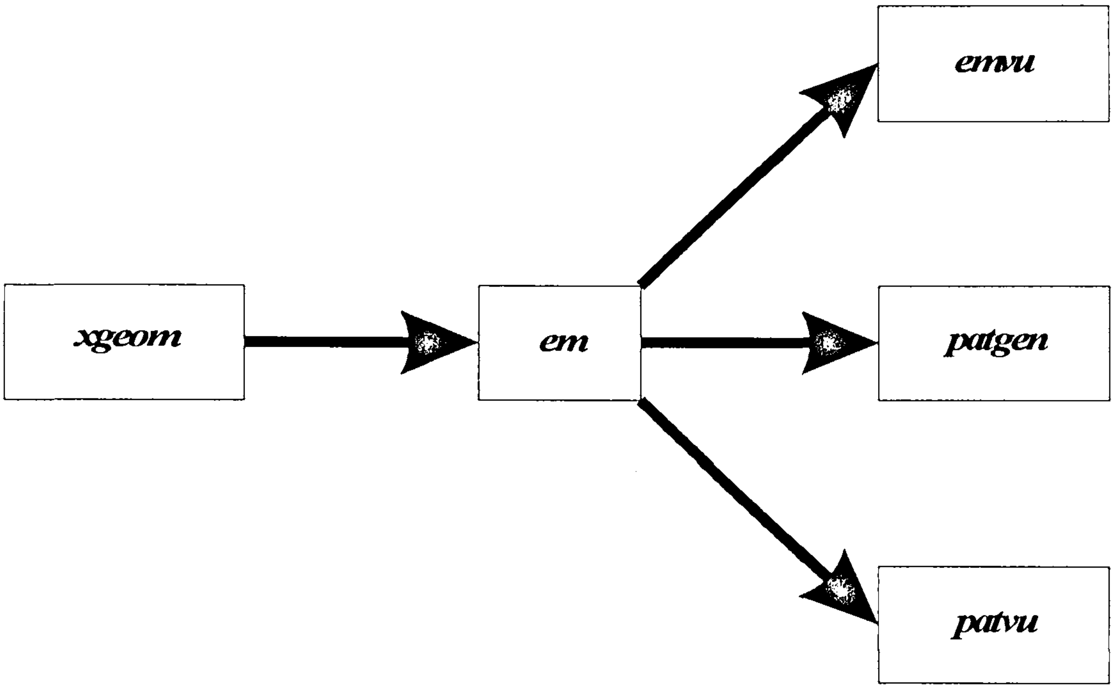

Figure 9.3.1.1 Relationship of Sonnet programs [9.3.1.1].

Xgeom is an X-Windows system mouse based program used to capture microstrip (and coplanar) circuit geometry for input to the electromagnetic analysis program, ***em***. After capturing the circuit with ***xgeom*** file we save this with a name ending in "geo". Using the "geo" file as input ***em*** automatically subsections the circuit and performs the electromagnetic analysis. The smaller the subsections are made, the more accurate the result is and the longer it takes to get the result. A "cell" is the basic building block of all subsections, and each subsection is built from one or more cells.

The dielectric parameters may be computed for more than two layers. This includes the thickness, dielectric constant and loss tangent. Using the ***xgeom*** dielectric menu we can easily access to the layers and change their parameters. ***Xgeom*** also gives us the option to change the metallization parameters used by ***em*** which are the metallization resitivity (DC and skin effect) and the metallization reactance.

After reading an ASCII ".geo" file, describing the circuit, em reads an ASCII ".an" file which specify the analysis frequencies (default "clt.an"). Thus, before doing an analysis, we usually edit this file in order to specify the range and the unit of the frequency, as seen in figure 9.3.1.2 .

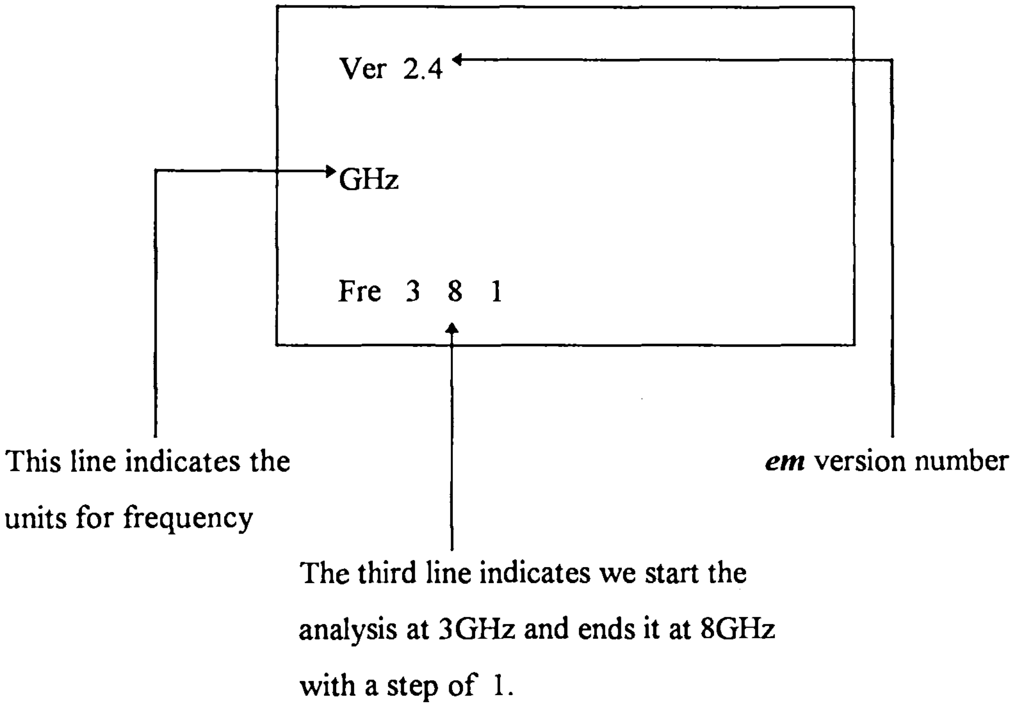

```
Ver 2.4

GHz

Fre 3 8 1
```

This line indicates the units for frequency

em version number

The third line indicates we start the analysis at 3GHz and ends it at 8GHz with a step of 1.

Figure 9.3.1.2 ASCII ".an" file specifying the Analysis frequency [9.3.1.1].

Em can also analyse coplanar structures well because the ground planes and the dielectric layer thickness can be made any value without compromising the accuracy of the speed.

Patgen is an analysis tool which calculates far field antenna patterns for arbitrary 3-D planar geometries and are viewed with ***patvu***. Since antennas are not the subject of this thesis we are not considering this further.

Emvu is an X-Windows system, mouse based program used to view results from an ***em*** analysis as a colour shaded plot. ***Em*** saves the resulting current density information in a file format ready for input to ***emvu***. Thesis information may be important in order to improve our design. The file ends with ".jxy", where "j" means current density and the "xy" refers to the directions of the current (z-directed current is not shown).

9.3.2 Coplanar Strips Interdigital Delay Line

9.3.2.1 Description

The schematic drawing of the structure proposed is shown in figure 9.3.2.1.1. It consists of 164 interdigital fingers of equal length d, finger width w, a finger spacing s and a total length ℓ. p is the length which represents the periodicity of the transmission line. If $p << l$, an amount of lumped capacitance per unit length C_0/p is added to the shunt capacitance C. However, for the structure shown in figure 9.3.2.1.1 this effect has to be taken into account twice, and then the phase velocity and the characteristic impedance Z0 become respectively: $[(C + 2C_0/p)\ L_S\ ]^{-1/2}$ and $[L\ /(\ C + 2\ C_0/p\ )]^{-1/2}$ [9.3.2.1.1]. Here, L_S is the series inductance. Due to the fringing electric fields about the fingers, the amount by which the capacitance per unit length increases is greater than the corresponding amount by which the inductance per unit length decreases. In order to exploit the fringing electric fields produced by the fingers, we need to increase the finger length and keep the finger width fixed.

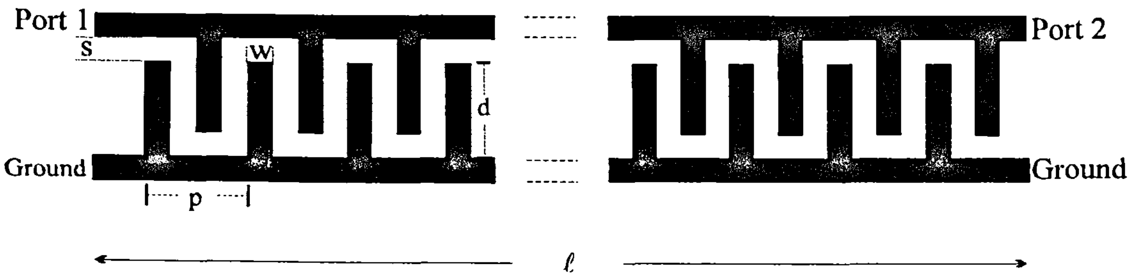

Figure. 9.3.2.1.1 Coplanar interdigital delay line under simulation.

For the simulation of the structure shown in figure 9.3.2.1.1 we assumed the relative permittivity ε_r = 10.8, the substrate thickness h = 0.64 mm, the copper cladding thickness t = 35μm, w = 0.3 mm, s = 0.3 mm and ℓ = 99 mm. The simulation was carried out varying the finger length from 0.6 to 4.2 mm (with a step of 0.3mm) and keeping all the other parameters fixed. Because we will need to compare the simulated results with the experimental results, in chapter 10, we have chosen w and s equal to 0.3mm, which is readily achievable with typical etching tolerances.

9.3.2.2 Simulation Results of Insertion Loss and Return Loss of The Slow Wave Coplanar Line

Perhaps one of the most difficult parts of the simulation is to know in which frequency range the investigation will be carried out. We started investigating insertion loss responses in a wide band from 0.5GHz to 20GHz. Figures 9.3.2.2.1, 9.3.2.2.2, 9.3.2.2.3 and 9.3.2.2.4 show the simulated insertion loss of the interdigital delay line described in figure 9.3.2.1.1 for a lengths 0.9mm, 1.5mm, 2.1mm and 2.7mm, respectively. Let us pick up the response for 2.1mm finger length and try to understand its behaviour. In order to understand its behaviour let us assume that this structure (2.1mm) has a characteristic impedance of 62Ω and a group velocity of 6.3×10^7 m/s. These results were taken from figures 9.3.2.3.12 and 9.3.2.4.5, respectively and they will be proved to be correct later on in this chapter. In the frequency response presented in figure 9.3.2.2.3 there is a large number of ripples caused by impedance mismatch from the transmission line (62Ω) to the source (50Ω) and to the load (50Ω). This can be checked if we look at the response for 2.7mm finger length, presented in figure 9.3.2.2.4. We see much less ripples because this is a 56 Ω impedance (to be proved later on) transmission line. The resonant peak appears at the frequencies for which the distance between the two parallel strips (d + s) is a multiple of λ/2. For the 1.5mm finger length response we have the fundamental resonant frequency of 18×10^{9}GHz. So it gives $(\lambda / 2) = (v_g / 2f) = 2\text{mm}$, which is not much different from 1.5 + 0.3 = 1.8mm.

Figure 9.3.2.2.5 shows the insertion loss of the interdigital delays with finger lengths of 1.5mm, 2.1mm and 2.7mm. The resonant frequency shifts down as the finger length increases. This happens because the total capacitance increases as the finger length increases. Increasing the capacitance the group velocity decreases and the fundamental resonant frequency of the delay with longer finger shifts down to keep λ/2 constant.

Looking at all these figures again one see that from 0.5GHz to 3GHz the insertion loss varies only between -3dB to -1dB in all plots. This way, considering this frequency range we are presenting simulated results of characteristic impedance from d = 0.6mm to d = 4.2mm.

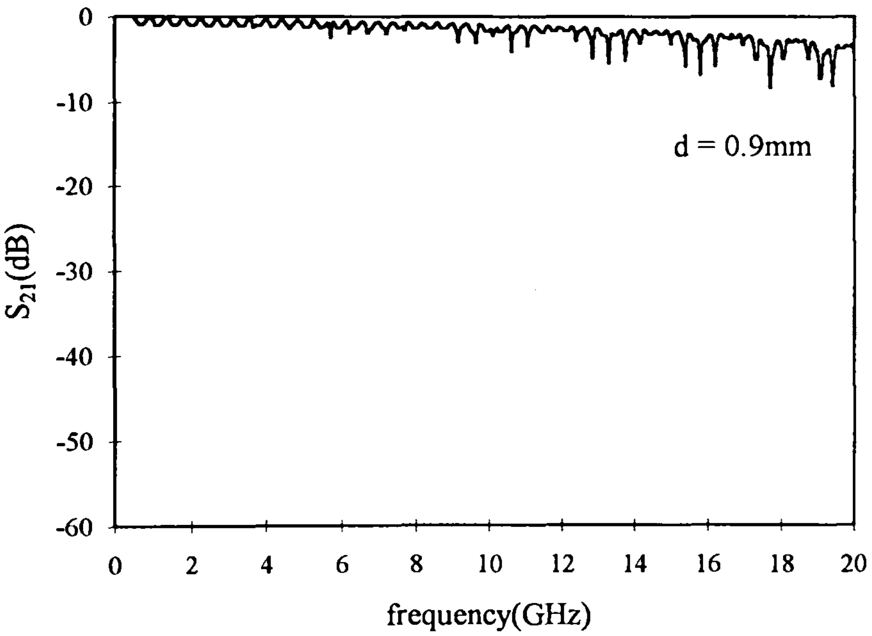

Figure 9.3.2.2.1 Insertion loss result from the simulation of the interdigital delay line with finger length 0.9mm, raging from 0.5GHz to 20 GHz.

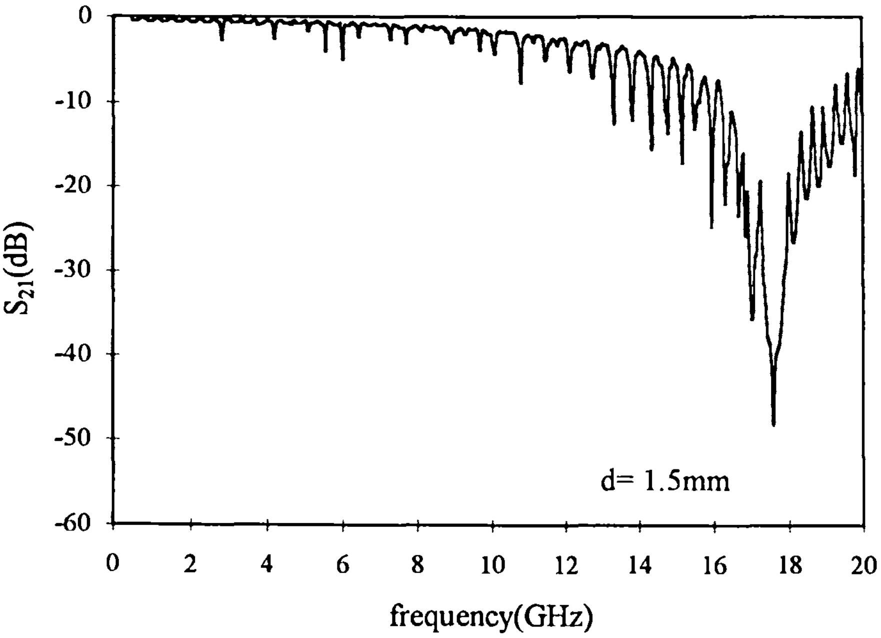

Figure 9.3.2.2.2 Insertion loss result from the simulation of the interdigital delay line with finger length 1.5mm, raging from 0.5GHz to 20 GHz.

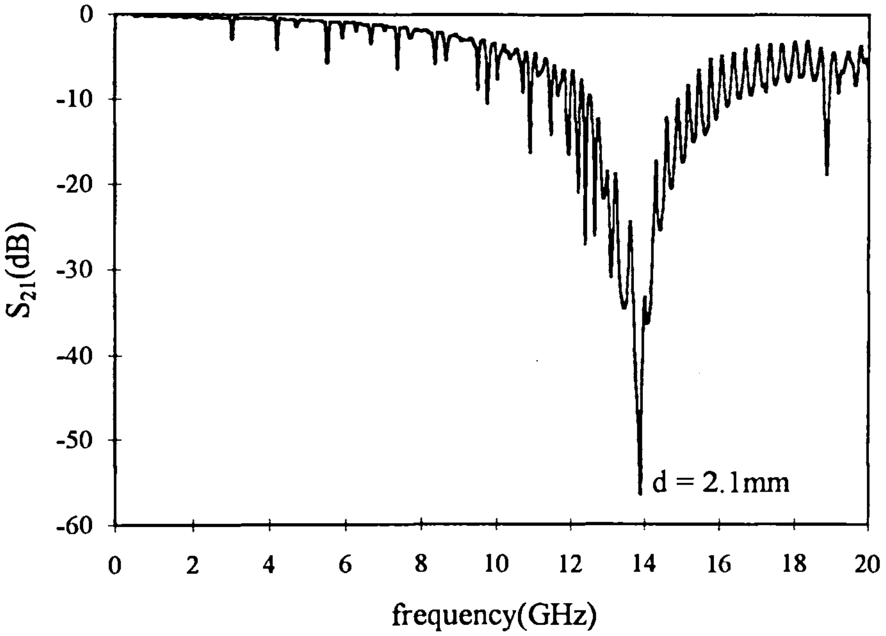

Figure 9.3.2.2.3 Insertion loss result from the simulation of the interdigital delay line with finger length 2.1mm, raging from 0.5GHz to 20 GHz.

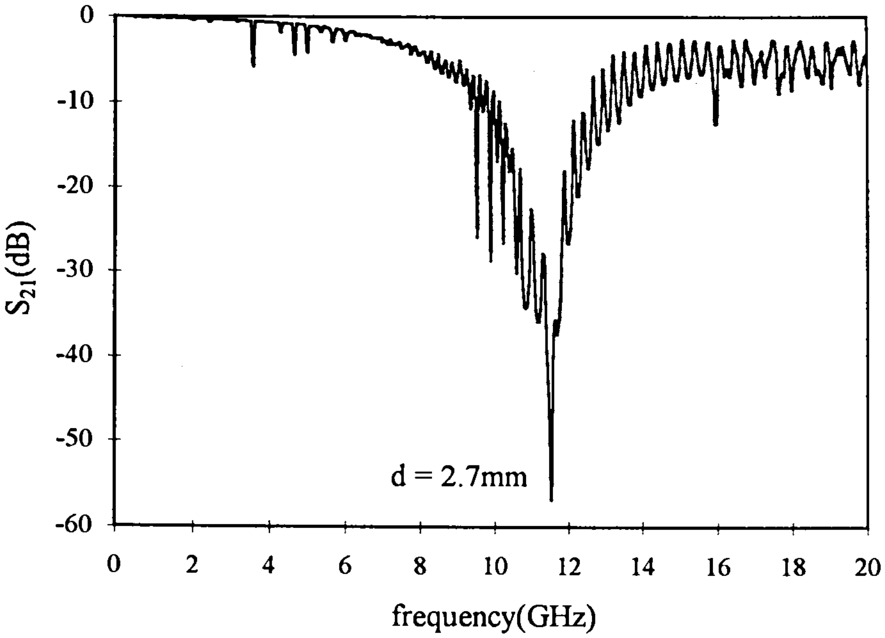

Figure 9.3.2.2.4 Insertion loss result from the simulation of the interdigital delay line with finger length 2.7mm, raging from 0.5GHz to 20 GHz.

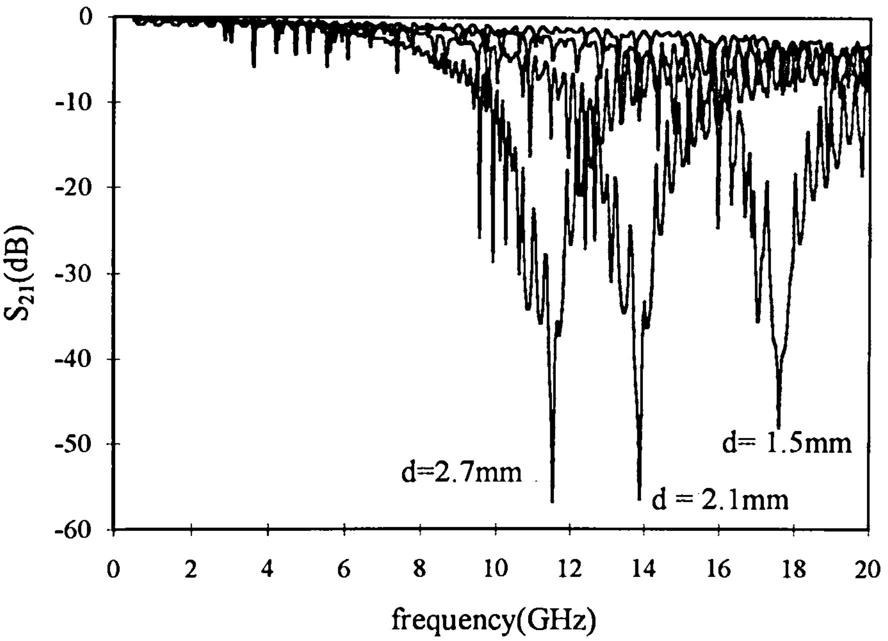

Figure 9.3.2.2.5 Insertion loss result from the simulation of the interdigital delay lines with finger lengths 1.5mm, 2.1mm and 2.7mm, raging from 0.5GHz to 20 GHz.

9.3.2.3 Simulation Results of Characteristic Impedance

Looking back at section 8.4 of chapter 8, we now can use equation 8.4.3 in order to calculate the characteristic impedance from the S-parameters (magnitude and phase) given by the simulation. Before starting the simulation itself we shall need to understand the derivation of the characteristic impedance for the case when the delay line in figure 9.3.2.1.1 is a simple coplanar strips structure with line width 0.3mm, line spacing 0.3mm and finger length 0mm.

Figure 9.3.2.3.1 shows a mismatched transmission line to both source and load. Let us calculate its insertion loss and return loss.

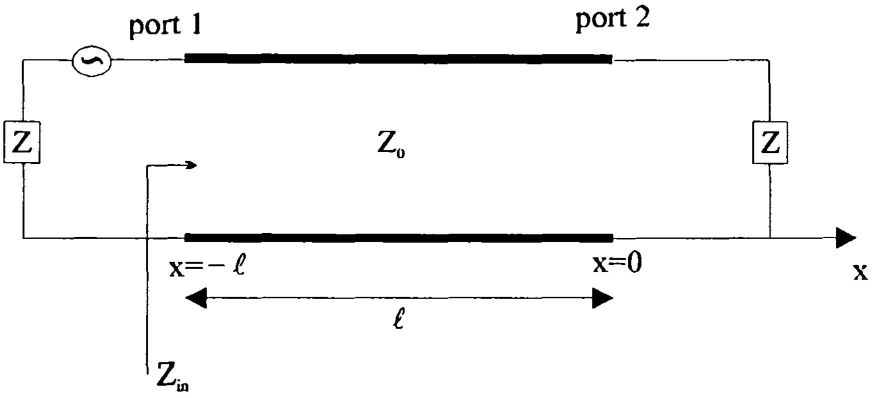

Figure 9.3.2.3.1 Transmission line with identical load and source impedances, Z. Z_0 is the characteristic impedance of the transmission. Z_{in} is the input impedance.

The amplitude of the reflection coefficient at port 1 looking into the transmission line $|S_{11}|$ is given by the equation [9.3.2.3.1]

$$|S_{11}|=\left|\frac{Z_{in}-Z}{Z_{in}+Z}\right| \qquad \text{equation 9.3.2.3.1}$$

$$Z_{in}=Z_0\frac{Z+jZ_0\tan\beta\ell}{Z_0+jZ\tan\beta\ell} \qquad \text{equation 9.3.2.3.2}$$

The amplitude of the transmission coefficient from port 1 to port 2, $|S_{21}|$ may be determined considering the relation between $|S_{11}|$ and $|S_{21}|$ [9.3.2.3.2], which is

$$|S_{21}| = \sqrt{1-|S_{11}|^2} \qquad \text{equation 9.3.2.3.3}$$

Incident and reflected waves combine to produce a resultant that varies in amplitude along the line. One cycle of variation for the function $\tan\beta\ell$ occupies a range of $\beta\ell = \pi$ and the impedance variation is repeated for each half-wave length of line, namely, $\beta\ell = n\pi$ or $\ell = n\lambda / 2$. In terms of frequency it is

$$f_n = n\frac{c_0}{2\ell\sqrt{\varepsilon_{eff}}} \qquad \text{equation 9.3.2.3.4}$$

Using the design equations for a coplanar strip, already described in section 7.3, we find $\varepsilon_{eff} = 5.9$ and $Z_0 = 99\Omega$. Using the Mathcad program described in section Ap.III.3 of appendix III, based on equations 9.3.2.3.1, 9.3.2.3.2 and 9.3.2.3.3 we plotted the theoretical frequency responses for this simple coplanar strips, as shown in figure 9.3.2.3.2. The simulated frequency responses are also illustrated in figure 9.3.2.3.3, which seem to be in good agreement with the theoretical results.

The frequency corresponding to the nulls 1, 2, 3 and 4 shown in figure 9.3.2.3.2 can now be calculated directly using equation 9.3.2.3.4, which gives 0.623GHz, 1.247GHz, 1.871GHz and 2.495GHz , respectively. The discussion about these nulls becomes very important in the inverse process as we need to find the unknown characteristic impedance using the S-parameters obtained from the simulation described in section 8.4 of chapter 8. Let us suppose now that we do not know the characteristic impedance of this transmission line but we have the S-parameters, magnitude and phase, from simulation. Thus, the characteristic impedance may by found using equation 8.4.3. The Mathcad program described in section Ap.III.4 of appendix III was then used to obtain the characteristic impedance response for the whole range of frequency. Figure 9.3.2.3.4 shows the characteristic impedance response raging from 0.5GHz to 3GHz.. The moving average depends on the number of points and how linear they are together. In the case of figure 9.3.2.3.4 we have that the simulated value of characteristic impedance, after 40 period is 93Ω, which is 94% of the value applying the design equations of section 6.3. The values in the vicinity of the frequency where the line becomes resonant (around the nulls 1, 2, 3 and 4 of figure 9.3.2.3.2) were discarded. This is because at these frequencies S_{11} and S_{22} approach zero and their accurate determination is no longer possible [9.3.2.3.3]. Thus, these values will be neglected in the determination of the characteristic impedance of the interdigital delays.

Now we will present the simulated characteristic impedance responses for the interdigital delay line of figure 9.3.2.1.1 with different finger lengths. The responses for the structures with finger lengths of 0.6mm, 0.9mm, 1.2mm, 1.5mm 1.8mm 2.7mm and 3.9mm are plotted from figure 9.3.2.3.5 to 9.3.2.3.11. The linearity of the points is a function of the finger length and the frequency. The higher the frequency the more irregular the results are as the frequency approaches to the stop band. The longer the finger the higher the lumped capacitance. Increasing the total capacitance the characteristic impedance of the line decreases, as a result. This decreases the magnitude of the reflection coefficients, $|S_{11}|$ and $|S_{22}|$, and then increase the linearity of the data.

Figure 9.3.2.3.12 summarises all the results (from d = 0.6mm to d = 4.2mm) for characteristic impedances as a function of the finger length. The longer the finger, compared to the finger width, the closer it is to a purely capacitive element, leading to a charge distribution throughout the fingers, as seen in figure 9.3.1.4. Thus, as the finger length increases the characteristic impedance decreases. We can now pick out a delay of finger length of 3.3mm for a 50Ω transmission line.

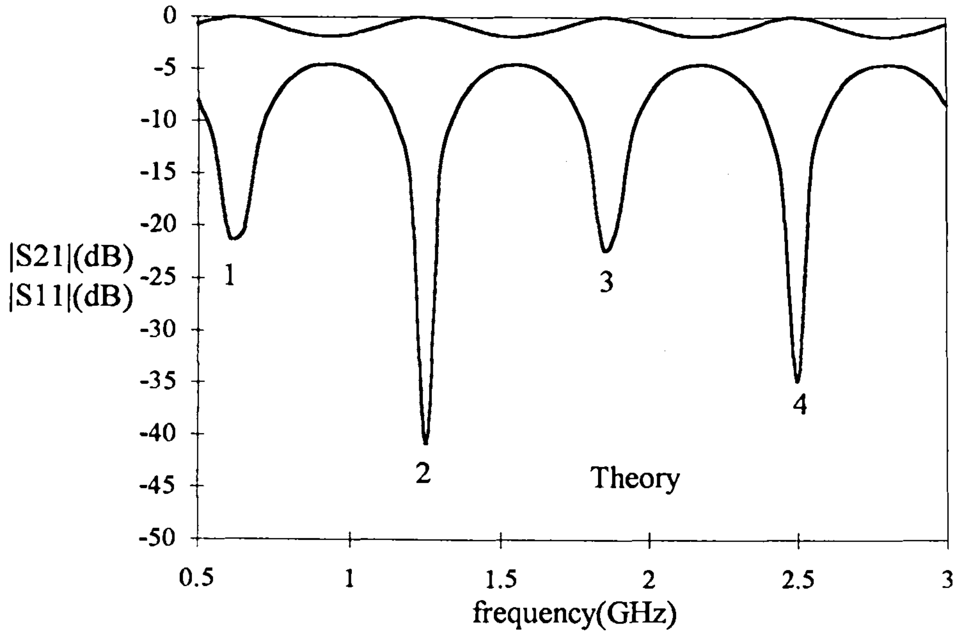

Figure 9.3.2.3.2 Theoretical frequency response for the lossless coplanar strips a with $\varepsilon_r = 10.8$, w = 0.3mm, s = 0.3mm and ℓ = 99mm. The upper trace is the insertion loss and the lower is the return loss in dB.

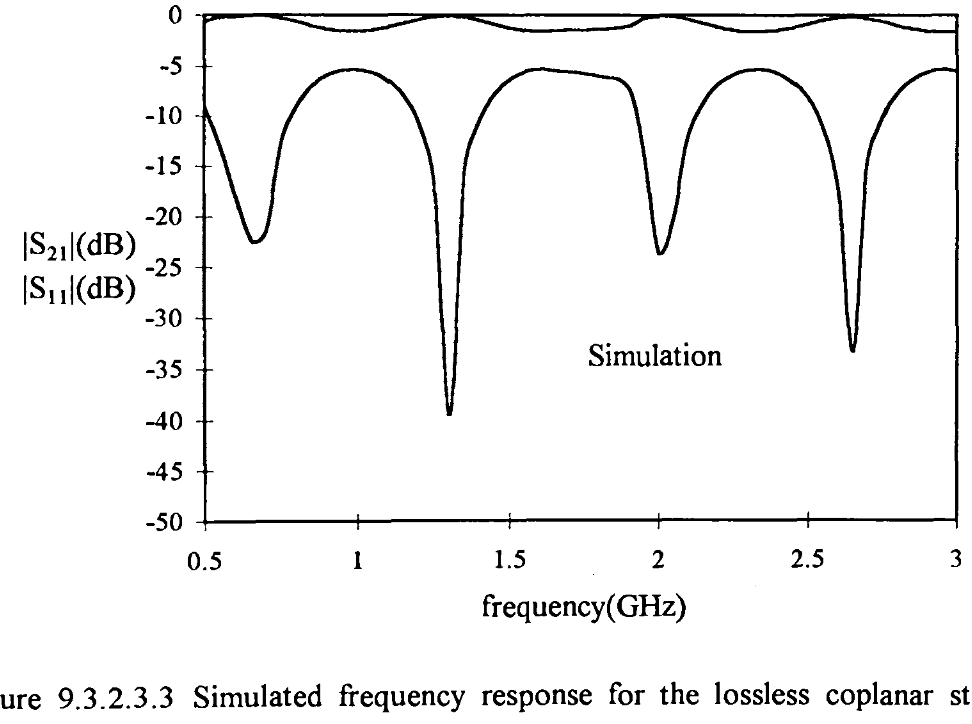

Figure 9.3.2.3.3 Simulated frequency response for the lossless coplanar strips with $\varepsilon_r = 10.8$, w = 0.3mm, s = 0.3mm and ℓ = 99mm. The upper trace is the insertion loss and the lower is the return loss in dB.

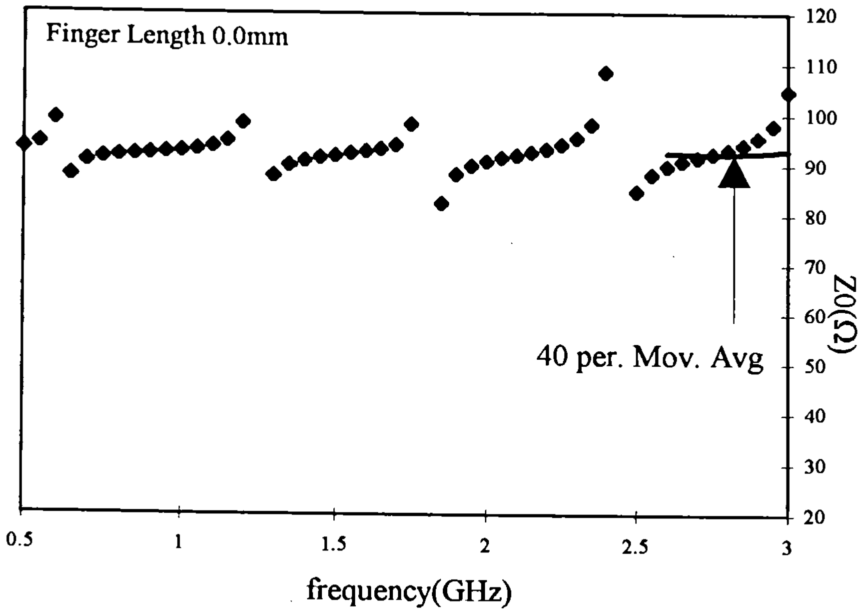

Figure 9.3.2.3.4 Simulated characteristic impedance response for the coplanar strips with $\varepsilon_r = 10.8$, w = 0.3mm, s = 0.3mm and $\ell = 99$mm.

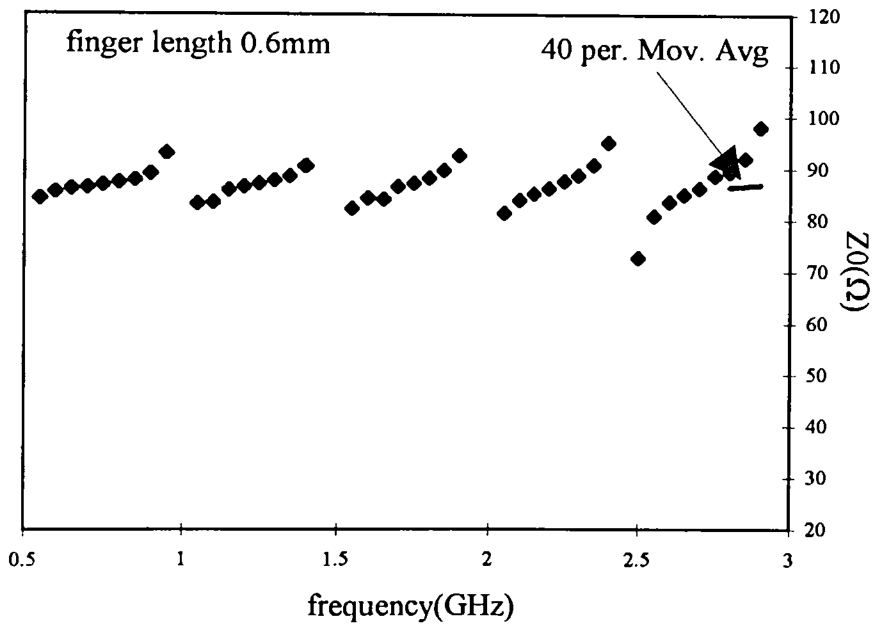

Figure 9.3.2.3.5 Simulated characteristic impedance response for the interdigital delay line with finger length 0.6mm .

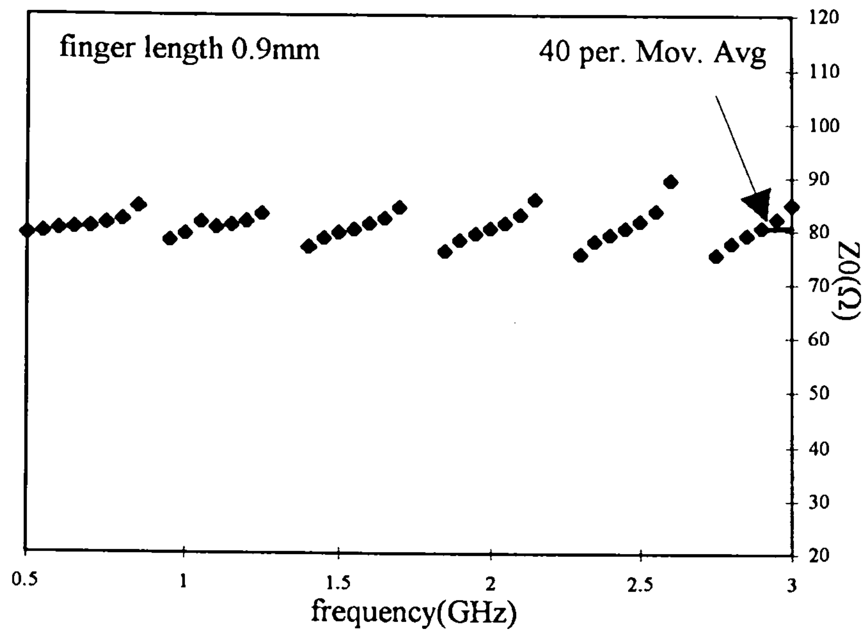

Figure 9.3.2.3.6 Simulated characteristic impedance response for the interdigital delay line with finger length 0.9mm.

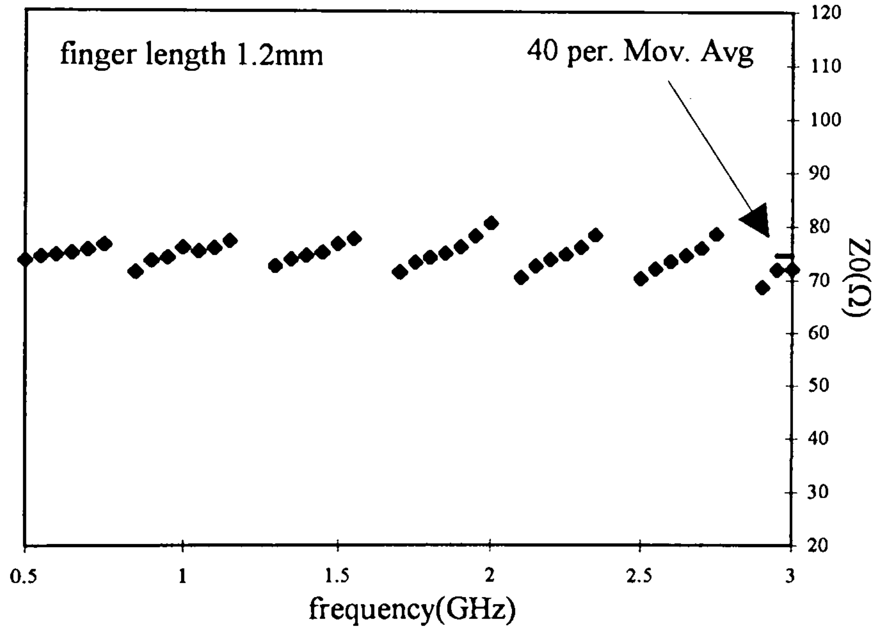

Figure 9.3.2.3.7 Simulated characteristic impedance response for the interdigital delay line with finger length 1.2mm .

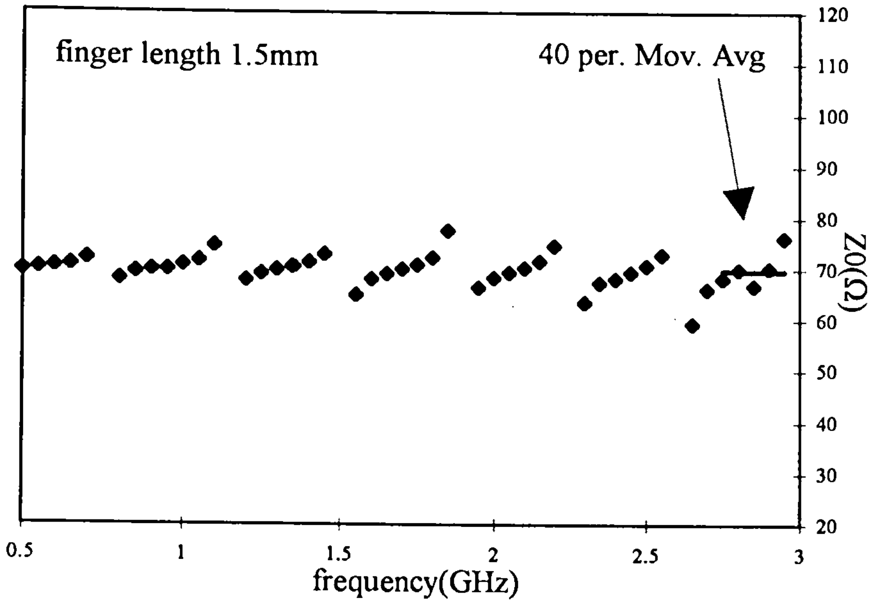

Figure 9.3.2.3.8 Simulated characteristic impedance response for the interdigital delay line with finger length 1.5mm .

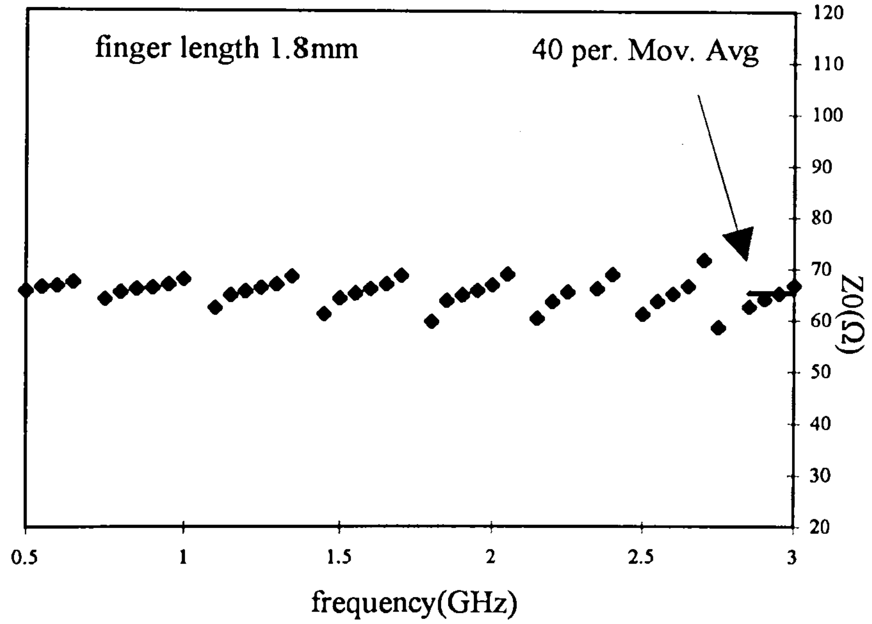

Figure 9.3.2.3.9 Simulated characteristic impedance response for the interdigital delay line with finger length 1.8mm .

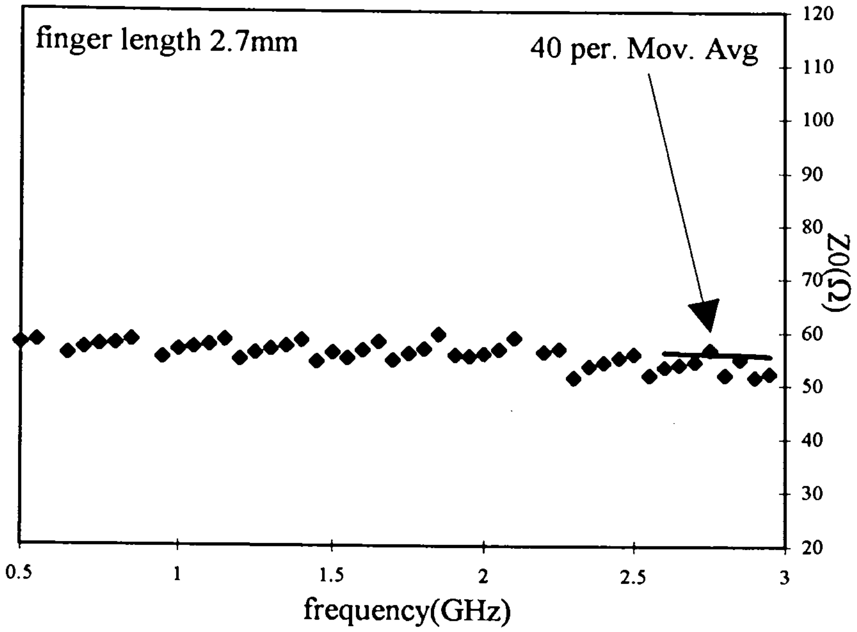

Figure 9.3.2.3.10 Simulated characteristic impedance response for the interdigital delay line with finger length 2.7mm .

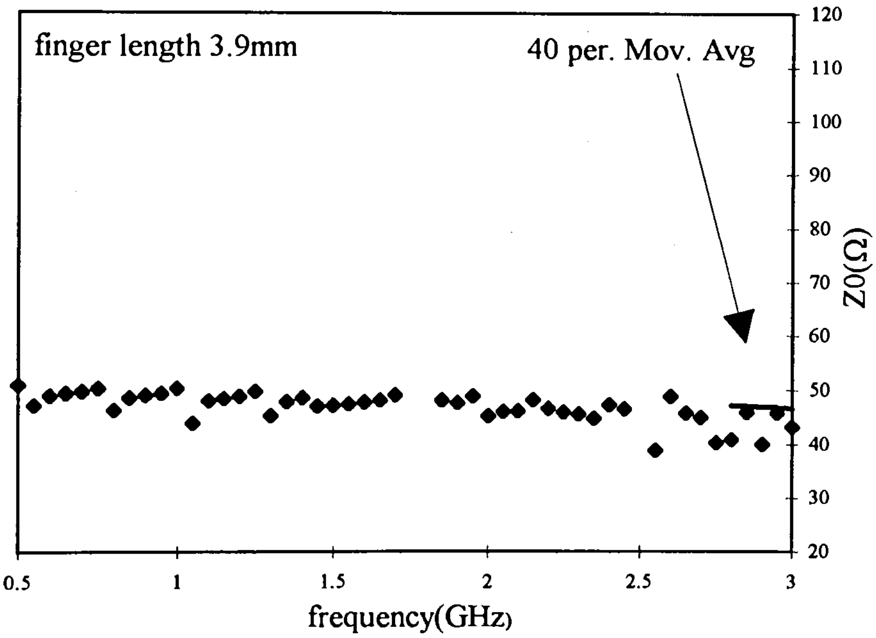

Figure 9.3.2.3.11 Simulated characteristic impedance response for the interdigital delay line with finger length 3.9mm .

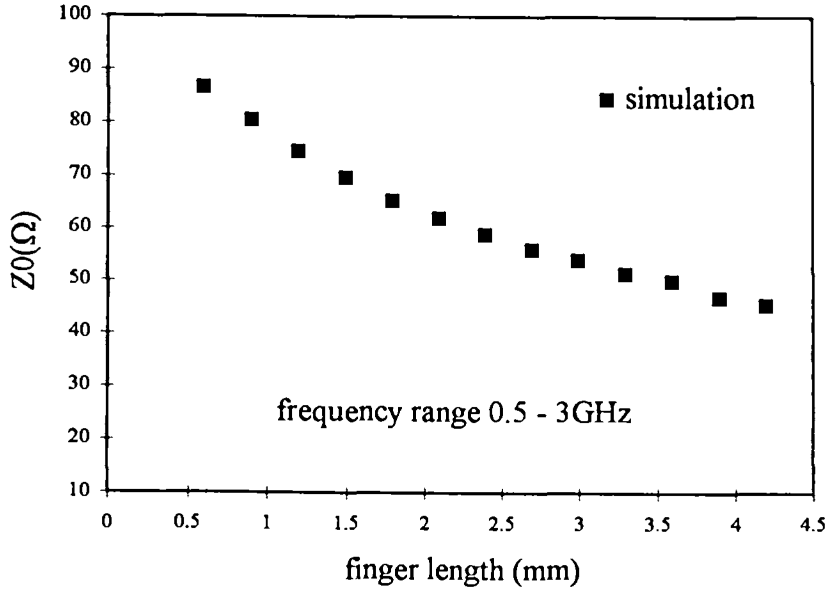

Figure 9.3.2.3.12 Simulated characteristic impedance as a function of the finger length of the interdigital delay lines.

9.3.2.4 Simulating Results of Group Delay and Group Velocity

Simulated group delay and insertion phase responses for the interdigital delay line with two different finger lengths are plotted from figures 9.3.2.4.1 to 9.3.2.4.4. In both cases we see a small level of dispersion in the frequency range shown. This dispersion results in a nearly linear variation of the phase with respect to the frequency. Thus, the group velocity and phase velocity for these structures are nearly identical. In addition to this, as the capacitance increases (from d = 0.6mm to 1.2mm) the group velocity slows down and the interdigital delay becomes electrically longer, increasing $\beta\ell$ as a result. Thus, comparing figure 9.3.2.4.1 with figure 9.3.2.4.3 we see that the number of sharp 360° transitions increases as the finger length increases from 0.6mm to 1.2mm.

Considering equation 8.5.3 of chapter 8 we calculated their corresponding group delays which are plotted in figures 9.3.2.4.2 and 9.3.2.4.4. The moving averages are indicated. The simulated results of group delay and group velocity for the delay lines are plotted as a function of the finger length from 0.6mm to 4.2mm, see figures 9.3.2.4.5 and 9.3.2.4.5, respectively. As the finger length goes from 0.6mm to 4.2mm, keeping all the other parameters fixed, the total capacitance increases leading to a decrease in the group velocity. Thus, the group delay increases by about 250%. For the 50Ω line with finger length 3.3mm the group velocity is 4.8 × 10^7m/s. This is 0.4 times slower than the CPS with zero finger length on the same substrate.

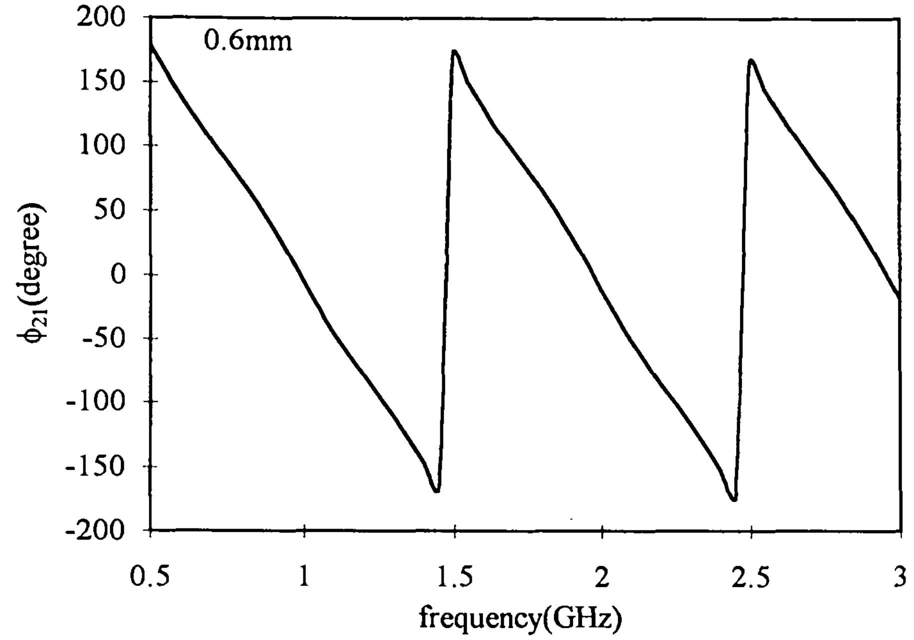

Figure 9.3.2.4.1 Simulated insertion phase for the interdigital delay line with finger length 0.6mm .

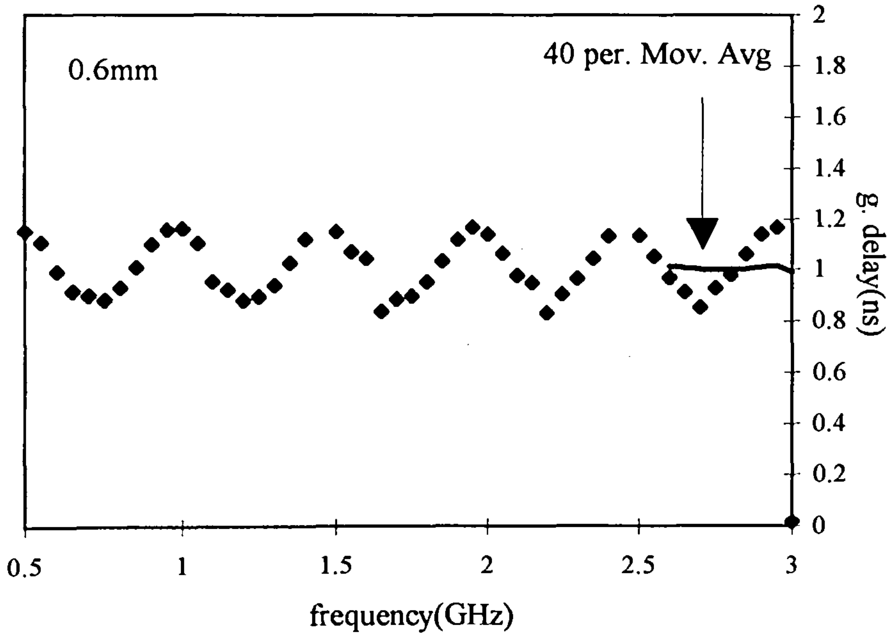

Figure 9.3.2.4.2 Simulated group delay for the interdigital delay line with finger length 0.6mm .

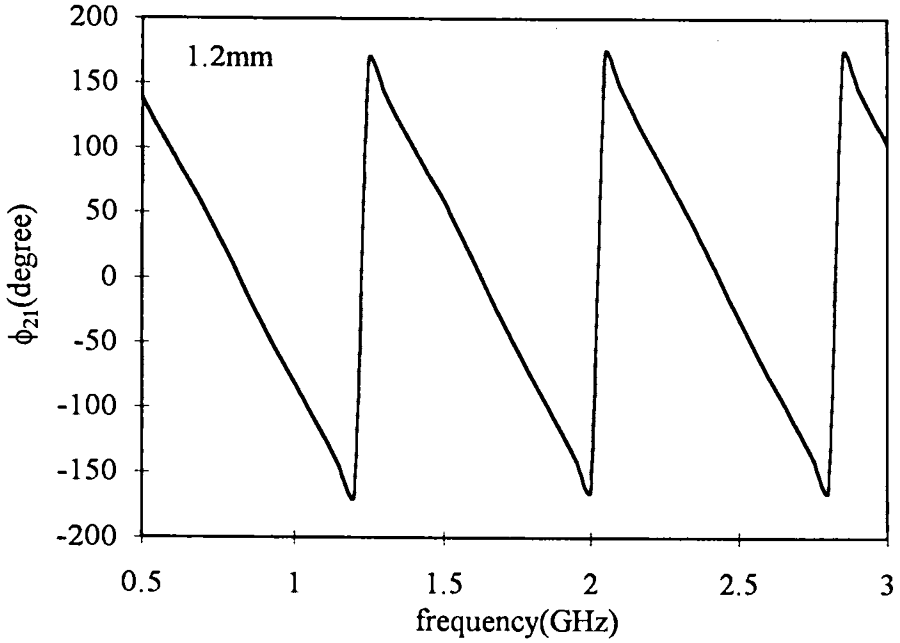

Figure 9.3.2.4.3 Simulated insertion phase for the interdigital delay line with finger length 1.2mm .

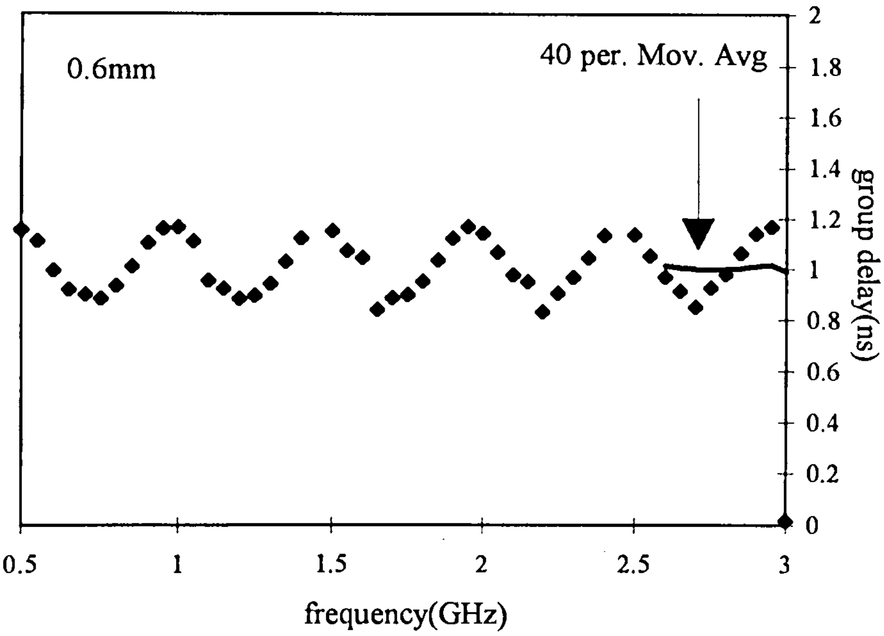

Figure 9.3.2.4.4 Simulated group delay for the interdigital delay line with finger length 1.2 mm .

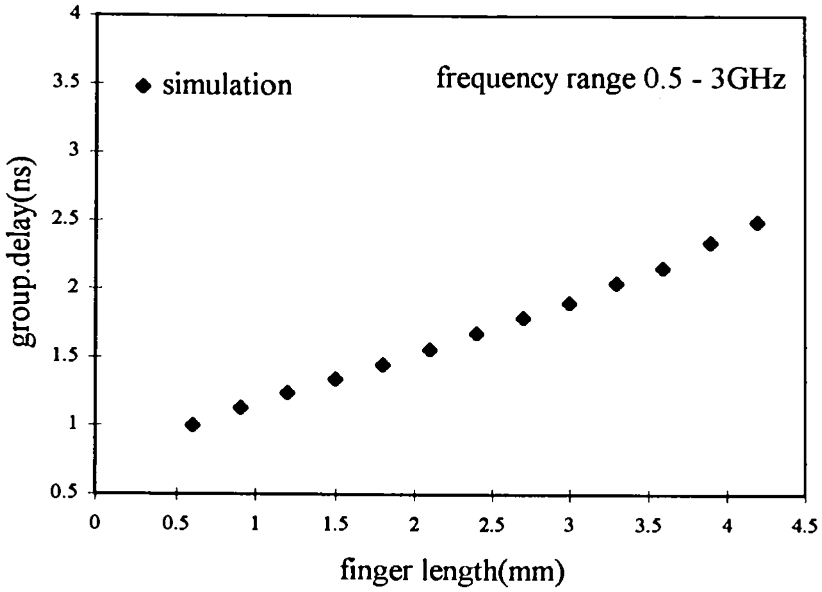

Figure 9.3.2.4.5 Simulated group delay as a function of the finger length of the interdigital delay lines.

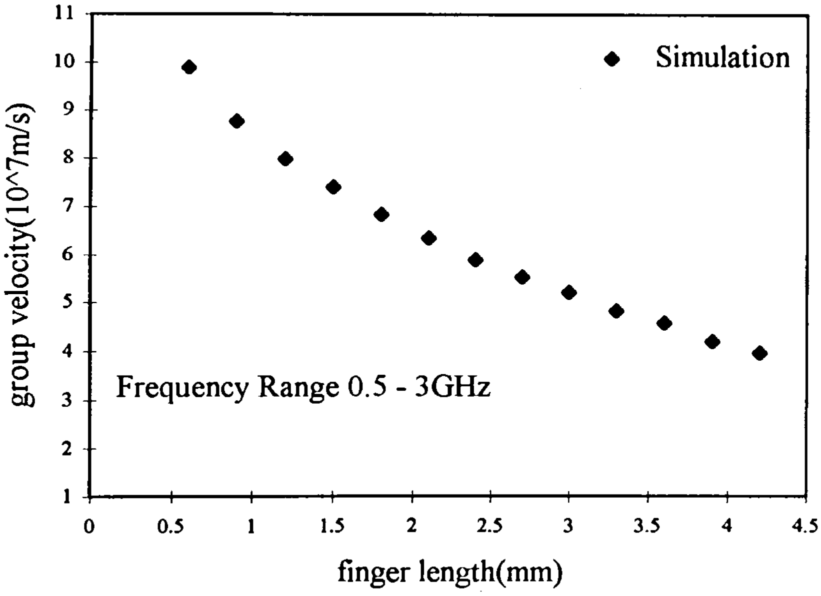

Figure 9.3.2.4.6 Simulated group velocity as a function of the finger length of the interdigital delay lines.

9.4 Power Splitter

9.4.1 Design equations

The purpose of this section is to describe the design equations of a 2-way unequal output impedance power splitter. Because the interdigital delay lines with different finger lengths have different characteristic impedances, as shown in figure 9.3.2.3.12, an unequal output impedance power divider may be used to feed two different delays in the interferometers of figure 9.2.1 and keep the structure matched. A power splitter is a simple three-port network that can be used for power division or power combination. In order to evaluate the design equation let us consider the circuit configuration shown in figure 9.4.1.1. It is a generalised case compared with the classical Wilkinson power divider [9.4.1.1] because we are considering here different output impedances. The power divider is designed so that when fed from port 1, a match is seen and the power out of port 3 is k^2 times the power out of port 2. The voltage between arm 2 and ground (V_2) is equal to that between arm 3 and ground (V_3) when measured at equal distances from port 1 [9.4.1.2].

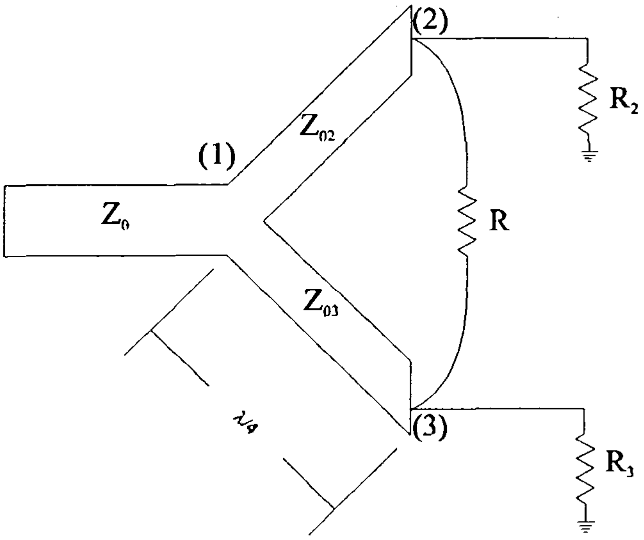

Figure 9.4.1.1 Power splitter with unequal output impedances R_2 and R_3.

The design equations start with the relation between the impedances looking into arm 2 and 3 from port 1, which are Z_{i2}, Z_{i3}, respectively.

The power out of port 2 is given by reference [9.4.1.2]. This is given by

$$P_{o2} = \frac{V_2^2}{2Z_{i2}} \qquad \text{equation 9.4.1.1}$$

The power out of port 3 is given by

$$P_{o3} = \frac{V_3^2}{2Z_{i3}} \qquad \text{equation 9.4.1.2}$$

The relation between the impedances looking into arm 2 and 3 from port 1 which satisfies the above condition ($V_1 = V_2$) can be found by

$$\frac{P_{03}}{P_{02}} = k^2 = \frac{Z_{i2}}{Z_{i3}} \qquad \text{equation 9.4.1.3}$$

To see a match at port 1, it follows

$$Z_0 = \frac{Z_{i1}Z_{i2}}{Z_{i1} + Z_{i2}} \qquad \text{equation 9.4.1.4}$$

Substituting equation 9.4.1.3 into equation 9.4.1.4, after simple manipulations we have

$$Z_{i3} = \frac{1+k^2}{k^2} Z_0 \qquad \text{equation 9.4.1.5}$$

and then

$$Z_{i2} = \left(1+k^2\right)Z_0 \qquad \text{equation 9.4.1.6}$$

The output impedances R_2 and R_3 are chosen to be

$$R_2 = kZ_0 \qquad \text{equation 9.4.1.7}$$

$$R_3 = \frac{Z_0}{k} \qquad \text{equation 9.4.1.8}$$

Parad et. al [9.4.1.2] have proved that for this choice the output transformers have identical phase-transfer characteristics. Here we are just assuming that is true.

The characteristic impedances of the arms 2 and 3 are found using the quarter wave transformer matching condition, so we have

$$Z_{02} = \sqrt{Z_{i2}R_2} \quad \text{and} \quad Z_{03} = \sqrt{Z_{i3}R_3} \qquad \text{equation 9.4.1.9}$$

Substituting equations 9.4.1.5, 9.4.1.6, 9.4.1.7 and 9.4.1.8 into the above equations we find

$$Z_{02} = Z_0\sqrt{k\left(1+k^2\right)} \qquad \text{equation 9.4.1.10}$$

$$Z_{03} = Z_0\sqrt{\frac{1+k^2}{k^3}} \qquad \text{equation 9.4.1.11}$$

With this design, the voltage at port 2 and port 3 are equal. Hence, an isolation resistor (R) maybe placed between these two ports without causing any power dissipation. Parad et al. [9.4.1.2] have also proved that the value of this resistor which gives infinity isolation and perfect match at the center frequency is

$$R = Z_0\frac{1+k^2}{k^3} \qquad \text{equation 9.4.1.12}$$

Note that the above equation reduces to the equal output impedances power splitter for k = 1 giving

$$R_2 = R_3 = Z_0 \qquad \text{equation 9.4.1.13}$$

$$Z_{02} = Z_{03} = Z_0\sqrt{2} \qquad \text{equation 9.4.1.14}$$

$$R = 2Z_0 \qquad \text{equation 9.4.1.15}$$

Equal (coplanar strips) and unequal (coplanar strips) output impedance power splitters will be designed, fabricated and measured and their results in transmission mode will be presented in chapter 10.

Chapter 10

Digital Instantaneous Frequency Measurement Subsystem

10.1 Coaxial Instantaneous Frequency Measurement

Conventional IFM systems use delay lines made by coiling coaxial cables. In order to demonstrate the importance of the use of coplanar IFMs in terms of size and weight we set up a simple coaxial IFM system. In addition to this, it is a good way to check in practice the design equations described in section 9.2 of chapter 9.

Four separate interferometers were set in order to investigate the use of the design equations described in chapter 9. In view of the specifications of the power splitter/combiners used in this experiment we assumed the values of the bandwidth and the central frequency, 1GHz and 9 GHz, respectively. Since we know the bandwidth, the shortest delay τ_1 may be determined by equation 9.2.7, which gives $(\tau_1 - \tau)_{\min} = 1\text{ns}$. Here $(\tau_1 - \tau)_{\min}$ is the minimum delay difference of the system and τ is the fixed delay throughout the interferometers. Assuming $\tau = 1\text{ns}$ we have $\tau_1 = 2\text{ns}$. The output of this discriminator gives a frequency response of just one peak, or null. For the other three interferometers we may use equation 9.2.7 in the n-peak (or null) case. Taking n = 3, n = 5 and n = 7, we have $\tau_2 - 1 = 3\text{ns}$, $\tau_3 - 1 = 5\text{ns}$ and $\tau_4 - 1 = 7\text{ns}$. This gives $\tau_2 = 4\text{ ns}, \tau_3 = 6\text{ ns}$ and $\tau_4 = 8\text{ ns}$. Figure 10.1.1 summarises the interferometers with their respective delays.

The physical length of each coaxial delay is given by the equation

$$L_\tau = \frac{\tau_c}{C_c Z_c} \qquad \text{equation 10.1.1}$$

where τ_c is the delay time of the coaxial cable. C_c and Z_c are the capacitance and the impedance of the coaxial cable, respectively. A semi-rigid coaxial cable of $C_c = 96$ pF/m and $Z_c = 50\Omega$ was used. This gives $L_\tau = 20.8\text{cm}$, $L_{\tau 1} = 41.6\text{cm}$, $L_{\tau 2} = 83.2\text{cm}$, $L_{\tau 3} = 124.6\text{cm}$ and $L_{\tau 4} = 166.4\text{cm}$.

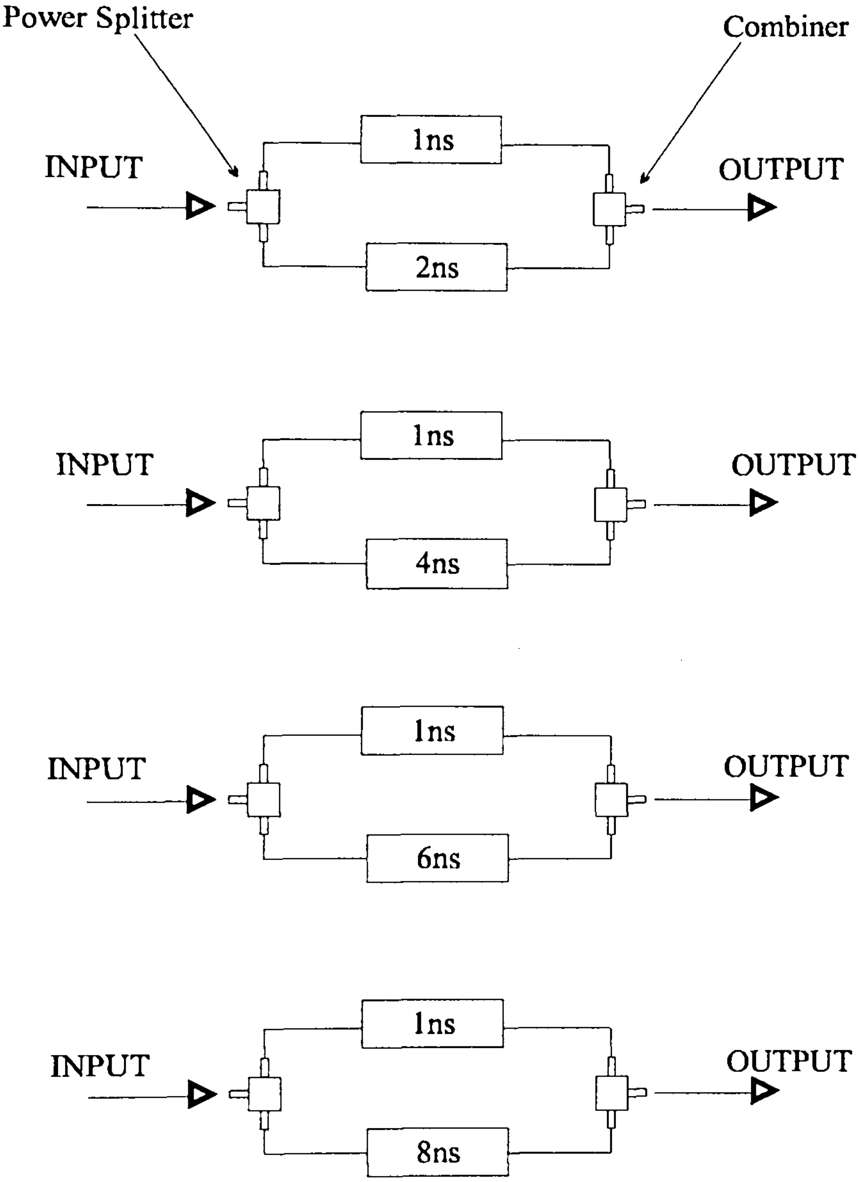

Figure 10.1.1 Four separate interferometers. The first delay of each interferometer has a fixed value of 1ns and second is stepped by 2ns.

The advantage of having a system with four separate interferometers is that we can check each part easily. We measured their respective insertion losses connecting each interferometer to a HP8720A network analyser. In agreement with the design equations we have figure 10.1.2 with one point of minimum, figure 10.1.3 with three points of minimum, figure 10.1.4 with five points of minimum and figure 10.1.5 with seven points of minimum. These figures represent the interferometers 2-1ns, 4-1ns, 6-1ns and 8-1ns, respectively. Putting these interferometers together using a 4-way power splitter or three 2-way power splitters with such length of delays is a very difficult task. The number of coaxial connections and poor bends may increase the mutual reflection. In addition to this, the size of the whole system, even with a low resolution, may became unacceptable. The next section will describe the design and measurement of an uniplanar IFM using coplanar transmission lines.

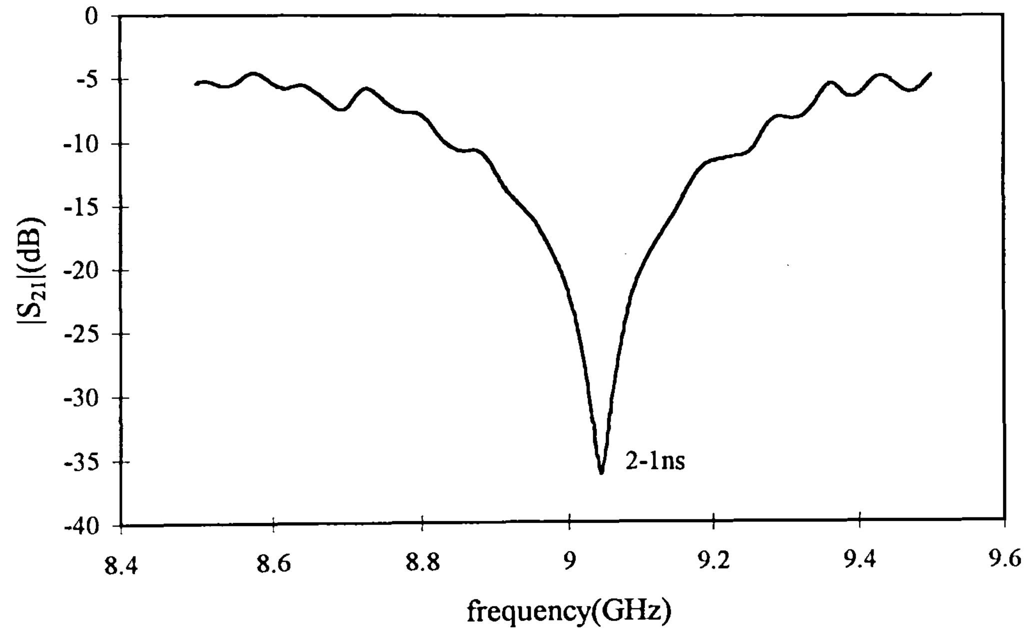

Figure 10.1.2 Frequency response of the first interferometer of figure 10.1.1, 2ns-1ns.

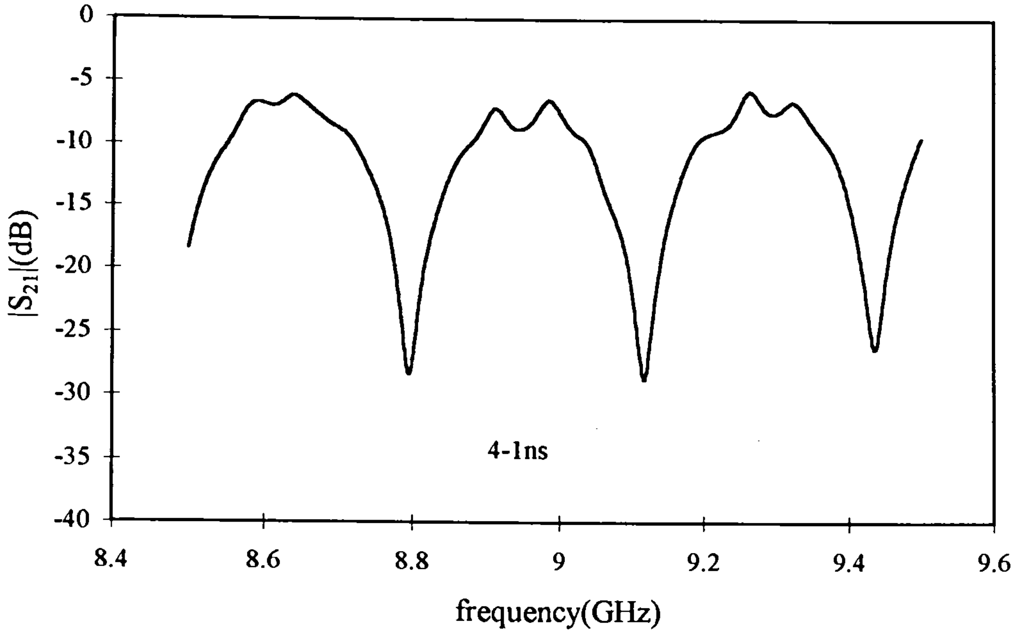

Figure 10.1.3 Frequency response of the second discriminator of figure 10.1.1, 4ns-1ns.

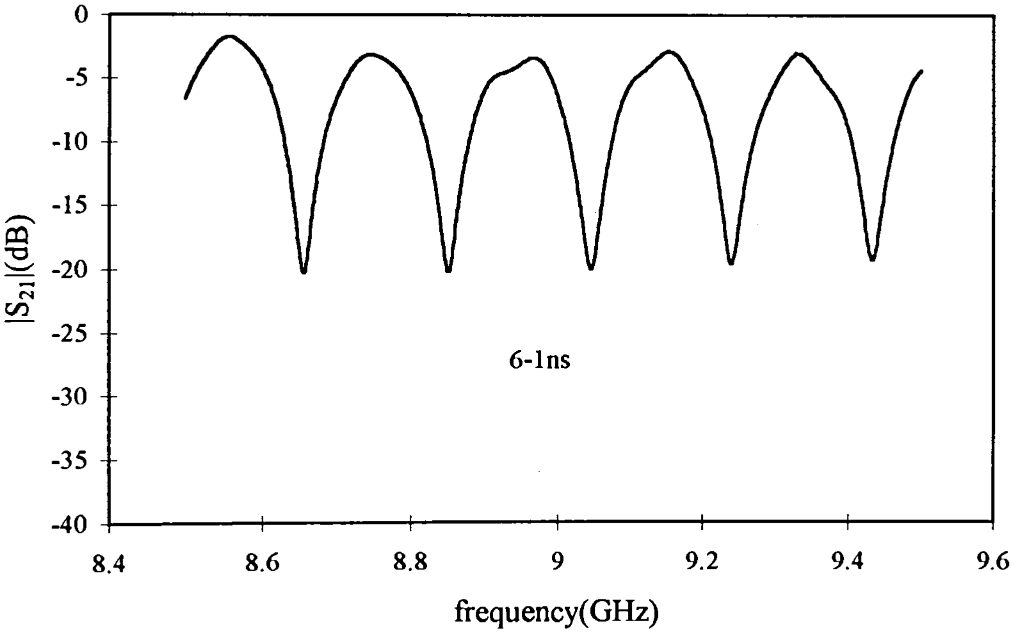

Figure 10.1.4 Frequency response of the third discriminator of figure 10.1.1, 6ns-1ns.

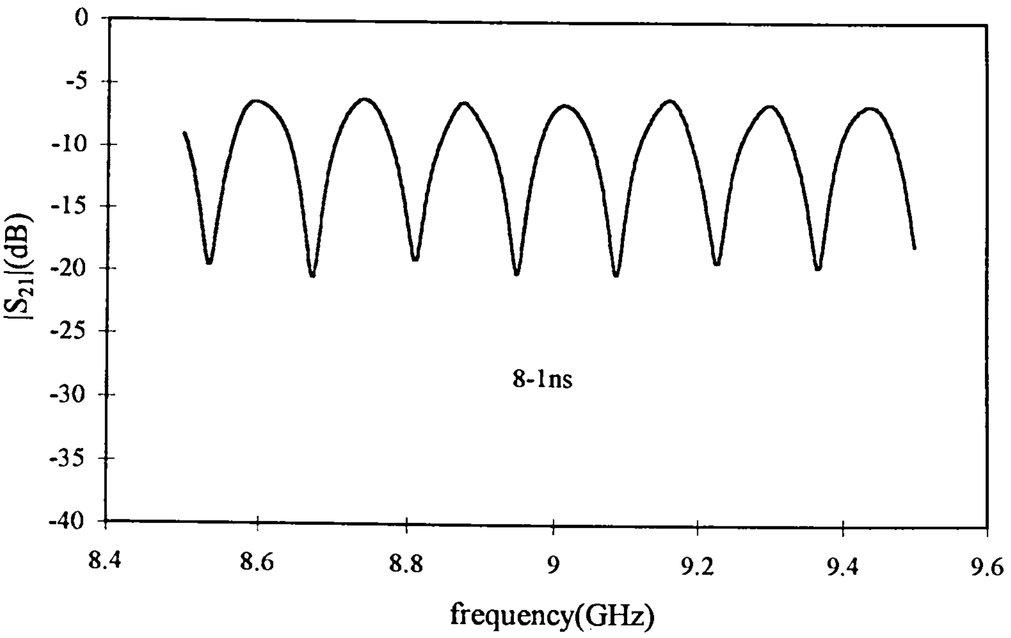

Figure 10.1.5 Frequency response of the fourth discriminator of figure 10.1.1, 8ns-1ns.

10.2 Interdigital Delay Line Experimental Results

10.2.1 Group Delay and Group Velocity

Several structures of different finger lengths, based on the coplanar strips interdigital delay line described in section 9.3.2.1 of chapter 9, were etched on only one side of an RT/duroid 6010 substrate with relative permittivity $\varepsilon_r = 10.8$, height $h = 0.64$ mm, conductor thickness $t = 35\mu m$, $w = 0.3$ mm, $s = 0.3$ mm and $\ell = 99$ mm. Keeping all the other parameters fixed the finger length was varied from 0.6 to 4.2mm and the fabrication itself was accomplished by a single photo-resist pattern, followed by the etch.

In the experimental procedure gold plated SMA connectors were used to link the coplanar strips to coaxial cables. In order to achieve the best possible impedance match, the centre conductor had the same width of the strip, 0.3mm. The ground strip was carefully soldered, with no gap, to the flange of the connector, as shown in figure 10.2.1.1. The device was then connected with coaxial cables to a HP8720A network analyser. After carrying out a proper calibration, the group delay was measured and the moving average (40 period) of 800 points was then calculated. Figure 10.2.1.2 summarises the group delay results of both measurement and simulation for a frequency range of 0.5-3 GHz. From the results of group delay we plotted the group velocity, $v_g = \ell/\tau_g$, versus the finger length and these are summarised, together with the simulation, in figure 10.2.1.3. Simulated and experimental results seem to be in good agreement.

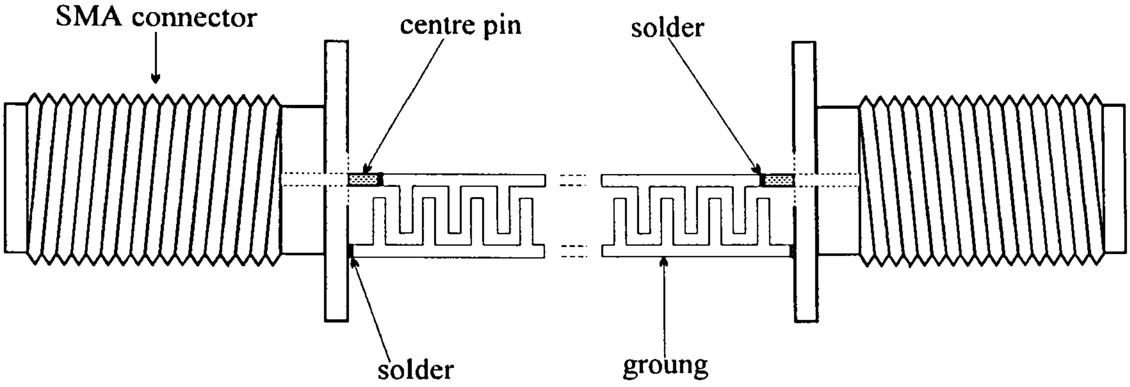

Figure 10.2.1.1 Interdigital delay line soldered to SMA connectors.

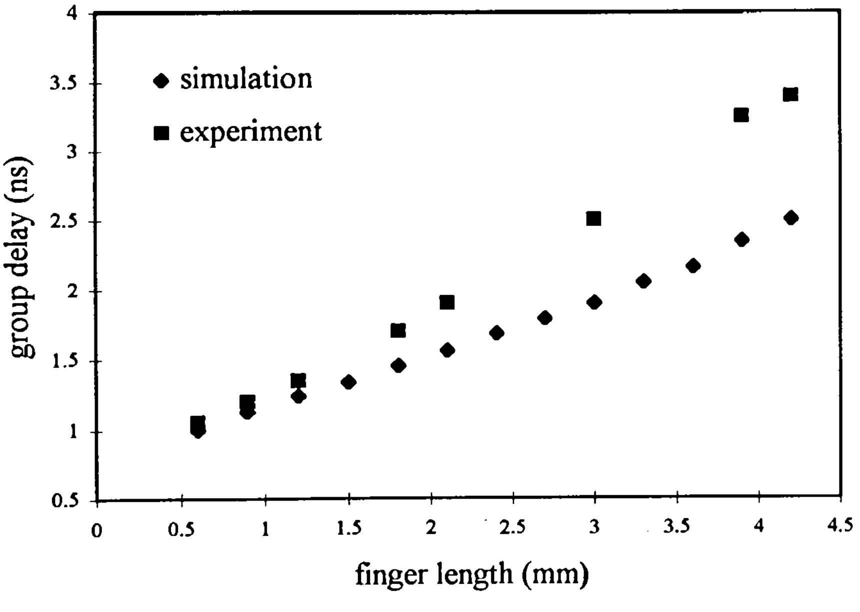

Figure 10.2.1.1 Experimental and simulated results of group delay as a function of the finger length of the interdigital delay line. Frequency range 0.5-3GHz.

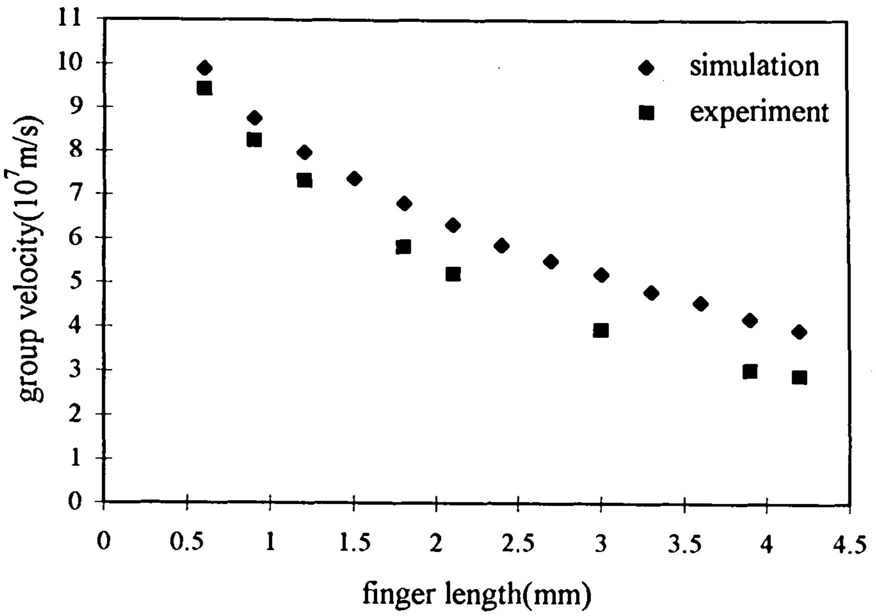

Figure 10.2.1.2 Experimental and simulated results of group velocity as a function of the finger length of the interdigital delay line. Frequency range 0.5-3GHz.

10.2.2 Characteristic Impedance Results from Time Domain Response

Looking back at section 8.6 of chapter 8 time domain measurements can locate transmission path discontinuities, identify the impedance type and magnitude of each discontinuity and multiple signal paths [10.2.2.1]. In this section we are using the time domain response with the main purpose of finding the magnitude of the characteristic impedance of the interdigital delay lines.

The experimental data of Z_0 was obtained by carrying out a reflection measurement in the time domain low pass mode on the HP8720A Network Analyser, which provides the best resolution for a given bandwidth in the frequency domain. The low pass mode requires that the start and stop frequency are harmonically related, with the N^{th} harmonic corresponding to the start frequency times the number of points [10.2.2.1]. For example, for a start frequency of 130MHz with 51 points we have a stop frequency of 6.63GHz. Exceptionally the network analyser sets 201 points with start and stop frequencies of 130MHz, 13.13GHz, respectively. We chose 201 points in order to approach the best average value of the characteristic impedance.

The time domain low pass mode may be used to give either the step or impulse response. As we were interested in finding Z_0 and comparing it with the simulated results, we measured the step response of the interdigital delay lines with different finger lengths, from 0.6 mm to 4.2 mm. In the experimental procedure the network analyser was connected to one side of the device presented in figure 10.2.1.1 and an open circuit was connected to the other side of it. Figures 10.2.2.1 and 10.2.2.2 show the step response for the finger lengths 0.9mm and 1.5mm, respectively. The horizontal axis, ranging 0ns to 4ns, represents the two-way travel time to the discontinuity, and the vertical axis represents the reflection coefficient in a real format, Re(S_{11}). Apart from the oscillations, the traces show four different stages, the transition from a 50Ω coaxial cable to the interdigital delay line, the interdigital delay line itself, the transition from the interdigital delay line to the open circuit and the open circuit itself. The oscillations around the second transition seem to be related to the coaxial connectors. However, we are only interested in finding the characteristic impedance of the interdigital transmission lines. Looking at the first transition of figure 10.2.2.1, it is possible to find the characteristic impedance of the interdigital delay line. We can perform this calculation because we know the impedance of the coaxial line and the real part of the reflection coefficient at the discontinuity. Both figures 10.2.2.1 and 10.2.2.2 have the interdigital delay line section with their respective characteristic impedance indicated. Figure 10.2.2.3 summarises the characteristic impedance results obtained by both measurement and simulation for a frequency range of 0.5-3 GHz. The simulated and experimental results seem to be in good agreement.

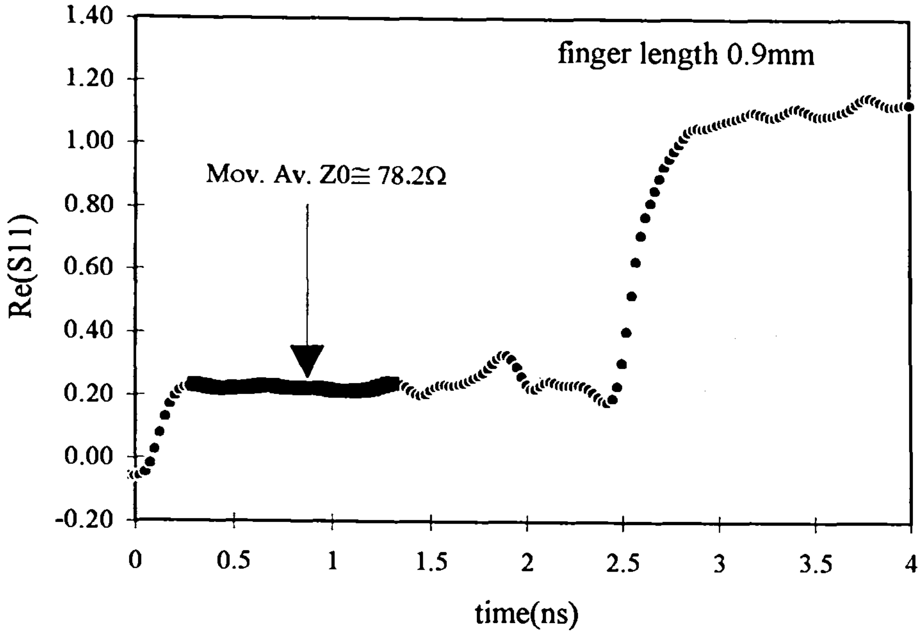

Figure 10.2.2.1 Low pass step response for the interdigital delay line of 0.9mm finger length, connected to an open circuit. The moving average impedance (40 periods) of the interdigital delay line is indicated.

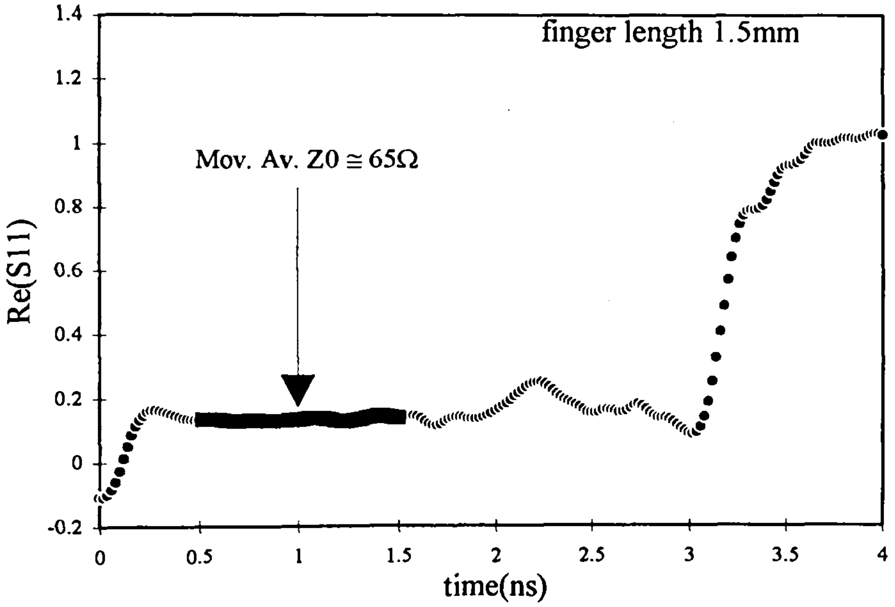

Figure 10.2.2.2 Low pass step response for the interdigital delay line of 1.5mm finger length, connected to an open circuit. The moving average impedance (40 periods) of the interdigital delay line is indicated.

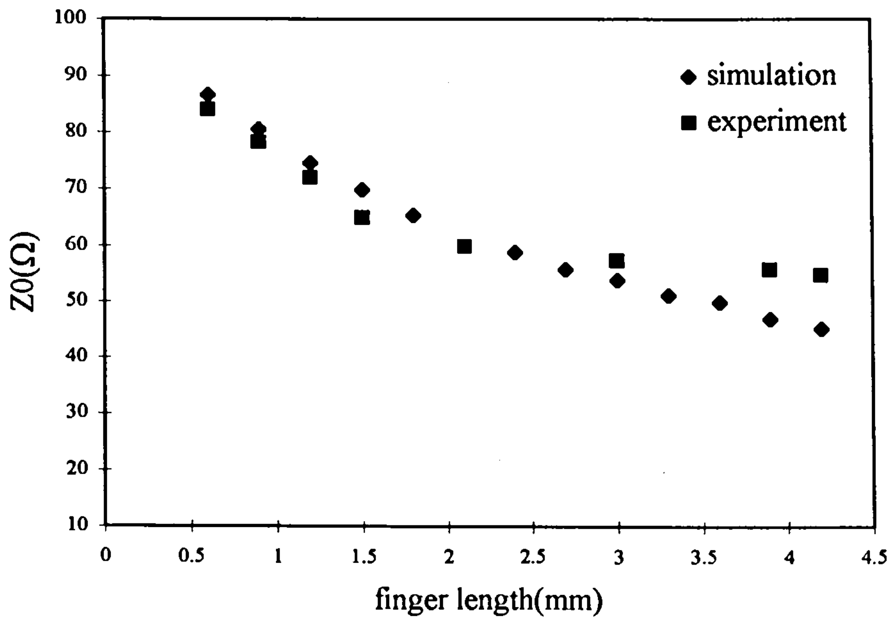

Figure 10.2.2.3 Experimental and simulated results of characteristic impedance as a function of finger length of the interdigital delay line. Frequency range 0.5-3GHz.

10.3 Coplanar Power Splitter

10.3.1 Design

The power splitter illustrated in figure 10.3.1.1 uses coplanar strips as its principal transmission line type. It consists of a small section of coplanar wave guide from port 1 to the splitting junction (A) and two coplanar strip quarter wave lengths. For the design of the CPW we used the design equations described in section 7.2 of chapter 7. The Mathcad program described in section Ap.III.1 of appendix III was used to do the calculations. Considering $s = 0.3$mm and $w = 0.7$mm, the program gives $Z_0 \cong 50\Omega$. In the case of the quarter wave length coplanar strip we used the design equations for two asymmetric coplanar strips found in the reference [10.3.1.1]. The calculations were carried out using the Mathcad program described in section Ap.III.5 of appendix III. Assuming for the inner strip, $w_1 = 0.5$mm and for the outer strip, $w_2 = 5$mm we found $Z_0 \cong 71\Omega$. For the central frequency we chose the same frequency of the interdigital delay line, which is 1.5Ghz.

Perhaps the most difficult part of this design is connecting the two quarter-wave lines to the input 50Ω lines. As a rule of thumb we considered 90^0 as the splitting angle between the two arms after the connection [10.3.1.2]. It is important to keep the same impedance of 71Ω along the two quarter-wave lines. The distance between the two arms has to be taken from the length of a 100Ω chip resistor connected between the inner strips to increase the isolation between the ports 2 and 3. The output coplanar strips are at 180^0 angle with each other.

The device was etched on only one side of an RT/duroid 6010 with relative permittivity $\varepsilon_r = 10.8$, height $h = 0.64$ mm, conductor thickness $t = 35$. The fabrication itself was accomplished by a single photo-resist pattern, followed by the etch. The artwork was implemented using Corel Draw software and a laser printer of 600dpi, see figure 10.3.1.2. The next section will show the experimental results.

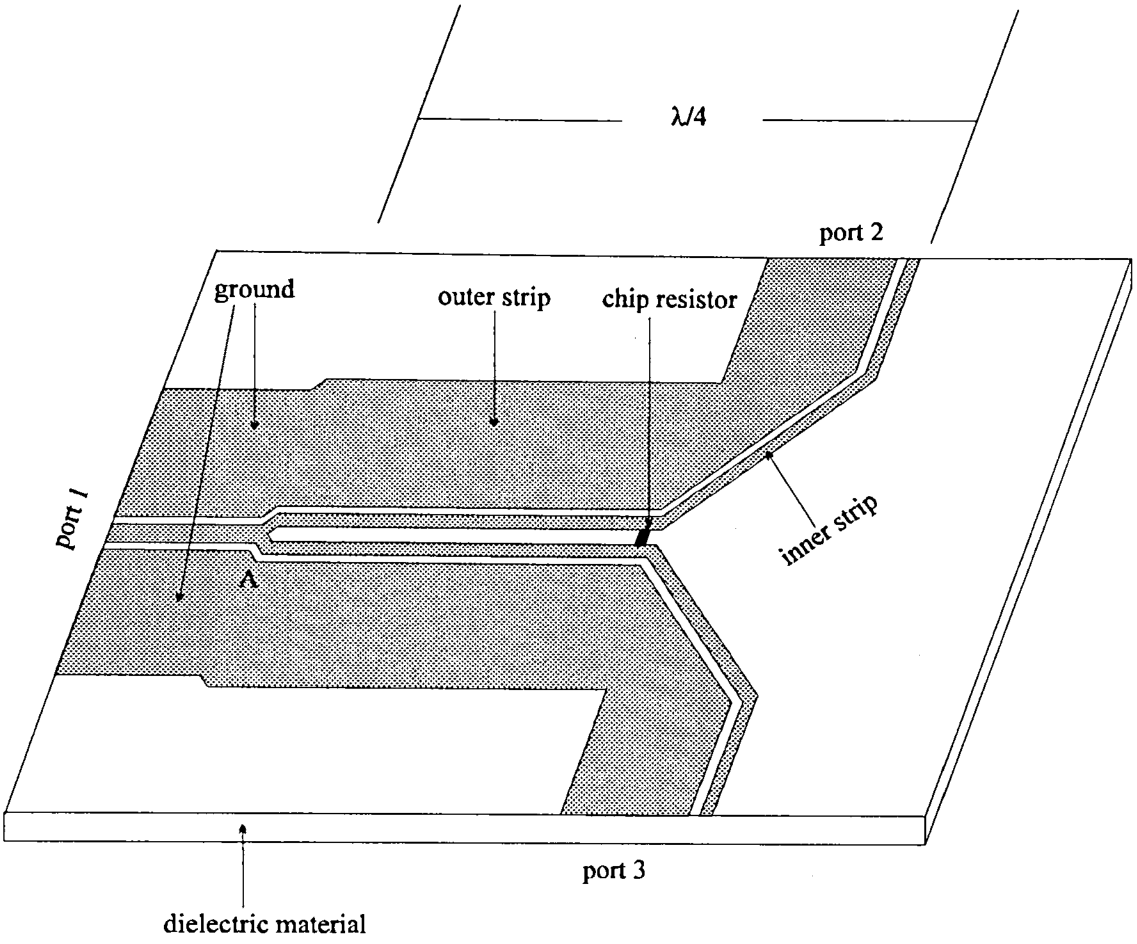

Figure 10.3.1.1 Microstrip power splitter. 3D view in bigger scale.

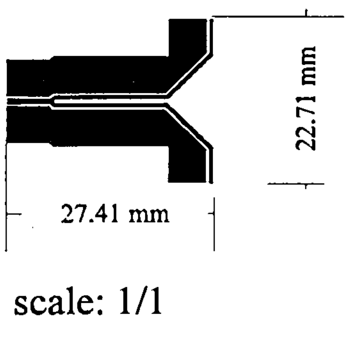

Figure 10.3.1.2 Coplanar power splitter artwork in scale of 1/1.

10.3.2 Insertion Loss Response

Figure 10.3.2.1 shows the amplitude in dB of S_{31} and S_{21} from 13MHz to 2.3GHz. The maximum difference between the two output responses is 0.5dB at 1.7 GHz. This balanced coplanar power splitter has an insertion loss value of only 0.2dB plus 3dB splitting loss at 1.15GHz.

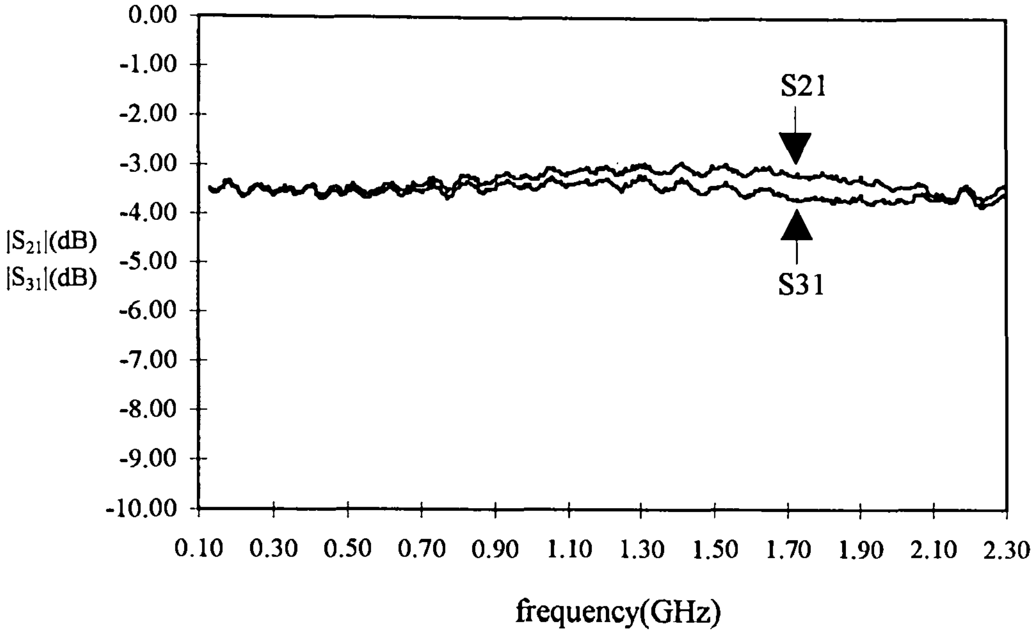

Figure 10.3.2.1 Insertion loss responses from port 1 to port 2 and from port 1 to port 3.

Figures 10.3.2.2 and 10.3.2.3 demonstrate the importance of using a chip resistor to increase the isolation between port 2 and 3. The use of chip resistor improves the isolation from -13dB to -16dB at 1.15GHz. These results indicate that it is possible to fabricate a balanced coplanar power splitter without using airbridges. Figures 10.3.2.4 and 10.3.2.5 present the insertion losses measured at ports 2 and 3. In the procedure a 50Ω impedance load has always been connected to one output when the other is measured. This can be easily analysed using circuit theory [10.3.2.1], which gives a value for the return loss of 6dB. However both results from figures 10.3.2.4 and 10.3.2.5, are different to the 6dB value predicted theoretically. The chip resistor absorbs reflected power when the circuit is operated in an out-of-balance. The technique developed in this section will be very important to design the unequal output impedance power splitters in the IFM system, which will be described later on in this chapter.

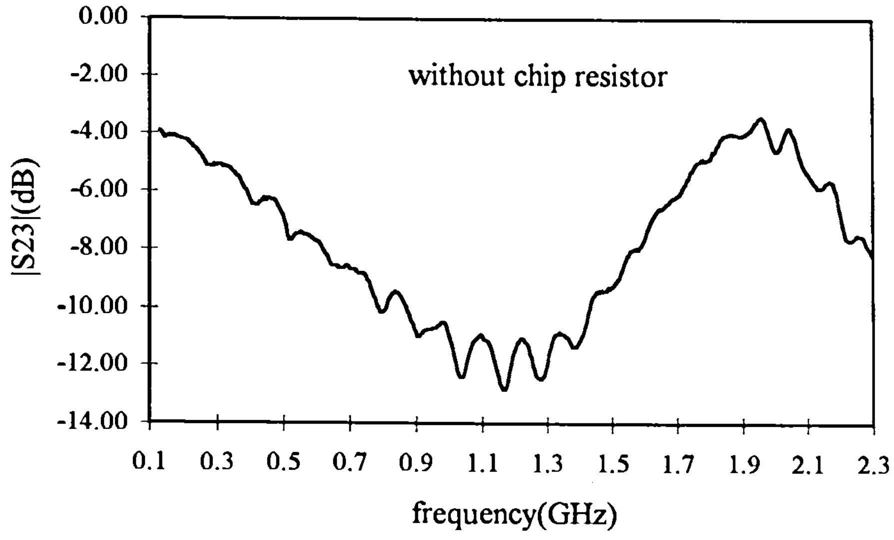

Figure 10.3.2.2 Isolation between ports 2 and 3 without using chip resistor.

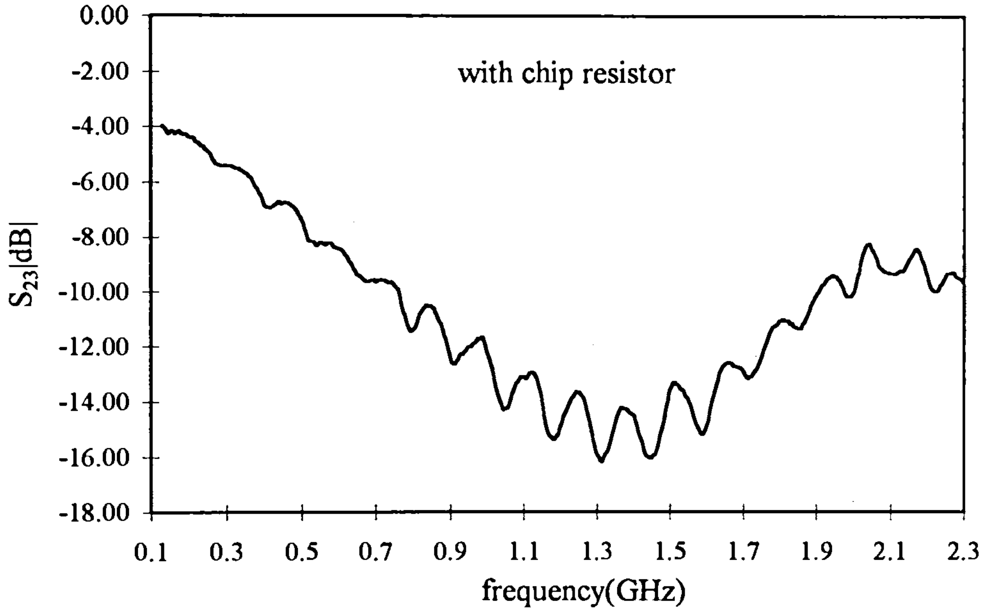

Figure 10.3.2.3 Isolation between ports 2 and 3 using chip resistor.

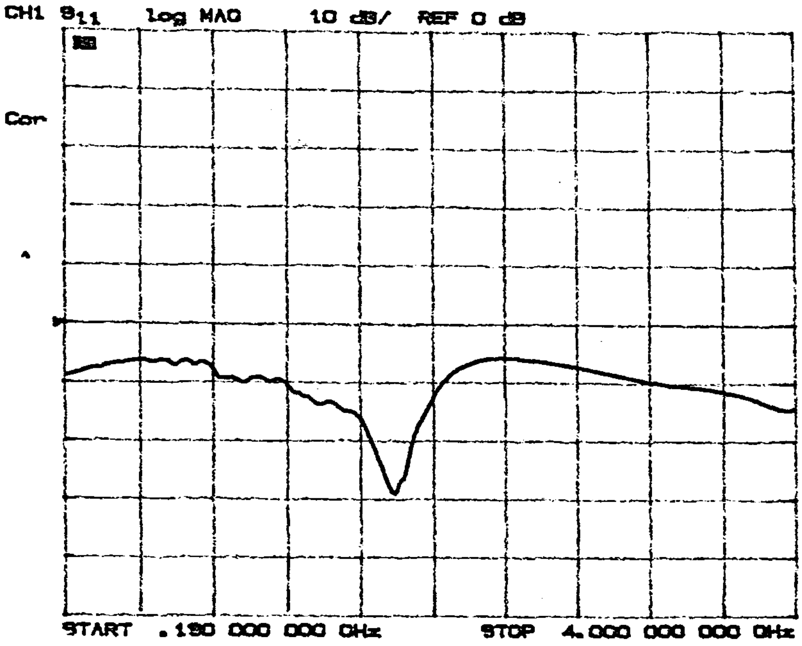

Figure 10.3.2.4 Return loss at port 2 using chip resistor.

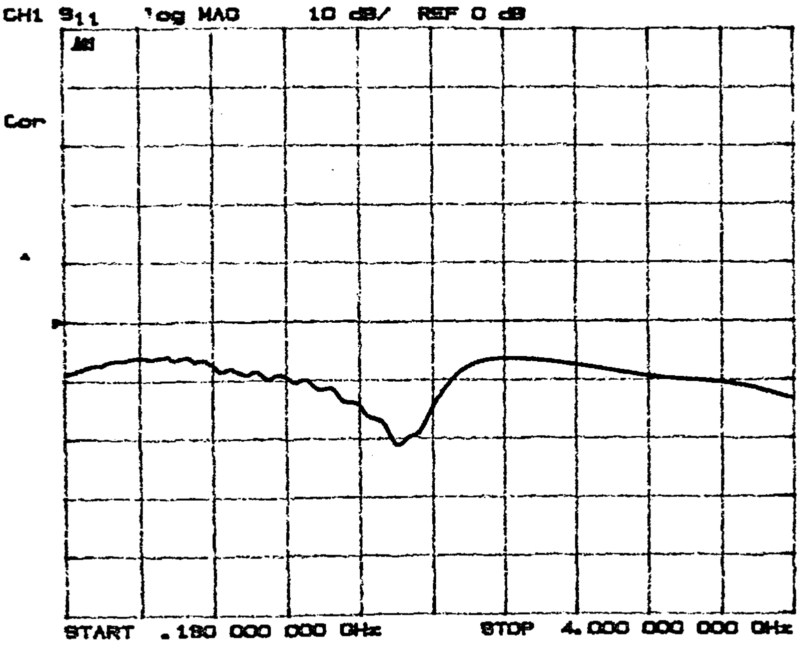

Figure 10.3.2.5 Return loss at port 3 using chip resistor.

10.4 Coplanar Instantaneous Frequency Measurement Subsystem

10.4.1 Design of the Interferometers

Two uniplanar interferometers were designed, fabricated and measured. Figure 10.4.1.1 shows the bigger one with its components indicated. It consists of four coplanar wave guides with finite ground sections, two coplanar strips power splitters with unequal output impedances, one coplanar strip delay line and one coplanar strip interdigital delay line. The top view of the first and the second interferometers in a scale of 1/1 with their respective block impedance diagram are shown in figures 10.4.1.2a, 10.4.1.2b, 10.4.1.3a and 10.4.1.3b. Now we will describe step by step how the two interferometers were performed.

The design of the coplanar IFM started choosing the group delays of the interdigital transmission lines of the first (τ_1) and second (τ_2) interferometers. From the group delay results, summarised in figure 10.1.1.1, we chose $\tau_1 = 1\text{ns}$ and $\tau_2 = 2\text{ns}$. The second step was to find the characteristic impedances of the interdigital transmission lines. From the characteristic impedance results, summarised in figures 10.1.2.3, we can easily find the values of characteristic impedance that correspond to the chosen values of group delays. We found 62Ω for τ_1 and 52Ω for τ_2. The third step was to choose the characteristic impedance and the group delay values for the coplanar strips (CPS) line used as the first delay line in the interferometers, as illustrated in figure 10.4.1.1. These values are constant and do not change when we pass from one discriminator to the other. Thus, we chose a CPS delay line of $\tau = 4\text{ns}$ and 86Ω. As we can see comparing figure 10.4.1.2a with figure 10.4.1.3a, the width of the lines of their first delay lines are not the same, even though they have the same characteristic impedances. We may check this looking at the CPS design equations, described in section 7.3 of chapter 7. If we vary both s and w keeping the ratio s/(2w + s) constant, the characteristic impedance does not change.

The fourth step was to design the unequal output impedance power splitters with their respective CPW quarter wave transformers, that connect the input of the power splitters to the 50Ω impedance CPWs. They were designed using the equations described in section 9.4.1 of chapter 9 for a central frequency of 2GHz. The calculations were carried out by using the Mathcad program described in section Ap.III.6 of appendix III. Because of the symmetry of the interferometers, the results from the Mathcad program might be duplicated to implement the whole structure. The characteristic impedances of each section are indicated in figures 10.4.1.2b and 10.4.1.3b. The chip resistors used to increase the isolations between the outputs of the power splitter (or inputs of the combiners) were also designed by the program but are not indicated in figures 10.4.1.2b and 10.4.1.3b.

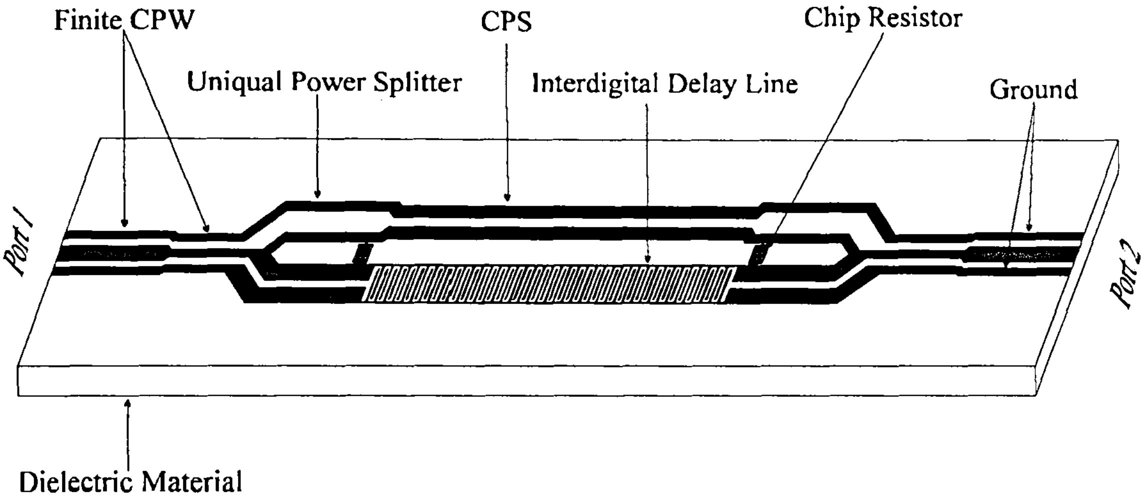

Figure 10.4.1.1 3D view of the bigger discriminator in a scale of 1.4/1.

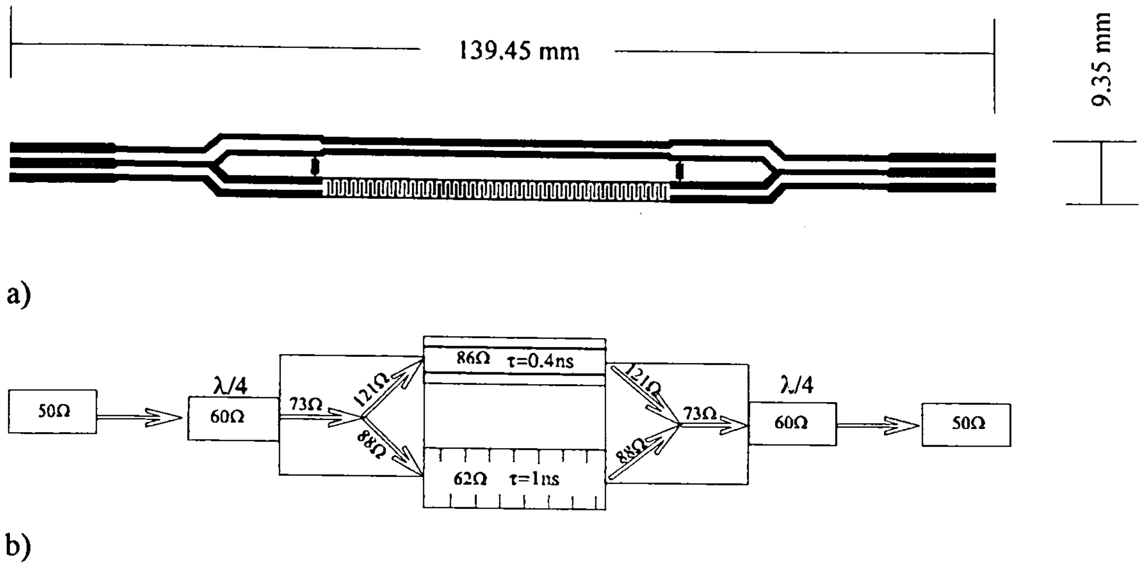

Figure 10.4.1.2 a) First uniplanar discriminator in a scale of 1/1. b) Impedance block diagram of the first interferometer.

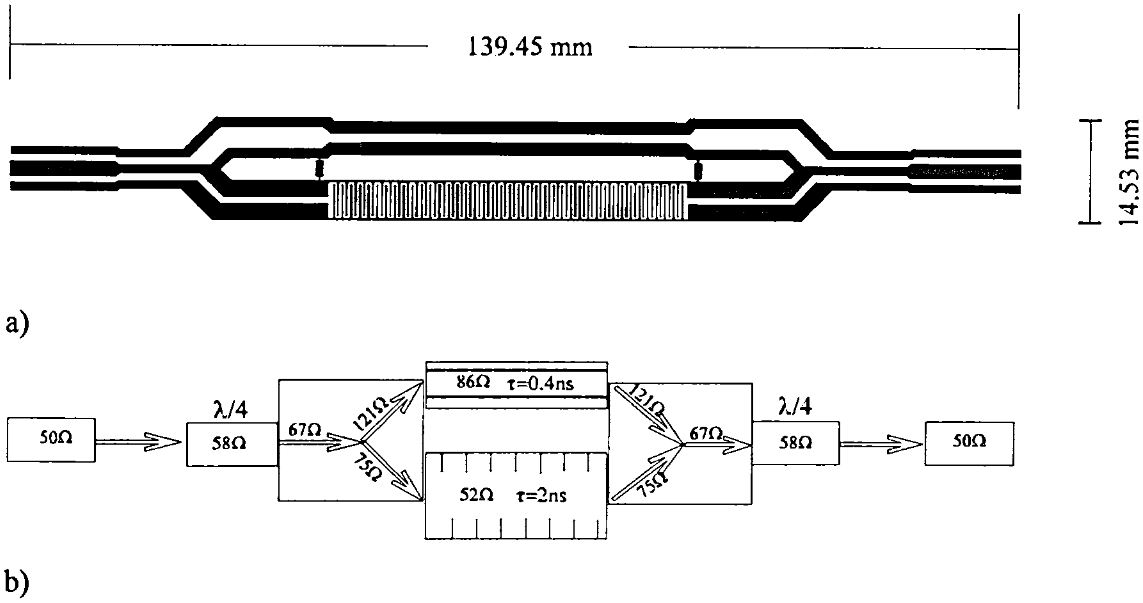

Figure 10.4.1.3 a) Second uniplanar discriminator in a scale of 1/1. b) Impedance block diagram of the second interferometer.

10.4.2 Experimental Results of each Interferometer

The frequency responses in transmission mode were measured for the two interferometers. The theoretical results based on the design equation described in section 9.2 of chapter 9 were also found. Figures 10.4.2.1 and 10.4.2.2 summarise the results. In the experimental procedure SMA connectors were used to link the coplanar wave guides to the coaxial cables. The devices were connected with coaxial connectors to a HP8720A network analyser and the insertion loss responses were then measured.

The theoretical results were obtained using the design equations for a single stage of a typical IFM subsystem described in section 9.2 of chapter 9 in logarithm scale. We used the equation: $\text{output} = 20\log\left\{\cos\left[(2\pi f / 2)\left(n_p / \Delta f\right)\right]\right\}$, where n_p is the number of peaks over a given Δf. The purpose of doing this is just to compare the distribution of peaks over Δf and not the amplitude of the responses. Figure 10.4.2.1 shows the results for the interferometer with a delay difference of 0.4-1ns. Figure 10.4.2.2 shows the results for the interferometer with a delay difference of 0.4-2ns, for the same bandwidth. The design equations gave an output response of nearly two peaks. The additional length that arises when the coplanar wave guide sections are placed before the interferometers makes the total length of the structure increase leading to a shift in the centre frequency. The oscillations found in both of them seem to have originated from the coaxial connections and from the poor bonds of the chip resistors. Thus, the results can be sensibly improved. In figure 10.4.2.2 we see that the frequency difference between the two adjacent points of minimum is 0.5GHz for both theoretical and experimental responses. It is a good sign since for ideal readout frequencies at the output of each interferometer, the detection threshold needs to yield frequency bands of equal width.

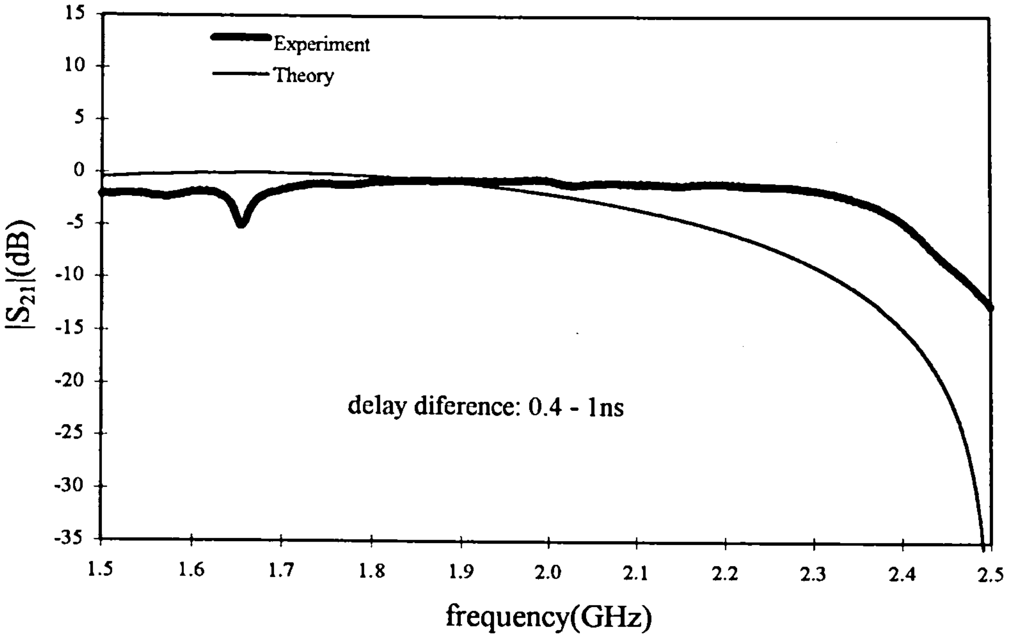

Figure 10.4.2.1 Theoretical and measured results of the device illustrated in figure 10.4.1.2a

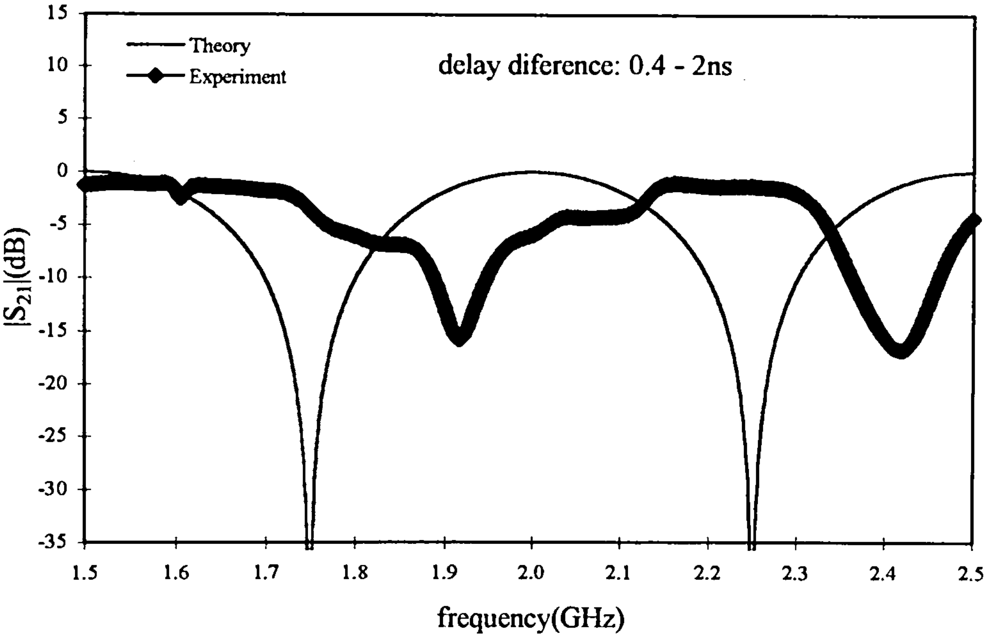

Figure 10.4.2.2 Theoretical and measured results of the device illustrated in figure 10.4.1.3a

10.4.3 IFM System Results

The two interferometers were then connected to the coplanar power splitter described in section 10.3.1 by using SMA connectors and two SMA 90^0 connections, as shown in figure 10.4.3.1. In the procedure a 50 Ω impedance load has always been connected to one output when the other is measured. The output responses in decibels are shown in figures 10.4.3.2 and 10.4.3.3. The modulation, i.e. the difference between maxima and minima of the interference pattern is about 16dB in figure 10.4.3.3. The insertion loss is only 2dB larger than the value of 3dB of the power splitter at the input. This is an improvement over with the coplanar superconducting version published by Biehl et. al [10.4.3.1], which reports an insertion loss of 3dB larger than the value of 6dB of a four-way power splitter. Liang et. al [10.4.3.2] used two-way microstrip Wilkinson power divider and adjustable microstrip to get the wanted delays. This power divider had a return loss of 15dB at 4GHz over $\Delta f = 0.5$GHz. Better analyse could be carried out comparing the results in figures 10.4.3.2 and 10.4.3.3 with a whole microstrip version. However, a typical commercially microstrip IFM usually introduce a large number of phase correlators after the discriminators to increase the resolution of the system where the comparison become somewhat difficult. The manufactures of microstrip IFM generally only supply technical information about: instantaneous bandwidth, minimum pulsewidth, volume etc. A full microstrip version of figure 10.4.3.1 could be performed as a future work.

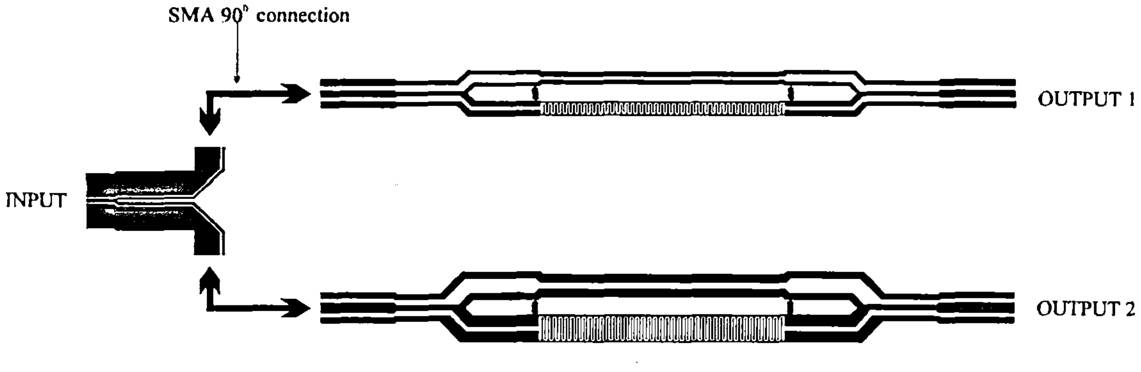

Figure 10.4.3.1 Instantaneous frequency measurement system for two bits readout frequency. The two interferometers are connected to the equal output impedance power splitter described in section 10.2.

The larger the number of coaxial connections the higher the reflections, comparing figure 10.4.3.2 with figure 10.4.2.1 Oscillations confuse the coding process as the signal is converted from analog to a digital code and have to be reduced to a negligible level. The uniplanar integration of the coplanar power splitter with the interferometers is a point of discussion in the section 11.2 of chapter 11.

Figure 10.4.3.3a shows in the same plot the responses of the outputs of the IFM for the coding process. The dashed line represents a chosen threshold detection, which yields frequency bands of about equal widths at the output of each interferometer. Figure10.4.3.3b shows the expected output of the both interferometers after 1 bit A/D conversion. Figure 10.4.3.3b summarise the digital frequency response for the chosen detection.

The results presented so far demonstrate the need to use superconductors in Coplanar Instantaneous Frequency Measurement Subsystem. Compared to copper delay lines, superconducting delay lines offer lower loss, which may increase the difference between the maxima and minima of the interference pattern and may decrease the insertion loss. These features highly improve the threshold detection and in turn, the readout frequency. The particular coplanar interferometers described in this work are very suitable for superconducting application since each interferometer may be fabricated in only one side of the substrate. In addition to this the interferometers were designed so that no airbridges were needed to keep the circuit balanced. The use of airbridges in a superconducting system does not seem to be a good idea, as the bonds may break at very low temperature if they are not performed properly. The interferometers designed in this work used coplanar strips as the principal component of the circuit. Coplanar Strips (see figure 7.3.1 of chapter 7) is a dual structure and may make the whole circuit cost effective since a larger number of interferometers may be performed for a given die size. Thus, at the moment we are designing a superconducting version of these interferometers. In section 11.2 of chapter 11 we will describe the techniques used.

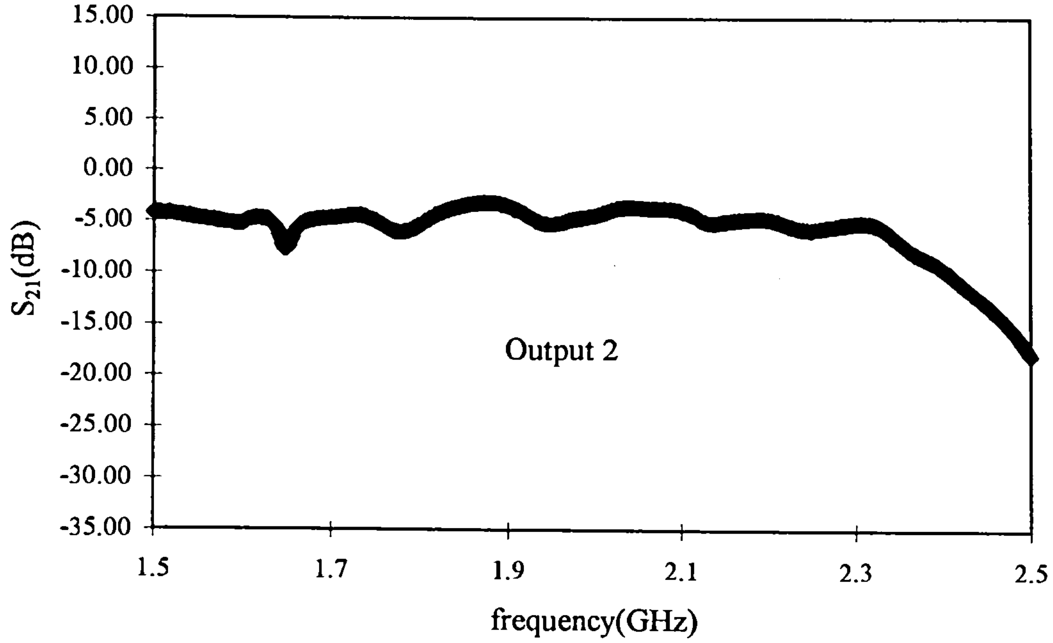

Figure 10.4.3.2 Frequency response from the output 2 of the IFM system

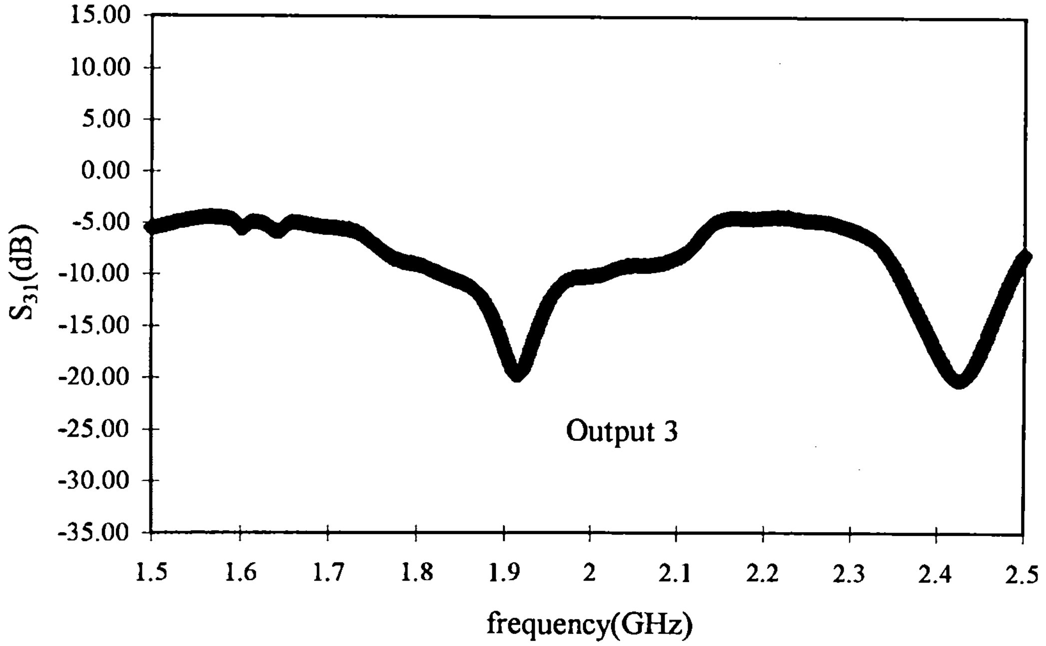

Figure 10.4.3.3 Frequency response from the output 3 of the IFM system.

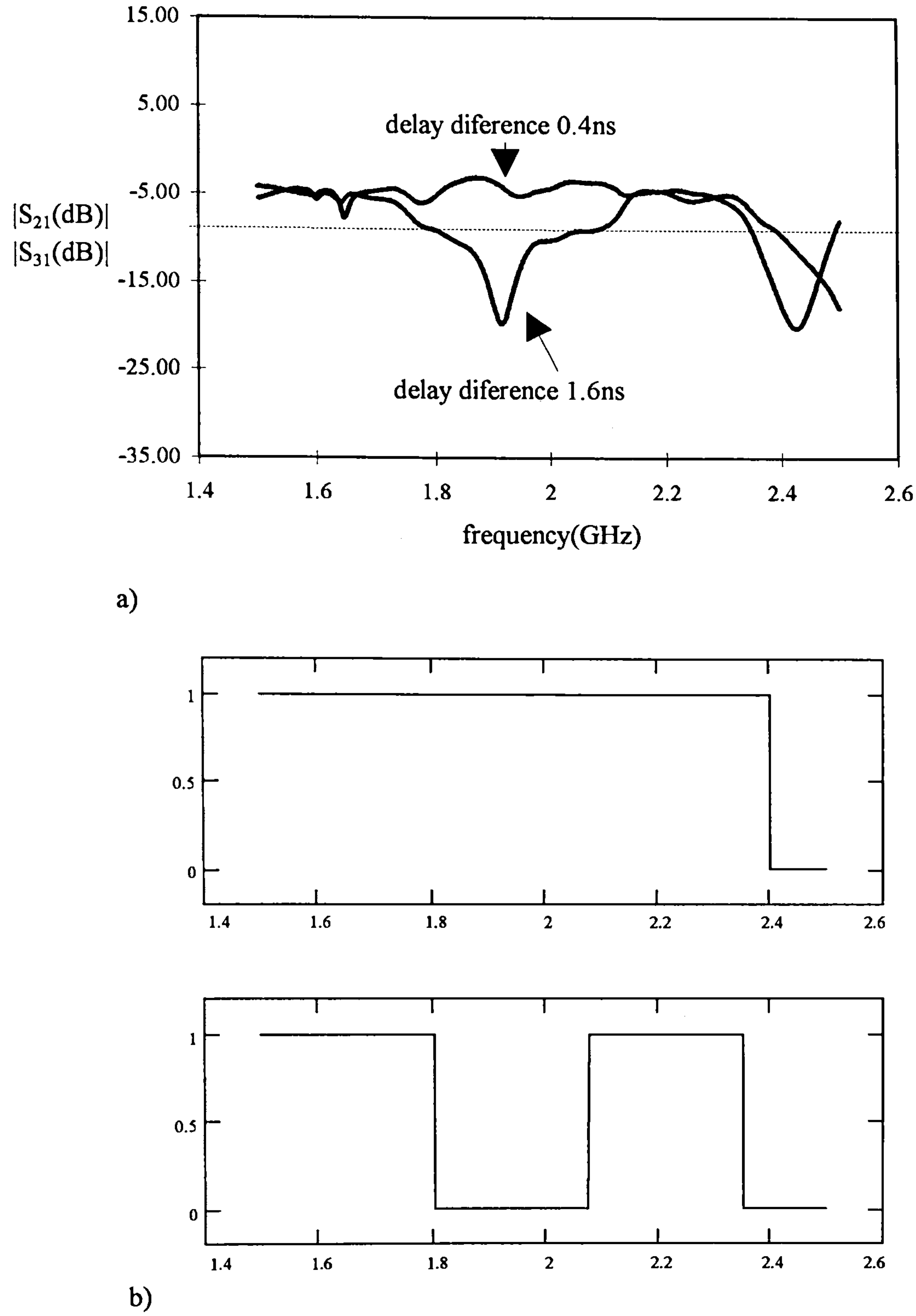

c)

0.6ns	1	1	1	1	1	1	1	1	1	0
1.6ns	1	1	0	0	0	1	1	1	0	0

Figure 10.4.3.4 Experimental result of the 2-bit IFM. a) before threshold detection. b) expected responses after 1 bit A/D conversion. c) expected table of the one step binary code

Chapter 11

Conclusions and Further Work

11.1 Conclusions

The surface impedance of superconducting thin films was derived from the two-fluid model considering local electrodynamics. The quality factor of wide microstrip resonator was then evaluated and checked using the Wheeler incremental inductance rule.

A new expression for unloaded Q_o was developed considering the effect of both the thickness and penetration depth of superconducting thin films, having a penetration depth of the same order as the thickness. This was done by mixing the effective surface impedance concept, the two-fluid model theory and the wide microstrip limit.

A wide microstrip resonator was used to find surface resistance values of YBCO-laser ablated thin films on MgO substrate and YBCO granular films made by dipping pyrolysis on zirconia (YSZ). The resonator response was measured in a transmission mode using a HP8720A network analyser. The best measured laser-ablated thin film had $R_s = 5m\Omega$ at 77K and 7.3GHz and the best thick film made by pyrolysis had $R_s = 9m\Omega$ at 77K and 4.8GHz. From the result it was suggested that the findings of the surface resistance, without taking account the thickness of the film, overestimates the intrinsic surface resistance results. This was about 2.4 times bigger than the results taking the thickness of the film into account.

Propagation of waves on a superconducting wide microstrip were discussed as a function of YBCO thin film thickness considering different substrate thicknesses for double-side deposited superconducting films. It was suggested that, for a given value of λ, a travelling wave on such a line would be slowed down more and more as t_i and h were made smaller and smaller. Moreover the attenuation of the transmission line would be increased leading the unloaded Q to be decreased when it was used in a resonator. This is an important indication in the process of miniaturising microstrip resonators.

Coplanar instantaneous frequency measurement subsystems were investigated as the second part of this work. For the first time a interdigital coplanar line was used as a component of an IFM. Coplanar wave guide, coplanar strips, coplanar unequal output impedance power splitter and coplanar interdigital delay line were integrated without bends or air bridges

Coplanar strips interdigital delay lines were simulated, fabricated and measured at a frequency range of 0.5-3 GHz. The simulation process used Sonnet software in order to find the magnitude and phase of the S-parameters, assuming a lossless conductor. From the phase of S_{21} group delay was then predicted assuming a linear phase change over a step of frequency of 50MHz. Characteristic impedances of the interdigital delays were predicted using the conversion from ABCD matrix to S-parameters.

The experimental results of Z_0 were obtained using a reflection measurement in a time domain low pass mode of the HP8720A network analyser. As the finger length went from 0.6 mm to 4.2 mm, keeping all the other parameters fixed, the group delay increased by about 250% and the characteristic impedance decreased by about 45%. The simulated and experimental results were in good agreement.

A coplanar power splitter was designed, fabricated and measured using coplanar strips as its principal transmission line type. This balanced power splitter had an insertion loss of only 0.2dB plus 3dB splitting loss at a centre frequency of 1.15GHz.

Extending the design of the coplanar power splitter to an unequal output impedance power splitter and on the basis of the results of the group delay and characteristic impedance, it was possible to design the coplanar interferometers. Two interferometers with delay differences of 0.6ns and 1.6ns were designed, fabricated and measured at the central frequency of 2GHz over $\Delta f = 1$GHz. Theoretical and experimental responses were given together and were in good agreement. The frequency difference between two adjacent points of minimum was 0.5GHz for both theoretical and experimental responses. It is a good sign since for ideal readout frequencies at the output of each interferometer, the detection threshold needs to yield frequency bands of equal width.

A two-bit IFM was then set up connecting the two interferometers to the coplanar power splitter. The insertion loss for both outputs were only 2dB larger than the value of 3dB of power splitter at the input. This is an improvement comparing with the superconducting version published by Biehl et. al [10.4.3.1], which reports an insertion loss of 3dB larger than the value of 6dB of a four-way power splitter.

11.2 Further Work

The coplanar interferometers described in this work looks very promising for superconducting coplanar IFM application [11.2.1]. Depending on the desired frequency resolution and the bandwidth, more and more interferometers can be introduced by using the group delay and the characteristic impedance results of the interdigital delays.

The total coplanar integration of the interferometers with the power splitters is not an easy task. Great efforts are being made in this direction. The major problem is connecting the input of each interferometer (CPW) to each arm of the power splitters (CPS) and keep the whole structure balanced. A second option seems to be the use of coplanar wave guide power splitter with finite ground planes at the input of each interferometer, instead of coplanar strip power splitters (see figure 7.4.1). However, because the necessity of using airbridges, as the CPW arms bend, it is not a ideal solution to the problem.

The use of superconducting delay lines in instantaneous frequency measurement system seems to be extremely advantageous, since low loss is required. A superconducting version of an interdigital delay line using a barrier layer of Yttria Stabilised Zirconia (YSZ) between $YBa_2Cu_3O_{7-\delta}$ and alumina (Al_2O_3) substrate is currently been implemented using the technique, described in section 5.5 of chapter 5. The zirconia barrier layer deposition on alumina by plasma spray has been found to be very good even on large substrates.

Two interferometers made by superconducting thin film (YBCO) are also been designed for the bandwidth 1.5 GHz to 3GHz and will soon be fabricated. Initially, they will be fabricated on two separated substrates and eventually on a single 2"-MgO wafer using only one side of the substrate. Reduction of the dimensions of the whole structure seems not to be the biggest challenge since the principal components are based on coplanar strips. Actually the more difficult task remains to integrate the equal power splitters to the interferometers and keep the structure balanced.

Appendix I

Additional Complex Formulation

The objective of this appendix is to derive the real and imaginary parts of coth(a + jb), which was used in chapter 4 to split the effective surface impedance of superconducting thin films into its real an imaginary parts. Let us start from the equation below

$$\coth(a+jb)=\frac{\cosh(a+jb)}{\sinh(a+jb)} \qquad \text{equation Ap. I.1}$$

However

$$\frac{\cosh(a+jb)}{\sinh(a+jb)}=\frac{\left[e^{(a+jb)}+e^{-(a+jb)}\right]/2}{\left[e^{(a+jb)}-e^{-(a+jb)}\right]/2} \qquad \text{equation Ap. I.2}$$

$$\frac{\left[e^{(a+jb)}+e^{-(a+jb)}\right]/2}{\left[e^{(a+jb)}-e^{-(a+jb)}\right]/2}=\frac{\left(e^{a+jb}+e^{-a-jb}\right)}{\left(e^{a+jb}-e^{-a-jb}\right)}\cdot\frac{\left(e^{a-jb}-e^{-a+jb}\right)}{\left(e^{a-jb}-e^{-a+jb}\right)} \qquad \text{equation Ap. I.3}$$

$$\frac{\left(e^{a+jb}+e^{-a-jb}\right)}{\left(e^{a+jb}-e^{-a-jb}\right)}\cdot\frac{\left(e^{a-jb}-e^{-a+jb}\right)}{\left(e^{a-jb}-e^{-a+jb}\right)}=\frac{e^{2a}+e^{-2jb}-e^{2jb}-e^{-2a}}{e^{2a}-e^{-2jb}-e^{2jb}+e^{-2a}} \qquad \text{equation Ap. I.4}$$

$$\frac{e^{2a}+e^{-2jb}-e^{2jb}-e^{-2a}}{e^{2a}-e^{-2jb}-e^{2jb}+e^{-2a}}=\frac{\left(e^{2a}-e^{-2a}\right)-\left(e^{2jb}-e^{-2jb}\right)}{\left(e^{2a}+e^{-2a}\right)-\left(e^{2jb}+e^{-2jb}\right)} \qquad \text{equation Ap. I.5}$$

$$\frac{\left(e^{2a}-e^{-2a}\right)-\left(e^{2jb}-e^{-2jb}\right)}{\left(e^{2a}+e^{-2a}\right)-\left(e^{2jb}+e^{-2jb}\right)}=\frac{\sinh(2a)-\sinh(2jb)}{\cosh(2a)-\cos(2jb)} \qquad \text{equation Ap. I.6}$$

So we find

$$\coth(a+jb)=\frac{\sinh(2a)-\sinh(2jb)}{\cosh(2a)-\cos(2jb)} \qquad \text{equation Ap. I.7}$$

On the other hand

$$\sinh(2jb)=j\sin(2b), \qquad \text{equation Ap. I.8}$$

and

$$\cos(2jb)=\cosh 2b \qquad \text{equation Ap. I.9}$$

Substituting equations Ap. I.8 and Ap. I.9 into eq. Ap. I.7, one gets

$$\coth(a+jb)=\frac{\sinh(2a)-j\sin(2b)}{\cosh(2a)-\cosh(2b)} \qquad \text{equation. Ap. I.10}$$

Separating the previous equation we have

$$R_e\left[\coth(a+jb)\right]=\frac{\sinh(2a)}{\cosh(2a)-\cosh(2b)} \qquad \text{equation Ap. I.11}$$

Or

$$R_e\left[\coth(a+jb)\right]=\frac{2\sinh a.\cosh a}{2\sinh^2 a+1-\left(1-2\sinh^2 b\right)} \qquad \text{equation Ap. I.12}$$

then

$$R_e\left[\coth(a+jb)\right]=\frac{\sinh a.\cosh a}{\sinh^2 a+\sinh^2 b} \qquad \text{equation. Ap. I.13}$$

And

$$\mathrm{I_m}\left[\coth(a + jb)\right] = \frac{-\sin 2b}{\cosh(2a) - \cosh(2b)} \qquad \text{equation Ap. I.14}$$

then

$$\mathrm{I_m}\left[\coth(a + jb)\right] = \frac{-\sin b.\cos b}{\sinh^2 a + \sinh^2 b} \qquad \text{equation Ap. I.15}$$

Appendix II

Effective Propagation Parameters of Superconducting Wide Microstrip

For many reasons which have already been discussed, the hybrid copper/superconducting resonator device produces low Q_o values. One of the factors responsible for this is the term R_{sc} in the equation 4.3.7, which represents the surface resistance of the copper ground plate.

The principal goals of this appendix are briefly to introduce a superconducting microstrip device made totally of superconductor rather than the Cu/HTS hybrid (see figure II.1) and to apply the effective surface impedance concepts to evaluate some parameters of microwave propagation. This way, both the effective surface resistance and the effective inductance concepts will be used to investigate the influence of film thickness on wave propagation in a superconducting transmission line. Phase velocity, attenuation coefficient and quality factor will be plotted as a function of thin film thickness.

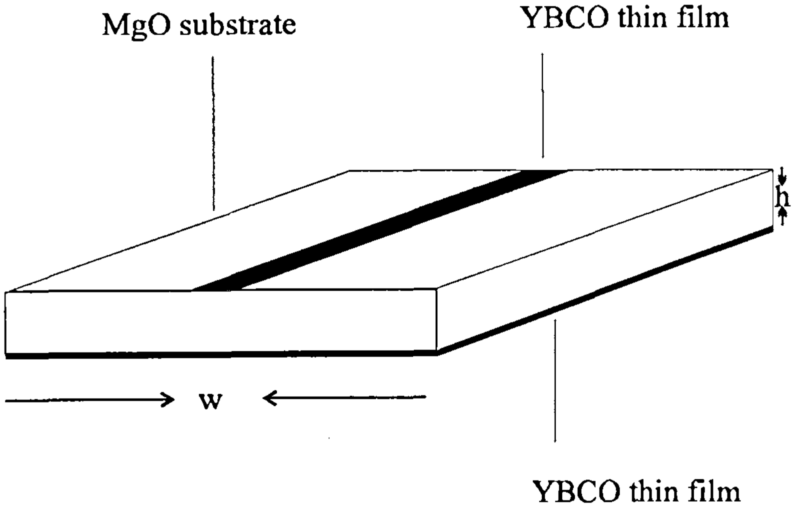

Figure II.1 Sketch of the all superconducting wide microstrip.

Phase velocity for a superconducting wide microstrip is given by

$$v = \frac{1}{\sqrt{LC}} = \sqrt{\frac{1}{(L + L_w)(C)}} \qquad \text{equation Ap.II.1}$$

Assuming again a pure TEM mode, local electrodynamics and frequency in the range of $\omega^2\tau^2 << 1$, and substituting equation 3.2.7, equation 4.3.2 and equation 3.2.3 into the previous equation one obtains

$$v = \sqrt{\frac{1}{\left\{\frac{\mu_o h}{w} + \frac{2}{w}\left[\frac{\mu\lambda\omega \coth(t_i / \lambda)}{\omega}\right]\right\}\frac{\varepsilon_o w \varepsilon_r}{h}}} \qquad \text{equation Ap.II.2}$$

Here we assumed that the filling factor of the dielectric was $q = 1$. As a result, the effective permittivity $\varepsilon_{eff} = \varepsilon_r$ and ε_r is the relative permittivity of the substrate.

Rewriting the above expression we have

$$v = \frac{c_o.(\varepsilon_r)^{-1/2}}{\left[1 + (2\lambda / h)\coth(t_i / \lambda)\right]^{1/2}} \qquad \text{equation Ap.II.3}$$

Here c_o is the light velocity in free space which is given by $c_o = (\mu_o\varepsilon_o)^{-1/2}$. Assume the following data as an example: $c_o = 3.10^8$m/s, relative permittivity of MgO, $\varepsilon_r = 9.6$ and penetration depth at 77K, $\lambda \cong 296$ nm. One can use equation Ap. II.3 and plot 'v' as a function of the thickness of thin film, as shown in figure Ap.II.2.

For all curves one can see that phase velocity is less than c_o, in free space [Ap. II.1] . This is due to two reasons: a dielectric slowing factor is proportional to $\varepsilon_r^{1/2}$, and when L_w increases with respect to L.

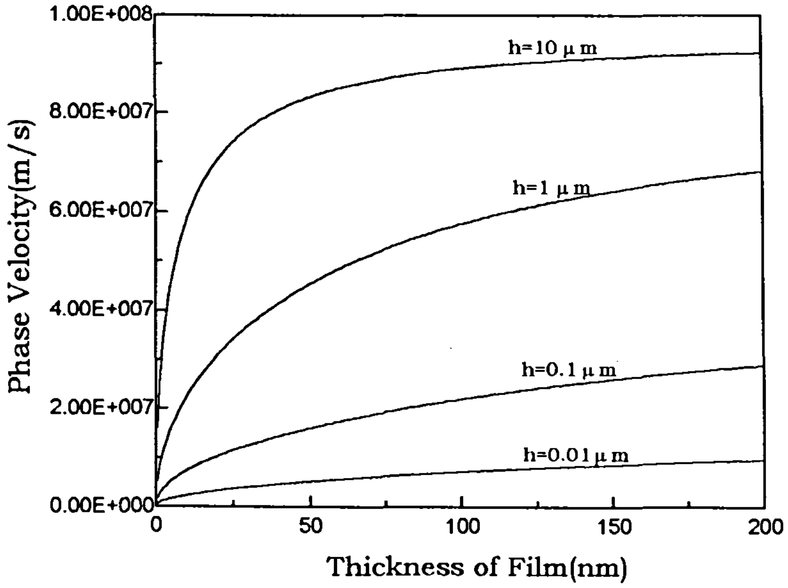

Figure Ap.II.2 Phase velocity (in m/s) as a function of the thickness of the thin film for four different substrate thicknesses (h).

In addition to this, one can see that the phase velocity decreases when both the film thickness and the dielectric thickness decrease. This occurs due to their relations with the penetration depth λ given by λ/h and $\coth(t_i/\lambda)$ in the denominator of equation Ap.II.3. This gives the change in L_w.

Thus, the shapes of the curves are strictly related to the penetration depth and then to the process of attenuation along of this transmission line.

In the case of $\lambda \rightarrow 0$, when both the temperature and the frequency are sufficiently low, the propagation constant γ is purely imaginary indicating no attenuation.

An approximate expression for the case of low losses is given by [Ap.II.2].

$$\alpha_S = \frac{R_{series}}{2\sqrt{\frac{L+L_W}{C}}} \qquad \text{equation Ap.II.4}$$

For the structure in figure II.1 equation 4.3.5 Assuming $R_{ss} = R_{sc}$ in equation 4.3.5 we have

$$R_{series} = \frac{2R_{ss}}{w}\left\{\coth(t_i/\lambda) + \left[\frac{t_i/\lambda}{\sinh^2(t_i/\lambda)}\right]\right\} \qquad \text{equation Ap.II.5}$$

Substituting equation 3.2.7, equation 4.3.2, equation 3.2.3, and equation Ap.II.5 into equation Ap.II.4 one obtains

$$\alpha_s = \frac{\frac{2R_{ss}}{2w}\left[\coth(t_i/\lambda) + \frac{t_i/\lambda}{\sinh^2(t_i/\lambda)}\right]\cdot\sqrt{\frac{\varepsilon_r\varepsilon_o}{\mu_o}}\cdot\left(\frac{w}{h}\right)}{\sqrt{(2\lambda/h)\coth(t_i/\lambda)+1}} \qquad \text{equation Ap.II.6}$$

or

$$\alpha_s = \frac{R_{ss}\left[\coth(t_i/\lambda) + \frac{t_i/\lambda}{\sinh^2(t_i/\lambda)}\right]\cdot\sqrt{\frac{\varepsilon_r\varepsilon_o}{\mu_o}}}{h\sqrt{(2\lambda/h)\coth(t_i/\lambda)+1}} \qquad \text{equation Ap.II.7}$$

In terms of phase velocity one gets

$$\alpha_s = \frac{R_{ss}v\sqrt{\varepsilon_r\varepsilon_o/\mu_o}}{hc_o}\cdot\left[\coth\left(\frac{t_i}{\lambda}\right) + \frac{t_i/\lambda}{\sinh^2(t_i/\lambda)}\right] \qquad \text{equation Ap.II.8}$$

To summarise, at frequency in the range of $\omega^2\tau^2 << 1$ and temperature such as $\sigma_1 << \sigma_2$ (see section 2.3.3), the attenuation coefficient α_s for an all superconducting wide microstrip of any thickness is given by

$$\alpha_s = \frac{R_{ss}\left[\coth\left(\frac{t_i}{\lambda}\right) + \frac{t_i/\lambda(t_i)}{\sinh^2(t_i/\lambda)}\right]\cdot\sqrt{\frac{\varepsilon_r\varepsilon_o}{\mu_o}}}{h.\sqrt{\frac{2\lambda}{h}\coth(t_i/\lambda)+1}} \qquad \text{equation Ap.II.9}$$

Where from section 2.2

$$R_{ss} = \omega\mu_o\frac{\lambda^3}{\delta^2} \quad \text{and} \quad \delta = \left(\frac{2}{\mu\omega\sigma_n}\right)^{1/2}$$

Then

$$R_{ss} = \frac{\omega^2\sigma_n\mu_o{}^2\lambda^3}{2} \qquad \text{equation Ap.II.10}$$

Substituting the previous equation into equation Ap.II.9, one has a final expression for α_s,

$$\alpha_s = \frac{(\varepsilon_r)^{1/2}\,\omega^2\sigma_n\mu_o\lambda^3\left\{\coth\left[\frac{t_i}{\lambda}\right] + \frac{t_i/\lambda}{\sinh^2[t_i/\lambda]}\right\}}{2c_o\sqrt{2\lambda h\coth[t_i/\lambda]+h^2}} \qquad \text{equation Ap.II.11}$$

Note that α_s depends on the operating frequency, penetration depth, the relative permittivity of the dielectric spacer, the conductivity of the normal charges and both the thin film and the dielectric thicknesses. In the process of miniaturising microstrip lines the variation of α_s with respect to both the dielectric and the YBCO thin film thicknesses are two points of fundamental interest. To determine σ_n, it is necessary to set up the experiment and find the R_{ss} value for these parameters. In order to plot our expression we shall assume a typical value of $R_{ss} \cong 10^{-4}\Omega$ at 7.3GHz and 77K. Thus, from equation Ap.II.10 one obtains $\sigma_n \cong 2.3\times10^6$ ($\Omega^{-1}m^{-1}$).

Assuming the same parameters of figure Ap.II.2 and $\omega = 2\pi\times7.3\times10^9$Hz, figure Ap.II.3 plots α_s as a function of the film thickness.

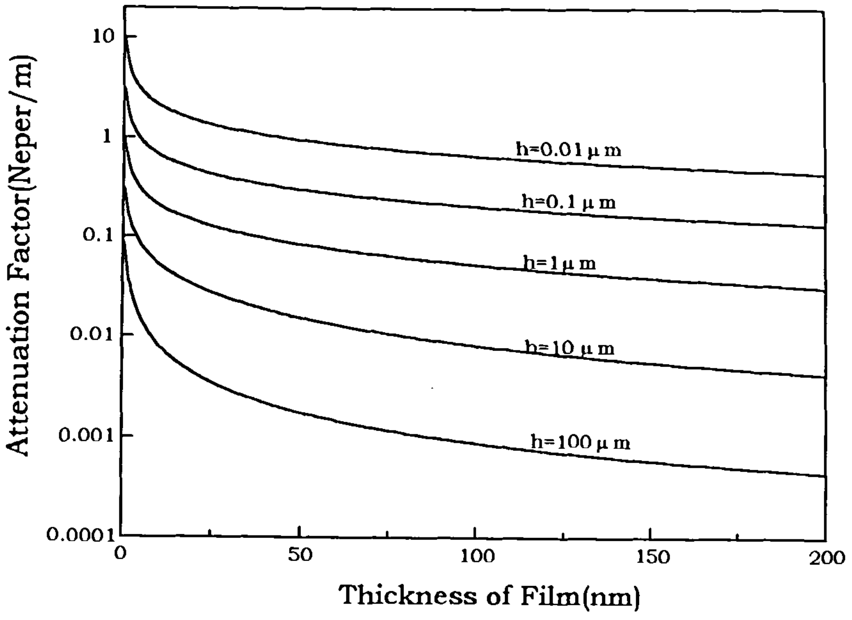

Figure Ap.II.3 α_s as a function of the thin film thickness for four different substrate thicknesses: 100μm, 10μm, 1μm, 0.1μm, and 0.01μm.

From figure Ap.II.3 one can see that the loss increases as both t_i and h decrease. Keeping the thickness of the film fixed, one can see that the lowest level of loss is on the highest substrate thickness curve (h=100μm). This certainly comes about because the fields are propagating basically through the dielectric and just a relative small amount of them penetrates into the superconducting surface.

The top curve (h=0.01μm) represents the opposite situation, where a considerable amount of field propagates into the superconducting surface producing the lowest level of phase velocity (see figure Ap.II.2). In addition, for all curves (in figure Ap.II.3) one can be seen that the loss increases as the thickness of film decreases, being much more prominent as ti << λ.

It is now necessary to find an expression for the quality factor due to the conduction losses for a half-wave open-end microstrip resonator as w >> h.

For a line of length ℓ, the resonant frequencies f_n are found from the condition that

$$\frac{2\ell}{\lambda_n} = n \quad \text{(n an integer)} \qquad \text{equation Ap.II.12}$$

Where

$$\lambda_n = \frac{c}{f_n\sqrt{\varepsilon_r}} \qquad \text{equation Ap.II.13}$$

Here ε_r is the relative dielectric constant of the inserted substrate and c is the speed of the light in free space. The unload quality factor Q_o of this resonator can be found as follows [Ap.II.3].

$$Q_o = \frac{\pi}{2\alpha\ell} \qquad \text{equation Ap.II.14}$$

Taking the first resonant mode (n = 1) and substituting ℓ from the equation Ap.II.12 into the equation Ap.II.14 one gets

$$Q_o = \frac{\pi}{\lambda_1\alpha} \qquad \text{equation Ap.II.15}$$

Substituting equation Ap.II.13 and equation Ap.II.11 into equation Ap.II.15 one finds

$$Q_o = \frac{\sqrt{h^2 + 2\lambda h \coth[t_i/\lambda]}}{\omega\sigma\mu\lambda^3\left\{\coth[t_i/\lambda] + \frac{t_i/\lambda}{\sinh^2[t_i/\lambda]}\right\}} \qquad \text{equation Ap.II.16}$$

Assuming the same parameters again, Q_o as a function of t_i is plotted in figure II.4 for five different substrate thicknesses. Figure Ap.II.4 suggests that Q_o increases as both t_i and h increase.

To sum up, for a given value of λ of the order of t_i, a travelling wave on such a line will be slowed down more and more as t_i and h are made smaller and smaller. Moreover the attenuation of the transmission line will be increased leading the unload Q to be decreased.

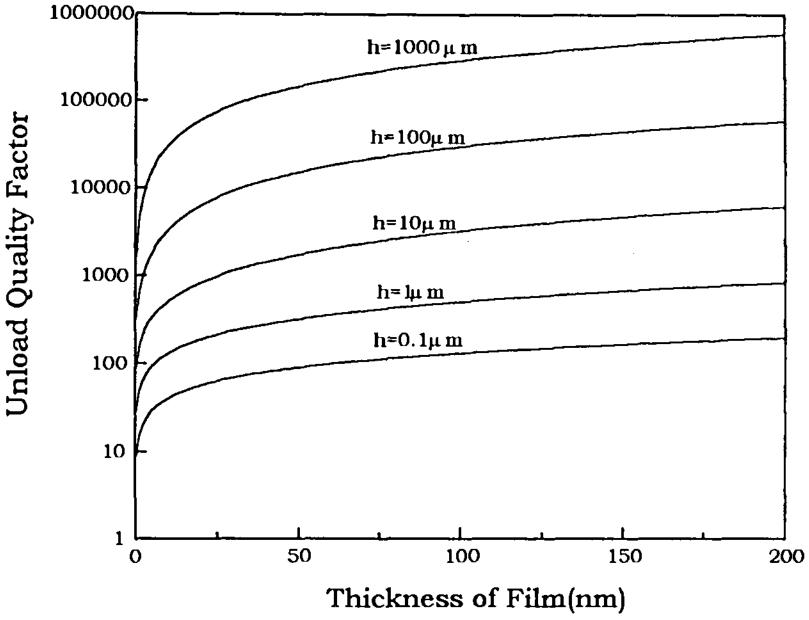

Figure Ap.II.4 Unloaded Q_o as a function of t_i for five different substrate thicknesses: 0.1μm, 1μm, 10μm, 100μm and 1000μm.

Appendix III

Mathcad Programs

The aim of this appendix is to present the principal Mathcad programs used along this thesis. Most equations used herein were formulated and discussed previously.

Ap. III.1Coplanar Wave Guide

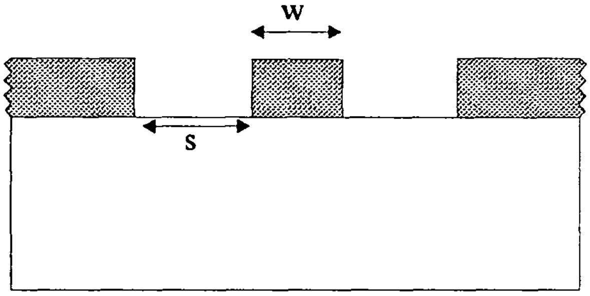

$s := 0.3\cdot10^{-3}, 0.6\cdot10^{-3} .. 100\cdot10^{-3}$	Line spacing range
$w := 1.4\cdot10^{-3}$	Strip width
$\varepsilon r := 10.8$	Relative permittivity
$b(s) := w + 2\cdot s$	See section 6.2
$k(s) := \frac{w}{b(s)}$	Heliptical function parameters
$k1(s) := \sqrt{1 - k(s)^2}$	

ELIPTICAL FUNCTION

$$M(s) := \begin{cases} \pi\cdot\dfrac{1}{\ln\left(2\cdot\dfrac{1+\sqrt{k1(s)}}{1-\sqrt{k1(s)}}\right)} & \text{if } 0.0\le k(s)\le 0.7 \\ \dfrac{1}{\pi}\cdot\ln\left(2\cdot\dfrac{1+\sqrt{k(s)}}{1-\sqrt{k(s)}}\right) & \end{cases}$$

Here, M(s)=K(k)/K'(k), see section 6.2

$\varepsilon\mathrm{eff}(\varepsilon r) := \frac{\varepsilon r+1}{2}$ Effective Permittivity

$Z0(s,\varepsilon r) := \frac{30\cdot\pi}{\sqrt{\varepsilon\mathrm{eff}(\varepsilon r)}}\cdot\frac{1}{M(s)}$ Characteristic impedance

GENERATING THE MATRIX OF THE DATA

$i := 1..98$

$s_i := (0.3+(i-1)\cdot 0.1)\cdot 10^{-3}$

$M_{i,1} := k(s_i)$ $M_{i,2} := Z0(s_i,1)$ $M_{i,3} := Z0(s_i,3)$ $M_{i,4} := Z0(s_i,6)$ $M_{i,5} := Z0(s_i,10)$

$M_{i,6} := Z0(s_i,20)$ $M_{i,7} := Z0(s_i,40)$ $M_{i,8} := Z0(s_i,120)$

WRITEPRN(cpw) := M Writing the matrix to a PRN data file

Ap. III.2 Coplanar Strips

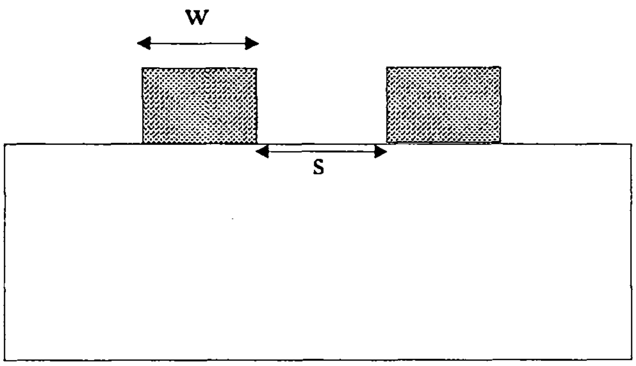

$s := 0.01\cdot 10^{-3}, 0.02\cdot 10^{-3} .. 6.5\cdot 10^{-3}$ Line spacing range

$w := 1.4\cdot 10^{-3}$ Strip width

$\varepsilon r := 10.8$ Relative permittivity

$b(s) := s + 2\cdot w$ Lateral dimension

$k(s) := \frac{s}{b(s)}$ eliptical function parameters

$k1(s) := \sqrt{1-k(s)^2}$

ELIPTICAL FUNCTION

$$M(s) := \left| \begin{array}{l} \pi \cdot \dfrac{1}{\ln\left(2 \cdot \dfrac{1+\sqrt{k1(s)}}{1-\sqrt{k1(s)}}\right)} \quad \text{if } 0.0 \le k(s) \le 0.7 \\ \dfrac{1}{\pi} \cdot \ln\left(2 \cdot \dfrac{1+\sqrt{k(s)}}{1-\sqrt{k(s)}}\right) \end{array} \right.$$

Here, M(s)=K(k)/K'(k), see section 6.2

$$\varepsilon\mathrm{eff}(\varepsilon r) := \left(\frac{\varepsilon r + 1}{2}\right)$$

Effective Permittivity

$$Z0(s, \varepsilon r) := \frac{120\pi}{\sqrt{\varepsilon\mathrm{eff}(\varepsilon r)}} \cdot M(s)$$

Characteristic impedance

GENERATING THE MATRIX OF THE DATA

$i := 1..98$

$s_i := (0.3 + (i-1) \cdot 0.1) \cdot 10^{-3}$

$M_{i,1} := k(s_i)$ $M_{i,2} := Z0(s_i, 1)$ $M_{i,3} := Z0(s_i, 3)$ $M_{i,4} := Z0(s_i, 6)$ $M_{i,5} := Z0(s_i, 10)$

$M_{i,6} := Z0(s_i, 20)$ $M_{i,7} := Z0(s_i, 40)$ $M_{i,8} := Z0(s_i, 120)$

$\mathrm{WRITEPRN}(cps) := M$

Writing the matrix to a PRN data file

Ap. III.3 Insertion Loss and Return Loss of a Lossless Transmission Line Mismatched to both Source and Load

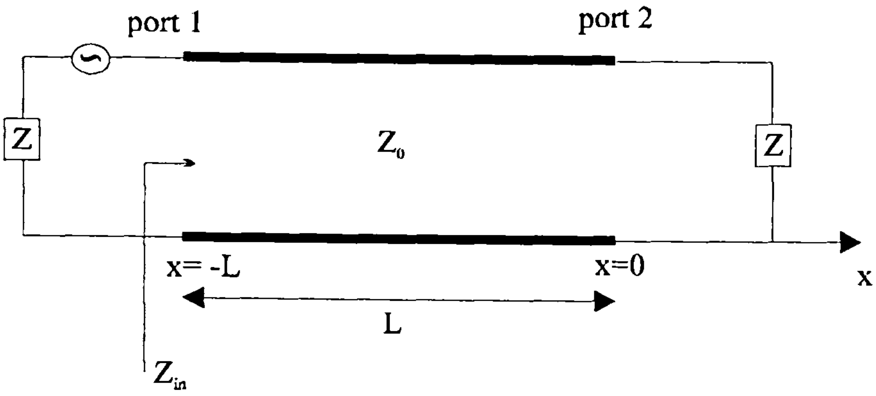

$j := \sqrt{-1}$

$Z := 50$	Source and load impedances
$f := 0.5\cdot 10^9, 0.55\cdot 10^9 .. 20\cdot 10^9$	Frequency Range
$Z0 := 99$	Characteristic impedance of the transmission line
$L := 99\cdot 10^{-3}$	Length of the transmission line
$\varepsilon\mathrm{eff} := 5.9$	Effective Dielectric Constant
$\Gamma(f) := j\cdot\frac{2\cdot\pi\cdot f}{3\cdot 10^8}\cdot\sqrt{\varepsilon\mathrm{eff}}$	j ω divided by Phase velocity

S-PARAMETERS AS A FUNCTION OF FREQUENCY

$$S11(f,Z0) := \frac{Z0\cdot\frac{(Z + Z0\cdot\tanh(\Gamma(f)\cdot L))}{Z0 + Z\cdot\tanh(\Gamma(f)\cdot L)} - Z}{Z0\cdot\frac{(Z + Z0\cdot\tanh(\Gamma(f)\cdot L))}{Z0 + Z\cdot\tanh(\Gamma(f)\cdot L)} + Z}$$

$$S12(f) := \sqrt{1 - (|S11(f)|)^2}$$

GENERATING THE MATRIX OF THE DATA

$i := 1,2 .. 391$

$f_i := (10^9)\cdot(0.5 + (i - 1)\cdot 0.05)$

$M_{i,1} := f_i$

$M_{i,2} := 20\cdot\log(|S12(f_i)|)$

$M_{i,3} := 20\cdot\log\left(\left|S11\left(f_i\right)\right|\right)$

$\mathrm{WRITEPRN}(aj) := M$ Writing the matrix to a PRN data file

Ap. III.4 Characteristic Impedance from S-Parameter

$Z := 50$ Load and source impedances are equals to 50 ohms

$i := 1..51$ Matrix from simulation

$j := 1..8$

$M := \mathrm{READPRN}(d0)$ d0 is the Mathcad variable

TAKING THE DATA FROM MATRIX, PHASE HAS TO BE IN RADIANS

$$f_i := M_{i,1} \quad S11_i := M_{i,2} \quad S12_i := M_{i,4} \quad S21_i := M_{i,6} \quad S22_i := M_{i,8}$$

$$\Phi 11_i := M_{i,3} \quad \Phi 12_i := M_{i,5} \quad \Phi 21_i := M_{i,7} \quad \Phi 22_i := M_{i,9}$$

Conversion from ABCD to S-parameter

$$B_i := \frac{Z\cdot\left[\left(1+S11_i\cdot e^{i\cdot\Phi 11_i}\right)\cdot\left(1+S22_i\cdot e^{i\cdot\Phi 22_i}\right)-S12_i\cdot e^{i\cdot\Phi 12_i}\cdot\left(S21_i\cdot e^{i\cdot\Phi 21_i}\right)\right]}{2\cdot\left(S21_i\cdot e^{i\cdot\Phi 21_i}\right)}$$

$$C_i := \frac{\frac{1}{Z}\cdot\left[\left(1-S11_i\cdot e^{i\cdot\Phi 11_i}\right)\cdot\left(1-S22_i\cdot e^{i\cdot\Phi 22_i}\right)-S12_i\cdot e^{i\cdot\Phi 12_i}\cdot\left(S21_i\cdot e^{i\cdot\Phi 21_i}\right)\right]}{2\cdot\left(S21_i\cdot e^{i\cdot\Phi 21_i}\right)}$$

CHARACTERISTIC IMPEDANCE (Ω) ACCORDING TO EQUATION 7.4.3 OF CHAPTER 7

$$Z0_i := \sqrt{\frac{B_i}{C_i}}$$

$\mathrm{WRITEPRN}(z) := Z0_i$ Writing the prn file

Ap. III.5 Coplanar Power Splitter

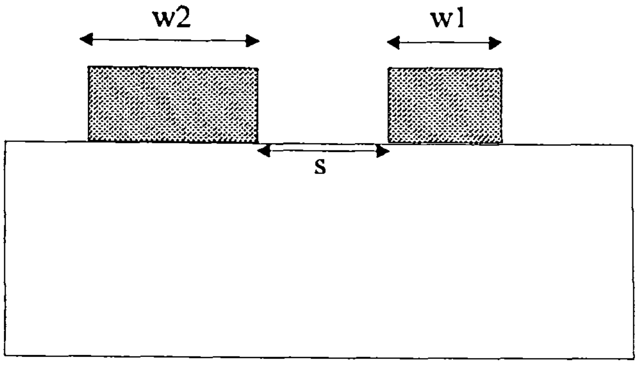

$w2 := 0.5 \cdot 10^{-3}$	Strip width 2
$w1 := 5 \cdot 10^{-3}$	Strip width1
$s := 0.3 \cdot 10^{-3}$	Line spacing
$\mu o := 4 \cdot \pi \cdot 10^{-7}$	Permeability of free space
$h := 64 \cdot 10^{-5}$	Substrate Thickness
$\varepsilon o := 8.85 \cdot 10^{-12}$	Permittivity of free space
$\varepsilon r := 10.8$	Relative permittivity
$co := 3 \cdot 10^{8}$	Velocity of light in free space
$\eta o := 377$	$(\mu_0/\varepsilon_0)^{-1/2}$

CHARACTERISTIC IMPEDANCE CALCULATION [APIII.5.1]

$b := w2 + s \qquad d := w1 + s$

$$k := \sqrt{\frac{s}{b} \cdot \left(1 + \frac{b}{d} - \frac{s}{d}\right)}$$

$$kL := \sqrt{1 - k^2} \qquad \lambda 1 := \frac{\pi}{2} \cdot \left(\frac{2 \cdot w2}{h} + \frac{s}{h}\right)$$

$$t1 := \frac{e^{\lambda 1} - 1}{e^{\lambda 1} + 1} \qquad \lambda 2 := \frac{\pi \cdot s}{2 \cdot h}$$

$$t2 := \frac{e^{\lambda 2} - 1}{e^{\lambda 2} + 1} \qquad \lambda 3 := \frac{\pi}{2} \cdot \left(\frac{2 \cdot w1}{h} + \frac{s}{h}\right)$$

$$t3 := \frac{e^{\lambda 3} - 1}{e^{\lambda 3} + 1}$$

$$k1 := \sqrt{\frac{(t1 - t2)\cdot(t3 - t2)}{(t1 + t2)\cdot(t3 + t2)}}$$

$$k1L := \sqrt{1 - kL^2}$$

ELIPTICAL FUNCTIONS [APIII.5.2]

$$M1 := \left| \begin{array}{l} \pi \cdot \dfrac{1}{\ln\left(2 \cdot \dfrac{1 + \sqrt{kL}}{1 - \sqrt{kL}}\right)} \quad \text{if } 0.0 \le k \le 0.7 \\ \dfrac{1}{\pi} \cdot \ln\left(2 \cdot \dfrac{1 + \sqrt{k}}{1 - \sqrt{k}}\right) \end{array} \right.$$

$$M2 := \left| \begin{array}{l} \pi \cdot \dfrac{1}{\ln\left(2 \cdot \dfrac{1 + \sqrt{k1L}}{1 - \sqrt{k1L}}\right)} \quad \text{if } 0.0 \le kL \le 0.7 \\ \dfrac{1}{\pi} \cdot \ln\left(2 \cdot \dfrac{1 + \sqrt{kL}}{1 - \sqrt{kL}}\right) \end{array} \right.$$

$$\varepsilon eff := 1 + \frac{(\varepsilon r - 1)}{2} \cdot M1 \cdot M2$$ Effective Permittivity

$$Z0 := \frac{\eta o}{2 \cdot \sqrt{\varepsilon eff}} \cdot M1$$ Impedance- in Ohms

$$Z0 = 71.4504$$

QUARTER WAVE TRANSFORMER CALCULATION

$$vp := \frac{co}{\sqrt{\varepsilon eff}}$$ Phase Velocity

$$\lambda := \frac{vp}{f}$$ Wave Length

$$f := 1.5 \cdot 10^9$$ Central Frequency

$$\frac{\lambda}{4} = 0.02058$$ Quarter wave length

Ap. III.6 Unequal Output Impedance Power Splitter For IFM Discriminators based on Design Equations Section 8.4.1 of Chapter 8.

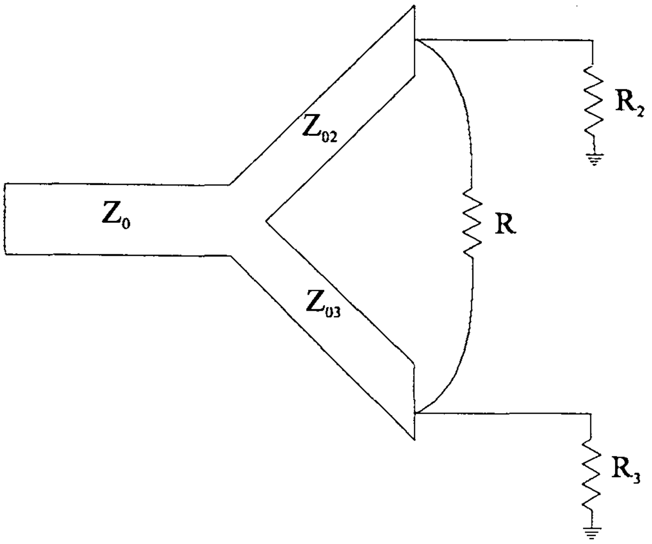

Even though this is a symmetric situation, this program only refers to the power splitters of the left hand side of the interferometer.

$c := 3 \cdot 10^8$	Light velocity of free space(m/s)
$\varepsilon r := 10.8$	Dielectric constant
$f := 2 \cdot 10^9$	Central frequency(Hz)

INPUTING MATRIX OF THE CHARACTERISTIC IMPEDANCES OF THE DELAYS TO BE CONNECTED TO THE OUTPUT OF THE POWER SPITTERS

$i := 1..2$ number of discriminators

$$M := \begin{pmatrix} 86 & 62 \\ 86 & 52 \end{pmatrix}$$

$Z2_i := M_{i,1}$	Output impedance of arm 2
$Z3_i := M_{i,2}$	Output impedance of arm 3

ISOLATION RESISTORS

$$k_i := \sqrt{\frac{Z2_i}{Z3_i}}$$

$$R_i := Z0_i \cdot \left[\frac{1 + (k_i)^2}{k_i}\right]$$

QUARTER WAVE TRANSFORM ARMS IMPEDANCES

$$Z02_i := Z0_i \cdot \sqrt{k_i \cdot \left[1 + (k_i)^2\right]}$$ Arm2 characteristic impedance

$$Z03_i := Z0_i \cdot \sqrt{\frac{1 + (k_i)^2}{(k_i)^3}}$$ Arm3 characteristic impedance

CPW QUARTER WAVE TRANFORMER CONNECTING A 50Ω LINE TO THE INPUT OF THE POWER SPLITTER.

CPW QUARTER WAVE LENGTH

$$\varepsilon ff := \frac{\varepsilon r + 1}{2}$$ Effective dielectric constant, see section 6.2 of

chapter 6

$$\lambda := \frac{c}{\sqrt{\varepsilon ff}} \cdot \frac{1}{f}$$ Wave length

$$\frac{\lambda}{4} = 0.015$$ Quarter wave length

IMPEDANCE OF THE QUARTER WAVE TRANSFORMER

$$Z_i := \sqrt{50 Z0_i}$$ (MKS UNIT SYSTEM)

SUMMARY

Power splitter

R_i	$Z02_i$	$Z03_i$	$Z0_i$
148	122.435	88.267	73.021
138	123.541	74.699	66.873

Quarter wave transformer

Z_i
60.424
57.824

$$\frac{\lambda}{4} = 0.015$$

Published in the proceedings of 1995 SBMO/MTT-S International Microwave Optoelectronics
Coference, P019, july, Rio De Janeiro, Brazil

High Temperature Superconducting Microstrip Resonators for the Measurement of Films Made by Pyrolysis

M.T. De Melo, M. J. Lancaster, H. Yokota and C. E. Gough

Superconducting Research Group, The University of Birmingham, Edgbaston, Birmingham, B15 2TT, U.K.

Abstract - Microwave surface impedance measurements are reported for textured granular YBCO films made by a novel spray pyrolysis method on the surface of a YSZ substrate. A parallel plate resonator was formed by placing the film and substrate on top of a copper ground plane. Microwave measurements were made at nitrogen temperatures on the fundamental mode at ~ 4.7GHz. A model has been developed to extract the penetration depth and impedance of the finite thickness granular film. We obtain values for penetration depth $\lambda_g \sim 3.6\mu m$ and, using independent measurements of the critical current and grain size, a surface resistance $R_g \sim 13 m\Omega$.

1. Introduction

Microstrip resonators offer a good compromise between achievable Q values and ease of manufacture. The fact that there is no direct electrical contact between the film and the transmission line and also that the losses are basically concentrated in the two parallel conducting plates makes such resonators suitable for physical characterisation of HTSC films. Only one-sided deposition makes them inexpensive devices. Most practical high-T_c superconducting films have a penetration depth of the order of the film thickness. In such structures, there are considerable differences between the effective surface impedance and the intrinsic surface impedance [1]. Taking these differences into account we present an expression for the unloaded Q of the resonator based on the two-fluid model and standard transmission line theory. This enables us to obtain the intrinsic surface resistance of the YBCO films.

2. Theory

In order to calculate the effective surface impedance of a film of thickness t consider a plane wave propagating in the z direction into the upper plate, shown in fig.1. For simplicity, consider a lossless dielectric between plates of a wide microstrip (w>>h). Since the magnetic field can penetrate into a superconductor, giving an electrical field is induced in the x-direction perturbing the electric field between plates and then given rise to a TM mode [p.132 of the reference 2]. The ratio of the magnitude of the electric field $E_x(z=0)$ to that of the magnetic field $H_y(z=0)$ at the surface gives the effective surface impedance Z_{eff}.

This also can be treated as a short length of transmission line, which is a convenient method for taking into account the thickness of the conducting strip. First, let us consider the top plate in fig.1.

Standard impedance theory transforms the load impedance Z_o (impedance of the free space) to a new impedance Z_{eff} (effective impedance) per unit length, given by

$$Z_{eff} = \left(\frac{Z_{SS}}{w}\right)\frac{Z_o + Z_{SS}\tanh(\gamma\, t)}{Z_{SS} + Z_o\tanh(\gamma\, t)} \quad (1),$$

where the intrinsic impedance of the film is $Z_{ss}= (j\omega\mu_o/\sigma)^{1/2}$, the complex propagation constant $\gamma= (j\omega\mu_o\sigma)^{1/2}$. t is the thickness of the film and $Z_o = (\mu_o/\varepsilon_o)^{1/2}$. σ is the complex conductivity defined from the Gorter and Casimir two-fluid model for the superconductor. At microwave frequencies $\sigma \gg \omega\varepsilon_o$, so we get

$$Z_{eff} = \left(\frac{1}{w}\right)\left(\frac{j\omega\mu_o}{\sigma}\right)^{1/2} \cdot \coth\left[\left(j\omega\mu_o\sigma\right)^{1/2} t\right] \quad (2),$$

This expression holds true for both normal conductors and superconductors.

Assuming the displacement current is negligibly small, R. E. Matick [p.242 of reference 3] derives the above expression by using Maxwell's equations, the two-fluid model, London's equation and appropriate boundary conditions. Z. Y. Shen showed that equation 2 is correct for wide superconducting strips with thickness t, ranging from $t \ll \lambda_L$ to $t > \lambda_L$, where λ_L is the London's penetration depth [p.86 of reference 4].

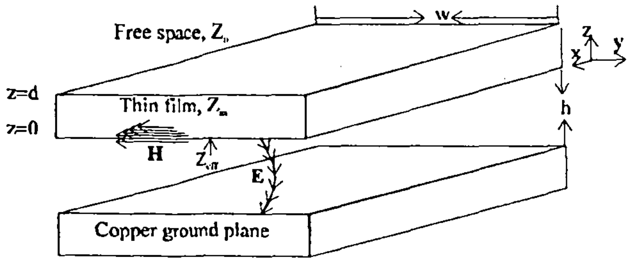

Fig. 1 Wide microstrip (w>>h). Assume that there is a lossless substrate between the plates.

For further insight into how films behave equation 2 needs to be split into its real and imaginary parts. From the Gorter and Casimir two-fluid model, we have $J=(J_n+J_s)E=(\sigma_1-j\sigma_2)E$. Here the normal fluid consists of unpaired charge carriers, where these carriers are identical to conduction electrons above T_c with a normal current density $J_n=\sigma_1 E$. The superconducting fluid consists of paired charge carriers, where the supercurrent density is given by $J_s=-j\sigma_2 E$. Assuming frequencies in the range of $\omega\tau<<1$ (typically for $f<10^{11}$Hz), where τ is the scattering time from Drude's theory for metal, we have $\sigma_2=1/\omega\mu_o\lambda_L^2$ [p.126 of the reference 2].

For microwave frequency range at liquid nitrogen temperature, we also have $\sigma_1<<\sigma_2$. Equation 2 then reduces to

$$Z_{eff}=\left(\frac{Z_{ss}}{w}\right)\coth\left[(t/\lambda_L)\left(1+j\frac{\sigma_1\omega\mu_0\lambda_L{}^2}{2}\right)\right] \qquad (3)$$

This equation can be split into real and imaginary parts by using coth(a+jb)=[sinh(2a)-jsinh(2b)]/[cosh(2a)-cos(2b)] and $Z_s=R_s+jX_s$. In addition, assuming a wide microstrip (w>>h) geometry, we can write $Z_{eff}=R_{eff}+jX_{eff}$ [5], where

$$R_{eff}=\frac{R_{ss}}{w}\left[\coth\left(t/\lambda_L\right)+\frac{t/\lambda_L}{\sinh^2\left(t/\lambda_L\right)}\right] \qquad (4.a)$$

$$X_{eff}=\frac{X_{ss}}{w}\left[\coth\left(t/\lambda_L\right)\right]=\omega\frac{L_{keff}}{w} \qquad (4.b),$$

where from two-fluid model $X_s=\mu_o\omega\lambda_L$ and $R_s=\omega\mu\lambda_L{}^3/\delta_n{}^2$.

The total inductance per unit length is given by $L_T=\phi/I$, where I is the current flowing along the line and ϕ is the sum of the flux between stripline, ground plane and flux through the conductor. The effect of the kinetic inductance of the superconducting carriers on the total inductance enables us to write the total inductance of the wide microstrip L_T as $L_T=L_m+L_{kef}$ [6]. Here L_m is the magnetic inductance between stripline and L_{kef} is the effective kinetic inductance. The external inductance per unit length for a wide microstrip is approximately given by $L_m=\mu_o h/w$.

A transmission line acts as a resonator at those frequencies for which it is an integer number n of half wavelengths long. The unloaded quality factor Q is given by $Q=2\pi f L_T/R$, where f_n is the microwave frequency of the resonant modes and R is the series resistance of the transmission line. Assuming that R_c is the surface resistance of the copper ground plane we finaly have a expression for Q as a function of both the film thickness and the penetration depth.

$$Q=\frac{2\pi f_n\mu[h+\lambda\coth(t/\lambda)]}{R_S[\coth(t/h)+\frac{t/\lambda}{(\sinh(t/\lambda))^2}]+R_C} \qquad (5)$$

3. Experiment and Results

Homogeneous Y-Ba-Cu and Ba-Cu-Ag solutions with the molar ratio of Y:Ba:Cu=2:1:1 and Ba:Cu:Ag=3:5:X (X=0-1.5)(035) where prepared by mixing the Y-oxylate and Ba, Cu and Ag-naphthenates in toluene [7]. Firstly, the 211 solution was coated on YSZ and heated in air to 500°C. This was repeated several times to build up a suitable film thickness. The films were then calcined at 900°C for 30-60 minutes to yield a 211 film. A controlled thickness of 035 (Ag) film was then formed on the surface of the 211 film. The two film sandwich was then heated under reduced pressure to form a silver loaded, textured, 123-YBCO film of ~ 1μm thickness by solid state reaction on the surface of the YSZ substrate. The films were then annealed under oxygen at 450°C.

Fig.2 shows the temperature dependence of magnetic susceptibility for a typical film. The films have a sharp superconducting transition at 90K.

The copper/superconducting microstrip resonator was formed by lying a sliced section of the thin film coated YSZ substrate on top of a copper ground plane as shown in Fig.3. The substrate dimensions were 2.4mm x 1.1mm x 9.4mm. The device was mounted in a brass housing, which remained hermetically sealed in liquid nitrogen at 77K. The microwave power was capacitively coupled into the ends of the resonators using k-connector pins. The coupling gap was at about 0.3 mm. Electrical contact between the copper ground plane and the box was aided by a thin layer of indium as well as by a BeCu spring.

The resonator response was measured in transmission using a HP8720A network analyser with a computer interface.

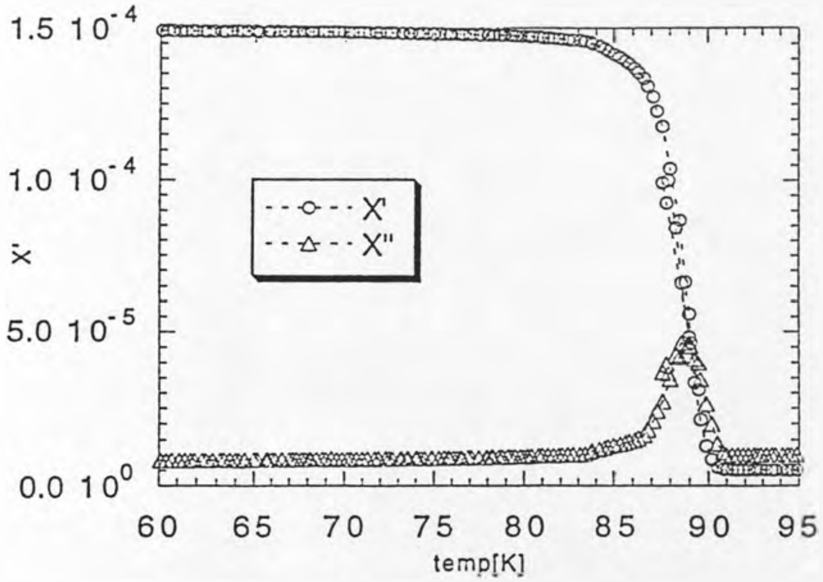

Figure.2 Temperature dependence of magnetic susceptibility.

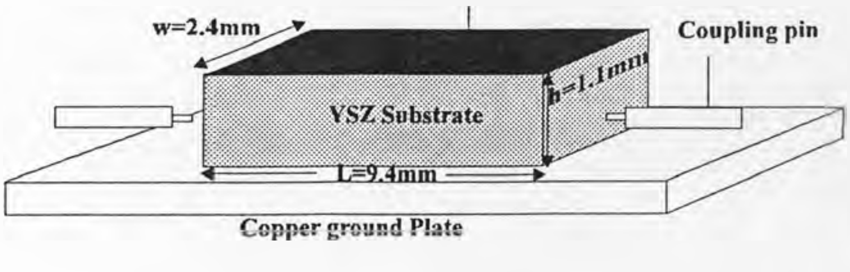

Figure.3 Hybrid 'copper/YBCO film made by pyrolysis' resonator device.

Figure.4 shows the frequency response of the superconducting resonator in range 0.13-20GHz for the same film as in figure.1. Four sharp resonance's peaks are shown.

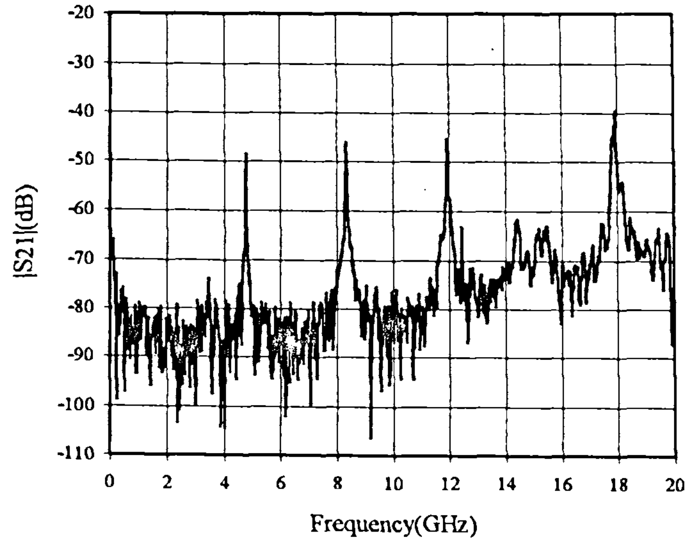

Figure.3 Frequency response from 0.13GHz to 20GHz.

The lower frequency resonant peaks are well defined and show no distortion over an extended dynamic range as shown in Figure.4.

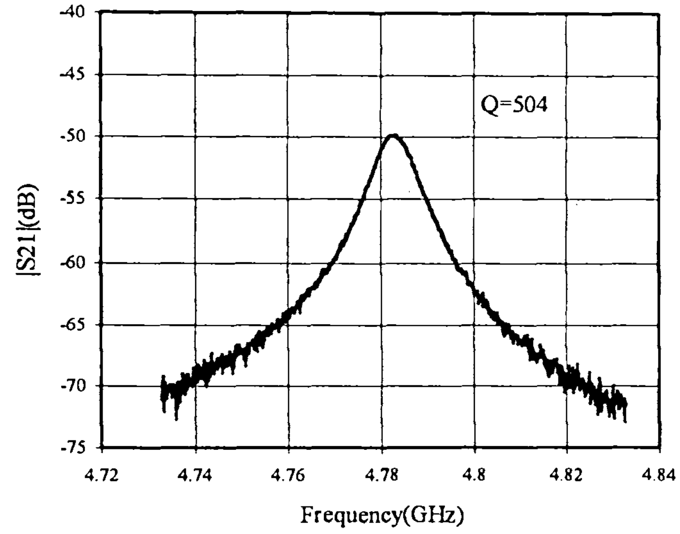

Figure.4 Frequency response around the fundamental resonance peak $f_o \cong 4.784$GHz. Loaded Quality factor $\cong$ 504.

4. Surface Resistance Calculation

For the above resonator the intrinsic surface resistance of the superconducting thick film (R_s) can be extract from the measured frequency response, shown in fig 4, by using the equation 5.

For an 'all copper resonator' we obtained $R_c \cong 17\text{m}\Omega$, in good agreement with published values. The films were ~ 1μm thick with a textured granular structure with grain size also ~ 1μm as determined from SEM surface measurements. Assuming a granular model, we can obtain an expression for the effective penetration depth [8] given by

$$\lambda_g = \left(\frac{\phi_o}{2\pi\mu a J_c} \right)^{1/2},$$

where ϕ_o is the flux quantum, a the grain size and J_c critical current density. λ_g was estimated from the measured critical current at 77K (2×10^3A/cm^2) to be 3.6μm (i.e. larger then the film thickness), so that the microwave surface resistance will be essentially identical to the dc resistance. Using the above expression for the Q-value, we derived a value for the surface resistance of 13mΩ.

4. Conclusion

YBCO films have been prepared on YSZ by the combination of dip pyrolysis and a diffusion reaction processes. The surface resistance of a typical film has been measured using a hybrid 'copper/YBCO film' resonator. The frequency response was measured over the frequency range 0.13GHz to 20GHz. The surface resistance at 4.784GHz was 13mΩ, at 77K, where the effect of the film thickness on the surface impedance has been taken into account.

Acknowledgements

This work was supported by the UK Science and Engineering Research Council. M. T. de Melo was supported by the Brazilian agency CNPq.

References

[1] N. Klein, H. Chaloupka, G. Muller, S. Orbach, H. Piel, B. Roas, L. Schultz, U. Klein and M. Peiniger, "The Effective Microwave Surface Impedance of High-Tc Thin Film". J. Apply. Phys., 67(11), pp. 6940-6945, 1990.

[2] T. V. Duzer & C. W. Turner, Principles of Superconductive Devices and Circuits: Elsevier, 1981.

[3] R. E. Matick, Transmission Lines for Digital and Communication Networks: McGraw-Hill Book Company, 1969.

[4] Z. Y. Shen, High temperature Superconducting Microwave Circuits: Artech house, 1994.

[5] P. Hartemann, "Effective and Intrinsic Surface Impedances of High -Tc Superconducting Thin Films". IEEE Transations on Applied Superconductivity, no 2, pp. 228-235, 1992.

[6] J. M Pond, K. R. Carrol, J. S. Horwitz, D. B. Chrisey, M. S. Osofsky and V. C. Cestone, "Penetration Depth and Microwave Loss Measurements with a $YBa_2Cu_3O_{7-\delta}$ / $LaAlO_3$ / $YBa_2Cu_3O_{7-\delta}$". Appl. Phys. Lett, 59(23), pp. 3033-3035, 1991.

[7] H. Yokota and J. S. Abell, "Preparation of YBCO films on YSZ and Silver Substrates by the Dipping Pyrolysis Process". M^2S - HTSC, Grenoble, France, July 1994, to be published.

[8] C. E. Gough in Superconducting Technology (edited by K. Fosshein). pp. 87-111, 1991.

Presented In the IEEE Colloquium on Advanced Signal Processing, Savoy Place, 29 November 1996

COPLANAR STRIPS INTERDIGITAL DELAY LINE FOR INSTANTANEOUS FREQUENCY MEASUREMENT SYSTEMS

M T De Melo, M J Lancaster and J S Hong

Abstract

The authors have studied a coplanar interdigital delay line with different finger lengths. Results of characteristic impedance and group delay are presented. Measurement results agree well with simulation and the transmission line seems attractive for the design of coplanar instantaneous frequency measurement subsystem (IFM). A prototype system is briefly discussed.

Introduction

Coplanar waveguide (CPW) is used extensively for microwave components including filters, couplers, mixers and amplifiers for the emerging wireless communication industry. However, as these components become more complex, problems occur due to imbalances between the two ground planes. This leads to unwanted slotline modes and signal distortion especially when bends are extensively needed. One possible solution to this problem is to use coplanar strips (CPS), however it is difficult to achieve 50Ω lines with this type of circuit on a high permittivity substrate. For a relative permittivity $\varepsilon_r = 10.8$, the line width w needs to be approximately 20 times bigger than the spacing s to attain a characteristic impedance of 50Ω. One method of getting around this is to increase the capacitance of the structure by using slow-wave transmission lines. Slow-wave transmission lines are extensively used to reduce the size of monolithic microwave integrated circuits (MMICs). This work aims to optimise a comb transmission line with coplanar strip interdigital fingers to be used as a delay line. Increasing the finger length, keeping all the other parameters fixed, one can easily reach 50Ω guaranteeing the etching tolerances. It is proposed to use high temperature superconductors to overcome the additional loss.

Instantaneous frequency measurement (IFM) subsystems are widely used in electronic warfare and electronic intelligence systems for the determination of unknown signals over a broad frequency band [1]. The discriminators provide different time delay intervals, where the delay signals are compared with the original ones for measuring the instantaneous frequency. The frequency resolution of the IFM depends on the length of the delays, which become in practice the principal elements of the subsystem. The delay lines are often designed with high numbers of bends in order to achieve the desired resolution. However, these bends increase the mutual reflections through the delays. Combining the results of group delay and characteristic impedance for the coplanar strip interdigital delay, it looks possible to integrate these delays with coplanar power splitters; and then form uniplanar IFM systems, without bends.

Slow-wave line structure

The schematic drawing of the structure proposed is shown in figure. 1. The particular line investigated consists of 164 interdigital fingers of equal length ℓ, finger width w, finger spacing s and total length L. d is the unit cell length representing the periodicity of the transmission line. If $d \ll \lambda$, an amount of lumped capacitance per unit length C_d/d is added to the shunt capacitance C.

School of Electronic and Electrical Engineering, Birmingham University, Edgbaston, Birmingham, B15 2TT, UK.

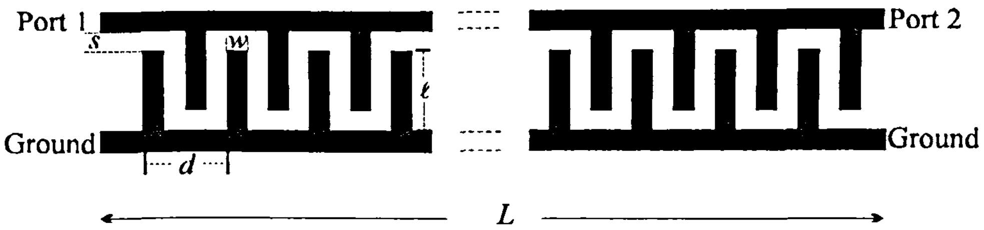

Figure 1 Coplanar Interdigital Delay Line under test.

For the structure shown in figure 1 the phase velocity and the characteristic impedance Z_0, become: $[(C + 2C_0/d)\, L_S\,]^{-1/2}$ and $[L_S\,/(\,C + 2\,C_0/d\,)]^{1/2}$, respectively. Here, L_S is the series inductance [2]. Due to the fringing electric fields about the fingers, the amount by which the capacitance per unit length increases is greater than the corresponding amount by which the inductance per unit length decreases. In order to exploit the fringing electric fields produced by the fingers, we need to increase the finger length and keep the finger width fixed.

The *ABCD* matrix of a lossless transmission line section of length *L*, line impedance Z_0 and phase constant β is given by

$$\begin{bmatrix} A & B \\ C & D \end{bmatrix} = \begin{bmatrix} \cos(\beta L) & j Z_0 \sin(\beta L) \\ (1/Z_0) j \sin(\beta L) & \cos(\beta L) \end{bmatrix} \qquad (1)$$

From the above equation one can relate Z_0 to only *B* and *C* elements. If we use the conversion from *ABCD* matrix to *S*-parameters and assume the source and load reference impedance as Z, we then have [3]

$$Z_0 = \sqrt{\frac{B}{C}} = \left[Z^2 \frac{(1+S_{11})(1+S_{22}) - S_{12}S_{21}}{(1-S_{11})(1-S_{22}) - S_{12}S_{21}} \right]^{1/2} \qquad (2)$$

Note that the *ABCD* matrix is not for a unit cell of the line, it represents the entire transmission line.

Group delay is the measurement of signal transmission time through a test device. It is defined as the derivative of the phase characteristic with respect to frequency. Assuming linear phase change $\phi_{21}(2) - \phi_{21}(1)$ over a specified frequency aperture f(2) – f(1), the group delay can, in practice, be obtained approximately by

$$\tau_g = -\frac{1}{2\pi}\left(\frac{\phi_{21}(2) - \phi_{21}(1)}{f(2) - f(1)}\right) \qquad (3)$$

Simulation and Experiment

The structure shown in figure 1 was etched on only one side of an RT/duroid 6010 with relative permittivity $\varepsilon_r = 10.8$, dielectric thickness $h = 0.64$ mm, conductor thickness $t = 35\,\mu\text{m}$, $w = 0.3$ mm, $s = 0.3$ mm and $L = 99$ mm. In order to find the line impedance and delay the simulation was carried out varying the finger length ℓ from 0.6 to 4.2 mm and keeping all the other parameters fixed. The devices were fabricated, measured and simulated.

The simulation used sonnet software in order to find the magnitude and phase of the *S*-parameters, assuming a lossless conductor. Afterwards, equations 2 and 3 were used to find Z_0 and τ_g, respectively. In the experimental procedure each device was connected with coaxial connectors to a HP8720A network analyser. After carrying out a proper calibration, the devices were then measured. This way, the group delay measurement was implemented, and figure 2 summarises the group delay results from both measurement and simulation for a frequency range of 0.5-3 GHz. As the finger length increases the lumped capacitance per unit length increases. It slows down the group velocity leading to an increase in the group delay. The longer the finger length, compared to the finger width, the closer it is to a purely capacitive element.

The experimental data of Z_0 were obtained using a reflection measurement in time domain low pass function of the HP8720A . The same devices were all measured again and the results are summarised in figure 3. Looking at the beginning of the curve on the left hand side, the figures seem to agree with the classical coplanar strips formulation, as we found $Z_0 = 99\Omega$ for $\ell = 0$ [4]. As we expected, Z_0 decreased as the finger length increased, due to the rise in $2C_0/d$, achieving 50Ω at $\ell = 3.9$mm. As the finger length goes from 0.6 mm to 4.2 mm, τg increases about 150% and Z_0 decreases about 45%.

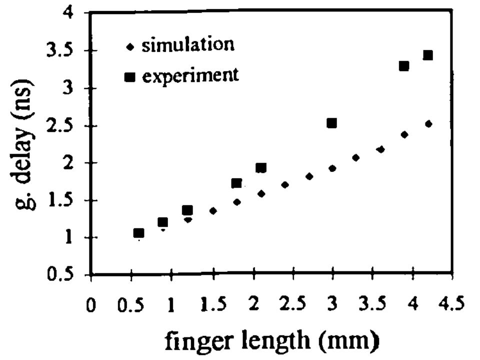

Figure 2 Group delay as a function of finger length at a Frequency range of 0.5-3 GHz.

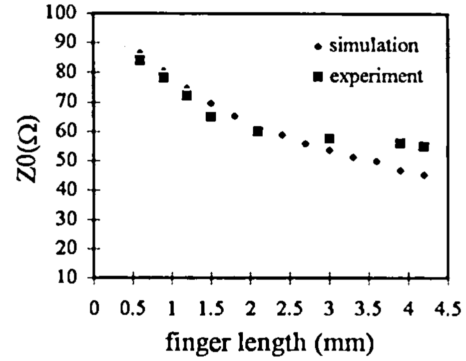

Figure 3 Characteristic Impedance as a function of finger length at a frequency range of 0.5-3 GHz.

These results look promising as far as an IFM application is concerned. Referring to a single stage of a typical IFM, a coplanar unequal output impedance power splitter can be designed to feed two delays with different characteristic impedances. The length of the second delay of each discriminator may be increased to achieve better resolution. The results from figures 1 and 2 may be used together to redesign the coplanar unequal output impedance power splitter to achieve the exact impedance matching. Figure 4 shows a prototype system fabricated based on results of figures 1 and 2. Coplanar wave guide, coplanar strips, coplanar unequal output impedance power splitter and coplanar interdigital delay line are integrated without bends or air bridges. The chip resistors used to increase the isolations between the outputs of the power splitter (and the input of the combiner) are not shown below.

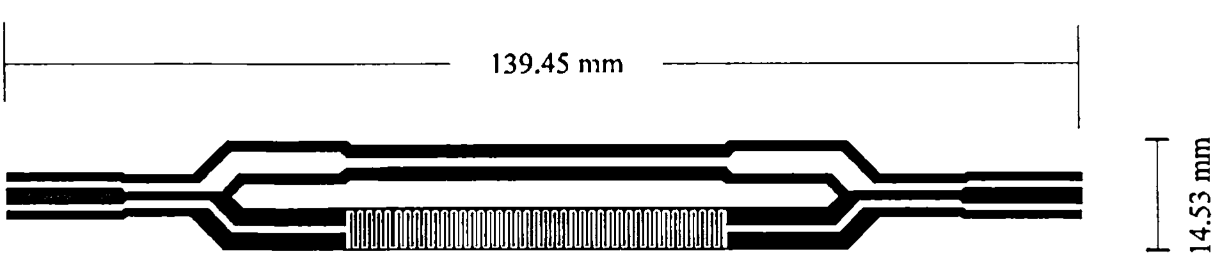

Figure 4 Uniplanar single stage of the IFM under test, scale 1/1.

The design has a delay difference of 1.6ns. Two output traces versus frequency from 1.5GHz to 3GHz are presented in figure 5. The theoretical one was obtained using the design equations for a single stage of a typical

IFM subsystem [5]. The oscillations in the experimental trace originated from the coaxial connections and the chip resistors bonds.

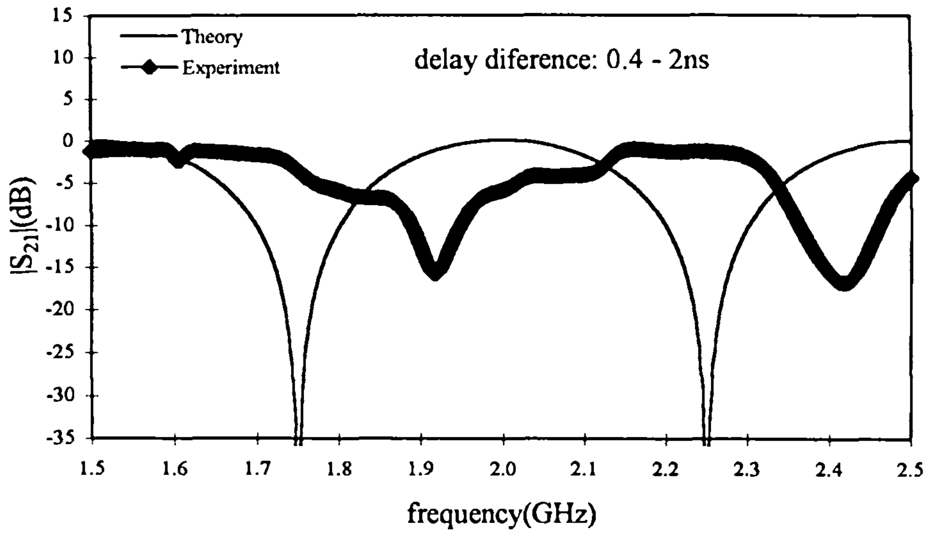

Figure 5 Theoretical interferometer output and measured scattering parameter in dB versus frequency.

Conclusions

Coplanar strips interdigital delay lines have been fabricated, simulated and measured at a frequency range of 0.5-3 GHz. As the finger length goes from 0.6 mm to 4.2 mm, keeping all the other parameters fixed, the group delay increases by about 150% and the characteristic impedance decreases about 45%. A prototype of uniplanar IFM with a delay difference of 1.6ns was fabricated and measured based on the results of the characteristic impedance and the group delay. We are currently performing measurements on a superconducting version of the IFM using a barrier layer of Yttria Stabilised Zirconia (YSZ) between $YBa_2Cu_3O_{7-\delta}$ and an alumina (Al_2O_3) substrate [6].

References

1. Liang, G C, Shien C F, Withers R S, Cole B F, Johansson M A and Suppan L P: "Superconductive digital instantaneous frequency measurement subsystem", IEEE Trans., MTT-16, pp 2368-2375, 1993.
2. Collin, R E: "Foundation for Microwave Engineering" (McGraw-Hill, 1992).
3. Kiziloglu K, Dagli N, Matthaei G L and Long S I: "Experimental analysis of transmission line parameters in high-speed gas digital circuit interconnects", IEEE Trans., MTT-39, pp 1361-1367, 1991.
4. Wen C P: "Coplanar waveguide: a surface strip transmission line suitable for nonreciprocal gyromagnetic device applications", IEEE Trans., MTT-17, pp 1087-1090, 1969.
5. East P W: "Design techniques and performance of digital IFM" *IEE Proc.*, Vol. 129, Pt. F, No. 3, June, 1982.
6. Watcham S C, Porch A, Kharel A P, Shields T C and Abell J S: "Yttria stabilised zirconia barrier layers by atmospheric plasma spraying" Proceeding of the 125th TMS Annual Meeting, 2-8 February 1996, Anaheim, California, USA.

References

[1.1] Onnes, H. K., "The resistance of pure mercury at helium temperature", Leiden comm 120b, (1911)

[1.2] Shen Z. Y., "High-Temperature Superconducting Microwave Circuits", Artech House, p1, (1994)

[1.3] Lyons W. G. and Withers R. S., "Passive Microwave Device Applications of high T_c Superconducting Thin Films", Microwave Journal, p85, November, (1990)

[1.4] Belohoubek E., Kalokitis D., Fathy A., Denlinger E., Pique A., Wu X. D., Gree S. M. and Venkatesan. "High Temperature Superconducting Components For Microwaves Systems. Applied Superconductivity", vol1, Nos 10-12, p1555, (1993)

[1.5] Babbitt R., Lenzing E., Wilber W., and Rachlin A., "Fabrication and Evolution of Superconducting Devices". Microwave Journal, p40, April (1991)

[1.6] Liang, G. C., Shien, C. F., Withers, R. S., Cole, B. F., Johansson, M. A. and Suppan, L. P., "Superconductive Digital Instantaneous Frequency Measurement Subsystem", IEEE Transation on Microwave Theory and Techniques , vol. 16, p2368, (1993)

[1.7] Goddard N. E., "Instantaneous Frequency-Measurement Receivers", IEEE Transation on Microwave Theory and Techniques, Vol. MTT-20, p292, March (1972)

[2.1.1] Wheeler, H. A., "Formulas for the Skin Effect", Proceedings of the I.R.E., 30, p412, (1942)

[2.2.1] Matick, R. E., "Transmission Lines for Digital and Communication Networks", McGraw - Hill Book Company, p108, (1969)

[2.2.2] Davidson C. W., "Transmission Line for Communications", The Macmillan Press LTD, p183, (1978)

[2.2.3] Ashcroft, N. W. & Mermin, N. D., "Solid State Physics", W. B. Saunders Company, chapter1, (1976)

[2.2.4] David R. Tilley and John Tilley., "Superfluidity and Superconductivity", Adam Hilger, p143.(1990)

[2.2.5] Matick, R. E., "Transmission Lines for Digital and Communication Networks", McGraw - Hill Book Company, p125, (1969)

[2.3.1.1] London F. and H. London, "The Electromagnetic Equations of The Superconductor", Proc. Roy. Soc. (London), vol. A149, p71, (1935)

[2.3.1.2] Cyrot M. and D. Pavuna, "Introduction to Superconductivity And High-Tc Materials", World Scientific Publishing Co. Pte. Ltd, p50, (1992)

[2.3.1.3] Ashcroft, N. W. & Mermin, N. D., "Solid State Physics", W. B. Saunders Company, p737, (1976)

[2.3.2.1] Bardeen, J., Cooper L. N. and Schrieffer J. R., "Theory of superconductivity ", Phys. Rev., 108, p1175, (1957) [2.3.2.2] Tinkam, M., "Introduction to Superconductivity", McGraw-Hill Kogakusha Ltd, p7, (1975)

[2.3.2.3] Pippard, A. B., "An Experimental and Theoretical Study of the Relation Between Magnetic Field an Current in a Superconductor", Proc. Roy. Soc. (London), A216, p547, (1953)

[2.3.2.4] Piel, H. and Muller, G., "The Microwave Surface Impedance of High-Tc Superconductors", IEEE Transactions On Magnetics, 27, p854, (1991)

[2.3.3.1] Duzer, T. V. & Turner, C. W., "Principles of Superconductive Devices and Circuits", New York, Oxford, p126, (1981)

[2.3.3.2] Gallop, J. C. and Radcliffe, W. J., "Characterisation of Microwave Surface Impedance of High Temperature Superconductors", Supercond. Sci. Technol., 4, p568, (1991)

[2.3.3.3] Sheen D. M., Ali S. M., Oates D. E., Withers R. S. and Kong J. A., "Current Distribution, Resistance, and Inductance for Superconducting Strip Transmission Lines", IEEE Transaction on Applied Superconductivity, 1, no 2 , p108, (1991)

[2.3.3.4] Rauch W. and E. Gotnik., "Microwave Properties of YBa_2Cu3O_{7-X} Thin Films Studied With Coplanar Transmission Line Resonators", J. Appl. Phys, vol.74(4), p1866, (1993)

[2.3.4.1] C. E. Gough in Superconducting Technology (edited by K. Fosshein), p98, (1991)

[2.3.4.2] Hinken, J. H., "Superconductor Electronics", Spring-Verlag, p62, (1989) [3.1.1] Schneider, M. V., "Microstrip Lines for Microwave Integrated Circuits", Bell System Technical Journal, 48, p1421, (1969)

[3.1.2] Pucel, R. A. and Massé, D. J., "Losses in Microstrip", IEEE Transactions on Microwave Theory and Techniques , MTT-16, p342, (1968)

[3.1.3] Bhal, I., J. and Trivedi, D., K., "A Design's Guide to Microstrip Line", Microwaves, May, p174, (1977)

[3.2.1] Matick, R. E., "Transmission Lines for Digital and Communication Networks", McGraw - Hill Book Company, p318, (1969)

[3.3.1] Pozar, D. M., "Microwave Engineering" Addison-Wesley Publishing company, p338, (1990)

[3.3.2] Pozar, D. M., "Microwave Engineering", Addison-Wesley Publishing company, p72, (1990)

[3.4.1] Pucel, R. A. and Massé, D. J., "Losses in Microstrip", IEEE Transactions on Microwave Theory and Techniques , MTT-16, p342, (1968)

[3.4.2] Schneider, M. V., "Microstrip Lines for Microwave Integrated Circuits", Bell System Technical Journal, 48, p1421, (1969)

[3.5.1] Wheeler, H. A., "Formulas for the Skin Effect", Proceedings of the I.R.E., 30, p412, (1942)

[3.5.2] Davidson C. W., "Transmission Line for Communications", The Macmillan Press LTD, p186, (1978) [3.5.3] Schneider, M. V., "Microstrip Lines for Microwave Integrated Circuits", Bell System Technical Journal, 48, p1421, (1969)

[3.5.4] Wheeler, H. A., "Formulas for the Skin Effect", Proceedings of the I.R.E., 30, p412, (1942)

[3.5.5] Schneider, M. V., "Microstrip Lines for Microwave Integrated Circuits", Bell System Technical Journal, 48, p1421, (1969)

[4.1.1] Klein, N., Chaloupka, H., Muller, G., Orbach, S., Piel, H., Roas, B., Schultz, L., Klein, U. and Peiniger, M., "The Effective Microwave Surface Impedance of High-Tc Thin Film", J. Appl. Phys., 67(11), p6940, (1990)

[4.1.2] Hartemann, P., "Effective and Intrinsic Surface Impedances of High -Tc Superconducting Thin Films", IEEE Transactions on Applied Superconductivity, 2, p228, (1992)

[4.1.3] Pinto R., Chourey A., G. and Apte P., R., "Effective Surface Resistance of $LuBa_2Cu_3O_{7-\delta}$ Thin Films", Appl. Phys. Lett. 64(16), p2166, (1994)

[4.1.4] Robert E. T., Rodrigue G. P. and Palmer N. P., "Field Response of Ultra-Thin Type II Superconducting Transmission Lines", IEEE Transactions on Applied Superconductivity, 4, p65, (1994)

[4.2.1] Klein, N., Chaloupka, H., Muller, G., Orbach, S., Piel, H., Roas, B., Schultz, L., Klein, U. and Peiniger, M., "The Effective Microwave Surface Impedance of High-Tc Thin Film", J. Appl. Phys., 67(11), p6940, (1990) [4.2.2] Cheng, D. K., "Field and Wave Electromagnetics", Addison - Wesley Publishing Company, p395, (1983)

[4.2.3] De Melo, M. T., M. Phil. Thesis, University of Birmingham, p36, (1995)

[4.2.4] Porch, A. and Lancaster, M. J., "Coplanar Resonator Fabricated from Thin Film $YBa_2Cu_3O_7$". Submitted to J. Appl. Phys., (1992)

[4.3.1] Pond, J. M., Carrol, K. R., Horwitz, J. S., Chrisey, D. B., Osofsky, M. S. and Cestone, V. C., "Penetration Depth and Microwave Loss Measurements with a $YBa_2Cu3O_{7-\delta}$ / $LaAlO_3$ / $YBa_2Cu_3O_{7-\delta}$",Appl. Phys. Lett., 59(23), p3033, (1991)

[5.1.1] Lynds L., Weinberger B. R., Potrepka D. M., Peterson G. G. and Lindsay M. P., "High Temperature Superconducting Thin Films: The Physics of Pulsed Laser Ablation", Physica C, 159, p61, (1989)

[5.1.2] Watcham S C, Porch A, Kharel A P, Shields T C and Abell J S: "Yttria stabilised zirconia barrier layers by atmospheric plasma spraying" Proceeding of the 125th TMS Annual Meeting, 2-8 February 1996, Anaheim, California, USA

[5.2.1] Shindé S. L. and Rudman D. A., "Interfaces in High-Tc Superconducting Systems", Spring-Verlag, p5, (1994)

[5.2.2] Cyrot M. and D. Pavuna, "Introduction to Superconductivity And High-Tc Materials", World Scientific Publishing Co. Pte. Ltd, p213, (1992) [5.2.3] Hein M. A. in "Studies of High-Temperature", Vol. 18, A. Narlikar Editor, Nova Science Publishers, New York, p141, (1996)

[5.3.1] Lancaster M. J., Woodall P., Muirhead C. M., Gough C. E., Abell S., Wellhofer F., Edwards P. P., Greaves C., Huang F. and Maclean T. S. M. in "Research Report of School of Electronic & Electrical Engineering of The University of Birmingham", p22, (1992)

[5.3.2] Jedamzik D., "Thin Film Growth and Properties of High-Tc Superconductors", GEC Journal of Research, Vol. 18, No. 2, p92, (1990)

[5.3.3] Lynds L., Weinberger B. R., Potrepka D. M., Peterson G. G. and Lindsay M. P., "High Temperature Superconducting Thin Films: The Physics of Pulsed Laser Ablation", Physica C, 159, p61, (1989)

[5.4.1] Yokota, H. and Abell, J. S., "Preparation of YBCO films on YSZ and Silver by the Dipping Pyrolysis Process", Physica C, 235-240, p629, (1994)

[5.4.2] Manabe T., Kond W., Mizuta S. and Kumagi T., "Preparation of Superconducting Ba2YCu3O7-y-Ag composite films on sapphire by the dipping pyrolysis process", Appl. Phys. Lett. 60(26), p3301, (1992)

[5.4.3] Kumagi T., Manabe T., Kond W., and Mizuta S., "Preparation of high Jc Ba2YCu3O7-y-Ag composite films on SrTiO3 (100) Substrate by the dipping- pyrolysis process", Appl. Phys. Lett. 61(8), p990, (1992) [5.5.1] Watcham S. C., Porch A., Kharel A. P., Shields T. C. and Abell J.S. Proceeding of the 125th TMS Annual Meeting, 2-8 February (1996), Anaheim, California, USA

[5.5.2] Ramakrishnan T. V. and Rao C. N. R., "Superconductivity Today ", Edited by S. F. Biswas, p36, (1992)

[6.1.1] Reible, S. A. and Wilker, C. W., "Parallel Plate Resonator for Accurate RF Surface loss Measurements", IEEE Transactions on Magnetics, 27, p2813, (1991)

[6.1.2] Kuhn, M., Klinger, M., Baranyak, A. and Hinken, J. H., "HTSC Inverted and Conventional Geometry Microstrip Resonator for UHF Frequencies", IEEE Transactions on Magnetics, 27, p2809, (1991)

[6.1.3] Porch A., Ph.D. thesis. Faculty of Physics and Chemistry, University of Cambridge, June (1991)

[6.4.1] Pond, J. M., Carrol, K. R., Horwitz, J. S., Chrisey, D. B., Osofsky, M. S. and Cestone, V. C., "Penetration Depth and Microwave Loss Measurements with a $YBa_2Cu3O_{7-\delta}$ / $LaAlO_3$ / $YBa_2Cu_3O_{7-\delta}$", Appl. Phys. Lett., 59(23), p3033, (1991)

[6.6.1] De Melo, M. T., Lancaster M. J. and Gough C. E., "High Temperature Superconducting Microwave Resonators for the Measurements of films made by pyrolysis", Proceedings of 1995 SBMO/MTT-S International Microwave Optoelectronics Coference., P019, july, Rio de Janeiro, Brazil.

[6.6.2] Woodall P., Lancaster M. J., Maclean T. S. M., Gough C. E. and Alford N. McN., "Measurement of the Surface Resistance of $YBa_2Cu_3O_{7-\delta}$ By The Use of A Coaxial Resonator", IEEE Transactions on Magnetics, 27, No. 2, p1264, (1991)

[6.7.1] Pozar, D. M., "Microwave Engineering", Addison-Wesley Publishing company, p342, (1990)

[6.7.2] Porch, A., Ph.D. thesis, p.56. Faculty of Physics and Chemistry, University of Cambridge, June (1991)

[6.7.3] Neifeld R. A., Potenziani E., Sinclair W. R., Hill III W., Turner B. and Pinkas A., "Properties of the ablation process for excimer laser ablation of $Y_1Ba_2Cu_3O_7$", J. Appl. Phys. 69(2), p1107, January (1991)

[6.7.4] Porch, A., Lancaster M. J., Humphreys R. G. and Chew N. G. "Surface Impedance Measurements of $YBa_2Cu_3O_7$ Thin Films Using Coplanar Resonators". IEEE Transactions on Applied Superconductivity, 3, p1719, (1993)

[7.1.1] Wen C. P., "Coplanar Waveguide: A Surface Strip Transmission Line Suitable for Nonreciprocal Gyromagnetic Devices Applications", IEEE Transactions on Microwave Theory and Techniques , MTT-17, NO. 12, p1087, (1969)

[7.1.2] Davis, M. E., Williams E. W. and Celestini A. C. "Finite-Boundary Corrections to the Coplanar Waveguide Analysis", IEEE Transactions on Microwave Theory and Techniques, p594, September (1973)

[7.1.3] Hatsuda T., "Computation of Coplanar Type Strip-Line Characteristics by Relaxation method and its application to Microwave Circuits", IEEE Transactions on Microwave Theory and Techniques, Vol. MTT-23 no.10, p795, October (1975)

[7.2.1] Gupta K. C., Garg R. and Bahl I. J., "Microstrip Lines and Slotlines", Artech House, p258, (1979)

[7.2.2] Wen C. P., "Coplanar Waveguide: A Surface Strip Transmission Line Suitable for Nonreciprocal Gyromagnetic Devices Applications", IEEE Transactions on Microwave Theory and Techniques , MTT-17, NO. 12, p1087, (1969)

[7.2.3] Mathews J. and Walker R. L., "Mathematical Methods of Physics", W. A. Benjamin, Inc. p206, (1970)

[7.2.4] Hilberg W., "From Approximations to Exact Relations for Characteristic Impedances", IEEE Transactions on Microwave Theory and Techniques, Vol. MTT-17 no.5, p259, May (1969)

[7.3.1] Jaisson, D., "An Asymmetrical Coplanar Waveguide for use with a Coplanar Wilkinson Power", Microwave Journal, , november, p68, (1995)

[7.3.2] Gupta K. C., Garg R. and Bahl I. J., "Microstrip Lines and Slotlines", Artech House, p259,(1979) [7.4.1] Veyres C., and Fouad Hanna V., "Extension of the application of conformal mapping techniques to coplanar lines with finite dimension", Int. J. Electron., vol.48, no1, p 47, July (1980)

[7.4.2] Mathews J. and Walker R. L., "Mathematical Method of Physics", W. A. Benjamin, Inc. p206, (1970)

[7.4.3] Ghione G. and Naldi C. U., "Coplanar waveguides for MMIC applications: Effect of upper Shielding, conductor backing, finite-extent ground planes and line-to-line coupling", IEEE Transation on Microwave Theory and Techniques, Vol. MTT-35 no.3, p260, March (1987)

[7.4.4] Wentworth M. S., Neikirk, D. P. and Brahce C. R., "The high-frequency characteristic of tape automated bonding (TAB) interconnects", IEEE Transation on components, hybrids, and manufacturing technology, Vol.12, no.3, p340, September (1989)

[8.1.1] Pozar, D. M., "Microwave Engineering", Addison-Wesley Publishing company, p.220, (1990)

[8.1.2] Gupta K. C., Garg R. and Chadha R., "Computer Aided Design of Microwave Circuit", Artech House, p25, (1981)

[8.1.3] Gupta K. C., Garg R. and Chadha R., "Computer Aided Design of Microwave Circuit", Artech House, p433, (1981)

[8.2.1] Fooks E. H. and Zakarevivius R. A., "Microwave Engineering Using Microstrip Circuits", Prentice Hall, p16, (1990) [8.2.2] Pozar, D. M., "Microwave Engineering", Addison-Wesley Publishing company, p221, (1990)

[8.3.1] Fooks E. H. and Zakarevivius R. A., "Microwave Engineering Using Microstrip Circuits", Prentice Hall, p28, (1990)

[8.3.2] Collin R. E., "Foundation for Microwave Engineering", McGraw-Hill, Inc., p258, (1992)

[8.4.1] Pozar, D. M., "Microwave Engineering", Addison-Wesley Publishing company, p235, (1990)

[8.4.2] Kiziloglu K., Dagli N., Matthaei G. L. and Long S. I., "Experimental analysis of Transmission Line Parameters in High-Speed GaAs Digital Circuit Interconnects", IEEE Trans., MTT-39, p1361, (1991)

[8.5.1] Blinchikoff H. J. & Zverev A. I., "Filtering In the Time and Frequency Domains", John Wiley & Sons., p66, (1976)

[8.5.2] Hewlett Packard, "HP 8720A Network Analyser System Operating and Programming manual", Part No. 08720-90015 , March (1988)

[8.6.1] Mathews J. and Walker R. L., "Mathematical Method of Physics", W. A. Benjamin, Inc. p102, (1970)

[8.6.2] Blinchikoff H. J. & Zverev A. I., "Filtering In the Time and Frequency Domains", John Wiley & Sons., p21, (1976) [9.1.1] Goddard N. E., "Instantaneous Frequency-Measurement Receivers", IEEE Transation on Microwave Theory and Techniques, Vol. MTT-20, p292, March (1972)

[9.1.2] Bauman R., "Digital Instantaneous Frequency Measurement for EW Receivers", Microwave Journal. p147, February (1985)

[9.1.3] Livingston, N.J., "Ultra-Wideband IFM Receivers", Microwave Journal. p142, April (1991)

[9.1.4] Sullivan W. B., "Simultaneous Signal Errors in Wideband IFM Receivers", Microwave Journal, p86, September (1995)

[9.1.5] Liang, G. C., Shien, C. F., Withers, R. S., Cole, B. F., Johansson, M. A. and Suppan, L. P., "Superconductive Digital Instantaneous Frequency Measurement Subsystem", IEEE Transation on Microwave Theory and Techniques , vol. 16, p2368, (1993)

[9.1.6] Biehl, M., Vogt, A., Herwig, R., Neuhaus, M., Crocoll, E., Lochschmied, R., Scherer, T. and Jutzi, W., "A 4 Bit Instantaneous Frequency Meter at 10 Ghz with Coplanar YBCO Delay Line", ASC-94, Boston, Massachusetts, USA, October, (1994)

[9.1.7] Jaisson, D., "A Suspended Bridge For Coplanar Waveguides", Microwave Journal, p280, May (1995)

[9.2.1] Liang, G. C., Shien, C. F., Withers, R. S., Cole, B. F., Johansson, M. A. and Suppan, L. P., "Superconductive Digital Instantaneous Frequency Measurement Subsystem", IEEE Transactions on Microwave Theory and Techniques, vol. 16, p2368, (1993)

[9.2.2] East P. W., "Design Techniques and Performance of Digital IFM". IEE Proc., Vol. 129, Pt. F, No. 3, June, (1982)

[9.2.3] Lancaster M. J., "Passive Microwave Device Applications of High Temperature Superconductors", Cambridge University Press, (1996)

[9.3.1.1] Sonnet Software, Inc. "Sonnet User's Manual", Release 2.4, September (1993)

[9.3.2.1.1] Collin R. E., "Foundation for Microwave Engineering", McGraw-Hill, Inc., p551, (1992)

[9.3.2.3.1] Pozar, D. M., "Microwave Engineering", Addison-Wesley Publishing company, p97, (1990)

[9.3.2.3.2] Collin R. E., "Foundation for Microwave Engineering", McGraw-Hill, Inc., p555, (1992)

[9.3.2.3.3] Spickermann R. and Dagli N. "Experimental Analysis of Millimeter Wave Coplanar Waveguide Slow Wave Structures on GaAs", IEEE Transactions on Microwave Theory and Techniques, vol. 42, p1918, (1994)

[9.4.1.1] Wilkinson, E. J., "An N-Way Hybrid Power Divider", IRE Transactions on Microwave Theory and Techniques, vol. 8, p116, (1960) [9.4.1.2] Parad L. I. And Moynihan R. L., "Split-Tee Power Divider", IEEE Transaction on Microwave Theory and Techniques, vol. 13, p91, (1965)

[10.2.2.1] Hewlett Packard, Hp 8720A Network Analyser System Operating and Programming manual, part No. 08720-90015 , March (1988)

[10.3.1.1] Wadell B. C., Transmission Line Design Handbook, Artech House, p85, (1991)

[10.3.1.2] Laverghetta T., "Microwave Materials and Fabrication Techniques", Artech House, p78, (1991)

[10.3.2.1] Pozar, D. M., "Microwave Engineering", Addison-Wesley Publishing company, p394, (1990)

[10.4.3.1] Biehl, M., Vogt, A., Herwig, R., Neuhaus, M., Crocoll, E., Lochschmied, R., Scherer, T. and Jutzi, W., "A 4 Bit Instantaneous Frequency Meter at 10 Ghz with Coplanar YBCO Delay Line", ASC-94, Boston, Massachusetts, USA, October, (1994)

[10.4.3.2] Liang, G. C., Shien, C. F., Withers, R. S., Cole, B. F., Johansson, M. A. and Suppan, L. P., "Superconductive Digital Instantaneous Frequency Measurement Subsystem", IEEE Transation on Microwave Theory and Techniques , vol. 16, p2368, (1993)

[11.2.1] De Melo, M. T., Lancaster M. J. and Hong, J. S., "Coplanar Strips Interdigital Delay Line For Instantaneous Frequency Measurement Systems", Colloquium on Advanced Signal Processing For Microwave Application, IEEE, Savoy Place, London, UK, 29 November, (1996) [Ap.II.1] Abbas, F., Davis, L. E. and Gallop, J. C., "Field Solution for a Thin-Film Superconducting Parallel-Plate Transmission Line", Physica C, 215, pp132, (1993)

[Ap.II.2] Matick, R. E., "Transmission Lines for Digital and Communication Networks", McGraw - Hill Book Company, p16, (1969)

[Ap.II.3] Pozar, D. M., "Microwave Engineering", Addison-Wesley Publishing company, p338, (1990)

[ApIII.5.1] Wadell B. C., Transmission Line Design Handbook, Artech House, p85, (1991)

[ApIII.5.2] Gupta K. C., Garg R. and Bahl I. J., "Microstrip Lines and Slotlines", Artech House, p275, (1979)